A Simple Force Feedback Accelerometer/Seismometer Based on a Tuning Fork Displacement Sensor

by
David Stuart-Watson

Thesis Presented for the Degree of
DOCTOR OF PHILOSOPHY
in the Department of Electrical Engineering
UNIVERSITY OF CAPE TOWN
August 2005

Declaration

This thesis is being presented for the degree of Doctor of Philosophy in the Department of Electrical Engineering at the University of Cape Town. It has not been submitted before for any degree or examination at this or any other university. This author confirms that it is his own original work. Portions of the work have been published in condensed form in the journal *Review of Scientific Instruments* and in the conference proceedings at the *First African Control Conference (2003)*: the author confirms in accordance with University rule GP7 that he was the primary researcher in all instances where work described in this thesis was published under joint authorship.

David Stuart-Watson

15 August 2005.

Acknowledgments

I would like to thank my supervisor, Prof. J. Tapson, for all his help and support throughout the project. I would also like to thank B. Prenzlow for all the technical and non-technical discussions shared in the office. My family, friends and especially Sarah Makin also deserve my thanks, not so much for the technical stuff, but all the important bits in between.

The author received financial support from the National Research Foundation (NRF) and the University of Cape Town.

Abstract

This thesis describes research into the use of a piezoelectric tuning fork as the displacement sensor in a simple force feedback seismometer. The research also includes the use of a second piezoelectric transducer as both the suspension system and the force transducer for the seismometer.

A simple inertial seismometer model, based on a damped mass-spring system, was developed. This model was used to explore the frequency response of the suspended mass, and its relative output displacement to an input displacement, velocity or acceleration.

An extended control model for the application of force feedback was discussed. A number of alternate displacement sensors, and their potential for use in force feedback seismometer systems, were investigated.

Each tine of the tuning fork was modelled as a separate vibrating cantilever. This mechanical model was then combined with an electrical equivalent circuit model. The overall model was then tested with actual data obtained from a $32.768kHz$ piezoelectric tuning fork. The actual data matched the theoretical response very closely, proving the accuracy of both the mechanical and electrical model. From a simple noise analysis on the system the fundamental limits of the tuning fork's ability to measure displacement was obtained.

Operating the tuning fork as a displacement sensor required the measurement of its output magnitude, and the phase measurement between the input and output sinusoidal waveforms. Digital measurement systems were excluded as they required very high sampling rates to achieve the required accuracy. Magnitude measurement was done using a simple filtered rectifier. The importance of isolating the phase measurement from the magnitude measurement led to the discussion of many different phase detectors. Logic gate phase detectors were, however, the only simple phase detectors capable of measuring phase without letting changes in magnitude influence the measurements.

A shift in displacement was modelled as a change in the forces in the piezoelectric tuning fork model. This change in force shifts the operating characteristics of the fork, which can then be modelled as simply a change in operating frequency. For any shift of displacement, modelled as a change in operating frequency, the output motion of the tuning fork can be divided into two transient motions and one steady state motion. A new method had to be developed for the combination of the transient and steady state responses into one total response. This total response was then used to develop both the control models and the controllers for keeping the tuning fork operating at a specific point in its resonant band. From the control models it was found that it is advantageous to use phase rather than magnitude to control the crystal.

For the application of the force feedback response, mechanical models of the piezoelectric transducers were derived, and the sensitivity of the suspension system was obtained. Numerous approach tests were also completed to find the most sensitive physical arrangement of the tuning fork seismometer. In the application of force feedback, two different control loops were required. Using phase and resonant frequency as the control variables in these loops proved to offer a better solution than using magnitude and phase.

A simple tuning fork seismometer was designed and tested. It was compared to two conventional devices to establish both the sensitivity and bandwidth. The object of the test was not to be completely noise free, but rather to test the concept of the tuning fork seismometer. The tests gave a bandwidth of *DC-25Hz*, with an estimated sensitivity of $23\mu g$. Noise signals produced in the operation and measurement limited the sensitivity and bandwidth.

This thesis explored the previously unexamined option of using a piezoelectric tuning fork in conjunction with a piezoelectric transducer to form a simple force balanced seismometer. The results obtained go some way in indicating the potential of using this system in future seismometer design.

Contents

Chapter 1

Introduction

1.1 Thesis Overview

The aim of this thesis was to investigate the use of a piezoelectric tuning fork as the displacement sensor in a simple force feedback seismometer. The investigation includes the use of a second piezoelectric transducer as both the suspension system and the force transducer of the force balance seismometer. Physically the piezoelectric transducer is located in close proximity to the tuning fork, and suspended in such a way that external motion of the ground produces a relative motion in the transducer.

Although never actually touching the tuning fork, the displacement of the transducer can be accurately measured by monitoring the forces between the tuning fork and transducer. The strength of these forces are highly dependent on the displacement between the two devices. The operating characteristics of the tuning fork are affected by these intersurface forces and will also change rapidly with a change in displacement. Therefore by monitoring the characteristics of the tuning fork, a very accurate measure of the displacement between the tuning fork and piezoelectric transducer can be obtained.

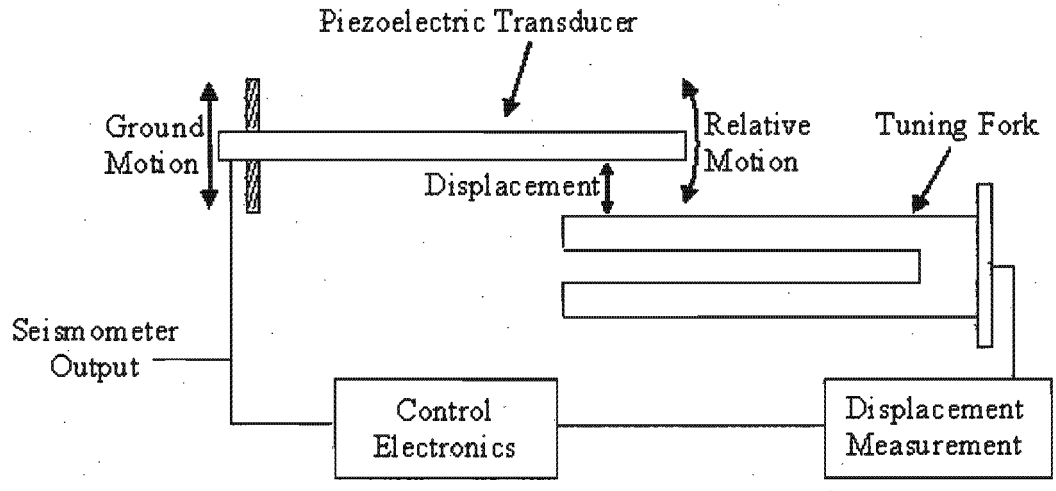

Figure 1.1.1: An Overview of the Force Feedback Tuning Fork Seismometer. *For any ground motion there will be a corresponding relative motion of the piezoelectric transducer. However, the tuning fork measures the relative motion and adjusts the voltage to the piezoelectric transducer. This moves the transducer back to its initial position effectively eliminating the relative motion. The control voltage to the piezoelectric transducer is proportional to the relative motion and becomes the output of the seismometer.*

However, the principle behind any force feedback seismometer is not to measure the relative displacement between the ground and the suspended mass, but rather to measure how much force is required to keep the mass still. In this case the force is supplied by applying a voltage to the piezoelectric transducer. For any given ground motion, the relative motion of the piezoelectric transducer is governed by the mass spring characteristics formed by the suspended transducer. However, the relative displacement motion is measured by the tuning fork and the voltage to the piezoelectric transducer is altered to move the transducer back to its original position. Thus, by accurate control of the transducer voltage, the relative motion between the tuning fork and the piezoelectric transducer is kept to an absolute minimum. The control voltage of the piezoelectric tuning fork is proportional to the relative motion and is used as the output of the seismometer.

This thesis builds up the study from the background on seismometers, to the modelling of all individual components, and finally to the construction and building of a simple tuning fork seismometer. It details the systems that control both the operation of the tuning fork and the displacement between the tuning fork and the transducer. The fundamental limits of the

operation of the tuning fork as a displacement sensor are discussed along with the various other factors that influence the bandwidth and sensitivity of the tuning fork seismometer.

In the rest of Chapter 1, the background of inertial force feedback seismometers is developed. The inertial seismometer is modelled as a damped suspended mass system, and the various equations governing its behaviour are derived. The force feedback principle is expanded, and includes a detailed control model for the system. Finally, various displacement sensors, and their potential for use in force feedback seismometers, are discussed.

In Chapter 2 the contact model for the interaction between the piezoelectric transducer and the tuning fork is developed. The contact model is separated into the intersurface forces, and the forces due to the motion of the air between the two surfaces. The intersurface forces are built up from interatomic forces which combine to form intermolecular forces, which are then combined to form the intersurface forces. Various equations modelling the effect of the passage of air between the surfaces are discussed in detail. The relative strengths and distance dependence of each component of the contact model play an important role in determining the optimal sensitivity position in Chapter 5 of the thesis.

Chapter 3 is concerned with the electrical and mechanical modelling of the piezoelectric tuning fork. A vibrating cantilever is used to model each of the tines of the tuning fork separately. The equivalent electrical circuit of the piezoelectric tuning fork is developed, along with a simple measurement circuit, in order to measure the vibration characteristics of the fork. The combined electrical and mechanical model is tested and found to be an accurate representation of the tuning fork behaviour. A noise analysis of the system is also completed to ascertain the fundamental limits of the tuning fork's ability to measure displacement.

The actual operation of the tuning fork is detailed in Chapter 4. The accurate measurement of phase and magnitude, which are the two main outputs from the fork, is discussed in terms of the required sensitivity and bandwidth. A model for a change in displacement, and its effects on the magnitude and phase characteristics of the tuning fork, is developed, and then thoroughly tested. Control models are developed and used to design feedback control systems, which keep the tuning fork crystal operating at a fixed point in its resonant band, using either phase or magnitude.

In Chapter 5 the application of the force feedback effect is discussed. Using similar electrical

and mechanical models to the ones developed in Chapter 3, the characteristics of the piezoelectric transducers are derived. Using the piezoelectric transducers the tuning fork is approached in several different physical arrangements. The theoretical models from Chapter 2 are used in conjunction with the approach test results to determine the optimal physical arrangement, and initial displacement, of the piezoelectric transducer and the tuning fork. Two different control strategies for the operation of the tuning fork and the application of force feedback are developed and discussed.

Chapter 6 details the construction and testing of a simple force feedback tuning fork seismometer. The testing procedure used and signal interpretation is also detailed. The output of the tuning fork seismometer is compared with other motion measurement devices to determine both its sensitivity and bandwidth. Although not completely noise free, the simple system goes along way to showing that the piezoelectric tuning fork in conjunction with a piezoelectric transducer can effectively be used as a seismometer.

1.2 An Introduction to Inertial Accelerometer/Seismometers

Seismometers, in their simplest sense, are instruments used to detect the surface motion, or seismic movements, of the ground. Many seismometers are specialised accelerometers designed specifically to measure the low magnitudes and frequencies of the Earth's accelerations. There are two distinct types of seismometers. Strain seismometers determine the ground motion from the strain measured between two points on the ground. The second type, inertial seismometers, measure the relative motion between the ground and a suspended mass. The instrument discussed in this thesis is a part of the second type, the inertial seismometers.

1.2.1 Inertial Accelerometers/Seismometers

1.2.1.1 The Basic Model

Two comprehensive works exist on the basics of seismometry: Erhard Wielandt's on-line book "Seismometry"[1] and "Instrumentation in Earthquake Seismology" by Havskov and Alguacil[2]. Both these texts were consulted when developing the basic model of a seismometer. The simplest way to model an inertial seismometer is as a mass-spring system. The mass, suspended by a

spring, will move in relation to movements of the ground. The relative motion is governed by the characteristics of the system, such as the spring constant and the size of the mass. The system will also contain damping forces caused by mechanical resistance in the spring as well as forces due to the passage of the mass through the surrounding medium. When the ground moves the mass tends to remain at rest, so there will be a difference between the movement of the ground and the mass. This differential motion can be recorded and analysed, and an accurate representation of the way the ground is moving can be obtained. A basic idea of an inertial seismometer modelled as a mass spring system is depicted in Figure 1.2.1.

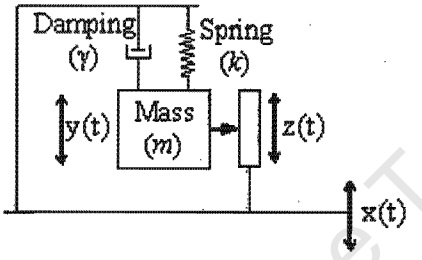

Figure 1.2.1: The Inertial Seismometer Modelled as a Mass-Spring System. *For an initial ground motion of $x(t)$ there will be a corresponding mass movement $y(t)$. The difference between the ground motion and the corresponding mass motion results in the measurable relative motion $z(t)$.*

Consider for a given ground displacement $x(t)$, there will be a corresponding absolute motion of the mass $y(t)$ and the relative motion between the ground and mass $z(t) = y(t) - x(t)$[1]. The acceleration of the mass $\ddot{y}(t)$ will be governed by any external force F applied to the mass as well as the force applied by the spring, which is proportional to the relative displacement, and the damping force, which is proportional to the relative velocity. This gives the following balanced equation for the forces present on the mass.

$$m\ddot{y}(t) = F - k.z(t) - \gamma.\dot{z}(t) \tag{1.1}$$

In order to obtain a measure for ground motion, Equation 1.1 is re-written in terms of $x(t)$ and $z(t)$ using the relation $z(t) = y(t) - x(t)$.

$$m.\ddot{z}(t) + \gamma.\dot{z}(t) + k.z(t) = F - m.\ddot{x}(t) \tag{1.2}$$

Equation 1.2 forms the basic model for the inertial seismometer. It is based heavily on the well documented mass spring system and the further developments of the model that follow are based on mathematical treatments very similar to those used to describe mass spring systems.

1.2.1.2 System Sensitivity

The inertial seismometer model, based heavily on a mass spring system, will be highly sensitive to frequency. At low frequencies the mass will follow the ground motion and there will be relatively no differential motion[2]. At higher frequencies the mass will move very differently in relation to the ground. Thus the mass spring system forms a high pass filter for the ground displacement. This filtering action will then have to be compensated for in the recording of the signals.

For any given sinusoidal ground motion it is reasonable to assume that the relative motion between the mass and the ground will also be sinusoidal, but of different magnitude and phase. The following equations can then be included into the model of the seismometer.

$$\begin{aligned} z(t) &= A\cos(\omega t) & x(t) &= B\cos(\omega t - \varphi) \\ \dot{z}(t) &= -A\omega\sin(\omega t) & \dot{x}(t) &= -B\omega\sin(\omega t - \varphi) \\ \ddot{z}(t) &= -A\omega^2\cos(\omega t) & \ddot{x}(t) &= -B\omega^2\cos(\omega t - \varphi) \end{aligned}$$

Substituting these equations into Equation 1.2 gives the following new equation for the model:

$$-m.A\omega^2\cos(\omega t) - \gamma.A\omega\sin(\omega t) + k.A\cos(\omega t) = F + m.B\omega^2\cos(\omega t - \varphi) \tag{1.3}$$

If it is assumed that no external force acts on the mass, a ratio between the magnitude of the relative motion between the ground and the mass and the magnitude of the motion of the ground can be found. This ratio can be used along with the measured relative motion of the mass to determine the magnitude of the ground vibration.

$$\frac{A}{B} = \frac{\omega^2\cos(\omega t - \varphi)}{-\omega^2\cos(\omega t) - \frac{\gamma}{m}\omega\sin(\omega t) + \frac{k}{m}\cos(\omega t)} \tag{1.4}$$

In order to increase the sensitivity, or the ratio between the amplitude of the relative motion and that of the ground, the variables in Equation 1.4 can be manipulated to good effect. Either increasing the mass or decreasing the spring or damping constants would increase the ratio between the magnitude of the relative and ground motion and increase the sensitivity of the device.

1.2.1.3 Relative Response to Sinusoidal Ground Motion

As mentioned previously, in order to determine the exact relative response of an inertial seismometer's mass to sinusoidal ground motion, similar mathematical treatments as those used in mass-spring systems are used. These mathematical techniques are laid out in a number of sources, namely Ralph Baierlein's "Newtonian Dynamics"[3] and Chapter 2 of "Mechanical and Structural Vibrations" by Fertis[4], and are slightly adapted for use in determining the relative response of an inertial seismometer to sinusoidal ground motion. Firstly Equation 1.2 developed in the previous section is re-arranged to form the following equation.

$$\ddot{z}(t) = \frac{F}{m} - \ddot{x}(t) - \frac{\gamma}{m}.\dot{z}(t) - \frac{k}{m}.z(t) \tag{1.5}$$

Using the substitutions, $\frac{\gamma}{m} = \frac{1}{\tau}$ and $\frac{k}{m} = \omega_o^2$ and again assuming that there is no external force acting on the mass, Equation 1.5 reduces to:

$$\ddot{z}(t) = -\ddot{x}(t) - \frac{1}{\tau}.\dot{z}(t) - \omega_o^2.z(t) \tag{1.6}$$

Once again, it can be assumed that for any sinusoidal ground motion the relative motion of the mass will also be sinusoidal, but of different amplitude and phase. This gives the following solutions for Equation 1.6:

$$\begin{aligned} z(t) &= B\cos(\omega t + \varphi) & x(t) &= A\cos(\omega t) \\ \dot{z}(t) &= -B\omega\sin(\omega t + \varphi) & \dot{x}(t) &= -A\omega\sin(\omega t) \\ \ddot{z}(t) &= -B\omega^2\cos(\omega t + \varphi) & \ddot{x}(t) &= -A\omega^2\cos(\omega t) \end{aligned} \tag{1.7}$$

The solutions for $z(t)$ can be re-written as:

$$\begin{aligned} z(t) &= B\cos(\omega t+\varphi) = (B)\cos(\varphi)\cos(\omega t) - (B)\sin(\varphi)\sin(\omega t) \\ \dot{z}(t) &= -B\omega\sin(\omega t+\varphi) = (-B\omega)\sin(\varphi)\cos(\omega t) + (-B\omega)\cos(\varphi)\sin(\omega t) \\ \ddot{z}(t) &= -B\omega^2\cos(\omega t+\varphi) = \left(-B\omega^2\right)\cos(\varphi)\cos(\omega t) - \left(-B\omega^2\right)\sin(\varphi)\sin(\omega t) \end{aligned} \tag{1.8}$$

Substituting these solutions into Equation 1.6,

$$\begin{aligned} \left(-B\omega^2\right)\left[\cos(\varphi)\cos(\omega t) - \sin(\varphi)\sin(\omega t)\right] &= -\frac{1}{\tau}(-B\omega)\left[\sin(\varphi)\cos(\omega t) + \cos(\varphi)\sin(\omega t)\right] \\ &\quad -\omega_o^2(B)\left[\cos(\varphi)\cos(\omega t) - \sin(\varphi)\sin(\omega t)\right] \\ &\quad +A\omega^2\cos(\omega t) \end{aligned} \tag{1.9}$$

This equation can be reduced to:

$$\left(B\left(\left[\omega^2-\omega_o^2\right]\cos(\varphi)+\frac{\omega}{\tau}\sin(\varphi)\right)+A\omega^2\right)\cos(\omega t) - B\left(\left[\omega^2-\omega_o^2\right]\sin(\varphi)+\frac{\omega}{\tau}\cos(\varphi)\right)\sin(\omega t) = 0 \tag{1.10}$$

When Equation 1.10 is solved at $\omega t = \frac{\pi}{2}$, $\cos(\omega t)$ will be zero, so the only way the equation can be solved is if the coefficient of $\sin(\omega t)$ is also equal to zero. Using this information an equation to solve for φ can be given as:

$$\frac{\sin(\varphi)}{\cos(\varphi)} = \tan(\varphi) = \frac{\frac{\omega}{\tau}}{\omega^2-\omega_o^2} \tag{1.11}$$

The terms $\sin(\varphi)$ and $\cos(\varphi)$ can then be evaluated using Equation 1.11 for $\tan(\varphi)$ and the simple trigonometry of a triangle,

In order to increase the sensitivity, or the ratio between the amplitude of the relative motion and that of the ground, the variables in Equation 1.4 can be manipulated to good effect. Either increasing the mass or decreasing the spring or damping constants would increase the ratio between the magnitude of the relative and ground motion and increase the sensitivity of the device.

1.2.1.3 Relative Response to Sinusoidal Ground Motion

As mentioned previously, in order to determine the exact relative response of an inertial seismometer's mass to sinusoidal ground motion, similar mathematical treatments as those used in mass-spring systems are used. These mathematical techniques are laid out in a number of sources, namely Ralph Baierlein's "Newtonian Dynamics"[3] and Chapter 2 of "Mechanical and Structural Vibrations" by Fertis[4], and are slightly adapted for use in determining the relative response of an inertial seismometer to sinusoidal ground motion. Firstly Equation 1.2 developed in the previous section is re-arranged to form the following equation.

$$\ddot{z}(t) = \frac{F}{m} - \ddot{x}(t) - \frac{\gamma}{m}.\dot{z}(t) - \frac{k}{m}.z(t) \tag{1.5}$$

Using the substitutions, $\frac{\gamma}{m} = \frac{1}{\tau}$ and $\frac{k}{m} = \omega_o^2$ and again assuming that there is no external force acting on the mass, Equation 1.5 reduces to:

$$\ddot{z}(t) = -\ddot{x}(t) - \frac{1}{\tau}.\dot{z}(t) - \omega_o^2.z(t) \tag{1.6}$$

Once again, it can be assumed that for any sinusoidal ground motion the relative motion of the mass will also be sinusoidal, but of different amplitude and phase. This gives the following solutions for Equation 1.6:

$$\begin{aligned} z(t) &= B\cos(\omega t + \varphi) & x(t) &= A\cos(\omega t) \\ \dot{z}(t) &= -B\omega\sin(\omega t + \varphi) & \dot{x}(t) &= -A\omega\sin(\omega t) \\ \ddot{z}(t) &= -B\omega^2\cos(\omega t + \varphi) & \ddot{x}(t) &= -A\omega^2\cos(\omega t) \end{aligned} \tag{1.7}$$

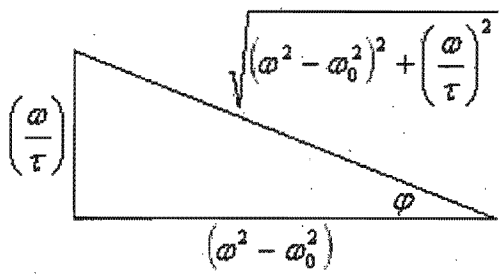

$$\sin(\varphi) = \frac{-\frac{\omega}{\tau}}{\sqrt{\left(\omega^2 - \omega_o^2\right)^2 + \left(\frac{\omega}{\tau}\right)^2}} \qquad \cos(\varphi) = \frac{-\left(\omega^2 - \omega_o^2\right)}{\sqrt{\left(\omega^2 - \omega_o^2\right)^2 + \left(\frac{\omega}{\tau}\right)^2}} \tag{1.12}$$

where the negative signs are intentionally included. Similarly, when equation 1.10 is evaluated at $\omega t = 0$ the coefficient of $\cos(\omega t)$ must equal zero. The equations for $\sin(\varphi)$ and $\cos(\varphi)$ stated in Equation 1.12 can now be used to determine B.

$$B\left(\frac{-\left(\omega^2 - \omega_o^2\right)^2 - \left(\frac{\omega}{\tau}\right)^2}{\sqrt{\left(\omega^2 - \omega_o^2\right)^2 + \left(\frac{\omega}{\tau}\right)^2}}\right) + A\omega^2 = 0$$

$$B = \frac{A\omega^2}{\sqrt{\left(\omega^2 - \omega_o^2\right)^2 + \left(\frac{\omega}{\tau}\right)^2}} \tag{1.13}$$

So for an external ground displacement $A\cos(\omega t)$ the relative motion will be:

$$z(t) = \frac{A\omega^2}{\sqrt{\left(\omega^2 - \omega_o^2\right)^2 + \left(\frac{\omega}{\tau}\right)^2}} \cos\left(\omega t + \left(\tan^{-1}\left(\frac{\frac{\omega}{\tau}}{\omega^2 - \omega_o^2}\right)\right)\right) \tag{1.14}$$

As mentioned before, and shown in Equation 1.14, both the magnitude and the phase of the inertial seismometer's relative response is highly dependent on the frequency of the ground motion. The relative response dependence on frequency therefore needs to be thoroughly understood so that accurate representations of the actual ground motion from the measurement of relative motion can be attained. Equation 1.14 can describe the relative motion of any suspended mass to an external drive motion. It is used in again in later chapters as a model for other components of the system.

1.2.1.4 Magnitude Frequency Response

To determine the frequency response of the magnitude of the relative motion in an inertial seismometer, only the steady state amplitude of Equation 1.14 is considered. This gives the magnitude frequency response of the seismometer as a function of the frequency of the ground motion ω as,

$$Z(\omega) = \frac{A\omega^2}{\sqrt{(\omega^2 - \omega_o^2)^2 + \left(\frac{\omega}{\tau}\right)^2}} \tag{1.15}$$

Now if the magnitude of the ground displacement, velocity and acceleration are considered to be A, $A\omega$ and $A\omega^2$ respectively, then the displacement magnitude transfer function of the inertial seismometer for the different modes of motion can be written as [1]:

$$H_d(\omega) = \frac{Z(\omega)}{A} = \frac{\omega^2}{\sqrt{(\omega^2 - \omega_o^2)^2 + \left(\frac{\omega}{\tau}\right)^2}} \tag{1.16}$$

$$H_v(\omega) = \frac{Z(\omega)}{A\omega} = \frac{\omega}{\sqrt{(\omega^2 - \omega_o^2)^2 + \left(\frac{\omega}{\tau}\right)^2}} \tag{1.17}$$

$$H_a(\omega) = \frac{Z(\omega)}{A\omega^2} = \frac{1}{\sqrt{(\omega^2 - \omega_o^2)^2 + \left(\frac{\omega}{\tau}\right)^2}} \tag{1.18}$$

The frequency behaviour of an inertial seismometer can now be determined using the above equations. These equations are used again in Chapter 5 when the force feedback is applied and the whole system is put together. The output displacement is a high-pass filter for input displacement with a corner frequency of $f_0 = \frac{\omega_0}{2\pi}$. At this frequency the ground displacement will be amplified by a factor of $\frac{\omega_0 m}{\gamma}$. The frequency response of the output displacement to input displacement is plotted in Figure 1.2.2.

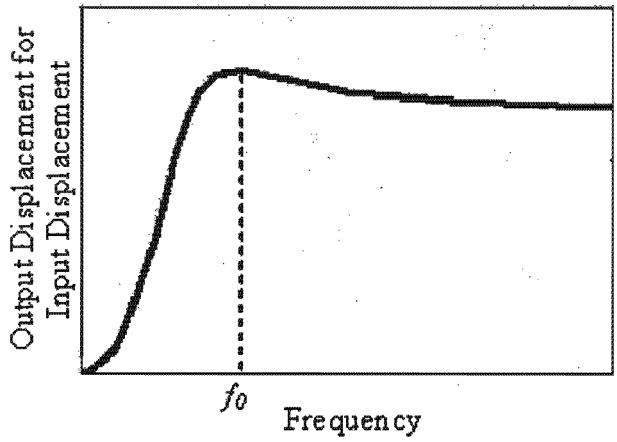

Figure 1.2.2: The Output Displacement for Input Displacement versus Frequency. *The magnitude frequency response of the output displacement is a high pass filter for input displacement.*

From Equation 1.17 the output displacement is a band-pass filter for input velocity. The corner frequency will again be $f_0 = \frac{\omega_0}{2\pi}$ and the output displacement magnitude at this frequency will be the velocity amplified by $\frac{m}{\gamma}$. Its basic frequency response is plotted in Figure 1.2.3.

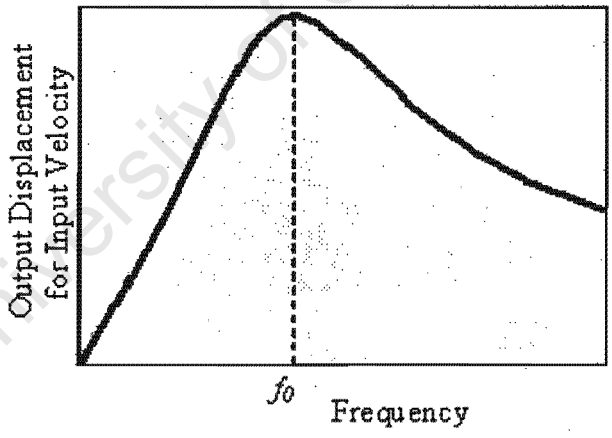

Figure 1.2.3: The Output Displacement for Input Velocity versus Frequency. *The magnitude frequency response of the output displacement is a band pass filter for input velocity.*

Finally, from Equation 1.18, the output displacement is a low-pass filter for input acceleration. Again the corner frequency is $f_0 = \frac{\omega_0}{2\pi}$ and the output displacement will be the input acceleration amplified by $\frac{m}{\omega_0 \gamma}$. Its basic frequency response is plotted in Figure 1.2.4.

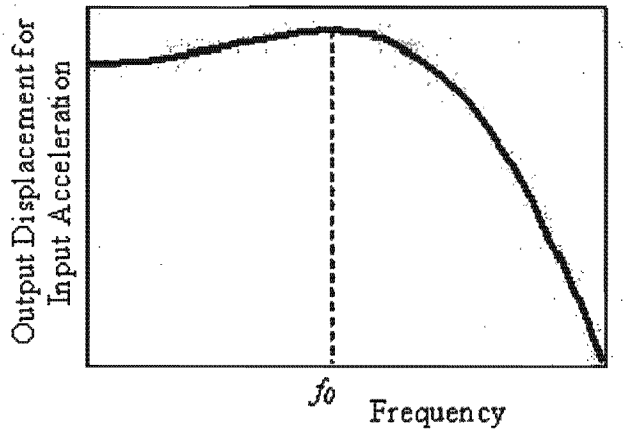

Figure 1.2.4: The Output Displacement for Input Acceleration versus Frequency.

The magnitude frequency response of the output displacement is a low pass filter for input acceleration.

Using Equations 1.16-1.18, the relative displacement measurement between the inertial seismometer's mass and the actual ground motion can be accurately determined, as long as the characteristics of the inertial seismometer are known. These characteristics can either be measured or determined from frequency response diagrams like those in Figures 1.2.2, 1.2.3 and 1.2.4.

1.3 The Force Balance Principle

1.3.1 Problems Associated with Passive Inertial Seismometers

The precision of an inertial seismometer is dependent on two basic components: the mechanical sensitivity determined by the mass spring system characteristics, and the electrical sensitivity determined by the properties of the transducer that measures the relative displacement between the mass and the ground. When an inertial force due to ground acceleration acts on the seismometer, the mass spring system converts the force into a relative displacement of the mass. The electronic transducer then converts these displacements into an electric signal that can be interpreted. Neither the mechanical conversion of inertial force or the electrical conversion of relative displacement is very precise and can lead to errors in measurement.

In the previous section on system sensitivity, Equation 1.4, which related the magnitude of the relative displacement of the mass as a function of the magnitude of the ground motion

and the mass spring characteristics, was defined. In order to maximise the relative output displacement of the inertial seismometer, the restoring force of the spring and damper need to be as small as possible. As system damping is generally constant, the spring constant would have to be decreased. However, due to changes in spring geometry, a low spring constant will result in non-linear measurements for a large range of seismic signals or ground motion magnitudes. When the restoring forces are reduced, the effects of hysteresis and viscosity remain constant. This means that these undesirable effects will grow in comparison to the signal.

Another difficulty with inertial seismometers is the transducer that converts the relative displacement of the mass into an electric signal. With the mechanical sensitivity increased by the reduction of the restoring force of the spring, the electronic transducer needs to remain accurate for the now extended range of the relative displacement. It is, however, quite difficult to build transducers capable of remaining linear and accurate for the large range of seismic magnitudes that need to be measured. These electronic difficulties as well as the mechanical sensitivity concerns contribute to the fact that passive inertial seismometers as discussed up to now cannot be optimised for precision and sensitivity at the same time.

1.3.2 Balancing the Forces

In order to solve these problems the force balance technique is used[1][2][5]. In passive inertial seismometers the force on the mass produced by the ground acceleration is determined by measuring the elongation of the spring using a transducer. In a force balance feedback system the unknown force on the mass is compensated by a known force generated by a transducer. The size of this compensating force is controlled by a circuit that determines the position of the mass, and then adjusts the force to move the mass back into its initial central position. The basic idea is illustrated in Figure 1.3.1.

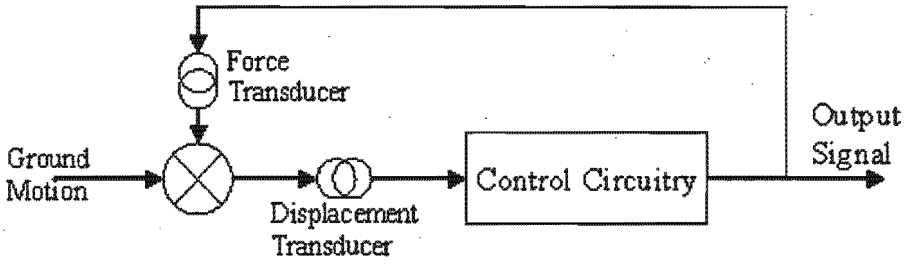

Figure 1.3.1: The General Force Feedback Control System. *The relative displacement is maintained by varying the input force to the system via the force transducer. The force transducer is controlled by the control circuitry using the measurements from the displacement transducer. The measurement of relative motion is now converted into a measure of how much force is required to restrict the relative motion.*

The force transducer, controlled by the circuitry, forces the mass to move with the ground, and reduce the relative motion to zero. The force produced by the transducer is therefore proportional to the size of the ground motion, and by monitoring the input signal to the force transducer a measure of the ground motion can be obtained. The ground acceleration is now converted into an electrical signal without relying on the mechanical precision of the mass spring system. The mechanical system is no longer used as a converter but only as a detector, and it allows sensitivity to be optimised without giving up precision. Owing to unavoidable feedback delays, the system bandwidth will be limited and other stability problems might occur. Optimisation of the control circuitry becomes vitally important in providing a high degree of sensitivity, precision and range.

1.3.3 Expanding the Control Model

In order for the inherent benefits of the force feedback system to be achieved, the control circuitry must be well designed. Mass movement must be kept to an absolute minimum if the errors present in the mechanical system are to be avoided. Reducing the restoring forces to optimise sensitivity will increase the tendency of the mass to move. This means enhanced sensitivity must encompass a faster, more accurate control circuit to keep the system functioning correctly. Understanding each component of the control loop becomes vitally important as does the understanding of the nature of the forces imposed on the mass by the ground motion.

Firstly by looking at the frequency response of the passive inertial seismometer discussed

in Section 1.2, a control transfer function for the relative displacement of the mass can easily be determined [6].

$$\text{Ground Displacement Transfer Function} = \frac{s^2}{s^2 + \frac{\gamma}{m}s + \frac{k}{m}} = \frac{s^2}{s^2 + \frac{1}{\tau}s + \omega_0^2} \quad (1.19)$$

$$\text{Ground Velocity Transfer Function} = \frac{s}{s^2 + \frac{\gamma}{m}s + \frac{k}{m}} = \frac{s}{s^2 + \frac{1}{\tau}s + \omega_0^2} \quad (1.20)$$

$$\text{Ground Acceleration Transfer Function} = \frac{1}{s^2 + \frac{\gamma}{m}s + \frac{k}{m}} = \frac{1}{s^2 + \frac{1}{\tau}s + \omega_0^2} \quad (1.21)$$

The relative mass displacement can easily be converted into the force on the mass by multiplying by the spring constant k. A more detailed block diagram than the one given in Figure 1.2.1 can now be developed and is illustrated in Figure 1.3.2.

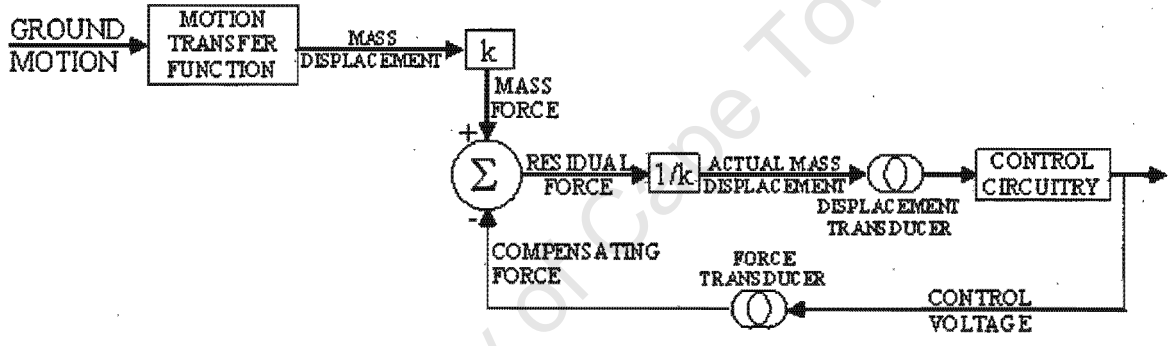

Figure 1.3.2: The Expanded Model for the Force Feedback Control System.

Using block diagram algebra a total transfer function for the whole force feedback system can be formed. This can then be used to determine the system bandwidth as well as the sensitivity to various forms of ground motion. The transfer function of each component will affect the overall system response so a thorough understanding of each part is imperative.

1.4 The Displacement Sensor

At the heart of any inertial seismometer, with or without a feedback system, is the sensor that measures the relative motion of the mass. Although some seismometers use velocity transducers to determine this relative motion, this thesis involves the use of displacement transducers. These displacement sensors measure the relative displacement between the ground and the mass of the system. The limits imposed by the displacement transducer characteristics are often the

fundamental limits to both sensitivity and bandwidth of the entire seismometer system. For inertial seismometers it is not always necessary that the displacement sensor has a long range, as the relative motion between ground motion and the mass is relatively small. For force feedback systems this movement should in fact be almost zero as the system controls the mass at a fixed position in relation to the ground. It is therefore much more important that the displacement sensors be fast and accurate, as these are the critical factors influencing the performance of the seismometer. There are numerous different types of displacement sensors, some more useful in seismometry design than others. A brief overview of the major types of displacement sensors is given in the next section.

1.4.1 Major Classes of Displacement Sensors

1.4.1.1 Resistive Displacement Sensors

These displacement sensors, commonly known as potentiometers, consist of an electrically conductive wiper that slides against a fixed resistive element[7]. These potentiometers can be either rotary or linear, depending on the displacement measurement required. The resistive element is then set up electrically in a voltage divider configuration for which the output is a function of wiper position. A voltage V_{in} is applied across two of the potentiometer terminals. The voltage V_{out} between the wiper terminal and the electrical ground can then be measured. This system would be implemented in an inertial seismometer by attaching the wiper to the mass whilst the fixed resistive element remains attached to the ground. The output voltage from the voltage divider would then be a function of the relative motion between the mass and the ground.

Most voltage measurement techniques require the use of an external resistance R_m, which will draw some current from the potentiometer circuit[7] $I_{out} = \frac{V_{out}}{R_m}$. This current results in a non-linear relation between the wiper position and the output voltage, which is proportional to the ratio between the external resistance of the measurement device and the total resistance of the potentiometer R_p. To reduce the non-linearity R_p should be much smaller than R_m. This will reduce the sensitivity of the measurement as the ratio between the input voltage and the potentiometer resistance $\frac{V_{in}}{R_p}$ is limited by the power rating of the potentiometer. For any reduction in R_p the input voltage will also have to be reduced, which will in turn reduce the output voltage sensitivity.

The accuracy or resolution of potentiometers largely depends on their construction. Potentiometers are usually constructed from resistive wires wound around a central insulated material. The conductive wiper is placed on the wound coils to produce the changing resistance. The density of the wound coils and the shape of the wiper determine the resolution of the potentiometer. If the contact tip area of the wiper is reduced to below the diameter of the resistive wire then the resolution is determined by the resistance of one turn of the wire. As the wiper moves from one turn to the next the amount of resistance wire change will be set by the size of the inner insulating material.

The major advantages of using this type of system are its simplicity and ease of use. It is also very cheap, as it requires only passive components. There are, however, some major disadvantages. The contact between the wiper and the element will produce both frictional and inertial loading, which will limit bandwidth as well as change the mass-spring characteristics of the overall system. The parts will also undergo wear which will shorten the lifetime of the system. As the technique is based on the use of resistors all the noise sources such as thermal sensitivity will also affect the precision of the sensor. Noise signals will also be caused by the intermittent contact between the various mechanical components of the potentiometer. Due to their low sensitivity and high noise resistive displacement sensors are not often used in seismometers.

1.4.1.2 Inductive Displacement Sensors

Based on magnetic circuits, these displacement sensors can be either self generating or passive[8]. Self generating inductive sensors generate a voltage due to the relative motion between a coil and core. Passive inductive displacement sensors require that an external power source is used. A ferromagnetic core drives flux between a powered coil and an un-powered coil. The reluctance, or flux drive limiting factor, of the system is easily altered by changing the location of both the coils and the core. Displacement measurement can then be based on this change in reluctance of a magnetic flux path. There are numerous configurations of the coils and core, depending on the type of displacement measurement required. Similarly to the resistive system, the core could be attached to the mass of the system whilst the coils are fixed on the ground. Changes in relative motion between the mass and the ground would now shift the reluctance which would

change the voltage induced in the un-powered coil.

In general the inductance of a wire can be given by [8]

$$L = N\frac{d\phi}{di} \tag{1.22}$$

where L is the inductance, N is the number of turns cut by the flux linkages, and ϕ is the flux. The voltage induced in the unpowered coil can now be given by [7]

$$V_{ind} = M\frac{di_p}{dt} \tag{1.23}$$

where M is the mutual inductance and i_p is the current flowing through the powered coil. From Equation 1.22 the sensitivity of the mutual inductance of the inductive displacement sensor will be dependent on the coil density of the windings, as well as the size and position of the core which determines the flux. The sensitivity can also be increased by increasing the current i_p, by either increasing the driving voltage or decreasing the resistance of the powered coil. As there is no actual contact between the coils, or between the coils and the core, the resolution should theoretically be infinite and even the slightest movement of the core should produce a change in the mutual inductance. Unavoidable noise sources does restrict the resolution of most commercially available inductive displacement sensors to the micrometer and submicrometer range[9][10], with the most sensitive claimed to measure with a resolution of $10nm$. The measurement of the induced voltage will cause similar problems to the voltage measurement in the resistive displacement sensors, and there is usually a trade off between high sensitivity and high linearity.

Although better than resistive displacement sensors, inductive sensors are quite a bit more complicated. Their effect on the mass spring dynamics of the system is neglible and can easily be incorporated into the whole system. The coils do require comprehensive shielding to prevent external signals corrupting the measured seismic signals. Stray capacitance is also a problem which causes additional errors in the measurement.

1.4.1.3 Capacitive Displacement Sensors

The capacitance between two plates is a function of the distance between them, the area of the plates and the permittivity of the material between them. This characteristic can be easily adapted to displacement sensing by fixing the permittivity and changing either the distance between the plates, or the contact area (by sliding the plates around). Simple passive electrical circuits can then be used to convert this change in capacitance to a usable signal. As there is no actual contact between the plates, there is no real adverse affect to the mechanical sensitivity of the seismometer. Capacitive sensors, however, usually have to be quite large and the plates quite close together in order to obtain the required sensitivities. Slight errors in the orientation of the plates can produce non-linear and inaccurate results when the plates are so closed together. The control systems fixing the plates would also have to keep them very still to prevent them from touching and producing large measurement errors.

As mentioned before capacitance displacements sensors use a variation of some parameter of the basic equation [8]

$$C = \frac{\varepsilon A}{D}$$

where C is the capacitance, ε is the dielectric of the medium between the plates and D is the distance between them. The dielectric constant of air at 20° at $1atm$ is 1.00059[11] giving: $\varepsilon = 8.859 * 10^{-12}$. The measurement of capacitance has been advanced by Marioli, Sardini and Taroni [12] to resolutions beyond $1fF$ for a range of about $10pF$. In the middle of this range for an interacting area of $1cm^2$ the resolution of the capacitance displacement sensor will be in the low nanometer range. For this example the plates would have to be initially located closer than $200\mu m$ from each other which could lead to the orientation and other errors discussed before. Capacitive displacement senors have been successfully utilised in force feedback seismometers in [5].

1.4.1.4 Ultrasonic and "Time-of Flight" Displacement Sensing

Ultrasonic transducers produce a pulse that will be reflected off nearby objects and sent back to the transducer. The time taken between the sent pulse and the reflected pulse can be used to determine the distance between the transducer and the reflective surface. This technique usually

involves far longer ranges than those required for an inertial seismometer. Major inaccuracies in the system can be caused by changing air conditions as well as misalignment of the reflective surface.

Other ultrasonic techniques are, however, used in the field of acoustic microscopy. A point source of ultrasound is produced in a fluid and the transducer acts alternately as a transmitter and a receiver[13]. The relative phase and amplitude between the sent signal and the received signal is then interpreted to determine the displacement between the transducer and the surface. High resolutions of below $20nm$ have been achieved as discussed by Quate[14]. The problem with achieving these high resolutions is that the operating frequency must be in the GHz range and the fluid between the surface and the transducer must be helium which has been cooled to about $0.1K$. These difficulties make it impractical to use ultrasonic displacement detection in a seismometer system.

1.4.1.5 Tunnelling Detection Scheme

A tunnelling detection scheme, as used in a scanning tunneling microscope, involves the monitoring of a tunneling current through an air gap between a tip and a surface. A voltage is applied between the tip and the surface and this produces the current through the air gap. Minute changes in the distance between the tip and the surface produce a change in the tunneling current. The size of the current can then be used to determine the distance between the tip and the surface. In order for the system to work the tip must be located about several angstroms from the surface.

Although highly sensitive to displacement, there are a few problems in using a tunneling displacement detection scheme for inertial seismometers. The extremely small range of these devices means that the mass cannot really move much at all under force feedback conditions, limiting the mechanical sensitivity of the system. The tunneling process is also sensitive to the material across which the tunneling process takes place, and contaminates present on the surfaces affect the process dramatically[16]. At these low ranges there will also be intersurface forces between the tunneling tip and the surface. This further complicates the problem and leads to errors in displacement measurement. Tunneling displacement detectors have, however, been incorporated into accelerometers and seismometers with some success [5][15].

1.4.1.6 Laser Interferometer Displacement Sensor

Laser interferometer sensors are successfully used in atomic force microscopes. They use lasers to monitor the deflection of a tip located very close to a surface. The intersurface forces responsible for the deflection of the tip vary according to the distance between the tip and the surface, but have a range of about 30nm. In the simplest form, as discussed in [16], a laser beam is focused on a lever supporting the force sensing tip, and the beam is then reflected back onto two closely spaced photodetectors. Any small change in the deflection of the lever will cause one photodetector to receive more light than the other one. The outputs of these photodetectors can then be put into a differential amplifier to determine the extent and the direction of the beam deflection. More complicated systems involving beam splitters and different noise reducing configurations are discussed in detail in the preceding chapters of [16].

As they can involve intersurface forces laser interferometers are also highly sensitive to changes in displacement. They are successfully used in atomic force microscopy right up to atomic resolutions. Lasers are however quite big and bulky and need to be focussed very carefully in order for the system to work. This adds to the size and the complexity of the seismometer.

1.4.2 The Tuning Fork Displacement Sensor

For this project the usual displacement sensors used in inertial seismometers were disregarded in favour of trying to use the tuning fork displacement sensor. This relatively small and easy to use device offers similar accuracies to the other atomic force displacement sensors. Grober, Acimov et al[17] establish that these tuning fork displacement sensors are possibly the most sensitive displacement sensors available. This thesis aims to show that the tuning fork displacement sensor can effectively be used in a simple force feedback system to significantly decrease the size of inertial seismometers without decreasing accuracy or bandwidth.

The tuning fork displacement sensor operates by vibrating a miniature high speed piezoelectric tuning fork at or near its resonant frequency. The tines of the tuning fork are then brought into close proximity with a surface. Because of the interactions between the surface and the tines, the characteristics of the tuning fork will change. The strength and direction of these interactions vary with displacement from the surface, so by monitoring the operating charac-

teristics of the tuning fork, the distance between the tines and the surface can be accurately determined. The tuning fork approaching a surface is shown in Figure 1.4.1.

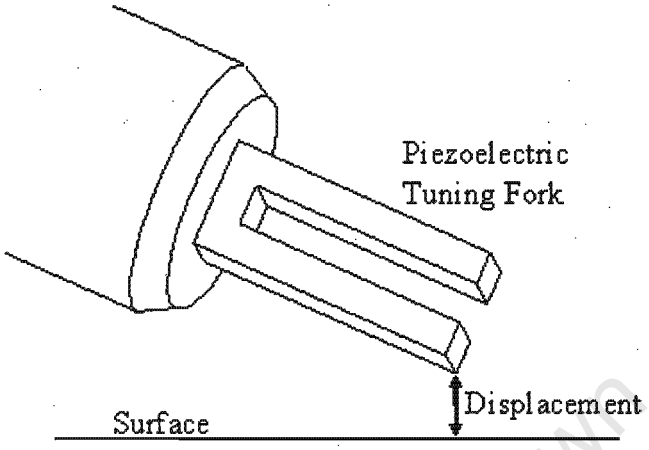

Figure 1.4.1: The Vibrating Tuning Fork Approaching a Surface. *Standard* $32.768kHz$ *piezoelectric tuning fork crystals are often used. The outer packaging is removed to access the actual fork protected inside.*

The operation of a piezoelectric tuning fork as the displacement transducer of force feedback seismometer requires that each component of the system be thoroughly understood. First off the interaction between the tuning fork and the approaching surface must be well characterised, so that the best operating distance can be determined. Accurate models of the tuning fork need to be developed so that the system can be controlled to make accurate displacement measurements possible. The effect that a change in displacement will have on the operating characteristics of the tuning fork also needs to be modelled so that the system can be accurately controlled in a force feedback set-up. This thesis aims to address each of these components to establish whether the piezoelectric tuning fork can be used as the displacement sensor in a force feedback seismometer system, and to determine the limits of its operation.

Chapter 2

The Contact Model

The force between the approaching surface and the tuning fork can basically be divided into two constituents. The first is the force associated with interatomic particles which gives rise to both intermolecular and intersurface forces. The other force is that associated with the passage of air between the vibrating piezoelectric tuning fork and the surface. These forces combine to give a total contact model between the tuning fork and the surface.

2.1 The Interaction Potential

2.1.1 Introduction

In the field of intersurface forces, it can be instructive to build the study from the bottom up. Two sources were consulted in detail when compiling this section on the interaction potential: "Intermolecular and Surface Forces" by Jacob Israelachvili [18] and Chapter 13 in "Scanning Force Microscopy" by Dror Sarid [19]. Much of the information presented in this section is summarised from these two sources. Interatomic forces combine to form molecules, which give rise to intermolecular forces. Intermolecular forces can then combine to form surfaces and structures which will in turn allow intersurface forces to be defined.

In nature there are four distinct forces. Two of these are weak and strong interactions that act between neutrons, protons and electrons. The other two forces are the electromagnetic and gravitational interactions that act between atoms and molecules as well as the sub-atomic particles mentioned before. The strong and weak interaction forces are short ranged ($< 10^{-5}mm$)

whereas the electromagnetic and gravitational forces have a far larger range, varying from subatomic to infinity.

Initially in the development of the theory of intermolecular forces it was believed that one simple force law, similar to Newton's gravitational law for gravitational force, would be found to account for all the intermolecular attractions. This gave an interaction potential between two molecules of the form:

$$w(r) = \frac{-Cm_1m_2}{r^n} \tag{2.1}$$

which is related to the force law between them given by:

$$F(r) = -\frac{d(w(r))}{d(r)} = \frac{-nCm_1m_2}{r^{n+1}} \tag{2.2}$$

Where m_1 and m_2 are the molecular masses, r is the separation, C is a constant and n is some integer believed to be of the order 4 or 5. The power law n is chosen by considering a region of space where the number density of the molecules within the region is ρ. Using an attraction potential between two molecules of the form $w(r) = -\frac{C}{r^n}$ all the interaction energies of one molecule with all the other molecules can be added together. Now if the region of space is spherical, the number of molecules in a region between r and $r + dr$ can be calculated using the formula for the volume of a spherical shell, where r is the radius and dr is the thickness. This gives $\rho 4\pi r^2 dr$ as the total number of molecules in the shell. The total interaction energy of one molecule with all other molecules in the system will therefore be given by:

$$Total\ Energy = \int_{\sigma}^{L} w(r)\rho 4\pi r^2 dr \tag{2.3}$$

where σ is the diameter of the molecules and L is the size of the system. Substituting in $w(r) = -\frac{C}{r^n}$ and performing the required integration gives:

$$Total\ Energy = \frac{-4C\rho}{(n-3)(\sigma^{n-3})}\left[1 - \left(\frac{\sigma}{L}\right)^{n-3}\right] \tag{2.4}$$

It has been determined experimentally that the interaction between molecules is finite and of a relatively small distance of about several hundred angstroms. Since σ must be smaller than

L which means that $\frac{\sigma}{L} < 1$, the large distance contributions to the interactions will disappear only for $n > 3$. This implies that the interaction is mainly between close neighbours and does not depend on the macroscopic size of the system. Gravity with an interaction potential power law of $n = 1$ is a much more far acting force, and macroscopic size remains a factor as can be seen with distant planets and stars interacting over vast distances.

As mentioned previously there is an association between the distance dependent interaction energy between two molecules, and the force field that exists between them. This is called the free energy and is actually the available mechanical energy.

A rough guide to the strength of the interaction energy between molecules can be obtained by comparing this energy to the thermal energy given by KT, where T is the temperature of the thermal bath surrounding the molecules and K is the thermal constant of the molecules. The relationship between the two energies can best be described by considering the liquid and gas states of a substance. Due to their greater separation the interaction energies between molecules in a gas will be much less than those in a liquid. If the amount of energy required to convert the liquid into a gas is considered as the energy required to move the molecules further apart, the link between thermal energy and interaction potential can be seen. The two energies can be related by the well known Boltzmann distribution,

$$\mu_L + KT \log X_L = \mu_G + KT \log X_G \tag{2.5}$$

where μ_L and μ_G are the interaction energy of a particle molecule in a liquid and gas state, and X_L and X_G are the concentrations of the molecule in liquid and gas form.

Intermolecular forces can be loosely classified into three categories. There are the purely electrostatic forces that arise from the Coulomb forces between charges. Secondly there are the polarisation forces that arise from dipole moments induced in atoms and molecules by the electric fields of nearby charges and permanent dipoles. Thirdly there are the forces that are quantum mechanical in nature. Such forces give rise to covalent or chemical bonding, and to the repulsive steric or exchange interactions that balance the attractive forces at short distance. These categories should not be considered rigid as certain important forces like van der Waal's force cannot be classified completely. Each of these categories are now considered separately.

2.1.2 Covalent or Chemical Bonding Forces

When two or more atoms come together to form a molecule, the forces holding the molecule together are called covalent forces and the bonds formed are called covalent bonds. Within the molecule electrons are shared between atoms so the discrete nature of the atoms is lost. The number of bonds that each atom can have, its stoichiometry or valency, depends on its position on the periodic table. These bonds are highly directional and this controls the atom orientation within a molecule. Covalent bonds are short ranged in the order of atomic separations. They, like most intermolecular interactions, decrease in strength with increasing distance.

2.1.3 Physical Bonds

Physical bonds give rise to forces between unbonded discrete atoms or molecules. Physical bonds lack the specificity and strong directionality of covalent bonds. Molecules can move about and rotate whilst still remaining bonded to each other. Physical bonds do not radically change the electron fields of the bonding atoms. Physical forces can be as strong as covalent forces, but are of significantly longer range, making them the regulating forces in all phenomena that do not involve chemical reactions. Physical bonds can be divided into Coulomb forces or charge-charge interactions and ionic forces.

The inverse square Coulomb force between two charged atoms, or ions, is by far the strongest of the considered physical forces. It is stronger even than then most of the chemical binding forces.

The Coulomb interaction energy between two charges q_1 and q_2 is given by,

$$w(r) = \frac{q_1 q_2}{4\pi\varepsilon_0\varepsilon}\frac{1}{r} \tag{2.6}$$

and the Coulomb interaction force can be given by

$$F(r) = -\frac{d(w(r))}{d(r)} = \frac{q_1 q_2}{4\pi\varepsilon_0\varepsilon}\frac{1}{r^2} \tag{2.7}$$

where ε is the dielectric constant of the medium and r is the distance between the two charges. For typical interatomic distances the energy of these bonds turns out to be in the

region of $200KT$ which is quite similar to the energies of the covalent bonds, indicating that Coulomb interaction is very strong and of long range.

One important aspect of Coulomb forces is range. The inverse distance dependence of the Coulomb energy appears to make it very long range, in apparent contradiction to what was said earlier about all intermolecular interaction energies having a distance dependence of at least $\frac{1}{r^3}$. Since positive atoms always have negative atoms nearby, whether in a lattice or a solution, the electric field becomes screened and the energy decays more rapidly than for a truly isolated ion.

Coulomb forces between ions can combine together to hold the ions together in a rigid lattice. These Coulomb forces can also be referred to as ionic forces and the bonds as ionic bonds. To determine the total interaction energy in the lattice the Coulomb energy of an individual ion must be summed with all the ions in the lattice and not just its nearest neighbours.

2.1.4 Interactions Involving Polar Molecules

In many molecules one of the atoms will tend to draw one or more of the shared electrons towards itself. For isolated molecules this results in an asymmetric displacement of electrons along the covalent bonds. This gives the molecule a permanent dipole. Such molecules are called polar molecules. Permanent dipole moments only occur in asymmetric molecules and thus not in single atoms. A characteristic dipole moment can be assigned to each type of covalent bond. The dipole moment of a polar molecule is defined as $u = ql$, where l is the distance between the two charges $+q$ and $-q$. The interactions involving polar molecules can be divided into the fixed dipole interactions and those where the dipole moment is induced.

2.1.4.1 Fixed Dipole Interactions

The first fixed dipole interaction is that between a charged atom and a polar molecule. If the length of the dipole is l, with charges $\pm q$ at both ends and the ion is positioned a distance r away and has a charge Q, then the total interaction energy will be the sum of the Coulomb energies of the ion with $-q$ and with $+q$ at each end of the dipole. The strength of each of these reactions will be dependent on the orientation of the dipole as this will determine the distance that each of the dipole charges is from the ion. The basic interaction can be seen in

Figure 2.1.1.

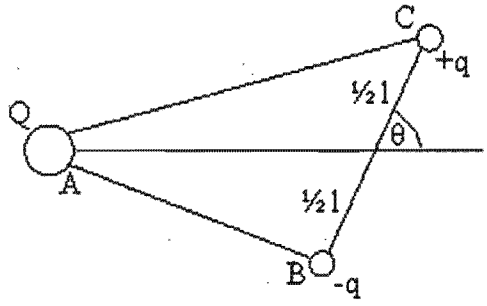

Figure 2.1.1: The Interaction Between a Dipole and and Ion. *A Similar arrangement can be used for all interactions involving polar molecules. The individual ion can be replaced by another fixed or induced dipole.*

At separations r exceeding the dipole length l the distances AB and AC can be written approximately as $AB \approx r + l\cos\theta$ and $AC \approx r - l\cos\theta$. The interaction energy can then be calculated by:

$$w(r,\theta) = \frac{-Qq}{4\pi\varepsilon_0\varepsilon}\left[\frac{1}{r - l\cos\theta} - \frac{1}{r + l\cos\theta}\right]$$

which can be simplified to give:

$$w(r,\theta) = \frac{Qu\cos\theta}{4\pi\varepsilon_0\varepsilon}\frac{1}{r^2} \tag{2.8}$$

When two polar molecules are near each other there is a dipole-dipole action between them. If two dipoles of moments $u_1$and u_2 are orientated far enough apart so that the length of the dipole l, becomes insignificant, the dipoles can be treated as point sources. The interaction may be derived using a similar procedure to that used for the ion-dipole interaction and is given by the following equation.

$$w(r,\theta_1,\theta_2,\varphi) = \frac{-u_1u_2}{4\pi\varepsilon_0\varepsilon}\frac{1}{r^3}\left[2\cos\theta_1\cos\theta_2 - \sin\theta\sin\theta_2\cos\varphi\right] \tag{2.9}$$

where θ_1, θ_2, and φ designate the orientation of the two dipoles. Equation 2.9 shows that the maximum attraction occurs when the two dipoles are lying in line.

The dipole-dipole interaction is not as strong as the previous two electrostatic interactions. They are already weaker than KT at distances of about $0.35nm$. If the dipoles are closer than

$r = 3l$, the dipole-dipole interaction is basically cancelled out by the coulomb charge between the four component charges. This free energy is less than the internal energy of the dipole, because some of the energy is taken up aligning the dipoles as they approach each other.

2.1.4.2 Interactions Involving the Polarisation of Molecules

The last categories of the electrostatic interactions that need to be considered are those that involve molecular polarisation. Basically this is the dipole moment induced in molecules by other nearby molecules. The dielectric constant of a medium is a reflection of the way molecules of the medium are polarised by the electric field. Besides the purely Coulombic interaction between two charges or dipoles, all other interactions so far considered are essentially polarisation type interactions.

All atoms and molecules are polarisable. Their polarisability α is defined as the strength of the induced dipole moment u_{ind} they acquire in a field E, such that:

$$u_{ind} = \alpha E \tag{2.10}$$

By displacing the electron cloud relative to the positively charged nucleus even non-polar molecules can be polarised by an external electric field.

A nearby ion a distance r away from a molecule will produce an electric field $E = \frac{ze}{4\pi\varepsilon_0\varepsilon}\frac{1}{r^2}$. This electric field will induce a dipole moment of:

$$u_{ind} = \alpha E = \frac{\alpha ze}{4\pi\varepsilon_0\varepsilon}\frac{1}{r^2} \tag{2.11}$$

This will lead to a reflected force field of the induced ion that acts back on the ion which is:

$$E_r = \frac{-2u_{ind}}{4\pi\varepsilon_0\varepsilon}\frac{1}{r^3} \tag{2.12}$$

so that the attractive force will be

$$F = (-ze)E_r = \frac{-2\alpha(ze)^2}{(4\pi\varepsilon_0\varepsilon)}\frac{1}{r^4} = -\frac{1}{2}\alpha E^2 \tag{2.13}$$

where E is the polarising field of the ion acting on the dipole. From Equation 2.13 it is

noted that the energy is half that expected for the interaction of an ion with a similarly aligned permanent dipole. This is because the dipole is induced rather than being fixed and some of the energy is used polarising the molecule. Looking at the displacement of the positive and negative charges in the molecule, internally absorbed energy can be calculated. A freely rotating dipolar molecule will orientate itself under the influence of an external field. In the presence of an electric field the orientations of a dipole will no longer time average to zero, but will rather be weighted along the direction of the field.

The interaction between a polar molecule and a non-polar molecule is similar to the ion-induced dipole interaction discussed earlier. The polarising field comes from a permanent dipole rather than a charge. For a fixed dipole orientated at a specific angle θ, to a line joining it to a polarisable molecule a distance r away, the dipole induced interactions can be calculated from the electric field of the dipole. Then the interaction energy can then be calculated using $w = -\frac{1}{2}\alpha_0 E^2$, giving:

$$w(r,\theta) = \frac{-u^2\alpha_0(1+3\cos^2\theta)}{2(4\pi\varepsilon_0\varepsilon)^2 r^6} \tag{2.14}$$

This interaction is not strong enough to orientate the molecules. Generally for two different molecules, with a permanent dipole moment u_1 and u_2 and polarisability α_{0_1} and α_{0_2} respectively, their net dipole induced dipole energy becomes:

$$w(r) = \frac{-[u_1\alpha_{0_2} + u_2\alpha_{0_1}]}{(4\pi\varepsilon_0\varepsilon)^2}\frac{1}{r^6} \tag{2.15}$$

2.1.5 Van der Waal's Forces

2.1.5.1 Dispersion Forces

Dispersion forces act between all atoms and molecules and make up the third and most important contribution to the total van der Waal's force between atoms and molecules. They play a role in adhesion, surface tension, physical absorption and other surface phenomena, and are in fact called dispersion forces as they are responsible for the dispersion of light in matter. They are characterised as follows:

- They are of comparatively long range and can be effective from distances greater than $10nm$ down to interatomic spacings of about $0.2nm$.

- These forces may be repulsive or attractive and in general the dispersion force between two molecules does not follow a simple power law.
- Dispersion forces also account for some orientation of molecules, although this orientation is usually weak.
- The dispersion interaction between two molecules is affected by the presence of other bodies. This non-additivity of dispersion interactions means that you cannot simply add the individual pair potentials to obtain the total interaction.

Dispersion forces are quantum mechanical in origin, and a thorough explanation of these origins requires a study of quantum electrodynamics beyond the scope of this discussion. The origin of van der Waal's dispersion forces can be understood intuitively by considering that, in every atom, there is an instantaneous dipole moment created by the electrons and nuclear protons. This instantaneous dipole will generate an electric field that polarises any nearby neutral atom, inducing a dipole moment in it. The resulting interaction between the two dipoles gives rise to an instantaneous attractive force between them. This interaction has a finite speed of propagation which means that retardation effects must be taken into account. Theses retardation effects are distance dependent and affect the interaction quite differently at different distances.

A simple semi-quantitative model for van der Waal's dispersion forces can be obtained by considering the interaction between two Bohr atoms. In the Bohr atom an electron is pictured to be orbiting a proton. The smallest distance between the electron and the proton is known as the first radius a_0. It is distance at which Coulomb energy $\frac{e^2}{4\pi\varepsilon_0 a_0} = 2h\nu$, where h is the Planck constant and ν is the orbiting frequency of the electron. The resulting value for a_0 is,

$$a_0 = \frac{e^2}{8\pi\varepsilon_0 h\nu} = 0.053nm \tag{2.16}$$

$h\nu$ is the electron energy at the first Bohr radius and is equal to the energy required to ionise the atom (known as the first ionisation potential).

The Bohr atom although having no permanent dipole will have an instantaneous dipole of moment $u = a_0 e$. This dipole will produce a field that will interact with a second atom giving

rise to an attractive interaction similar to the dipole induced dipole interactions discussed earlier. The energy of this interaction can therefore be given by:

$$w(r) = \frac{-u^2\alpha_0}{(4\pi\varepsilon_0)^2}\frac{1}{r^6} = \frac{-(a_0 e)^2\alpha_0}{(4\pi\varepsilon_0)^2}\frac{1}{r^6} \tag{2.17}$$

Substituting the electronic polarisability of the second Bohr atom $\alpha_0 = 4\pi\varepsilon_0 a_0^3$ into Equation 2.17:

$$w(r) \approx \frac{-\alpha_0^2 h\nu}{(4\pi\varepsilon_0)^2}\frac{1}{r^6} \tag{2.18}$$

A more accurate model was derived by London in 1930 using quantum mechanical perturbation theory. The London result adds a factor of $\frac{3}{4}$ to Equation 2.18. The interaction potential for dissimilar atoms can be written as:

$$w(r) = -\frac{3}{2}\frac{\alpha_{0_1}\alpha_{0_2}}{(4\pi\varepsilon_0)^2}\frac{h\nu_1 h\nu_2}{h(\nu_1+\nu_2)}\frac{1}{r^6} \tag{2.19}$$

2.1.5.2 Combining the Interactions: Van der Waal's between Polar Molecules

Three distinct types of forces contribute to the total long range interaction between polar molecules, collectively known as van der Waal's forces: those are the induction force, the orientation force and the dispersion force, each of which has an interaction free energy that varies with the sixth power of the distance. Thus for two dissimilar polar molecules we have:

$$w_{vdw}(r) = \frac{-C_{vdw}}{r^6} = -\frac{[C_{orient} + C_{ind} + C_{disp}]}{r^6} = -\frac{\left[\left(u_1^2\alpha_{0_2} + u_2^2\alpha_{0_1}\right) + \frac{u_1^2u_2^2}{3KT} + \frac{3\alpha_{0_1}\alpha_{0_2}h\nu_1\nu_2}{2(\nu_1+\nu_2)}\right]}{(4\pi\varepsilon_0)^2}\frac{1}{r^6} \tag{2.20}$$

There are some interesting and important properties of the combined van der Waal's forces listed below.

- Dominance of dispersion forces. For most situations the dispersion forces exceed the dipole dependent induction and orientation forces, with only highly polar molecules providing the exception. Total van der Waal's forces can even, in some molecules, increase when the dipole moments decreases. So dominant is the dispersion force that for dissimilar molecules of which one is non-polar, the resultant van der Waal's energy is almost completely dominated by the dispersion force.

- In various comparisons of experimental data with the theoretical values, the correlation between the two is surprisingly good.
- In the interactions between two dissimilar molecules A and B, the coefficient C_{vdw} for A-B is often very close to the geometric mean of the interactions between like molecules, A-A and B-B. This is an approximation but it works well for most molecules with the highly polar molecules again being the exception.

2.1.5.3 General Theory of van der Waal's Forces Between Molecules: The Mclachlan Model

The London Equation 2.19 has two serious disadvantages. It assumes that atoms and molecules have only a single ionisation potential or absorption frequency, and it cannot handle interactions of a molecule in a solvent. In 1963 Mclachlan generalised the van der Waal's theory of two atoms. It included the induction, orientation and dispersion force in one equation and could also be applied to interactions in a solvent medium. For two molecules 1 and 2 in a medium the Mclachlan model is given by,

$$w(r) = \frac{-6KT}{(4\pi\varepsilon_0)^2}\frac{1}{r^6}\sum_{n=0,1,2,..}^{\infty}\frac{\alpha_1(i\nu_n)\,\alpha_2(i\nu_n)}{\varepsilon_3^2(i\nu_n)} \tag{2.21}$$

where $\alpha_1(i\nu_n)$ and $\alpha_2(i\nu_n)$ are the polarisabilities of the molecules 1 and 2 and $\varepsilon_3(i\nu_n)$ the dielectric permittivity of medium 3 at imaginary frequencies $i\nu_n$ where,

$$\nu_n = \left(\frac{2\pi KT}{h}\right)n \tag{2.22}$$

Frequencies can often be denoted by ω where $\omega = 2\pi\nu$, Planck's constant can also be denoted by $\hbar$ where $\hbar = \frac{h}{2\pi}$.

2.1.6 Repulsive Forces

At very small interatomic distances the electron clouds of atoms overlap and there arises a very strong repulsive force that determines how closely two atoms can actually approach each other. These forces are quantum mechanical or chemical in nature, and are characterised by having

extremely short range and increasing sharply as two molecules come together. Unfortunately there is no general equation to describe their distance dependence. Instead there are a number of empirical potential functions which have been introduced over the years.

- Hard Sphere Potentials: If atoms are considered as incompressible hard spheres the repulsive force suddenly becomes infinite at certain interatomic separations. The radius of this atom or spherical molecule is called the hard sphere radius or the van der Waal's packing radius. The hard sphere potential can be described by,

$$w(r) = \left(\frac{\sigma}{r}\right)^n \tag{2.23}$$

  where $n = \infty$.

- The power law potential is more realistic in that it allows for the compressibility of atoms. The power law potential has little theoretical basis and is largely used for its mathematical convenience. The power law potential can be written as,

$$w(r) = \left(\frac{\sigma}{r}\right)^n \tag{2.24}$$

  where n is an integer usually taken to be between 9 and 16.

- Like the power law potential, the exponential potential also allows for the compressibility of atoms. Although having more theoretical justification than the power law potential its usage is also due to its mathematical convenience.

$$w(r) = ce^{\frac{-r}{\sigma_0}} \tag{2.25}$$

  where c and σ_0 are adjustable constants.

2.1.7 Total Intermolecular Pair Potentials: The Lennard-Jones Potential

The total intermolecular pair potential is obtained by combining the attractive and repulsive potentials into one equation. The best known of these equations is the Lennard-Jones or '6-12'

equation given as:

$$w(r) = \frac{A}{r^{12}} - \frac{B}{r^6} = 4\epsilon\left[\left(\frac{\sigma}{r}\right)^{12} - \left(\frac{\sigma}{r}\right)^{6}\right] \tag{2.26}$$

This equation is widely used due to its simplicity, and although it does contain a few errors it is a good approximation for the interaction potential between molecules. It has a steep repulsive force and an attractive force with an inverse sixth power law which is the same as the total van der Waal's forces. The force law can be obtained using $F(r) = \frac{dw(r)}{dr}$ to get:

$$F(r) = 24\epsilon\left[\frac{\sigma^6}{r^7} - 2\frac{\sigma^{12}}{r^{13}}\right] \tag{2.27}$$

The energy and force laws are plotted in Figure 2.1.2.

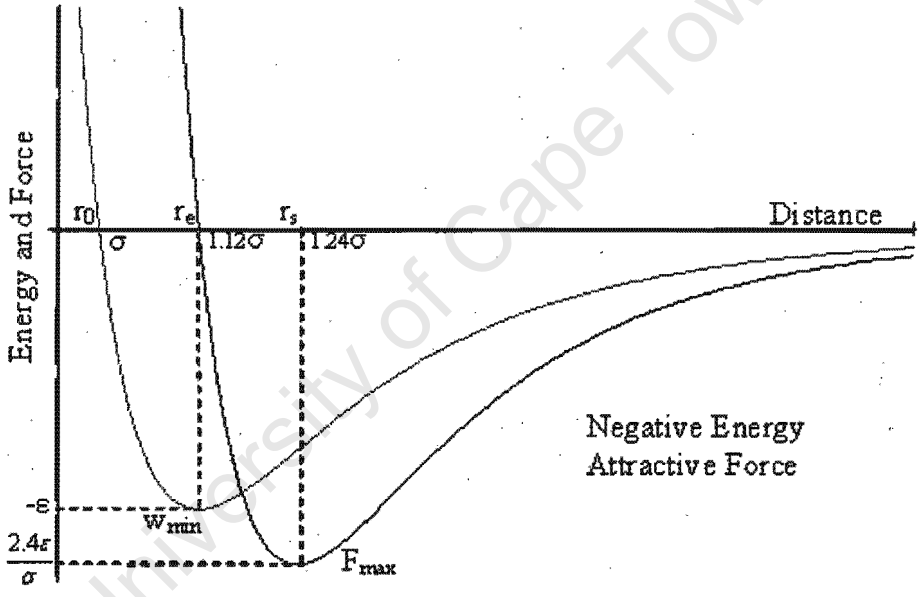

Figure 2.1.2: The Lennard-Jones Potential for Energy and Force. *Also known as the '6-12' potential the Lennard Jones potential is a reasonable approximation for intermolecular forces. The attractive force, or negative energy, component has a van der Waal's distance dependence of $n = 6$. The repulsive force component has a distance dependence of $n = 12$ in line with the experimental values.*

For the Lennard-Jones potential the value σ is no longer the size of the molecule, but rather the distance, r_0, between interacting molecules where the interaction energy is zero. The energy of the interaction, $w(r)$, is at a minimum when the interaction force, $F(r)$, is zero which is at

the distance $r_e = 1.12\sigma$. The maximum force will occur when $\frac{dF(r)}{dr} = 0$, which correlates to a distance $r_s = 1.24\sigma$. The values for the minimum energy and the maximum force are given in Figure 2.1.2.

2.1.8 Interaction Potentials of Macroscopic Bodies

2.1.8.1 Contrasts between Intermolecular, Interparticle and Intersurface Forces

Intermolecular forces are versatile in the sense that the same force can have different effects at short and long ranges. The properties of gases and the cohesive strength of solids and liquids are mainly due to the short range interaction that one molecule has with its nearest neighbours. Only the Coulomb interaction is effectively long ranged in that the energy decays slowly and remains strong at long distance. However the Coulomb force is often much reduced in most media, leaving the short range effects to dominate.

A very different situation arises when the interactions of macroscopic particles are considered. When all the pair potentials between all the molecules in each macroscopic body are summed the combination has the following properties,

- The net interaction potential is proportional to the size of the particles. This means that the energy can be larger than KT even at separations of more than $100nm$.
- That the energy and force decay much more slowly with the separation. This makes the interactions between macroscopic bodies of much longer range than those between molecules, even though the same basic force may be operating in both.
- If the force law is not purely attractive or repulsive all manner of behaviour may arise depending on the specific form of the long range distance dependence.

These differences mean that the interaction potential may change much more slowly and obey a very different distance dependence law to the intermolecular force and the Lennard-Jones potential.

2.1.8.2 Molecule-Surface Interaction

Assuming once again that the interaction potential between two atoms or small molecules is purely attractive and of the form $w(r) = -\frac{c}{r^n}$, the net interaction, assuming additivity, of a molecule and the planar surface of a solid made up of like molecules will be the sum of its interactions with all molecules in the body. This system is shown in figure 2.1.3:

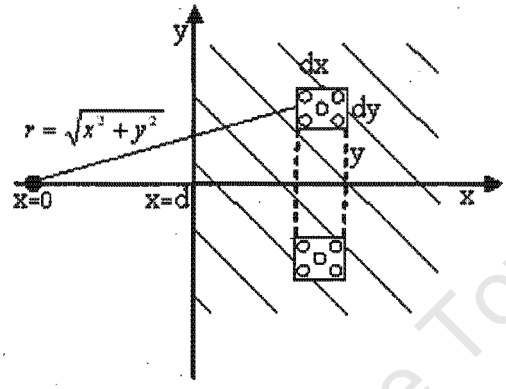

Figure 2.1.3: The Interaction Between a Single Molecule and a Surface. *The total interaction will be the sum of the all the interactions between the molecule at $x = 0$ and all the molecules in the surface. The surface encompasses all the area for $x > d$. The surface should also be considered as three dimensional so that dx and dy are the length and thickness of a circular ring of radius y.*

For molecules in a circular ring dy thick and dx long, with a radius y, the ring volume is $2\pi.x.dx.dy$. For a number density ρ, the number of particles in the ring will be $2\pi.x.dx.dy.\rho$. Substituting these values into the interaction equation and integrating across the limits will give the net interaction energy. For a molecule at a distance D away from the surface the net interaction will be:

$$w(d) = -2\pi C\rho \int_d^\infty dx \int_0^\infty \frac{ydy}{\left((x^2+y^2)^{\frac{1}{2}}\right)^n} = -\frac{2\pi C\rho}{n-2}\int_d^\infty \frac{dx}{x^{n-2}} = -\frac{2\pi C\rho}{(n-2)(n-3)d^{n-3}} \tag{2.28}$$

For van der Waal's forces where $n = 6$ Equation 2.28 becomes:

$$w(d) = -\frac{\pi C\rho}{6d^3} \tag{2.29}$$

2.1.8.3 Surface-Surface Interaction

Using the techniques that were seen in the previous section the interaction energy between two planar surfaces a distance D apart can now be defined. For infinite surfaces the interaction energy would be infinite so the energy per unit surface area is considered. The system is shown in Figure 2.1.4.

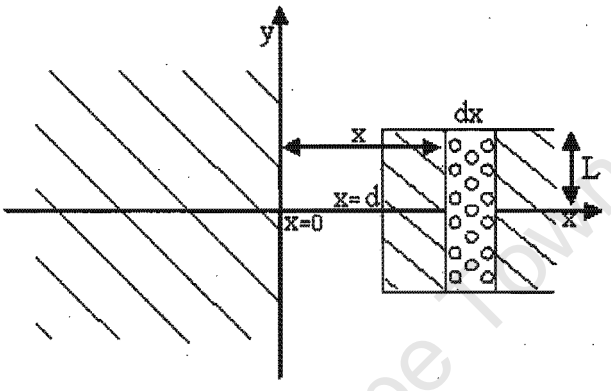

Figure 2.1.4: Two Interacting Surfaces. *The interaction between the two surfaces can be built up by considering the interaction between each molecule within the surface of unit area with all the molecules within the infinite surface depicted by all values where $x < 0$.*

Consider a thin sheet of molecules of unit surface area and thickness dx located a distance x away from an extended surface area. As it is of unit surface area, the total number of molecules in this strip will be ρdx. Using the molecule surface interaction equation from the previous section the interaction of the thin sheet with the surface will be:

$$\frac{-2\pi C\rho\,(\rho dx)}{(n-2)\,(n-3)\,x^{n-3}} \tag{2.30}$$

Thus the total interaction of the two surfaces will be:

$$w(d) = \frac{-2\pi C\rho^2}{(n-2)\,(n-3)} \int_d^\infty \frac{dx}{x^{n-3}} = \frac{-2\pi C\rho^2}{(n-2)\,(n-3)\,(n-4)\,d^{n-4}} \tag{2.31}$$

This integral is basically the summation of the effects of all the molecules in one surface with all the molecules in the other. This interaction is for one surface of unit area interacting with another surface of infinite area. In practice the interaction is more likely to be between two surfaces of unit area. The interaction potential described in Equation 2.31 is then only

strictly applicable when d is small compared to the surface area of the interacting surfaces.

2.1.8.4 Hamaker Constant

A very useful parameter when considering the interactions between macroscopic bodies is the Hamaker constant A, which is defined as[18][19]:

$$A = \pi^2 C \rho_1 \rho_2 \tag{2.32}$$

C is the coefficient in the molecule-molecule pair potential and $\rho_{1,2}$ are the number density of the molecules of the two interacting media. A is fairly constant and varies only on a small range $0.4 * 10^{-19} J < A < 4 * 10^{-19} J$.

For van der Waal's forces ($n = 6$) with the Hamaker constant in place the interaction energy between two surfaces becomes,

$$\frac{-A}{12\pi d^2} \tag{2.33}$$

The method used so far in calculating the force and interaction energy ignores the effects that neighbouring atoms would have on the interaction between any pair of atoms. The method simple summed the effects of single molecules to obtain the total interaction. The correct way to account for these contributions is to solve the problem self consistently using the method of images. This is what is done in the Lifshitz model for van der Waal's forces [18][19]. It can, however, be noted that the only thing changed by the application of these theories is the Hamaker constant with the basic expressions remaining the same.

2.1.9 Interaction Potential and the Tuning Fork

These models, although giving a very good idea, probably do not describe the interaction between the tuning fork and the surface exactly. This is because most of these models deal with ideal systems, where the physical approach is perfectly perpendicular and the exact size and shape of the approaching surfaces is known. Unfortunately for the tuning fork, this exact knowledge is very difficult to obtain. Hamaker constants, for instance, change greatly depending on the materials involved. They also can be quite difficult to determine. The tuning fork orientation may vary and this would result in non perpendicular motion in relation to the

surface. The size and shape of both interacting surfaces may change which would further complicate the model. Another area of uncertainty is the effect that the medium surrounding the interacting surfaces will have on the interaction. Changes in the medium will no doubt have an effect on the strength and distance dependence of the interaction, and would have to be included in the already complicated theoretical model.

However, these models do provide a very good idea of what happens in the interaction between the tuning fork and the surface. For most circumstances there will be a longer ranged attractive force whose distance dependence will vary depending on the size and orientation of the interacting surfaces. There should also be a much shorter ranged repulsive force, which will grow rapidly as the tuning fork approaches the surface. The size of these forces will be dependent on the interaction surface area and the make up of the two surfaces, and although the basic idea of the contact model is known the actual specifics would best be determined by experimentation.

2.2 Air Effects

The second component of the force that will be experienced by the tuning fork when it approaches a surface has to do with the effect that the movement of the surrounding air has on the characteristics of the tuning fork. As the tuning fork approaches the surface a change in both the stiffness and resistance of the surrounding air will be experienced. These effects will vary in strength with distance, so by monitoring the change in the tuning fork characteristics a determination of the fork height above the surface can be made. The extent of these air effects as well as their dependence on other variables such as pressure and surface area will be further developed in this section.

2.2.1 The Basic Idea

The tuning fork displacement sensor can be modelled as a vibrating surface located a relatively small distance away from a stationary surface. The movement of the vibrating surface would force air in and out of the gap between the surfaces. The situation is depicted in figure 2.2.1.

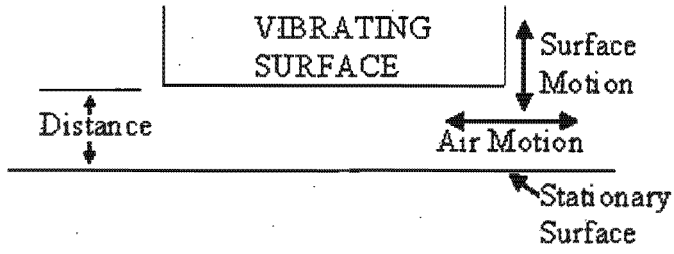

Figure 2.2.1: A Vibrating Surface above a Stationary Surface. *The surrounding air will move in and out of the gap between the two surfaces. Forces due to this air flow will be experienced by both surfaces which will affect the vibration characteristics of the tuning fork.*

Rule, Suellentrop and Perls [20] consider how the air will move in and out from between the two surfaces. As air is forced out between the gap the viscosity of the air causes the motion of the piston to be resisted. Also as the air cannot escape immediately there is an increase in pressure which results in an elastic force on the vibrating surface. At low frequencies, it is easier for the air to move out from in between the surfaces which reduces the pressure increase or elastic force on the vibrating surface. This means that the resistive frictional force will be maximum at low frequencies. At high frequencies much less air will be able to flow which means that the resistive forces will be small whilst the elastic forces increase.

Other than the distance between them, there will be other factors that influence the size and nature of the force between the vibrating surface and the stationary surface. The characteristics of the air between the surfaces, such as temperature and pressure, will change the way the air behaves, changing the force between the surfaces. Other major factors will be the size, shape and orientation of the two surfaces, each of which will greatly affect both the volume and shape of the air flow between the surfaces.

2.2.2 Mathematical Model

The theory for the air effects of the air gap between a vibrating circular piston and a stationary surface has been given in detail by Crandall in the book "Theory of Vibrating Systems and Sound"[21]. Although the book deals with sound transducers, the situation of one cylinder of arbitrary surface area vibrating above another stationary one is considered and can be applied to the approximation.

Basically, the vibration of the circular membrane will cause an increase in pressure in the air gap between the surfaces which will depend on the size of the vibration. The relationship for the pressure increase is given by the equation:

$$p = B\left(\frac{d}{D}\right) \tag{2.34}$$

Where B is the atmospheric pressure, D is the distance between the two surfaces and d is the vibration displacement. This change in pressure will cause a flow of air in the air gap. Air will either be forced out, if the displacement is towards the surface, or more air will be let in, if the one surface moves away from the other. The resistance coefficient to this flow of air is calculated using the equation for laminar flow between two plates,

$$R = \frac{12\mu}{D^2} \tag{2.35}$$

where μ is the viscosity of the air, and the inertia of the air has been neglected as it is small.

Using the velocity of flow and the resistance coefficient, Crandall, using Bessel functions for circular membranes, determines a pressure function for the air gap. By integrating across the volume, values for the total resistance and elastic stiffness of the air gap can be given as [21],

$$\begin{aligned} \text{Resistance} &= c = \frac{2\pi r B}{\omega \alpha D}\left[\frac{bei\alpha r.bei'\alpha r + ber\alpha r.ber'\alpha r}{bei^2\alpha r + ber^2\alpha r}\right] \\ \text{Stiffness} &= k = \frac{\pi r^2 B}{D}\left[1 - \frac{2}{\alpha r}\frac{ber\alpha r.bei'\alpha r + bei\alpha r.ber'\alpha r}{bei^2\alpha r + ber^2\alpha r}\right] \end{aligned} \tag{2.36}$$

where r is the radius of the vibrating membrane and α is function derived form the resistance coefficient $\sqrt{\frac{12\mu\omega}{BD^2}}$. The $ber\alpha r$ and $bei\alpha r$ functions are the real and imaginary parts of the Bessel function.

2.2.3 Other Models to Consider

Other models for the forces in the system do exist. In the paper "Effects of Air Damping in Non Contact Resonant Force Microscopy", Lévêque, Girard et al [22] calculate the viscous drag

forces present on the two plane discs using the Navier-Stokes equations as:

$$F = \frac{3\pi\mu r^4 V}{2D^3} \tag{2.37}$$

where V is the velocity of the plate, μ is the viscosity of the air, r is the radius of the plate and D is the distance between them. This solution is only for incompressible laminar flow. The paper also calculates the force between a perpendicularly vibrating sphere and the surface. The Navier-Stokes equations are approximated and integrated across the sphere to give the equation:

$$F = \frac{6\pi\mu R^2 V}{D} \tag{2.38}$$

This equation is also calculated for laminar incompressible flow.

2.2.4 Air Effects and the Tuning Fork

None of the above models will perfectly describe the air effects on the vibrating tuning fork as it approaches a surface. The models are rather for ideal shapes with perfect orientation and motion. The motion of the fork in relation to the surface will depend greatly on its orientation, unless perfectly orientated the motion will consist not only of perpendicular motion but will also contain a parallel component in relation to the surface. Also, the shape of the fork or the surface it approaches will not be entirely cylindrical, and the angle of the fork will also contribute to the mismatch with the models.

The models do, however, make many useful contributions to the understanding of how the tuning fork interacts with the approached surface. Considering the distance dependence of the models, the air effects should be of longer range than the forces caused by the intermolecular interaction between the surfaces. The air effects will also be highly dependent on the orientation of the tuning fork as it approaches the surface. The surface shape and size will also affect the system as well as the ambient conditions of the air such as pressure, temperature and viscosity. A combination of the models would be needed to precisely describe the interaction and would probably best be determined through experimentation.

Air effects on the whole have a detrimental effect on the operation of the tuning fork as a displacement sensor. The air effects damp the motion of the tuning fork and reduce its

sensitivity to force change. They also mask the intersurface forces reducing their strength and range. Ideally the air effects should be reduced by placing the tuning fork in a vacuum. This would eliminate all the forces such as: buoyancy, viscous damping and compression forces, which are associated with the passage of air around the system. Operating in a vacuum is, however, often very difficult to achieve practically. Although some experiments were carried out in a vacuum chamber, for the majority of the experimental work the operation and testing of the device had to be done in open air, where the air effects are very much a part of the contact model.

Now that we have a contact model for the interaction between the piezoelectric tuning fork and an approaching surface, we can move onto developing the models for the actual fork. The first step is to develop a model for how the tuning fork behaves mechanically when it vibrates. The link between the mechanical vibration and the electrical input and output signals also needs to be developed as well as the fundamental limits of the tuning fork's ability to measure displacement. All these issues are considered in detail in the next chapter.

Chapter 3

The Tuning Fork Displacement Sensor

3.1 Introduction

A tuning fork, structurally, is a relatively simple device. It follows a narrow U shaped design with two arms or tines connected by a middle section. Although it can theoretically be any shape, in most tuning forks the centre piece is semicircular. The tuning fork is specifically made to be highly symmetrical. Both tines are identical in shape and size, and the centre section is also symmetrical in design. This attention to symmetry is vital to the functioning of the tuning fork.

When considering how the tuning fork works it is useful to consider each tine individually first, and then combine the responses to ascertain how the device functions. Consider just one of the tines oscillating with a constant amplitude. This oscillation would produce a force on the centre piece proportional to the amplitude of the acceleration of the tine. According to Newton's third law, which states that any action will have an equal but opposite reaction, the centre piece will produce a force on the tine which is equal in size but opposite in direction to the force produced by the tine. The force produced by the centre piece on the tine restricts or damps the motion of the fork. Now if the second tine is oscillating with the same amplitude but in anti-phase to the first one as seen in Figure 3.1.1, the force produced on the center piece will be equal in size but opposite in direction to the force produced by the first tine. The force

from the two tines will cancel each other out producing a zero resultant force on the centre piece. With no force on the centre piece, there will be no force produced by the centre piece on the tines. This means that the damping on the tines is significantly reduced as the only forces restricting the motion are the forces between the tines and the medium in which it is operating, and the forces due to the internal resistivity of the material.

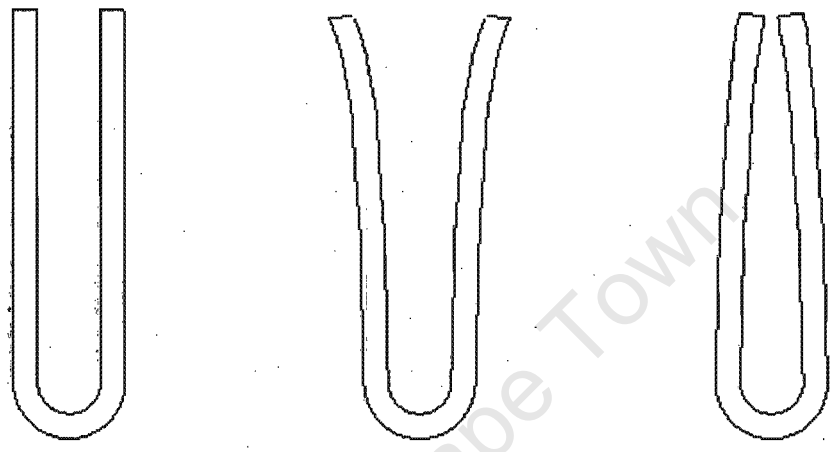

Figure 3.1.1: A Tuning Fork Vibrating in Anti-Phase. *The anti-phase motion of the two tines of the tuning fork results in zero force being exerted on the central section.*

3.2 Developing a Mathematical Model of the Tuning Fork

The simplest way to model a tuning fork's response is to consider each tine as a separate vibrating cantilever[23][24]. A cantilever in turn can be considered to be a simple beam anchored on the one end. Motion of the cantilever would be produced by an external force acting on the cantilever. The forces can be distributed or localised and can vary in both location and time. In order to determine the effects that these external forces would have on the cantilever, it is important to know some of the basic mechanical attributes of the system. The cantilever model developed in this section is also used again to model the behaviour of the piezoelectric transducers in Chapter 5.

3.2.1 Bending Cantilevers

Applying the bending theory to a cantilever yields some important equations for the general equation for motion of the cantilever. The general theory of bending theory is described in detail

in Chapter 1 of the Book "Scanning Force Microscopy" by Dror Sarid [25] and "Mechanics of Materials" by E. J. Hearn [26]. It is set out in Appendix A1. It gives rise to the equation

$$\frac{M}{I} = \frac{E}{R} = \frac{\sigma}{y} \tag{3.1}$$

where M is the total bending moment, I is the second moment of inertia, E is the Young's modulus of the material and R is the radius of the arc produced by the bending cantilever. The stress σ, and the distance from the neutral axis in the cantilever y, are also used in the bending equations. Using the expression for the curvature of a plane curve

$$\frac{1}{R} = \frac{\frac{d^2y}{dx^2}}{\left[1 + \left(\frac{dy}{dx}\right)^2\right]^{\frac{3}{2}}} \tag{3.2}$$

where for small deflection angles the denominator of Equation 3.2 can be approximated by unity. Equation 3.2 for the curvature of the lever can be equated to the bending theory equation:

$$\frac{d^2y}{dx^2} = \frac{M}{EI} \tag{3.3}$$

This can now be applied to the cantilever in Figure 3.2.1. The cantilever is anchored rigidly on its left side and has a force F acting at a point a, in a downward direction.

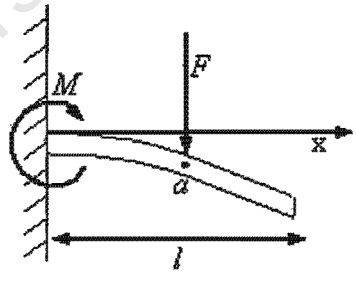

Figure 3.2.1: A Cantilever Bending in Response to a Centrally Placed Force.

The moment at any given point x, produced by a force acting at a point a is:

$$M = F(x - a) \tag{3.4}$$

Inserting this value for M into Equation 3.3 and integrating twice will give the deflection

of the beam as:

$$y = \frac{Fx^2(x - 3a)}{6EI} \tag{3.5}$$

Setting $x = a = l$ gives:

$$y = -\frac{l^3 F}{3EI} \tag{3.6}$$

3.2.2 Classical Solution to a Vibrating Cantilever

The classical solution is an exact solution which produces all the resonant frequencies of the lever together with the modes of vibration. In this method the equation of motion is first derived, and then solved using the boundary conditions of the lever. This solution was adapted from the book "Mechanical and Structural Vibrations" by Fertis [27]. Consider the cantilever in Figure 3.2.2 with length L, and an element of length dx located a distance x from the origin O. The exciting or driving force is called $q(t, x)$ and can vary with both time and displacement along the beam.

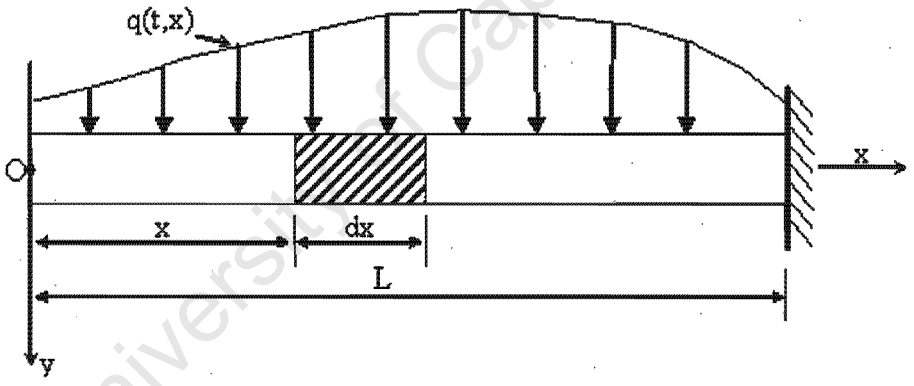

Figure 3.2.2: Uniform Elastic Beam Subject to an External Force. *The simple beam is anchored on the right hand side to form the cantilever. The force on the beam varies both in time and in position along the beam. An element of length dx can then be defined, located a distance x from the free end at O.*

The free body diagram of the individual element dx is presented in Figure 3.2.3. In this diagram M and $M + \left(\frac{\partial M}{\partial x}\right) dx$ are the dynamic moments acting on the sides of the element, V and $V + \left(\frac{\partial V}{\partial x}\right) dx$ are the dynamic shear forces, y is the vertical dynamic displacement, $\ddot{y}$ is the acceleration in the y direction, A is the cross sectional area and ρ is the mass density. The mass per unit length will therefore be $\rho A dx$ and the inertia force will be $\rho A \ddot{y} dx$.

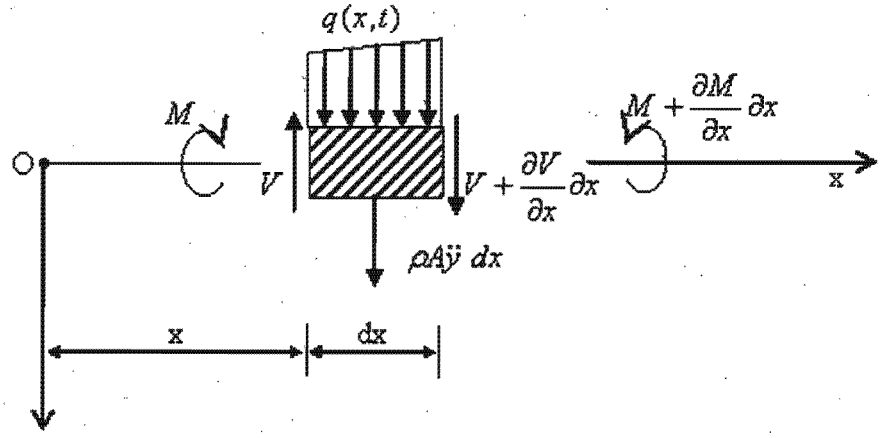

Figure 3.2.3: The Free Body Diagram of an Individual Element. *All the forces on the element of length dx located at a length x from the free end have been defined. These forces consist of: The applied force $q(x,t)$ that varies with both time and distance, the inertia or acceleration force $\rho A\ddot{y}dx$ that is proportional to the acceleration and the mass of the element and the final forces are the shear forces V and $V + \frac{\partial V}{\partial x}$, produced by the moments acting on the sides of the element.*

Applying Newton's second law of motion, which states that the force on an object is equal to the product of its mass and acceleration, to the above system gives:

$$\rho A\ddot{y}dx = q(t,x)\,dx - V + V + \left(\frac{\partial V}{\partial x}\right)dx \Rightarrow m\ddot{y} - \frac{\partial V}{\partial x} = q(t,x) \tag{3.7}$$

Now consider that the beam, which is initially horizontal when unloaded, is now deflected under the load. The slope at any point will be given by the equation:

$$i = \frac{dy}{dx} \tag{3.8}$$

For small curvatures, like those occurring in most practical situations,

$$dx = R\,di \tag{3.9}$$

where R is again the radius of the circle formed by the sloping beam, so therefore,

$$\frac{di}{dx} = \frac{1}{R}$$

$$\text{but } i = \frac{dy}{dx}$$

$$\therefore \frac{d^2y}{dx^2} = \frac{1}{R} \tag{3.10}$$

Now from the simple bending theory stated in Equation 3.1:

$$\frac{1}{R} = \frac{M}{EI} \tag{3.11}$$

Substituting Equation 3.10 into Equation 3.11 gives:

$$M = EI\frac{d^2y}{dx^2} \tag{3.12}$$

Again using simple bending theory the following equation can be derived for the considered cantilever:

$$V = \frac{\partial M}{\partial x} = -EI\frac{d^3y}{dx^3} \tag{3.13}$$

Equation 3.13 is negative due to the way the cantilever is bending when the load $q(t,x)$ is applied. Substituting Equation 3.13 into the Equation 3.7 derived from Newton's second law gives:

$$\rho A\ddot{y} - \frac{\partial}{\partial x}\left(-EI\frac{d^3y}{dx^3}\right) = q(t,x) \Rightarrow EI\frac{d^4y}{dx^4} + \rho A\frac{d^2y}{dt^2} = q(t,x) \tag{3.14}$$

This gives the free undamped vibration of the cantilever. In order to solve this differential equation the no load situation is considered. This situation is governed by the following equation:

$$EI\frac{d^4y}{dx^4} + \rho A\frac{d^2y}{dt^2} = 0 \tag{3.15}$$

For the following formulated solution it is assumed that the characteristics of the beam such as the second moment of inertia and Young's modulus remain constant throughout the beam.

Rotational and shear effects are also assumed to be zero. These approximations are fair for the tuning fork example as it is very close to a uniform bar, and when operating correctly should have very minor shear or rotational effects.

A solution $y(t,x)$ of Equation 3.15 will be composed of a function $Y(x)$ that only varies with x, and a function $f(t)$ that only varies with time.

$$y(t,x) = Y(x)f(t) \tag{3.16}$$

Substituting Equation 3.16 into Equation 3.15 gives the following equation:

$$EI\frac{\partial^4}{\partial x^4}\left[Y\left(x\right)f\left(t\right)\right] + \rho A\frac{\partial^2}{\partial t^2}\left[Y\left(x\right)f\left(t\right)\right] = 0$$

Using the product rule we get:

$$EI\frac{\partial^4 Y\left(x\right)}{\partial x^4}f\left(t\right) + \rho A\frac{\partial^2 f\left(t\right)}{\partial t^2}Y\left(x\right) = 0 \tag{3.17}$$

Equation 3.17 is rearranged so that the left hand side contains only functions of x, and the right hand side contains only functions of time t, giving:

$$\frac{EI}{\rho A}\frac{\partial^4 Y\left(x\right)}{\partial x^4}\frac{1}{Y\left(x\right)} = -\frac{\partial^2 f\left(t\right)}{\partial t^2}\frac{1}{f\left(t\right)} \tag{3.18}$$

The equations can be satisfied if, and only if, both sides are equal to the same constant. Taking this constant to equal ω^2 gives:

$$\frac{EI}{\rho A}\frac{\partial^4 Y\left(x\right)}{\partial x^4}\frac{1}{Y\left(x\right)} = \omega^2 \qquad and \qquad -\frac{\partial^2 f\left(t\right)}{\partial t^2}\frac{1}{f\left(t\right)} = \omega^2 \tag{3.19}$$

or

$$\frac{\partial^4 Y\left(x\right)}{\partial x^4} - \lambda^4 Y\left(x\right) = 0 \tag{3.20}$$

$$\frac{\partial^2 f\left(t\right)}{\partial t^2} - \omega^2 f(t) = 0 \tag{3.21}$$

where

$$\lambda^4 = \frac{\rho A \omega^2}{EI} \tag{3.22}$$

Equation 3.20 and Equation 3.21 are each determined separately in the next sections.

3.2.2.1 $Y(x)$ Solution

The solution for $Y(x)$ is considered in many sources[25][27][28][29]. A general solution is presented here. A solution $Y(x)$ of Equation 3.20 can be of the form:

$$Y(x) = Ce^{\psi x} \tag{3.23}$$

Where C and ψ are constants. Substituting the Equation 3.23 into Equation 3.20 and working through the mathematics gives:

$$\psi^4 = \lambda^4 \tag{3.24}$$

which gives the roots of ψ.

$$\begin{aligned} \psi_1 &= \lambda \qquad \psi_2 = i\lambda \\ \psi_3 &= -\lambda \qquad \psi_3 = -i\lambda \end{aligned}$$

Using these roots Equation 3.23 can be re-written as:

$$Y(x) = C_1 e^{\lambda x} + C_2 e^{-\lambda x} + C_3 e^{i\lambda x} + C_4 e^{-i\lambda x} \tag{3.25}$$

Using Euler's formula

$$\begin{aligned} e^{\pm\lambda x} &= \cosh \lambda x \pm \sinh \lambda x \\ e^{\pm i\lambda x} &= \cos \lambda x \pm i \sin \lambda x \end{aligned}$$

gives a trigonometric form of the Equation 3.25 as:

$$Y(x) = A_1 \cosh \lambda x + A_2 \sinh \lambda x + A_3 \cos \lambda x + A_4 \sin \lambda x \tag{3.26}$$

Equation 3.20 is a fourth order partial differential equation, and its solution yields the expression for the function $Y(x)$, which defines the shapes of the modes corresponding to the free undamped frequencies ω of an elastic beam. Since the considered cantilever has continuous mass and elasticity it will have infinite degrees of freedom. The frequencies of vibration will be infinite in number. Therefore we will have an infinite number of functions $Y(x)$ that define the corresponding mode shapes.

3.2.2.1.1 Normal Modes In order to determine the normal modes of the vibration of the cantilever, Equation 3.26 can be re-written when applying boundary conditions as:

$$Y(x) = A'(\cos \lambda x + \cosh \lambda x) + B'(\cos \lambda x - \cosh \lambda x) + C'(\sin \lambda x + \sinh \lambda x) + D'(\sin \lambda x - \sinh \lambda x) \tag{3.27}$$

The deflection, slope, moment and shear force of the deformed lever are proportional to y, $\frac{\partial y}{\partial x}$, $\frac{\partial^2 y}{\partial x^2}$, $\frac{\partial^3 y}{\partial x^3}$ respectively. At the anchor point of a vibrating lever, the deflection and slope will be zero, whilst at the free end the moment and shear force will be zero. Using these boundary conditions Equation 3.27 and its derivatives can be solved giving the following expressions:

$$0 = B'(\cos \lambda l + \cosh \lambda l) + D'(\sin \lambda l + \sinh \lambda l) \tag{3.28}$$

$$0 = B'(\sin \lambda l - \sinh \lambda l) + D'(-\cos \lambda l - \cosh \lambda l) \tag{3.29}$$

Combining Equations 3.28 and Equation 3.29

$$\frac{D'}{B'} = \frac{\cos \lambda l + \cosh \lambda l}{\sin \lambda l + \sinh \lambda l} = \frac{\sin \lambda l - \sinh \lambda l}{\cos \lambda l + \cosh \lambda l} \tag{3.30}$$

which reduces to the simple implicit equation:

$$\cos \lambda l \cosh \lambda l + 1 = 0 \tag{3.31}$$

The first values of λl and $\frac{D'}{B'}$ will be 1.875 and -0.7341 respectively. From the expression for λ, derived in Equation 3.22, the fundamental frequency ω, in radians per second, can be determined by the following equation:

$$\omega = \lambda^2 \sqrt{\frac{EI}{\rho A}} = \left(\frac{1.875}{l}\right)^2 \sqrt{\frac{EI}{\rho A}} \tag{3.32}$$

3.2.2.2 Solution for $f(t)$ - Mass Spring System

Equation 3.21 is a second order partial differential equation and has the same form as the equation that deals with the free, undamped harmonic vibration of a one degree mass spring system. The solution for this system is similar to the one developed in [3][27], which appears in Appendix A2. The developed solution is for damped systems and is given below as

$$x(t) = e^{\frac{-t}{2\tau}} \left[(x(0)) \cos(\omega_o' t) + \frac{1}{\omega_o'} \left[\dot{x}(0) + \frac{x(0)}{2\tau} \right] \sin(\omega_o' t) \right] \tag{3.33}$$

where τ is the damping time constant and ω_o' is the damped resonant frequency, which are both dependent on the characteristics of the mass spring system and are defined in Appendix A2. $x(0)$ and $\dot{x}(0)$ are the initial conditions of motion. For the undamped case the above solution is easily adapted to form the following solution for $f(t)$:

$$\begin{aligned} f(t) &= A \sin(\omega t) + B \cos(\omega t) \\ f(t) &= C \sin(\omega t + \varphi) \end{aligned} \tag{3.34}$$

where A, B and C are constants determined by the initial conditions of motion and ω is the undamped resonant frequency of the system.

3.2.2.3 The Combined General Solution

Equation 3.26 gives the general solution of Equation 3.20 and can be used for any beam of uniform mass and EI constants. The constants in the equation can be derived from the initial conditions of the beam. By substituting the Equations 3.26 and 3.34 into Equation 3.16 the

general solution for Equation 3.15 can be found,

$$\begin{aligned} y(t,x) &= (A_1 \cosh \lambda x + A_2 \sinh \lambda x + A_3 \cos \lambda x + A_4 \sin \lambda x)(A \sin(\omega t) + B \cos(\omega t)) \\ \text{or } y(t,x) &= (A_1 \cosh \lambda x + A_2 \sinh \lambda x + A_3 \cos \lambda x + A_4 \sin \lambda x)(C \sin(\omega + \theta)) \end{aligned} \tag{3.35}$$

The general solution for the free, undamped, transverse vibration of the cantilever has now been obtained. All the constants can be found by using the boundary conditions of the beam as well as the initial time conditions.

3.2.3 Equivalent Mass-Spring Model

In many practical systems a complex system can be replaced by an idealised simple one with similar characteristics for vibration and general dynamic analysis [27]. The complex analysis of a cantilever beam presented in the previous section may be replaced with an idealised one-degree mass-spring system.

The effective spring constant represents the transverse stiffness of the cantilever at the free end of the beam. From Equation 3.6 the deflection at the free end of the beam is given by:

$$y = -\frac{l^3 F}{3EI} \tag{3.36}$$

From basic physics the spring constant or compliance is defined as:

$$k = \left| \frac{F}{y} \right| \tag{3.37}$$

Which gives the effective spring constant of the cantilever as:

$$k = 3\frac{EI}{l^3} \tag{3.38}$$

In order to determine the effective mass of a cantilever Equation 3.38 is used in the form,

$$EI = \frac{kl^3}{3} \tag{3.39}$$

and substituted into Equation 3.32[25]:

$$\omega = \left(\frac{1.875}{l}\right)^2 \sqrt{\frac{kl^3}{3\rho A}} = \sqrt{\frac{\left(\frac{1.875}{l}\right)^4 kl^3}{3\rho A}} = \sqrt{\frac{(1.875)^4 k}{3\rho Al}} \tag{3.40}$$

As ρAl will equal the total mass of the cantilever m_c, Equation 3.40 can be rewritten as:

$$\omega = \sqrt{\frac{k}{0.2427 m_c}} \tag{3.41}$$

Equation 3.41 can be equated to the substitution equation in Chapter 1 that gives the general expression for the frequency of the fundamental mode of the mass spring system as $\omega_o = \sqrt{\frac{k}{m}}$. This gives the effective mass in the mass spring model of the cantilever as:

$$m_{eff} = 0.2427 m_c \tag{3.42}$$

3.3 Piezoelectric Conversion

3.3.1 Piezoelectric Material

Piezoelectricity is defined by Cady [30] as "electric polarisation produced by mechanical strain in crystals belonging to certain classes, the polarisation being proportional to the strain and changing sign with it". Piezoelectric materials are also characterised by the inverse piezoelectric effect where an electric polarisation will produce a mechanical strain in the material. The piezoelectric effect was discovered in 1880 by Jaques and Pierre Curie and has since then been developed into many different applications.

A piezoelectric tuning fork is generally made from a single crystal cut in such a way that the application of voltage across the crystal results in the anti-phase motion of the two arms. A picture of a typical tuning fork crystal which was used in this research is shown in Figure 3.3.1.

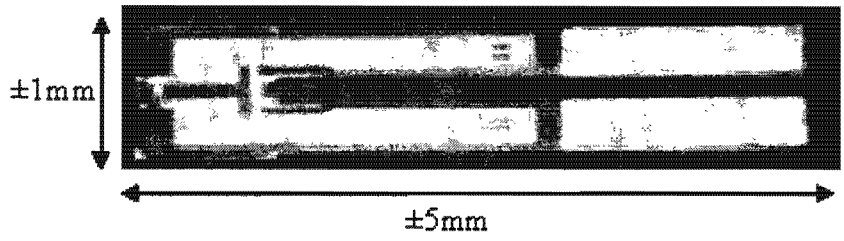

Figure 3.3.1: A Typical 32.768kHz Piezoelectric Tuning Fork.

3.3.2 Equivalent Circuit

In an electric circuit the tuning fork will behave as a two terminal passive network. According to V.E. Bottom in the book "Introduction to Quartz Crystal Unit Design"[31] it is useful when developing an equivalent circuit for a piezoelectric tuning fork to think of the system as a capacitor in which the dielectric vibrates in response to the applied electric field. Consider a simple piezoelectric crystal plate that has electrodes attached to either side. When a difference in potential is established between the electrodes a strain will exist within the crystal. Due to the piezoelectric effect the mechanical strain will be proportional to the electric field so an alternating field will produce an alternating strain in the material.

The current flowing into the resonator will thus consist of two components: the dielectric displacement current due to the capacitance of the plates, and the piezoelectric displacement current which depends on the size and shape of the crystal between the electrodes. The mechanical strain in the crystal, and thus the piezoelectric displacement current, will be dependent on frequency. For frequencies far removed from the resonant frequency the mechanical strain and the piezoelectric displacement current will be very small and the whole system is almost equivalent to the simple parallel plate capacitance given by

$$C_0 = k\varepsilon_o \frac{A}{e} \tag{3.43}$$

where A is the electrode area, e is the thickness, k the dielectric constant of the crystal. The impedance of the crystal can therefore also be defined as

$$Z = \frac{-j}{\omega C_0} \tag{3.44}$$

as the current flowing into the crystal is almost entirely due to the dielectric displacement current.

When the applied frequency is at the mechanical resonant frequency of the crystal the piezoelectric displacement current will be much greater than the dielectric displacement current. At the mechanical resonant frequency the strain and therefore the piezoelectric displacement current is in phase with the applied voltage. The whole system then appears to be a resistor in parallel with a capacitor. The total current into the crystal can then be calculated using the vector sum of the individual dielectric and piezoelectric displacement currents. At frequencies above the resonant frequency the piezoelectric displacement current lags behind the applied voltage and the crystal behaves like an inductor. At frequencies below the resonant frequency the piezoelectric displacement current leads the applied voltage and the crystal behaves like a capacitor.

A series circuit of a capacitor, inductor and resistor has the same frequency characteristics as the piezoelectric displacement current. At the resonant frequency the current is in phase with the applied voltage. At higher frequencies the inductive response will dominate and the current will lag the voltage. At lower frequencies the capacitive response will dominate and the current will lead the voltage. The total equivalent circuit for the piezoelectric circuit is therefore a series RLC circuit in parallel with the capacitance caused by the electrodes, commonly known as package capacitance. This circuit is shown in Figure 3.3.2 and is identical to the circuit developed by Mason [32].

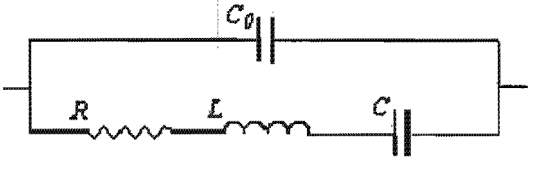

Figure 3.3.2: The Equivalent Circuit for the Piezoelectric Tuning Fork. *R, L, and C can be determined from the characterisitics of the tuning fork crystal. C_o is the package capacitance due to the electrode plating on the crystal.*

3.3.3 Eliminating the Package Capacitance

The effective series RLC circuit in the equivalent circuit is by itself a highly desirable circuit. It is a stable well understood system which can easily be equated to a damped mass-spring system.

The package capacitance caused by the electrodes on the surface of the crystal causes undesirable effects on the response of the RLC circuit. For this reason it is important to eliminate the package capacitance so that the piezoelectric tuning fork crystal behaves like an RLC circuit, which means there is an easy link between the electrical and mechanical descriptions of the tuning fork.

In order to eliminate the package capacitance an inverse effect is provided in parallel with the capacitor so that the overall effect will be zero. Another capacitor of equal value to the package capacitance is placed in parallel with the crystal. This capacitor is then driven with the inverted drive signal. This effectively cancels out the package capacitance and makes the total system response equal to the RLC circuit described by the tuning fork crystal characteristics. The package capacitance elimination system is outlined in Figure 3.3.3.

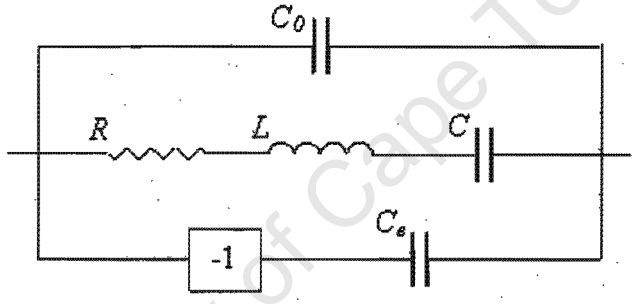

Figure 3.3.3: The Outline of the Package Capacitance Elimination System. *The effect of the package capacitance C_o is eliminated by driving another capacitor C_e in parallel with the inverse of the drive signal.*

Mathematically the system works as follows: the equation defining the impedance of the package capacitance was developed above and is of the form:

$$Z_p = \frac{-j}{\omega C_o} \tag{3.45}$$

the impedance of the inverter and elimination capacitor is similarly described by,

$$Z_e = \frac{jA}{\omega C_e} \tag{3.46}$$

where A is the gain of the inverter. The effect of both the capacitors in parallel can now easily be ascertained using simple circuit theory.

$$\begin{aligned} \frac{1}{Z_{TOTAL}} &= \frac{1}{Z_e} + \frac{1}{Z_p} \\ Z_{TOTAL} &= \frac{Z_e Z_p}{Z_e + Z_p} \\ Z_{TOTAL} &= \frac{A}{jA\omega C_o - j\omega C_e} \end{aligned} \tag{3.47}$$

In order for the package capacitance to be negated the total impedance for the two capacitors must be infinite. This will only happen when the denominator of equation 3.47 is zero. This relation gives us the following equation for the elimination of package capacitance.

$$AC_o = C_e \tag{3.48}$$

From equation 3.48 it is clear that the in order to eliminate package capacitance either the gain of the inverter can be fixed and an exact capacitor value found. Or, the far simpler and more accurate solution is to fix the size of the elimination capacitor and then vary the gain of the inverter.

3.3.4 A Simple Measurement Circuit

A simple circuit for both eliminating the package capacitance and converting the output current into a voltage was developed by Grober, Acimovic et al [17]. In that work a transformer bridge circuit is used to generate the two waveforms 180° apart. However, a simpler approach incorporating an inverting op-amp can also be used. This allows for far easier adjustment of the gain of the inverter so that the elimination circuit can be finely tuned. Similarly to that work [17] a simple op-amp current-to-voltage converter was used to convert the net current produced by the tuning fork crystal and the package capacitance into a voltage. The basic circuit diagram appears in Figure 3.3.4.

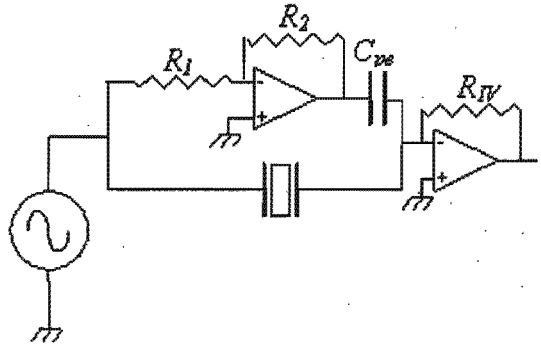

Figure 3.3.4: The Measurement and Package Capacitance Elimination Circuitry. *Once the effect of the package capacitance has been eliminated by the inverting op-amp and capacitor, the current to voltage converter will convert only the current from the RLC circuit into the measured voltage.*

R_1 and R_2 will set the gain of the inverter and adjust the magnitude of the effect that the capacitor C_{pe} will have in eliminating the package capacitance of the crystal. R_{IV} sets the gain of the current to voltage converter and will affect the gain across the whole circuit.

3.3.5 Mechanical to Electrical Conversion

From simple circuit theory it is known that current can be expressed as a rate of change of charge q, i.e. $i = \frac{dq}{dt}$ and $\frac{di}{dt} = \frac{d^2q}{dt^2}$. One of Kirchoff's laws applied to a closed loop circuit states that the sum of the voltages around the circuit should equal zero. For a simple RLC circuit in a closed circuit the following differential equation can be written,

$$Ri + L\frac{di}{dt} + \frac{q}{C} = 0 \Rightarrow L\frac{d^2q}{dt^2} + R\frac{dq}{dt} + \frac{q}{C} = 0 \tag{3.49}$$

Equation 3.49 is now analogous to the initial equation for the force on the mass in a damped simple harmonic oscillator given below.

$$m\ddot{x} + \gamma\dot{x} + kx = 0 \tag{3.50}$$

Using both equations the following comparisons can be made between the electrical and

mechanical characteristics.

$$m \approx L \tag{3.51}$$

$$\gamma \approx R \tag{3.52}$$

$$k \approx \frac{1}{C} \tag{3.53}$$

The mass is analogous to the inductor, the damping constant is analogous to the resistance and the spring constant is analogous to the inverse of the capacitance. By comparing the results from the simple harmonic oscillators described by the damped mass spring system in Appendix A2, the following characteristics of the RLC circuit:

$$\omega_o = \sqrt{\frac{k}{m}} = \frac{1}{\sqrt{LC}} \tag{3.54}$$

$$\tau = \frac{m}{\gamma} = \frac{L}{R} \tag{3.55}$$

can be determined using the electrical rather than mechanical characteristics. Once again ω_o is the resonant frequency and τ is the damping time constant.

3.4 Frequency Response of the Tuning Fork

There are many theories that can describe the frequency response of the piezoelectric tuning fork crystal. Up to this point the damped mass spring system has been considered as the model for the tuning fork. This model has been used in a number of tuning fork and cantilever studies [33][34][35] with some good results. The frequency response of this model along with some others is developed in this section. These models are then compared with real data to determine which gives the best description of the frequency response of the piezoelectric tuning fork crystal.

3.4.1 Sinusoidally Driven Mass Spring System

Theoretically, with the package capacitance removed the overall electrical response of the piezoelectric tuning fork should be very similar to the mass spring system. The frequency response

of the mass spring system is developed extensively in Chapter 1 and Appendix A2. By slightly adjusting Equation 1.14 the magnitude and phase response of the mass spring system can be given as:

$$Y = \frac{\frac{F}{m}}{\sqrt{\left(\omega_d^2 - \omega_o^2\right)^2 + \left(\frac{1}{\tau}\omega_d\right)^2}} \tag{3.56}$$

$$\tan(\varphi) = \frac{\frac{1}{\tau}\omega_d}{\omega_d^2 - \omega_o^2} \tag{3.57}$$

where Y is the amplitude and φ is the phase. F is the magnitude of the force driving the system and ω_d is the driving force frequency. Again $\omega_o = \sqrt{\frac{k}{m}}$ and $\frac{1}{\tau} = \frac{\gamma}{m}$ where k, γ, m are the characteristics of the mass spring system.

3.4.2 Lorentzian Response

H. A. Lorentz developed the theory which governs the rate of energy absorption for an electromagnetic wave passing through a gas. This description is taken from "Newtonian Dynamics" by Ralph Baierlein [3]. The rate of absorption will be dependent on the frequency of the incident wave. Relying on classical atomic structure Lorentz described the forces on the electrons oscillating in the field as:

$$m\ddot{x} = -kx - \gamma\dot{x} + qE_o \cos\omega_d t \tag{3.58}$$

The factor qE_o is the product of the electron's charge q and the magnitude E_o of the electric field. The other components are also easily equated to a damped mass spring system with $\gamma\dot{x}$ representing the radioactive damping, $m\ddot{x}$ is the acceleration force proportional to the mass of the electron and kx is the force exerted on the electron by the atom pulling back to an equilibrium position.

To determine absorption the process of energy exchange is investigated. Summing the kinetic and potential energies as

$$\frac{1}{2}m\dot{x}^2 + \frac{1}{2}kx^2 \tag{3.59}$$

and then differentiating Equation 3.59 with respect to time gives:

$$\dot{x}\left(m\ddot{x}+kx\right) \tag{3.60}$$

This can then easily be equated to the initial force Equation 3.58 giving the following relation for the energy in the system:

$$\frac{d}{dt}\left(\frac{1}{2}m\dot{x}^2+\frac{1}{2}kx^2\right)=-\gamma\dot{x}^2+\dot{x}qE_o\cos\left(\omega_d t\right) \tag{3.61}$$

The first term on the right is the energy dissipated due to radiation damping. The second term describes the rate at which energy is absorbed. The steady state condition is established very quickly and the energy absorption rate is the average steady state value over one oscillation cycle given by:

$$Energy\ Absorbtion\ Rate=\dot{x}qE_o\cos\left(\omega_d t\right) \tag{3.62}$$

The theory of sinusoidally oscillating systems has been developed in both Chapter 1 in the description of the general operating principles of the seismometer and in the Appendix A2 in the study of damped mass spring systems. From these studies a function for the velocity $\dot{x}$ of the particle can be written as,

$$\dot{x}=-\omega_d Y\sin\left(\omega_d t+\varphi\right) \tag{3.63}$$

Equation 3.63 can then be substituted into Equation 3.62 to give the following equation for the energy absorption rate,

$$Energy\ Absorbtion\ Rate=-\omega_d qE_o\sin\left(\omega_d t+\varphi\right)\cos\left(\omega_d t\right) \tag{3.64}$$

Using the identities

$$\begin{aligned}\sin\left(\omega_d t+\varphi\right) &= \sin\left(\omega_d t\right)\cos\left(\varphi\right)+\sin\left(\varphi\right)\cos\left(\omega_d t\right)\ \text{and}\\ \sin\left(\omega_d t\right)\cos\left(\omega_d t\right) &= \frac{1}{2}\sin 2\left(\omega_d t\right)\end{aligned}$$

and the fact that the absorption rate is an average over one oscillation, and is not an

instantaneous measure, equation 3.64 can be simplified to:

$$Energy\ Absorbtion\ Rate = -\omega_d q E_o A \sin(\varphi) \cos^2(\omega_d t) \tag{3.65}$$

Now, using the triangle equation for $\sin(\varphi)$ and the one oscillation average for $\cos^2(\omega_d t)$ Equation 3.65 can be further simplified to:

$$Energy\ Absorbtion\ Rate = \frac{(qE_o)^2}{2m} \frac{\frac{\omega_d^2}{\tau}}{\left(\omega_d^2 - \omega_o^2\right)^2 + \left(\frac{\omega_d}{\tau}\right)^2} \tag{3.66}$$

The Lorentzian function is developed by considering the absorption profile when the driving frequency ω_d is close to the natural frequency ω_o. In this region the difference in the denominator can be approximated as:

$$\omega_d^2 - \omega_o^2 = (\omega_d - \omega_o)(\omega_d + \omega_o) \approx 2\omega_o((\omega_d - \omega_o)) \tag{3.67}$$

Elsewhere ω_d is simply replaced by ω_o this further reduces equation 3.66 to:

$$Energy\ Absorbtion\ Rate = \frac{(qE_o)^2 \tau}{2m} \frac{\left(\frac{1}{2\tau}\right)^2}{(\omega_d - \omega_o)^2 + \left(\frac{1}{2\tau}\right)^2} \tag{3.68}$$

where the dimensionless factor on the right is known as the Lorentzian function.

3.4.2.1 Quality Factor Q

In dealing with harmonic systems like the simply damped mass spring system, it is often useful to develop dimensionless expressions to describe the operating characteristics of the system. The quality or Q factor is the most well known of these dimensionless expressions. The Q-factor is most easily derived using the Lorentzian function expressed in Equation 3.68 which is plotted in Figure 3.4.1.

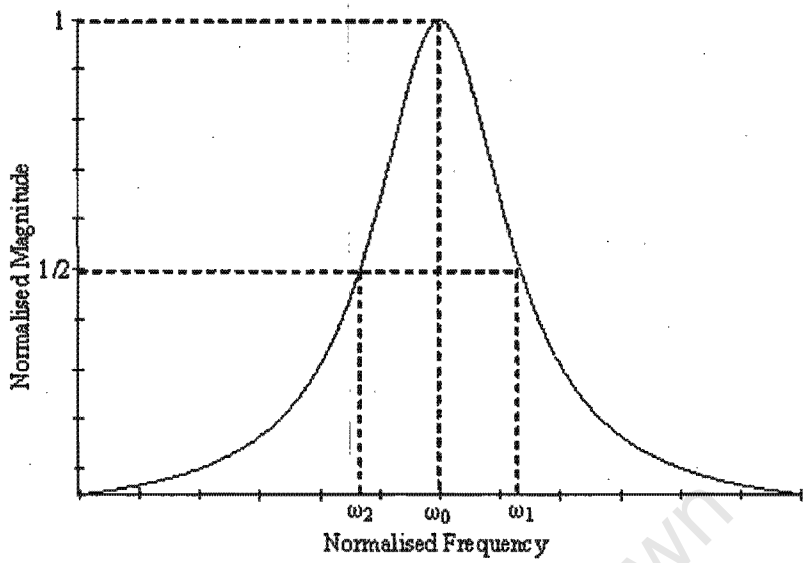

Figure 3.4.1: A Plot of the Idealised Lorentzian Response versus Frequency.

The frequencies ω_1 and ω_2 are the frequencies at which the amplitude of the output is exactly one half of the magnitude at the resonant frequency ω_o. Using the Lorentzian function these frequencies can be determined using the following method where the Lorentzian function is solved for half the maximum magnitude [3]:

$$\begin{aligned} \frac{\left(\frac{1}{2\tau}\right)^2}{(\omega_d-\omega_o)^2+\left(\frac{1}{2\tau}\right)^2} &= \frac{1}{2} \\ \frac{1}{2}(\omega_d-\omega_o)^2+\frac{1}{2}\left(\frac{1}{2\tau}\right)^2 &= \left(\frac{1}{2\tau}\right)^2 \\ \frac{1}{2}(\omega_d-\omega_o)^2 &= \frac{1}{2}\left(\frac{1}{2\tau}\right)^2 \end{aligned} \tag{3.69}$$

From Equation 3.69 it is clear that the Lorentzian function will be at half its maximum value when $|\omega_d-\omega_o| = \frac{1}{2\tau}$. Therefore the values of ω_d for when the magnitude of the Lorentzian function is one half of its maximum can be given as $\omega_o+\frac{1}{2\tau}$ and $\omega_o-\frac{1}{2\tau}$. The difference between the two half maximum frequencies is known as the full width half maximum (FWHM) value and is easily calculated for the Lorentzian function as:

$$FWHM = \left(\omega_o+\frac{1}{2\tau}\right)-\left(\omega_o-\frac{1}{2\tau}\right) = \frac{1}{\tau} \tag{3.70}$$

The Q-factor can now be defined using the resonant frequency and the value for the full width half maximum as [3]:

$$Q = \frac{Resonant\ Frequency}{FWHM} \tag{3.71}$$

and as the resonant frequency is known as ω_o and the full width half maximum can be expressed as $\frac{1}{\tau}$, Equation 3.71 can be re-written for the Lorentzian function as:

$$Q = \omega_o \tau \tag{3.72}$$

Equation 3.72 can be used only for systems that have a Lorentzian shaped frequency response. However the basic idea of determining the Q-factor from the resonant frequency and the width of the peak at half the maximum can be used for all frequency responses. The Q-factor and full width half maximum measurements are very useful in determining the damping time of harmonic systems. This value in conjunction with the resonant frequency can be used to determine all the basic characteristics of the harmonic system.

3.4.3 Calculating the Damping Time τ for other Theoretical Models

As mentioned in the previous section the damping time of an harmonic system can be determined by considering the quality or Q factor of the system. This developed into the simple Equation 3.72 for the Lorentzian function. We decided to develop a similar method to determine the system damping time for the other theoretical models. Although probably done by other people before, the results in this section were calculated without outside references. The model for the magnitude frequency response of the mass spring system in equation 3.56 can be converted into the dimensionless expression with a maximum value of one described by:

$$\text{Mass Spring} = \frac{\left(\frac{\omega_d}{\tau}\right)}{\sqrt{\left(\omega_d^2 - \omega_o^2\right)^2 + \left(\frac{\omega_d}{\tau}\right)^2}} \tag{3.73}$$

As the maximum value of Equation 3.73 is unity a similar treatment to that of the Lorentzian function can be followed whereby the equation is solved for when the value is one half of the

maximum value giving:

$$\begin{aligned}
\frac{\left(\frac{\omega_d}{\tau}\right)}{\sqrt{\left(\omega_d^2-\omega_o^2\right)^2+\left(\frac{\omega_d}{\tau}\right)^2}} &= \frac{1}{2} \\
\sqrt{\left(\omega_d^2-\omega_o^2\right)^2+\left(\frac{\omega_d}{\tau}\right)^2} &= \frac{2\omega_d}{\tau} \\
\left(\omega_d^2-\omega_o^2\right)^2 &= 3\left(\frac{\omega_d}{\tau}\right)^2 \\
\tau_{Mass\ Spring} &= \frac{\sqrt{3}\omega_d}{\left|\omega_d^2-\omega_o^2\right|}
\end{aligned} \tag{3.74}$$

Similar treatment of the energy response will give the following expression for τ:

$$\tau_{Energy} = \frac{\omega_d}{\left|\omega_d^2-\omega_o^2\right|} \tag{3.75}$$

As the Lorentzian response is just a simplification of the energy response the value calculated for the damping time will be the same. What is made clear, however, is that the damping time is $\sqrt{3}$ times larger for the mass spring system. This means that any damping time calculated using the Lorentzian function will be incorrect by a factor of $\sqrt{3}$. This can be corrected for by adjusting the mass spring model so that Equation 3.72 can be used. The new dimensionless mass spring model is given below.

$$\text{Adjusted Mass Spring} = \frac{\left(\frac{\omega_d}{\sqrt{3}\tau}\right)}{\sqrt{\left(\omega_d^2-\omega_o^2\right)^2+\left(\frac{\omega_d}{\sqrt{3}\tau}\right)^2}} \tag{3.76}$$

Using equation 3.72 the adjusted damping constant can also be used to define an adjusted damping factor $Q_{\sqrt{3}}$.

3.4.4 Comparison with Real Data

Now that a model for how the piezoelectric tuning fork behaves mechanically when under vibration has been developed, it can be tested with actual data from a tuning fork crystal. We can then see just how accurate the developed models are in predicting the response of the piezoelectric tuning fork. Using the circuit developed in Section 3.3.4, and illustrated in Figure

3.3.4, for eliminating the package capacitance, the magnitude frequency response of numerous tuning fork crystals was measured. The data collected was adjusted and normalised so that it could easily be compared to the theoretical models. The values for the theoretical models were taken from measurements done on the recorded data. The theoretical models were also adjusted slightly so that the maximum value was also one. The models that were used and the formulas are given below.

$$\begin{aligned} \textit{Mass Spring Magnitude} &= \frac{\frac{\omega_o}{\tau}}{\sqrt{\left[\omega^2 - \omega_0^2\right]^2 + \left[\frac{\omega}{\tau}\right]^2}} \\ \textit{Energy Magnitude} &= \frac{\left(\frac{\omega_d}{\tau}\right)}{\left(\omega_d^2 - \omega_o^2\right)^2 + \left(\frac{\omega_d}{\tau}\right)^2} \\ \textit{Lorentzian Magnitude} &= \frac{\left(\frac{1}{2\tau}\right)^2}{\left(\omega - \omega_0\right)^2 + \left(\frac{1}{2\tau}\right)^2} \end{aligned}$$

The real data and the theoretical models have been plotted in Figure 3.4.2. For the real data the tuning fork crystal was kept in its packaging so it could be operated within a vacuum. The resonant frequency was measured to be $f_o = 32764.92Hz$ and the full width half maximum is $1.608Hz$. These values were then used to calculate the theoretical responses. The value for the damping time τ for the mass spring amplitude was also adjusted by $\sqrt{3}$. As the Lorentzian response is just a simplification of the energy response there is no difference between them for frequencies so close to the resonant frequency.

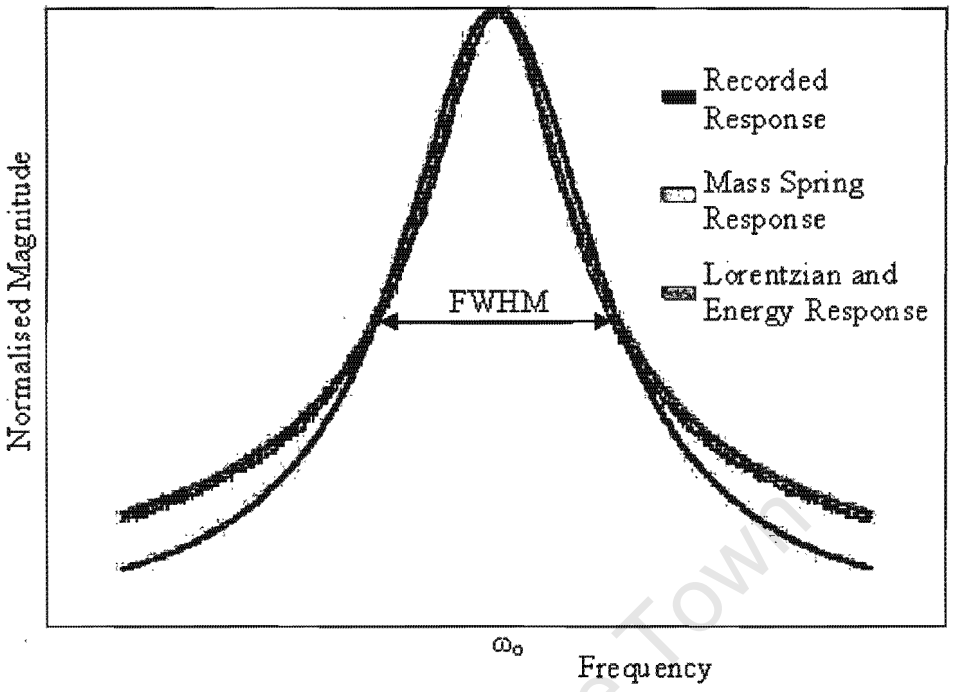

Figure 3.4.2: The Response of Recorded, Mass Spring, Lorentzian and Energy Responses versus Frequency. *The mass spring response with the adjusted time constant is very close to the recorded response. The Lorentzian and energy responses although quite similar to the recorded response for frequencies close to the resonant peak begin to differ as the frequency moves either up or down.*

From Figure 3.4.2 it can be seen that the adjusted mass spring model fits the recorded response very well. The characteristics of the mass spring model can thus be determined using the resonant frequency and either the full width half maximum, or the frequency at which the magnitude is one half of the maximum. The Energy and Lorentzian responses also fit well, but begin to fall away when the frequency moves away from the resonant frequency. The phase frequency response determined by the mass spring model as stated in Equation 3.57 was also compared to real data and found to agree fairly accurately. From these results we can conclude that the mechanical and electrical model developed in this chapter can describe the actual motion of the tuning fork very well. At frequencies very close to the resonant frequency the simpler Lorentzian model can be used but for a more accurate result only the mass spring model should be considered.

3.5 Noise Considerations and the Fundamental Limits to Displacement Detection

The fundamental limits to force and displacement detection using quartz tuning forks are detailed in [17]. By determining the noise floor of a piezoelectric quartz tuning fork it is possible to develop equations to give the limits of the ability of the fork to measure a change in displacement, which has a direct dependence on its ability to measure a change in force. The noise analysis is done on the simple measurement circuit, depicted in Figure 3.3.4, that we used previously. The noise can be split up into the electrical noise produced by the opamps and resistors, and the mechanical noise associated with the random motion of the tuning fork.

3.5.1 Electronic Noise

There are many sources of electronic noise varying from noise from the electrical components, to external noise sources like switching noise and unregulated power supplies. All of these noise sources do play a role in any circuit, but not all of them can be attributed to the fundamental limits associated with using the simple measurement circuit and the piezoelectric tuning fork. Many of the noise sources can be reduced or even eliminated by intelligent circuit design, correct component selection and adequate shielding from external interference signals. There are however a few unavoidable noise sources which are mentioned below.

3.5.1.1 Johnson Resistor Noise

Any resistor generates a noise voltage across its terminals known as Johnson noise [36]. This noise is caused by the electrons within any conductor moving around with a random thermal motion. This thermal noise is equal throughout the frequency spectrum and the actual noise voltage generated is given by,

$$V_{noise} = \sqrt{4k_B TRB}V/\sqrt{Hz} \tag{3.77}$$

where k_B is the Boltzmann's constant, T is the absolute temperature, R is the resistor and B is the bandwidth. Johnson noise is a special case of the noise in any resistant system caused

by chaotic Brownian motion of particles.

3.5.1.2 Stray Capacitance Noise

Any resistor will have a stray capacitance operating effectively in parallel with the resistor. This will mean that the impedance of the resistor is frequency dependent. The effect of this stray capacitance in parallel with the resistance is developed using simple circuit theory,

$$Z_{total} = \frac{R\frac{1}{j\omega C}}{R+\frac{1}{j\omega C}} = \frac{R}{1+j\omega CR}$$

the magnitude of the impedance can thus be written as:

$$Z_{total} = \frac{R}{\sqrt{1+(\omega CR)^2}} \tag{3.78}$$

which agrees with the expression developed experimentally in [17].

3.5.2 Mechanical Noise

The mechanical noise is produced by random fluctuations of the fork due to Brownian motion. This is the mechanical equivalent of the Johnson noise experienced by all conductors. As the tuning fork is piezoelectric, this mechanical noise is converted into an electrical signal in the measurement circuit. By considering the electrical characteristics of the fork, the noise can also be modelled in the same way to the Johnson noise discussed in the electrical section. This thermal noise comes from tuning fork's equivalent RLC circuit so it will not have a uniformly flat spectrum like the Johnson resistor noise, but will have a resonant peak described by the RLC characteristics. The maximum value of the noise voltage generated will occur at the resonant peak where just the tuning fork's equivalent resistance R is considered, and is given by:

$$V_{\max} = \sqrt{4k_BTR} \tag{3.79}$$

The output current noise due to thermal fluctuations of the arms of the fork can now be written by combining the maximum value of the noise with a dimensionless description of the

RLC circuit developed in the frequency response section:

$$I_{noise} = \sqrt{4k_BTR}\frac{1}{R}\frac{\left(\frac{\omega_d}{\tau}\right)}{\sqrt{\left(\omega_d^2 - \omega_o^2\right)^2 + \left(\frac{\omega_d}{\tau}\right)^2}} \tag{3.80}$$

where ω_o and τ were determined previously in Equations 3.54 and 3.55 as $\omega_o = \frac{1}{\sqrt{LC}}$ and $\tau = \frac{L}{R}$. The analysis developed is for the whole measurement circuit so the effect of the noise current must be considered across the final current to voltage converter. This gives the noise at the output that corresponds to the mechanical thermal motion of the fork as:

$$V_{Mechanical} = \sqrt{4k_BTR}\frac{Z_{total}}{R}\frac{\left(\frac{\omega_d}{\tau}\right)}{\sqrt{\left(\omega_d^2 - \omega_o^2\right)^2 + \left(\frac{\omega_d}{\tau}\right)^2}} \tag{3.81}$$

3.5.3 Combining the Noise Sources

From the results in [17] it is clear that the Johnson noise associated with the resistors, and the noise associated with the thermal motion of the fork are the two chief sources of noise. These noise sources can be added in quadrature meaning that the total noise will be the square root of the sum of each of the noise sources squared. If the resistors that make up the inverter are referred to as R_{I1} and R_{I2}, and the resistor associated with the current to voltage converter as R_{CV}, then the total voltage noise of the resistors can be written as:

$$V_{\text{Resistor Total}} = \sqrt{4k_BT\left(R_{I1} + R_{I2} + R_{CV}\right)}$$

and the noise current could be written as:

$$I_{\text{Resistor Total}} = \sqrt{4k_BT\left(\frac{R_{I1}R_{I2} + R_{I2}R_{CV} + R_{I1}R_{CV}}{R_{I1}R_{I2}R_{CV}}\right)}$$

The total combined current noise could then be written as:

$$I_{\text{Total Noise}} = \sqrt{4k_BT\left[\left(\frac{R_{I1}R_{I2} + R_{I2}R_{CV} + R_{I1}R_{CV}}{R_{I1}R_{I2}R_{CV}}\right) + \left(\frac{1}{R}\frac{\left(\frac{\omega_d}{\tau}\right)^2}{\left(\omega_d^2 - \omega_o^2\right)^2 + \left(\frac{\omega_d}{\tau}\right)^2}\right)\right]} \tag{3.82}$$

As can be clearly seen in equation 3.82 and as stated in [17] the total noise current will be

dominated by the noise caused by the random thermal motion of the arms of the fork. This will be true as long as the combination of resistances R_{I1}, R_{I2}, and R_{CV} is much greater than the effective resistance of the piezoelectric tuning fork.

3.5.4 Signal to Noise Ratio

Any input voltage to the piezoelectric tuning fork will produce a corresponding motion of the tines of the fork, and thus an output current is dependent on both the size and the frequency of the input voltage. As mentioned many times previously, the output can be defined using the mechanical characteristics of the fork which equate to the RLC characteristics of the circuit. At the resonant frequency the RLC response is purely resistive, and the current flowing through the crystal can be defined as:

$$I_{RLC} = \frac{V_{INPUT}}{R} \tag{3.83}$$

If the package capacitance has been eliminated this should be the maximum current produced by the device. Equation 3.83 can be re-written using the definitions for Q and the complex impedance. For the damped mass spring system equated to the RLC circuit,

$$Q_{\sqrt{3}} = \tau\omega_o = \frac{\omega_o L}{R}$$

and

$$\omega_o = \sqrt{\frac{k}{m}} = \frac{1}{\sqrt{LC}}$$

Combining these two equations to form a new expression for the effective resistance of the tuning fork crystal:

$$R = \frac{\frac{1}{\sqrt{LC}}L}{Q_{\sqrt{3}}} = \frac{\sqrt{\frac{L}{C}}}{Q_{\sqrt{3}}} = \frac{Z_{LC}}{Q_{\sqrt{3}}} \tag{3.84}$$

Equation 3.84 can now be combined with Equation 3.83 to give the output signal current in terms of the resonant complex impedance Z_{LC} and the $\sqrt{3}$ Q-factor. This equation is now simply combined with noise current equation 3.82 to give the signal to noise ratio for the tuning

fork measurement circuit.

$$\frac{S}{N} = \frac{V_{INPUT}\frac{Q_{\sqrt{3}}}{Z_{LC}}}{\sqrt{4k_BT\left[\left(\frac{R_{I1}R_{I2}+R_{I2}R_{RC}+R_{I1}R_{RC}}{R_{I1}R_{I2}R_{RC}}\right)+\left(\frac{Q_{\sqrt{3}}}{Z_{LC}}\frac{\left(\frac{\omega_d}{\tau}\right)^2}{\left(\omega_d^2-\omega_o^2\right)^2+\left(\frac{\omega_d}{\tau}\right)^2}\right)\right]}} \tag{3.85}$$

From Equation 3.85 it is clear that to improve the signal to noise ratio the Q-factor should be maximised.

3.5.5 Minimum Displacement

The actual amplitude of oscillation of the arms of the fork as a function of the size of the output voltage has been determined interferometrically in [17], and is denoted by the parameter α. The output voltage is simultaneously measured with the amplitude of one arm of the fork. Because of the configuration of the piezoelectric crystal the output voltage is sensitive only to the antisymmetric motion of the arms of the fork, giving $V_{out} = c\,(x_1 - x_2)$, where c is a constant and x_1 and x_2 are the motion of each of the arms of the fork. When driven by an external voltage the arms of the fork move only in directly opposite directions to each other. This antisymmetric motion means $x_1 = -x_2$. The equation defining the output voltage in relation to the motion of the arms of the fork can now be given as:

$$V_{out} = 2cx_1 = \frac{x_1}{\alpha}$$

The interferometric calibration done in [17] yields $\alpha = 59.6 \pm 0.1 pm/mV$.

Consider the noise equation associated with the thermal motion of the fork given in Equation 3.81. The power spectrum of this thermal noise is integrated in [17] to give the root mean square (RMS) voltage noise as:

$$V_{RMS}^2 = 4k_BTR\left(\frac{Z_{gain}}{R}\right)^2\left(\frac{\omega_o}{4Q}\right) \tag{3.86}$$

Equation 3.86 can be related to the thermal motion of the arms of the fork using the equations developed above,

$$V_{RMS}^2 = \langle c\,(x_1 - x_2)\rangle^2 \tag{3.87}$$

if the thermal motion of the arms of the fork is considered to be uncorrelated as they are

only weakly coupled, Equation 3.87 can be simplified to $V_{RMS}^2 = 2c^2 \left\langle (x_1)^2 \right\rangle$, which leads to the equation:

$$x_{RMS} = \sqrt{2}\alpha V_{RMS} \tag{3.88}$$

which describes the random motion of one arm of the piezoelectric tuning fork.

According to Young[37], equipartition theory for energy states that for a molecule, each component of velocity has, on average, an associated kinetic energy per molecule of $\frac{1}{2}k_BT$. This energy can be equated with the energy in a mass spring system $\frac{1}{2}kx^2$. The effective spring constant of the fork can now be defined alternatively as:

$$k = \frac{k_BT}{x^2} \tag{3.89}$$

The thermal energy in the tuning fork can now be thought of as an effective force acting on the fork. This force will have a flat power spectrum and is determined in [17] as:

$$S_f^{\frac{1}{2}} = \sqrt{\frac{4}{\omega_o Q}} \left(\frac{k_BT}{x_{RMS}} \right) \tag{3.90}$$

which will give the force noise floor of the piezoelectric tuning fork. In Chapter 2 the change in force between the tuning fork and the approaching surface was discussed. By calculating the change in force as a function of the piezoelectric tuning fork's displacement from the surface, the minimum detectable displacement is easily obtained from its calculated force noise floor. Once the piezoelectric tuning fork has been incorporated into a force feedback seismometer, the noise considerations and the fundamental limits to displacement detection can be used to determine how well the seismometer is operating, in terms of utilising the full sensitivity provided by the tuning fork. Before that can happen, however, systems for operating the tuning fork as a displacement detector still need to be developed. The next chapter details how the various outputs from the piezoelectric tuning fork operate the tuning fork as a displacement detector.

Chapter 4

Operating the Tuning Fork Crystal

The basic principle behind the use of a piezoelectric tuning fork as a displacement sensor was established in the previous chapters. The task now remains to use the models to develop a control strategy in which the tuning fork crystal will operate effectively. Many characteristics of the piezoelectric tuning fork's operation can be measured and evaluated to determine the displacement of the fork above a surface. Magnitude and phase can effectively be used as measurement signals, or as signals in the control system operating the tuning fork and the force feedback system. Other characteristics such as: resonant frequency, damping time constant and Q-factor can also be measured with good results. It is therefore important to understand the potential of each of the measurands in terms of their sensitivity, bandwidth and ease of measurement.

4.1 Measurands and Measurement

Only the magnitude and phase of the tuning fork crystal output signal may be measured without changing the input frequency. This means that the measurands such as resonant frequency and Q-factor are much more difficult to measure, as they require the input frequency to be swept through the resonant peak. The measurement of magnitude and phase and how they relate to the characteristics of the tuning fork become vital in the effective use of the displacement sensor. Although all stemming from the same characteristic equation for the damped mass spring model for the tuning fork, the response of each measurand is quite different in terms of

its sensitivity, bandwidth and ease of measurement.

An important aspect of measuring the outputs from the tuning fork is the isolation of one measurand from another, so that when measuring one, changes in the other do not affect the measurement. This is vital because when the characteristics of the tuning fork are suddenly changed each of the measurands will respond differently in terms of speed and sensitivity. This isolation, although fairly simple for magnitude measurement, turns out to be rather difficult for the measurement of phase.

Although resonant frequency and Q-factor cannot be measured directly from the output at a single frequency, by knowing the response of the tuning fork crystal and accurately measuring phase and magnitude, ideas about the other measurands can be obtained. For instance by studying the models of the tuning fork based on the mass spring system, the phase at the resonant frequency can easily be calculated. By keeping the system operating at this phase and monitoring the operating frequency, the resonant frequency of the system can be tracked. Also by knowing what is the maximum signal magnitude that the output can attain, a good idea of the Q-factor can be derived from accurate phase and magnitude measurements. The fast and accurate measurement of phase and magnitude thus becomes crucial to the effective operation of the piezoelectric tuning fork as a displacement sensor.

4.1.1 Magnitude

Magnitude is the most obvious of the measurands, and is basically the size of the output signal from the crystal. The output signal magnitude is directly related to the size of the vibration of the arms of the fork and can give a good indication of the forces experienced by the tuning fork. For the damped mass spring system it is simply defined as the maximum value that the output signal reaches in any cycle, and has the frequency response developed in Appendix A2 and given in equation 3.56 as:

$$Y = \frac{\frac{F}{m}}{\sqrt{\left(\omega_d^2 - \omega_o^2\right)^2 + \left(\frac{1}{\tau}\omega_d\right)^2}}$$

The tuning fork crystal is a piezoelectric device driven by a voltage as opposed to an external force. Using the piezoelectric properties and the equation for the mass spring system, the

electrical current magnitude can easily be calculated. With the input voltage replacing the external force, the magnitude of the electrical current will be affected by both the size of the input voltage and its frequency, with its frequency response dependent on the mechanical characteristics of the fork.

4.1.1.1 Measuring Magnitude

Magnitude as mentioned before is by definition the largest value that a sinusoidal signal reaches in one cycle. It is therefore necessary to monitor the signal for at least one cycle in order to determine what the magnitude is. This gives a base level for the minimum time of measurement at one period of the waveform driving the tuning fork crystal, thus limiting the bandwidth of the device to the frequency of the output signal. Magnitude measurement methods can be broken down into two types: digital and analogue measurement techniques.

The digital measurement techniques involve sampling the output signal and then using the data to determine the signal magnitude. In order to achieve an accurate representation of the data, digital measurement systems either need to sample one waveform at many points, or sample many similar waveforms and use mathematical techniques to reconstruct the output signal. The crystal will usually be operating at or very near its resonant frequency of 32.768 kHz. Although Nyquist sampling theory suggest that the measurement system can sample at twice the operating frequency to produce an accurate measurement, the theory only applies to static signals and in this application the output signal is by no means static with its magnitude constantly changing. This means that the digital measurement system will need to sample at very high rate in order for the maximum measurement speed to be attained. At lower sampling rates, a digital measurement system will require longer periods in order to produce an accurate output. These factors will produce unavoidable errors in the signal measurement, making digital systems an impractical choice for measuring the output magnitude.

Analogue measurement systems are much simpler to implement than their digital counterparts. Also limited by the period of the waveform, they use filtering techniques to provide a DC representation of the output signal magnitude. The output signal is rectified by using a full or half bridge rectifier, and then fed into a low pass filter to obtain the DC measurement. The characteristics of both the rectifier and the low pass filter become vitally important in deter-

mining both the accuracy and speed of the measurements. The rectifier should be full bridge to maximise sensitivity and limit the ripple size in the low pass filter. The cutoff frequency of the low pass filter will determine the bandwidth of the measurement and will have to be somewhat lower than the maximum measurement frequency. As the stop band of the filter will not be zero, there will be a ripple at the sinusoidal output signal frequency on the DC output from the low pass filter. The size of this ripple will be determined by the cutoff frequency and filtering characteristics of the low pass filter. The low pass filter characteristics also cause other undesirable effects such as phase delay and non-uniform pass band response. Analogue measurement of magnitude becomes a trade-off between speed and accuracy, and intelligent filter design becomes paramount. Although noisy and relatively slow, analogue measurement techniques provide a better solution for magnitude measurements than corresponding digital solutions. Techniques exist for improving both sensitivity and speed and are discussed later in the section.

4.1.2 Phase

The phase angle between the input and output signals is a vital measurand for determining the operating characteristics of the tuning fork crystal. The phase angle is related to the frequency of operation and can give good information on where in the resonant peak the system is operating. For the damped mass spring system the phase angle between the applied force and the mass output was determined in Equation 3.57 as:

$$\varphi = \tan^{-1}\left(\frac{\frac{1}{\tau}\omega_d}{\omega_d^2 - \omega_o^2}\right)$$

For the piezoelectric crystal the phase between the driving voltage and the output current will have a similar response to the damped mass spring system but with the added voltage to current phase shift of 90°. With the input voltage replacing the external force, the phase will be dependent on the characteristics of the mechanical response of the tuning fork and the frequency of the input voltage.

4.1.2.1 Measuring Phase

Phase measurement is a subject discussed by many authors on phase lock loops, and a number of the measurement strategies mentioned here were summarised from Egan's book "Phase Lock Loop Basics"[38]. Phase measurement, like magnitude, requires a complete waveform from each of the signals to calculate an accurate value for the phase angle between signals. There are other methods for determining phase from single samples of the signal size, but these require the magnitude of the signal to be known, which, as was shown above, requires an entire waveform to be sampled to calculate it accurately. Phase measurement is not however as straightforward as magnitude measurement, and many different techniques have been developed. These range from simple multipliers to complex digital analysers. When phase detectors are being described it is useful to define the two measurement signals as:

$$\begin{aligned} A &= A_1 \cos(\omega_1 t) \\ B &= A_2 \cos(\omega_2 t + \varphi) \end{aligned} \tag{4.1}$$

4.1.2.1.1 Logic Gates Some of the simplest phase detectors involve logic gates. They require a digital representation of the sinusoidal signal which can be simply provided using a comparator with one input grounded, and the other input connected to the sinusoidal signal. This will create a square wave which can then easily be converted to digital levels. When both sinusoidal signals are digital they can be combined using logic gates. The two most common methods are the flip-flop phase detector and the exclusive-or phase detector. In the flip-flop phase detector the digital signal for one input is fed into the *set* input of the flip-flop and the other digital signal is fed into the *reset* input of the flip-flop. The phase between the signals will now determine the duty cycle of the output. For the exclusive-or gate detector the input signals are the two digitised sinusoidal signals. The output produced will also have a duty cycle dependent on the phase between the sinusoidal signals, but will be at twice the frequency of the input signals. A simple idea of the logic gate phase detector response is given in Figure 4.1.1:

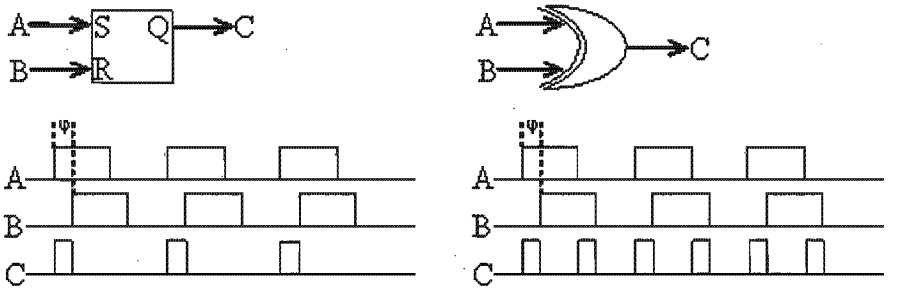

Figure 4.1.1: Two Simple Logic Gate Phase Detectors. *The sinusoidal input signals are converted to logic signals using comparators. The output from the phase detectors is a square wave with a duty cycle dependent on the phase φ between the two input signals.*

The output signal from the logic gates can be interpreted either by digitally sampling the signal and determining the duty cycle, or by filtering the output using an analogue filter. The output from the filter would then give a DC representation of the duty cycle of the output square wave, and thus a value for the phase angle between the two input waveforms. When functioning as the displacement detector in a force feedback seismometer the change in phase of the tuning fork will be very small. This will result in an equally small change in duty cycle of the output waveforms. A digital system would have to sample fast enough so that these small changes in phase would not be missed. This would mean a digital measurement system with massive sampling rates which may be difficult to commission. Although analogue filter outputs will contain ripple noise, using them may provide a better alternative to digital measurement.

The major advantage of measuring phase using logic gates is that the magnitude of the input sinusoidal signals is not a factor. Both the magnitude and the phase of the output current will change during the operation of the tuning fork as a displacement sensor, and it is important to isolate the phase angle measurement. The comparators produce square waves of both input sinusoidal signals at the same magnitude level, so that phase can be measured without worrying about variations in signal magnitude.

4.1.2.1.2 Mixers A mixer phase detector functions by providing an output signal that is composed of components at frequencies equal to both the sum and the difference of the two input signal frequencies. If the two input frequencies are the same, as will be the case of the input voltage and output current of the piezoelectric tuning fork, the difference frequency goes

to zero and produces a DC component proportional to phase. The other components of the signal must be filtered out to produce just the lower frequency DC component.

In [38] a simple mixer is described using the resistor and diode circuit shown in Figure 4.1.2. The driving signal V_i will consist of the two signals mentioned before in Equation 4.1. The non-linearity of the diode provides the desired mixed frequency signal when the two sinusoids are injected through the resistor.

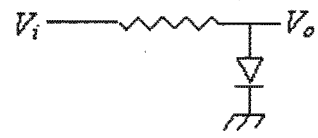

Figure 4.1.2: A Simple Mixer Circuit. *With both signals injected through the resistor the non-linearity of the diode provides a mixed frequency signal. This signal is then interpreted so that a measure of phase can be obtained.*

The diode nonlinearity can be expressed by the general non-linear MacLaurin expansion[38]:

$$V_o = a + bV_i + cV_i^2 + dV_i^3 + ...$$

The output component of greatest interest is that generated by the square law term,

$$\begin{aligned} V_{oc} &= c\left[A\cos(\omega_1 t) + B\cos(\omega_2 t + \varphi)\right]^2 \\ &= c\left[A^2\cos^2(\omega_1 t) + 2AB\cos(\omega_1 t)\cos(\omega_2 t + \varphi) + B^2\cos^2(\omega_2 t + \varphi)\right] \end{aligned} \tag{4.2}$$

using the trigonometric identity $\cos^2 x = \frac{1+\cos 2x}{2}$ equation 4.2 can be written as:

$$V_{oc} = c\left[\frac{A^2}{2}(1+\cos 2(\omega_1 t)) + 2AB\cos(\omega_1 t)\cos(\omega_2 t + \varphi) + \frac{B^2}{2}(1+\cos 2(\omega_2 t + \varphi))\right] \tag{4.3}$$

The higher frequency terms in Equation 4.3 can be filtered out to leave just the middle term and a filtered constant. The middle term can be re-written using a combination of the following trigonometric functions,

$$\begin{aligned} \cos(x+y) &= \cos x\cos y - \sin x\sin y \\ \cos(x-y) &= \cos x\cos y + \sin x\sin y \end{aligned}$$

which combine to give:

$$\cos x \cos y = \frac{1}{2}\left[\cos\left(x+y\right) + \cos\left(x-y\right)\right] \tag{4.4}$$

Using Equation 4.4, the filtered equation for 4.3 can be re-written as:

$$V_{oc} = c\left[\frac{A^2+B^2}{2} + AB\left(\cos\left(\omega_1 t + \omega_2 t + \varphi\right) + \cos\left(\omega_1 t - \omega_2 t - \varphi\right)\right)\right] \tag{4.5}$$

When, as in the tuning fork situation, both input frequencies are the same, the second term of Equation 4.5 reduces to a component of twice the input frequency which will be filtered out along with the other second harmonic functions, and a negative DC component equal to the cosine of the phase angle. The filtered output can now be written as:

$$V_{oc} = c\left[\frac{A^2+B^2}{2} - AB\left(\cos\left(\varphi\right)\right)\right] \tag{4.6}$$

The first rectification DC term cannot be removed by filtering and produces an extra highly undesirable DC component. This term can be removed by using balanced mixers[38] where the outputs of two mixers are combined to get rid of the rectification DC term. All the other components of the initial Mclaurin non-linear expansion will produce similar results to the one developed above.

Although it produces a fairly nice result for phase, mixers and balanced mixers have one major disadvantage. The phase measurement, recognised as the second DC term in Equation 4.6, is dependent not only on the phase between the two input signals but also on their magnitude. This means that the phase measurement cannot be separated from the magnitude measurement and changes in magnitude will greatly affect the apparent phase measured. Also the fact that the phase measurement has a sinusoidal response for different phase angles means that the non-linear response will make control difficult.

4.1.2.1.3 Simple Mathematical Operators Some of the simplest phase detectors involve performing basic mathematical operations on the input sinusoidal signals to produce an output proportional to the phase between the input signals. These mathematical operations are usually done using operational amplifiers or other chips designed for multiplying and dividing signals.

The effect of multiplying the two signals together has already been discussed in the analysis of the mixer phase detector, so the addition and subtraction examples will now be considered. Using the signals defined in Equation 4.1 the output for when the one input is subtracted from the other can be developed as follows.

$$\begin{aligned} Output &= A_1 \cos(\omega_1 t) - A_2 \cos(\omega_2 t + \varphi) \\ &= A_1 \cos(\omega_1 t) - A_2 [\cos \omega_2 t \cos \varphi - \sin \omega_2 t \sin \varphi] \end{aligned}$$

and when both inputs are at the same frequency:

$$Output = (A_1 - A_2 \cos \varphi) \cos(\omega_d t) + A_2 \sin \varphi \sin(\omega_d t) \tag{4.7}$$

The output consists of a combination of cosine and sine functions at the input drive frequency. This will produce a sinusoidal output whose magnitude and phase is dependent on the coefficients of the sine and cosine function. Therefore by looking at the coefficients of the functions it is simple to see how the output will respond to input signals of different phases. At zero phase, if both signals are of the same magnitude the output will be zero as both coefficients reduce to zero. This is fairly intuitive; at zero phase and equal magnitude the signals are identical so subtracting one from the other will obviously equal zero. When the signals are 180° out of phase the coefficient of the sine function will be zero and the coefficient of the cosine function will be at its maximum value, which will produce the maximum value of the total output magnitude. In between the zero phase and 180° the output will vary linearly across the range set out by the relative magnitudes of the input signals. This magnitude can then be used as a good reference for the phase angle. Very similar responses are obtained for when the two input signals are added together except that the output magnitude is at its maximum at zero phase and minimum at 180°. The output waveform for the subtraction phase detector for when two signals of equal magnitude are in phase and in antiphase is shown in Figure 4.1.3.

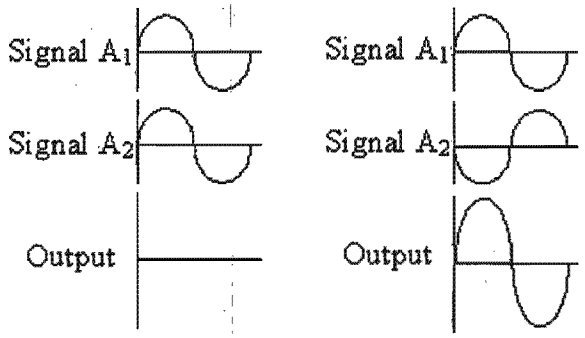

Equation 4.1.3: Operation of a Subtraction Phase Detector. *For two sinusoidal input signals of equal magnitude the output of a subtraction phase detector will also be a sinusoidal signal with a magnitude dependent on the phase between the input signals. The output will be at a maximum when the signals are in antiphase and at a minimum when they are perfectly in phase.*

Although potentially the simplest way of measuring phase, these systems are not without their problems. Firstly magnitude measurement is required to get a measure of phase, and the problems associated with magnitude measurement were detailed previously. Secondly and more importantly these phase measurements are also dependent on the magnitude of the input waveforms. This means that as with the mixers, the phase and magnitude measurements cannot be separated, which can lead to errors in correctly measuring the phase for signals whose magnitudes are not constant.

4.1.3 Multiplication of Signals in Order to Improve Measurement Response

The speed and accuracy of measurement for both phase and magnitude is ultimately dependent on the period of the output waveform. Thus an increase in sensitivity and bandwidth is only possible if the operating frequency increases. The mechanical properties of the tuning fork inhibit any increase in the input frequency as the tuning fork is only an effective displacement sensor when it is operated at or very near its resonant frequency. Thus an alternate means of increasing the frequency of the signals used for measurement must be developed if any improvements are to be made. In the discussion on mixer phase detectors it was shown that multiplying two sinusoidal signals together produces a signal in which one component is of a higher frequency and one component is of a lower frequency. By using these multiplication

techniques an output signal of higher frequency can be obtained for measurement. Considering Equation 4.4 for the multiplication of the two sinusoidal signals developed for mixer phase detectors below:

$$\cos x \cos y = \frac{1}{2}\left[\cos\left(x+y\right) + \cos\left(x-y\right)\right]$$

The resultant output for the signals considered in equation 4.1 can be written as:

$$\begin{aligned} \cos\left(\omega_1 t\right)\cos\left(\omega_2 t+\varphi\right) &= \frac{1}{2}\left[\cos\left(\omega_1 t+\omega_2 t+\varphi\right) + \cos\left(\omega_1 t-\omega_2 t-\varphi\right)\right] \\ &= \frac{1}{2}\left[\cos\left(\left(\omega_1+\omega_2\right)t+\varphi\right) + \cos\left(\left(\omega_1-\omega_2\right)t+\varphi\right)\right] \end{aligned} \tag{4.8}$$

It is clear from equation 4.8 that the multiplication of two sinusoidal signals produces a signal with two frequency components. One frequency component is at a frequency equal to the sum of the two input frequencies and the other component operates at the difference between the two input frequencies.

The two signals from the piezoelectric tuning fork are the input voltage and the output current which is converted back into a voltage by the measurement circuit. In order to increase the operating frequency of the output signals they must be multiplied with another sinusoidal signal. This will increase the frequency of the output signal according to equation 4.8. There are, however, two components to the output of the multiplication, and the lower frequency component will have to be removed using filters to allow the phase and magnitude to be measured. This filtering process is only really possible if the frequency gap between the two signals is large enough. This means that the sinusoidal signal that is multiplied with the input voltage and the voltage conversion signal of the output current must be of a frequency similar to the operating frequency of around 32.768 kHz. The process can be simplified by eliminating the external multiplication sinusoidal signal and just multiplying the signals by themselves. This will double the output frequency and produce a DC signal in the output as the lower frequency component which can easily be filtered out.

The signals can both be multiplied by the input drive voltage, producing two signals of twice the frequency and the same phase relation for measurement. If, however, the signals are squared or multiplied by themselves, the output signals will not only be of twice the frequency,

but the phase shifted frequency will now be phase shifted by twice the initial phase angle. This will effectively double the phase sensitivity of the phase response, as for any initial change in phase of the tuning fork's response the measured phase change will be twice as large. Both output signals will also contain a DC component which can be filtered out. The measured signals for the square of the input signals at frequency ω_d are shown below:

$$\cos(\omega_d t)\cos(\omega_d t) = \frac{1}{2}\left[\cos(2\omega_d t) + \cos(0)\right] \tag{4.9}$$

$$\cos(\omega_d t + \varphi)\cos(\omega_d t + \varphi) = \frac{1}{2}\left[\cos(2\omega_d t + 2\varphi) + \cos(-2\varphi)\right] \tag{4.10}$$

4.2 Developing the Dynamic Control Model

4.2.1 Effect that a Change of Displacement has on the Crystal

The contact model for the forces experienced between two closely spaced surfaces, and the model developed for the tuning fork using cantilever and damped mass-spring theory, can now be combined to develop a more complete model for displacement change. When the displacement between the tines of the tuning fork and the surface changes, there will be a change in the force between the surface and the fork. This change in force can then be modelled as a change in the mechanical characteristics of the damped mass spring model of the tuning fork. The fork will experience a force proportional to its displacement relative to the surface, which will manifest itself as an effective change in the spring constant of the mechanical mass-spring model. Due to the viscous air effects, the fork will also experience a force proportional to its velocity. This will produce a new characteristic equation for the balanced forces in the mass spring system,

$$m\ddot{x} + (\gamma + \Delta\gamma)\dot{x} + (k + \Delta k)x = 0 \tag{4.11}$$

where $\Delta\gamma$ and Δk are the change in relative damping and the spring constant, due to the change in displacement of the tuning fork from the surface. Similar systems of modelling a change in displacement have been used in other studies with reasonable success[33][34][35][39][40].

The changes in Equation 4.11 in turn produce changes in the characteristic equations:

$$\omega_o = \sqrt{\frac{(k+\triangle k)}{m}}$$
$$\tau = \frac{m}{(\gamma+\triangle\gamma)}$$

By considering these changes with respect to the magnitude and phase outputs of the damped mass spring motion for a sinusoidally driven system, it is easy to see how the response of the tuning fork will change for a change in displacement. Due to the change in effective spring constant, there will be a shift in resonant frequency proportional to the change in force, which is in turn proportional to the change in displacement. The change in the damping time constant τ will produce a change in the Q-factor and the maximum magnitude of the sinusoidally driven piezoelectric tuning fork. This change in operating characteristics brought on by a change in displacement and its effect on the magnitude frequency response is shown graphically in Figure 4.2.1.

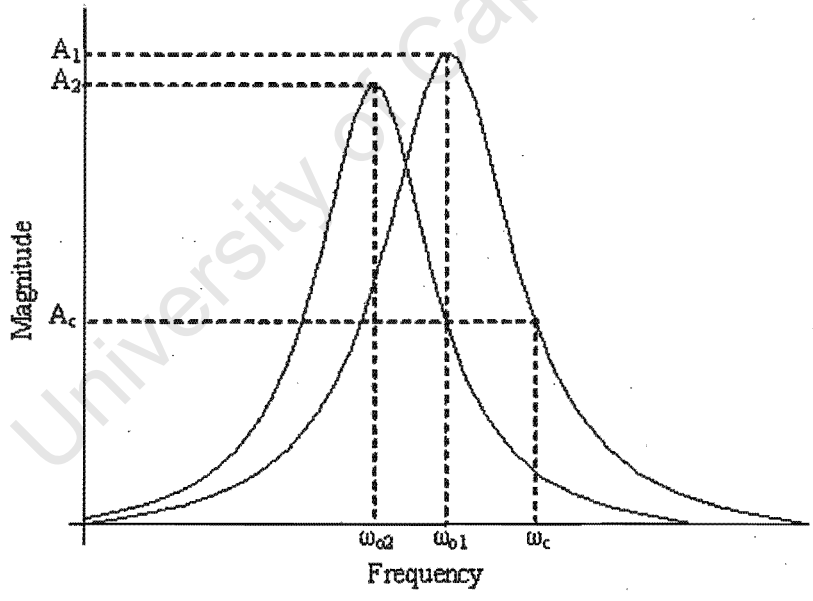

Figure 4.2.1: Change in Operating Characteristics and its Effect on the Magnitude Response for a Shift in Displacment. *At its first position the tuning fork operates with a resonant frequency ω_{o1} and a maximum magnitude of A_1. When the tuning fork's position is changed in relation to the surface the resonant frequency will change to ω_{o2} and the maximum magnitude will be A_2.*

Considering the situation when the system is operating at the first resonant frequency ω_{o1}: when the displacement changes, the resonant frequency will shift to ω_{o2} and the maximum magnitude will shift to A_2. The system, however, will still be operating at its initial frequency, which means that the output magnitude will fall to the level A_c, and the phase between the input and output signals will also change in accordance with the new damped mass spring characteristics. This change in magnitude and phase can be very closely approximated by keeping the displacement constant and shifting the drive frequency to ω_c. The accuracy of this approximation will be dependent on the difference between A_1 and A_2 and the change in the Q-factor. Therefore a simple model for the change in displacement can be formulated by considering the effects of shifting the input drive frequency. This model can be made even more accurate if the forces produced by the air effects when the displacement is changed are kept to a minimum, so that the difference between A_1 and A_2 and the change in the Q-factor can be minimised. The model for a change of displacement can then be thought of as an alteration of the spring constant force, which in turn will be modelled as a shift in input drive frequency. This model will help in the understanding and control of the tuning fork, as it is far easier to alter the input frequency accurately and repeatedly than it is to accurately change the displacement between the tuning fork tines and the surface.

4.2.2 System Response to a Change in Displacement

By modelling the change in displacement as an effective change in operating frequency, accurate models can be developed to describe the effects that a change in displacement will have on the operating characteristics of the tuning fork. The model for the total response of the tuning fork when the drive frequency changes now needs to be developed. From the studies on damped mass spring systems described in Appendix A2, the total response of the tuning fork when its input frequency is changed from ω_A to ω_B can be divided into a number of separate parts.

Firstly there is the steady state response for the new frequency ω_B. This response will describe the long term operating conditions of the fork once all the transients have died out. The steady state or particular response for the new frequency ω_B is given in the equation below, which comes from the mass-spring analysis for sinusoidal driving force completed in Appendix

A2.

$$x_{Steady\ State}(t) = \frac{\frac{F}{m}}{\sqrt{\left(\omega_o^2 - \omega_B^2\right)^2 + \left(\frac{1}{\tau}\omega_B\right)^2}} \cos\left(\omega_B t - \left(\tan^{-1}\left(\frac{\frac{1}{\tau}\omega_B}{\omega_o^2 - \omega_B^2}\right)\right)\right) \tag{4.12}$$

The first of the transients is associated with the build up of motion at the new frequency ω_B. The instant the drive frequency is shifted from ω_A to ω_B there will be no initial motion at the new frequency ω_B. This is a result of the build up transient acting initially with the same magnitude as the steady state response at ω_B but in exact antiphase with it. The steady state response at the new frequency ω_B and the transient associated with the build up of motion at the new frequency ω_B initially cancel each other out, but as the magnitude of the transient decays over time the combined response will build towards the steady state conditions at ω_B. The transient response associated with the build up of motion at the new frequency ω_B operates at the damped resonant frequency ω_o', and is given below in Equation 4.13.

$$x_{Transient(1)}(t) = e^{\frac{-t}{2\tau}}\left[\frac{\frac{F}{m}}{\sqrt{\left(\omega_o^2 - \omega_B^2\right)^2 + \left(\frac{1}{\tau}\omega_B\right)^2}} \cos\left(\omega_o' t - \left(\tan^{-1}\left(\frac{\frac{1}{\tau}\omega_B}{\omega_o^2 - \omega_B^2}\right) - \pi\right)\right)\right] \tag{4.13}$$

The second transient and final component of the total combined response is associated with the decay of motion at the old frequency ω_A. The motion is described by the undriven damped harmonic oscillator function. This transient motion also operates at the damped resonant frequency ω_o'. The initial magnitude and phase with respect to the drive signal will be determined by the steady state conditions at the old frequency ω_A. The transient associated with the decay of motion at the old frequency ω_A will also decay over time and is given below in Equation 4.14. The transient solutions also come from the analysis of the mass-spring system presented in Appendix A2.

$$x_{Transient(2)}(t) = e^{\frac{-t}{2\tau}}\left[\frac{\frac{F}{m}}{\sqrt{\left(\omega_o^2 - \omega_A^2\right)^2 + \left(\frac{1}{\tau}\omega_A\right)^2}} \cos\left(\omega_o' t - \left(\tan^{-1}\left(\frac{\frac{1}{\tau}\omega_A}{\omega_o^2 - \omega_A^2}\right)\right)\right)\right] \tag{4.14}$$

In order to develop the model for the frequency change, the separate responses need to be combined together to form one total response. This is made more difficult by the fact that

the transient and steady state responses can occur at two different frequencies. This means that the responses cannot be summed directly. They are instead reduced to vectors, and added together in a process explained extensively in the next section.

4.2.2.1 Combining the Transient and Steady State Responses

In order to determine the overall response of a mass spring system, the effects of the steady state and transient solutions have to be combined. This is difficult as the signals are at different frequencies and are at different phases relative to the drive signal. The transient signals occur at the damped resonant frequency, and the steady state signal occurs at the drive frequency. This combined equation will have the following form

$$\begin{aligned} x(t) &= x_{Steady\ State}(t) + x_{Transient(1)}(t) + x_{Transient(2)}(t) \\ &= \left[Y_{\omega_B}\cos\left(\omega_B t + \varphi_{\omega_B}\right)\right] + e^{\frac{-t}{2\tau}}\left[Y_{\omega_B}\cos\left(\omega_o' t + \left(\varphi_{\omega_B} - \pi\right)\right)\right] + e^{\frac{-t}{2\tau}}\left[Y_{\omega_A}\cos\left(\omega_o' t + \left(\varphi_{\omega_A}\right)\right)\right] \\ &= Y(t)\cos\left(\omega_B t + \varphi(t)\right) \end{aligned} \tag{4.15}$$

where Y_{ω_B} is the magnitude of the steady state solution and the initial magnitude of the transient associated with the build up of motion at the new frequency ω_B, Y_{ω_A} is the initial magnitude of the transient associated with the decay of motion at the old frequency ω_A, φ_{ω_B} and φ_{ω_A} are the phase of the steady state solution at the new frequency ω_B, and the transient associated with the decay of motion at the old frequency ω_A.

From Equation 4.15 it can be seen that the combination of the component signals will produce a single sinusoid at the new drive frequency ω_B, as this is the frequency at which the new steady state component will operate, which is the only long term component. The combined sinusoidal signal will have a magnitude and phase, relative to the drive signal, that vary with time. As the component signals are at different frequencies and phases, the effects cannot be summed directly, a new method must be found in order to determine how the phase and magnitude of the combined signal varies with time. Consider initially two sinusoidal waveforms of equal magnitude but of different frequencies ω_1 and ω_2 as seen in Figure 4.2.2:

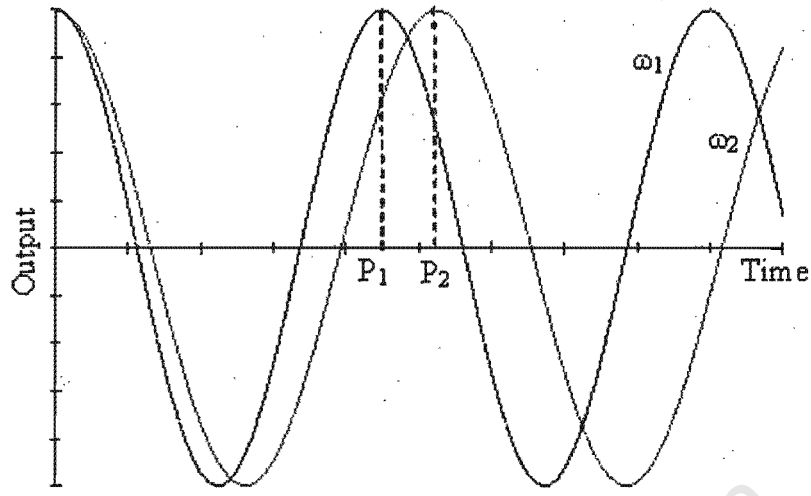

Figure 4.2.2: Two Sinusoidal Waveforms of Equal Amplitude but Different Frequencies.

If the two waveforms are in phase at $t = 0$, then by comparing the periods P_1 and P_2, it can be determined how far out of phase the two waveforms are after one period. First the time separation after one period is calculated,

$$Time\ Separation = P_2 - P_1 = \frac{2\pi}{\omega_2} - \frac{2\pi}{\omega_1} \tag{4.16}$$

This time separation can now be used to calculate the proportion that this time separation takes up of one period of a signal. Considering that one cycle or period consists of 2π radians, this percentage can be used to calculate the phase change after one period.

$$\begin{aligned} Phase\ Change\ per\ Cycle &= \left(\frac{\frac{2\pi}{\omega_2} - \frac{2\pi}{\omega_1}}{\frac{2\pi}{\omega_2}} \right) 2\pi \\ &= \left(1 - \frac{\omega_2}{\omega_1} \right) 2\pi \end{aligned} \tag{4.17}$$

The phase as a function of time can now be determined by calculating the phase change per unit time. The phase change per period is divided by the period of one of the waveforms to determine the phase change per unit time.

$$\varphi(t) = \left(\frac{\left(1 - \frac{\omega_2}{\omega_1}\right) 2\pi}{\frac{2\pi}{\omega_1}} \right) t = (\omega_1 - \omega_2)\, t \tag{4.18}$$

This simplified analysis will only remain accurate for small changes in frequency when compared to the frequency of the two waveforms, $(\omega_1 - \omega_2) \ll \omega_2$.

Now consider the real axis of a plot to be equal to the frequency of one of the waveforms. Any other waveform of another frequency can be plotted with reference to the initial waveform. This idea is shown below in Figure 4.2.3 for the two signals of magnitude A and B and frequency ω_1 and ω_2.

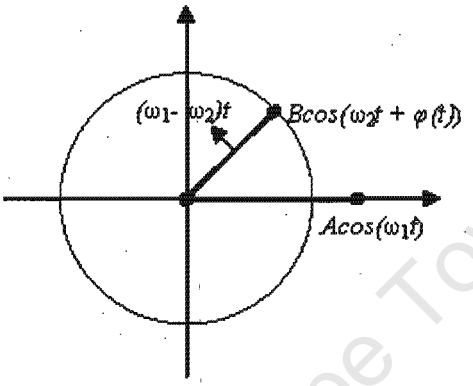

Figure 4.2.3: Two Sinusoidal Signals plotted Together on a Phase Plot. *When both signals are plotted on the same phase plot one of the phasors will rotate around the plot at a rate determined by the difference in frequency between them.*

From Equation 4.18 the phase between the two signals will change at a rate determined by the difference in frequencies. In Figure 4.2.3 this amounts to the plot of the second waveform rotating around a circle at a rate equal to the rate of phase change. By considering and combining the components of each signal in each of the axes, an equation for the total combined response can be determined.

This theory can be applied easily to the mass spring system. If the drive or forcing function is used as the reference signal the transient and steady state solutions can be plotted around the circle as follows in Figure 4.2.4.

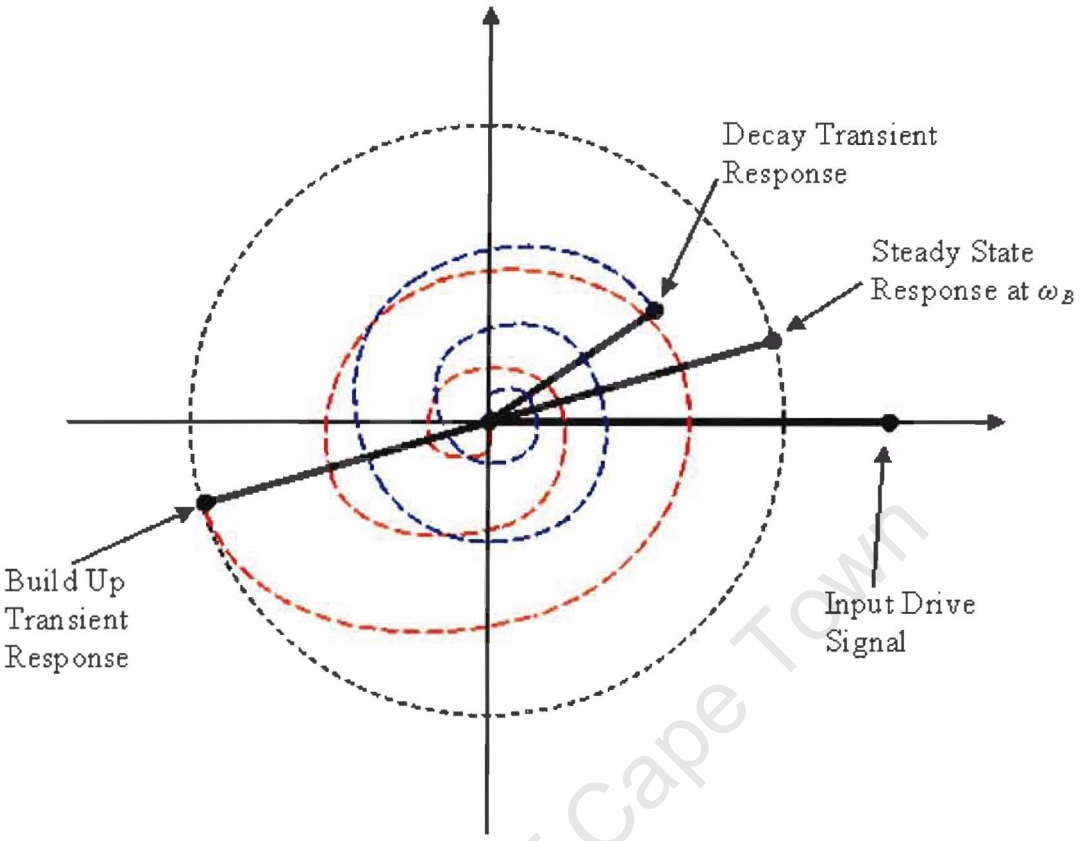

Figure 4.2.4: Component Responses of a Mass Spring System for a Shift in Input Driving Frequency Plotted around a Phase Circle. *The input drive signal is plotted along the real positive axis and is used as the reference signal. The input drive signal as well as the steady state solution both operate at the new drive frequency ω_B. As the two transient responses operate at the damped resonant frequency ω_o' the transient responses will rotate around the phase circle at $(\omega_B - \omega_o')\,t$, where t is time measured in seconds.*

The steady state solution is plotted around the dashed circle. As the steady state solution is at the same frequency as the drive signal, it will not rotate around the circle but remain at one point. The phase angle φ_{ω_B}, defined in Equation 4.12 as $\varphi_{\omega_B} = \tan^{-1}\left(\frac{\frac{1}{\tau}\omega_B}{\omega_o^2 - \omega_B^2}\right)$, will determine where along the circle the steady state solution lies. Its components with reference to the drive signal can be calculated using simple trigonometry,

$$\begin{aligned} \mathrm{Re}_{Steady\ State} &= Y_{\omega_B}\cos\left(\varphi_{\omega_B}\right) \\ \mathrm{Im}_{Steady\ State} &= Y_{\omega_B}\sin\left(\varphi_{\omega_B}\right) \end{aligned} \tag{4.19}$$

where as previously stated the real and imaginary components are with reference to the drive or forcing signal.

The transient solutions are not at the same frequency as the drive frequency, and thus they will rotate around at a rate dependent on the difference between the drive signal frequency and the damped resonant frequency. As the magnitude of the transient solutions diminishes with respect to time, the transient solutions will not form circles but will spiral down to the origin. The phase angles will determine the starting point of the transient solutions around the origin. The components of the transient solutions can now be resolved similarly to the steady state solution,

$$\begin{aligned} \mathrm{Re}_{Transient} &= e^{\frac{-t}{2\tau}}\left[Y_{\omega_B}\cos\left(\left(\omega_B-\omega_o'\right)t+\left(\varphi_{\omega_B}-\pi\right)\right)\right]+e^{\frac{-t}{2\tau}}\left[Y_{\omega_A}\cos\left(\left(\omega_B-\omega_o'\right)t+\left(\varphi_{\omega_A}\right)\right)\right] \\ \mathrm{Im}_{Transient} &= e^{\frac{-t}{2\tau}}\left[Y_{\omega_B}\sin\left(\left(\omega_B-\omega_o'\right)t+\left(\varphi_{\omega_B}-\pi\right)\right)\right]+e^{\frac{-t}{2\tau}}\left[Y_{\omega_A}\sin\left(\left(\omega_B-\omega_o'\right)t+\left(\varphi_{\omega_A}\right)\right)\right] \end{aligned} \tag{4.20}$$

The components of the solutions can now be added together to determine the total response,

$$\begin{aligned} \mathrm{Re}_{Total} &= Y_{\omega_B}\cos\left(\varphi_{\omega_B}\right)+e^{\frac{-t}{2\tau}}\left[Y_{\omega_B}\cos\left(\left(\omega_B-\omega_o'\right)t+\left(\varphi_{\omega_B}-\pi\right)\right)\right]+e^{\frac{-t}{2\tau}}\left[Y_{\omega_A}\cos\left(\left(\omega_B-\omega_o'\right)t+\left(\varphi_{\omega_A}\right)\right)\right] \\ \mathrm{Im}_{Total} &= Y_{\omega_B}\sin\left(\varphi_{\omega_B}\right)+e^{\frac{-t}{2\tau}}\left[Y_{\omega_B}\sin\left(\left(\omega_B-\omega_o'\right)t+\left(\varphi_{\omega_B}-\pi\right)\right)\right]+e^{\frac{-t}{2\tau}}\left[Y_{\omega_A}\sin\left(\left(\omega_B-\omega_o'\right)t+\left(\varphi_{\omega_A}\right)\right)\right] \end{aligned} \tag{4.21}$$

Where the magnitude and phase of the combined total response can be calculated using the following simple identities:

$$\begin{aligned} Magnitude &= Y(t)=\sqrt{\left(\mathrm{Re}_{Total}\right)^2+\left(\mathrm{Im}_{Total}\right)^2} \\ Phase &= \varphi(t)=\tan^{-1}\left(\frac{\mathrm{Im}_{Total}}{\mathrm{Re}_{Total}}\right) \end{aligned} \tag{4.22}$$

The start-up transient and the decay transient operate at the same frequency and are reduced at the same rate, so for simplicity they can be combined using the above phase plots into one single transient. The general properties of the combined response and its dependence on the positions of the signals around the phase plot are now considered.

4.2.2.1.1 General Properties of the Total Response In order to consider some of the properties of the combined response, it is simpler to use the case of combining two signals of the same magnitude and initial phase but of slightly varying frequencies. As was seen in the previous section, if these two signals are placed on a phase plot, the one signal will remain fixed at its initial phase whilst the other will rotate around the phase plot at a rate determined by the frequency difference between the two signals. By looking at the combined response of these two signals at a few different points in time, a number of general observations about combining signals of different frequencies can be made. Consider the system at different points in time shown below in Figure 4.2.5:

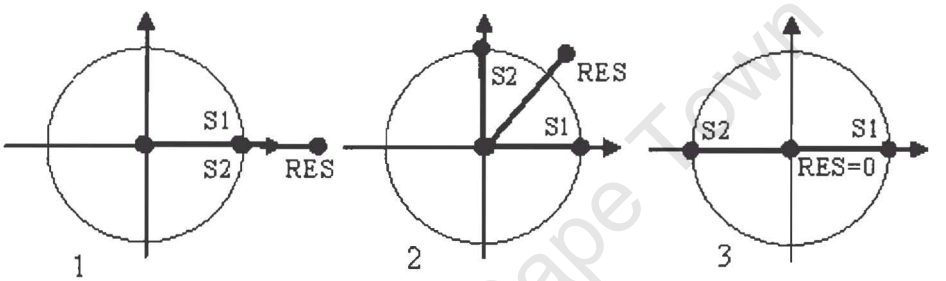

Figure 4.2.5: Combined Response of Two Sinusoidal Signals of Different Frequencies at Different Points in Time. *S1 and S2 are the two sinusoidal signals and RES is the resultant combined waveform.*

In the first instance the signals $S1$ and $S2$ are in phase with one another: this results in maximum magnitude and a phase of zero. In the second instance, $S2$ has rotated to 90° out of phase with $S1$. The magnitude of the total response has reduced to $\frac{\sqrt{2}}{2}$ of the maximum value and the phase has increased to 45°. In the final instance the signals are now 180° out of phase. The magnitude will now be at a minimum, which for signals of equal magnitude will be zero. The phase will be discontinuous at this point, as an instant before it will be approaching 90° and an instant after will be leaving -90° or 270°. The phase and magnitude response for the combination of the two signals is shown in Figure 4.2.6.

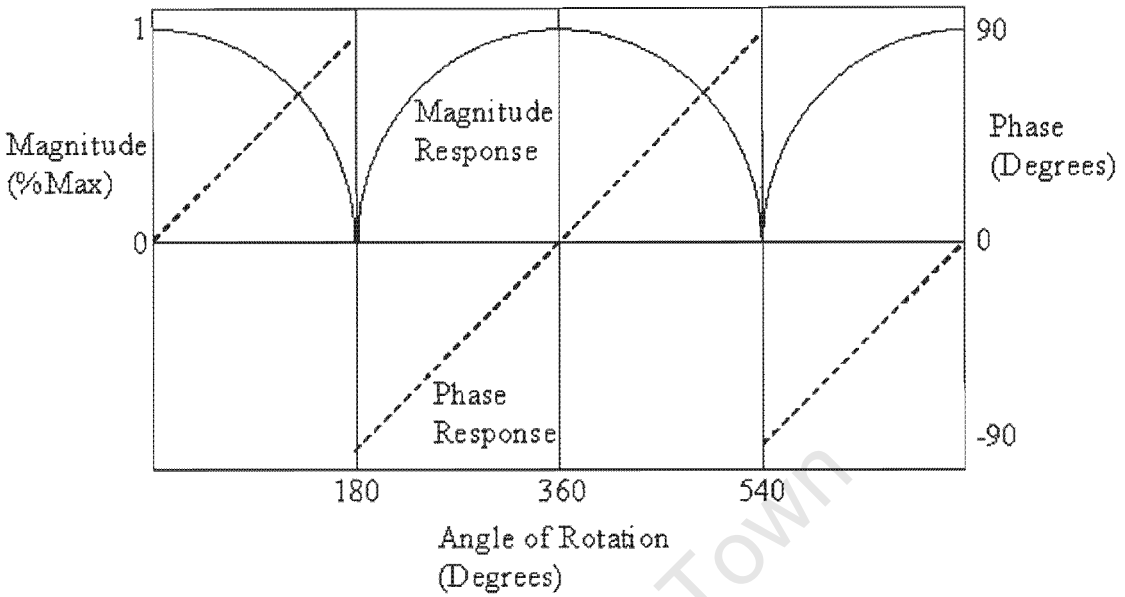

Figure 4.2.6: The Phase and Magnitude Responses for the Combined Response at Different Relative Phase Angles.

In situations where the one signal is smaller than the other there will always be a resultant even if the signals have rotated to 180° out of phase. This means that the phase response will no longer have a discontinuity and the response will become more and more sinusoidal as the one signal becomes smaller in relation to the other. For this case where one signal is smaller than the other the sinusoidal phase response will be 90° out of phase from the magnitude response.

The other property of the total response that should be considered is when both signals are at the same frequency but one signal is at a different initial phase and is decaying at a fixed rate. The phase and magnitude response of the combined resultant signal will be dependent on: the rate of decay of the signal, the initial phase displacement between the two signals, and the difference in magnitude. A rough idea of the relative speeds of the responses can be obtained by considering the equations that govern the responses.

Consider two signals at the same frequency with magnitudes A and B. Signal B is decaying at a rate set by e^{-t} and is φ degrees out of phase with signal A. If Signal A is lying at 0° on

the phase plane the magnitude response for this system using Equation 4.22 will be,

$$\begin{aligned} Magnitude &= \sqrt{(A + e^{-t}B\cos\varphi)^2 + (e^{-t}B\sin\varphi)^2} \\ &= \sqrt{A^2 + 2e^{-t}AB\cos\varphi + B^2\cos^2\varphi + e^{-2t}B^2\sin^2\varphi} \\ &= \sqrt{A^2 + 2e^{-t}AB\cos\varphi + e^{-2t}B^2} \end{aligned} \tag{4.23}$$

From Equation 4.23 it can be seen that the total rate of decay of magnitude will be dependent on the combination between the second and third terms of the equation. As the third term on its own would decay twice as fast as the second term on its own, the one which has the greatest effect within the combination will determine of overall response of the magnitude. Consider first how the phase between the two signals affects the response time of the magnitude. Initial phase only affects the second, slower, term of the equation, so when the initial phase angle results in the maximum value for this term it will coincide with the initial phase angle that results in the longest total response time for the magnitude.

When looking at the effect that the difference in initial magnitudes of the two signals will have on total response time of the magnitude response, it is more instructive to view Equation 4.23 in the form:

$$Magnitude = \sqrt{1 + 2e^{-t}\frac{B}{A}\cos\varphi + e^{-2t}\frac{B^2}{A^2}} \tag{4.24}$$

From Equation 4.24 it can be seen that when signal A is initially much bigger than signal B the second term will dominate and the magnitude response will be closer to e^{-t}. Similarly when signal B is much bigger than signal A the third term will dominate and the magnitude response will decay at a rate closer to e^{-2t}.

The phase response for this system can also be determined using Equation 4.22:

$$Phase = \arctan\left(\frac{e^{-t}B\sin\varphi}{A + e^{-t}B\cos\varphi}\right) \tag{4.25}$$

In order to determine how the initial phase between the signals will affect the response time of the phase it is necessary to consider the term within the brackets of Equation 4.25, and see how changes in phase and relative magnitude affect it. The numerator of this term within the brackets sets the basic rate of decay of the phase response and the behaviour of the denominator

will either speed up or slow down the overall rate of decay. Considering first how initial phase will affect the system when both signals are of equal magnitude. At 90° the second term of the denominator will be zero and the overall rate of decay will be set by the numerator decay exclusively. As the phase angle between the signals grows towards 180° the initial value of the denominator will drop below one as the second term becomes negative. However as the second term of the denominator degrades over time the total denominator value will tend back towards one. Having the initial value of the denominator less than one and having the numerator shrink as the denominator grows will speed up the overall response time. For phase angles below 90° the opposite effect occurs, both the numerator and denominator are shrinking at the same time which effectively slows down the overall response.

From the above explanation it follows that the initial relative magnitudes of the two signals would also have an effect on the overall speed of the phase response. If signal A was bigger than signal B the effect of the phase between the signals would be reduced. This would either speed up the response if the signals were less than 90° apart, or slow down the response if the signals were greater than 90° apart. If signal B were bigger than signal A then for all cases besides when the phase is 90°, the denominator and numerator's absolute values will shrink, which slows down the response time.

A special mention should be made of the case when the signals are either in phase or in antiphase. When completely in phase, the resultant of the combination will always be in phase as well, which means there will be no change in phase at all. When 180° out of phase, depending on which signal is initially bigger, the resultant will either always be in phase or will shift instantaneously from 180° out of phase, to completely in phase when one signal drops below the magnitude of the other.

4.2.3 Modelling the Piezoelectric Tuning Fork

Using the general properties of combined signals developed in the previous sections, the model for the tuning fork crystal's response to a change in drive frequency can be developed. The combination of the steady state and transient responses requires that both the magnitude and the phase of the signals with reference to the drive signal are precisely known. Once the initial conditions are used to determine the correct initial positions of the two waveforms,

the theoretical combined response can be formed. This response can then be easily compared to actual measured responses of the crystal to determine the accuracy of the model. Using Laplace transforms, the model can then be converted into equations that can be used to design the control systems for the crystal.

4.2.3.1 Initial Conditions

Consider again the shift in operating frequency from ω_A to ω_B. At the instant of frequency change, the tuning fork will still be operating at the amplitude and phase of the steady state response of the initial frequency, ω_A. This means that the initial condition of motion, for when the frequency is shifted, can be given by the steady state response at the initial frequency ω_A. The sum of all the component responses must initially add up to this initial condition. This becomes a useful fact when testing whether the transient and steady state conditions have been modelled correctly. However, this should always be the case, as the steady state response at the new frequency ω_B and the transient associated with the build up of motion at the new frequency ω_B will, initially, cancel each other out, and all that is left will be the transient associated with the decay of motion at the old frequency ω_A, which will initially be at the steady state conditions at the old frequency ω_A. The initial condition can also be used to quickly calculate the initial size and position of the combined response from both the onset transient and the decay transient. As the initial condition is the sum of all the component responses at the moment of frequency change, by subtracting the initial condition from the steady state response at the new frequency ω_B the initial position and size of the combined transient response can be determined. In Figure 4.2.7 the component responses have been plotted for a set frequency shift.

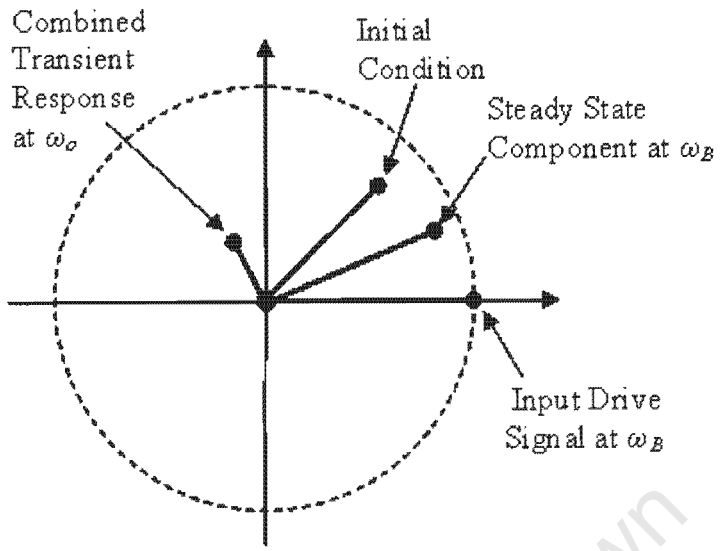

Figure 4.2.7: The Phase Plot Showing the Initial Condition of Motion Relative to the Steady State Response and the Combined Transient Reponse. *The initial condition will be the position of the combined response of the steady state and transient responses at the instant of frequency shift.*

For any given shift in input drive frequency the corresponding magnitude and phase response of the piezoelectric tuning fork can now be simulated. Firstly the steady state conditions at the old frequency must be determined. Then, either using the two transient responses, or the steady state conditions at the new frequency, the combined transient response can be easily be found. The total magnitude and phase response of the tuning fork crystal can now be determined by adding the components of the transient and steady state responses. The exact drive frequency as well as the damped resonant drive frequency must accurate so that the exact rate at which the transient responses will rotate around the phase plot can be determined.

4.2.3.2 The Final Model and its Comparison with Real Data

Enough is now known about the system to hopefully calculate a reasonably accurate model for the tuning fork crystal for when the input drive frequency altered. The parameters of the system can be determined using the measured steady state response, which was $Q_{\sqrt{3}} = 78362$, $Q_{FWHM} = 46974$, $f_0 = 32765.290Hz$, and $\tau = \frac{Q_{\sqrt{3}}}{2\pi(f_o)} = 0.381$.

For the first test the system was operated at the resonant frequency so that the transient

and steady state responses would be at the same frequency so there would be no oscillation on the phase or magnitude outputs. The frequency was stepped from 200mHz below the damped resonant frequency to the damped resonant frequency The steady state magnitude and phase as well as the initial magnitude and phase can then be calculated using Equations 3.56 and 3.57. Using the phase circle, the transient and steady state responses can then be combined to give the overall response for magnitude and phase. These simulated results can then be compared against real data obtained from a similar step test with an actual crystal. A comparison between the real and simulated responses for the magnitude appears in Figure 4.2.8.

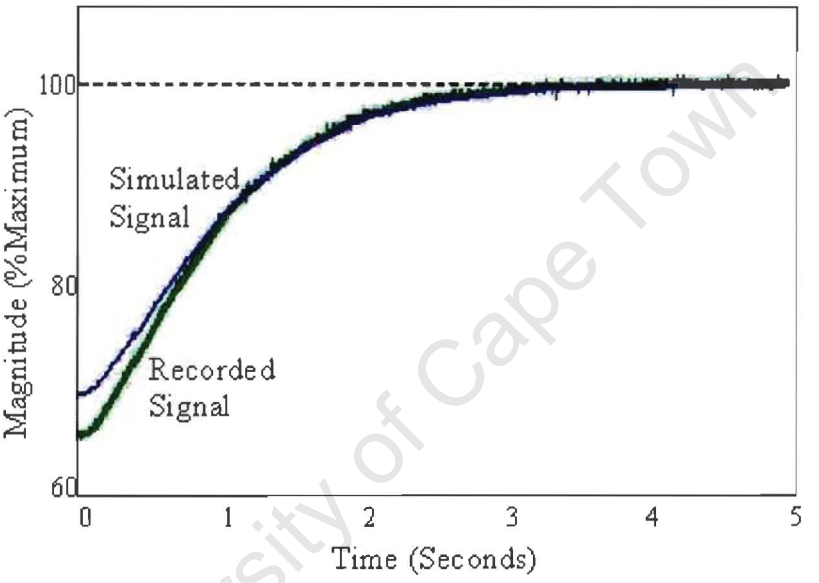

Figure 4.2.8: Simulated and Recorded Magnitude Response at the Resonant Frequency. *The output magnitude was recorded over a period of 5 seconds. The magnitude was measured using an active rectifier and then converted to a percentage of the maximum value of the magnitude at the resonant frequency.*

A comparison between simulated and recorded phase appears in Figure 4.2.9.

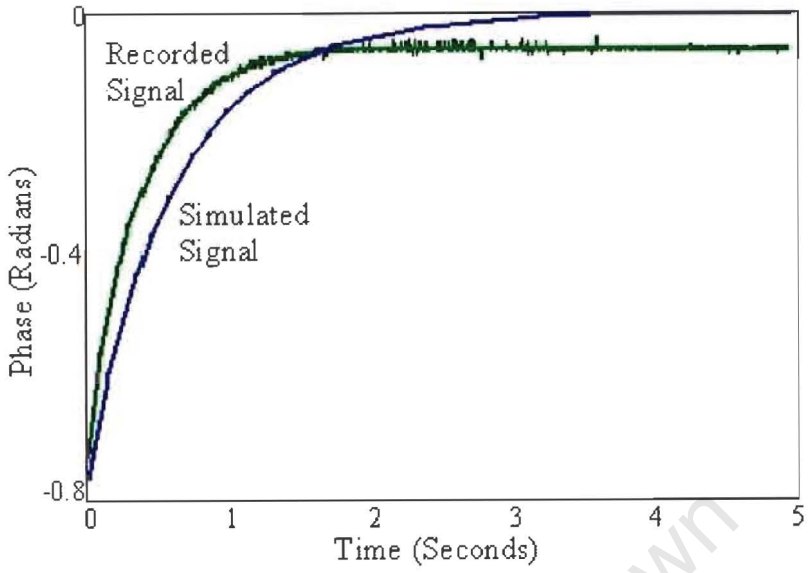

Figure 4.2.9: Simulated and Recorded Phase Responses at the Resonant Frequency. *The phase between the input drive signal and input voltage was recorded using a exclusive-or gate logic type detector. The output from the logic gate was then actively rectified to obtain the recorded output.*

From the plot in Figures 4.2.8 and 4.2.9 it is clear that the model provides a fairly good representation of the actual behaviour of the tuning fork crystal. Even though the shape of the response is well represented by the theoretical behaviour of the models, the speed of the theoretical response is some what slower than the actual measured response. This is especially obvious in the phase plot. The speed of the response is governed by the initial position of the steady state and transient responses on the phase plot as well as the decay rate of the transient determined by the mass spring characteristics. The errors in theoretical response could be attributed both to the measurement of the characteristics of the tuning fork, as well as the fact that the mass spring model probably does not describe the behaviour of the tuning fork exactly. Although the incorrect placement of the responses on the phase plot, which could be attributed to errors in measurement, will cause errors, the greatest problem is probably caused by the incorrect modelling of the damping in the system. Errors could also be attributed to imperfect cancellation of the package capacitance, and the fact that the actual step tests might not be exactly to the damped resonant frequency. These tests were also done in a relatively high vacuum as the tuning fork is still in its outer packaging. The limited viscous damping in

vacuum is another cause of the discrepancy between the measured and theoretical responses.

Another series of tests was completed in order to ascertain how well the model would work when the system is operating away from the damped resonant frequency. The frequency was stepped this time by 20mHz approximately 0.4Hz off resonance. The results for this test were collated and normalised so they could be shown on one plot. This plot of the normalised responses of phase and magnitude for both the simulated and recorded data appears in figure 4.2.10.

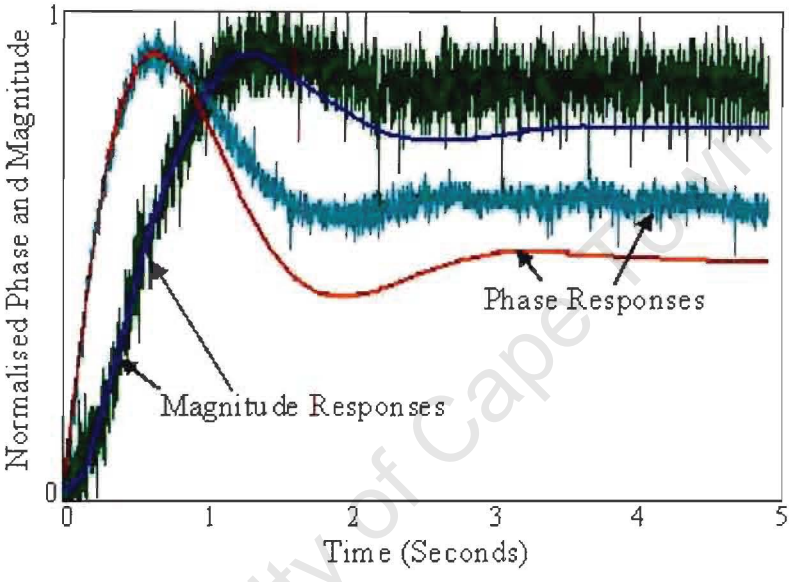

Figure 4.2.10: Phase and Magnitude Step Tests 0.4Hz off the Resonant Frequency. *Similar methods were used to measure both magnitude and phase. The results have been normalised.*

From Figure 4.2.10 it is clear that the theoretical simulated response follows the basic shape of the actual response fairly accurately. The measurement inaccuracies will still produce error, but it is clear that the modelling of the damping is still producing the largest error between the measured and theoretical responses. The responses are closer than the responses for the test at the damped resonant frequency, indicating that the damping constant should be dependent on the operating frequency position relative to the damped resonant frequency. This frequency dependence of the damping factor also seems to have a different effect on phase and magnitude. From the tests, the decay rate of the transients in the actual system seem to vary from $\frac{1}{\tau}$ to $\frac{1}{2\tau}$. These tests also indicate that the relatively simple model developed up to now does not

describe the actual behaviour of the tuning fork crystal exactly. The models do, however, model the shape of the responses very well and by slightly adjusting the decay rate of the transients can model the actual behaviour accurately. These slightly adjusted models could now be used to develop control models and a controller for the system.

4.2.3.3 Developing the S-plane model or G(s) for the System

In order to design an effective controller for the system it is useful to have an accurate s-plane model of the system. This can be done in two ways. Laplace transforms could be performed on the original time domain equations, or the response can be studied, and standard model responses can be applied to them. The second approach was attempted first, as if an accurate model can be obtained, it will be far easier than computing the rather complicated Laplace transforms of the time domain equations.

Looking at the responses in the previous section, it is obvious that the magnitude is an offset decaying cosine wave. As the phase response is 90° out of phase from the magnitude response, it can be similarly modelled as an offset decaying sine wave. The Laplace transforms of these offset decaying waveforms are well known to be [6][41]:

$$Magnitude = \text{Decaying Cosine Wave} = \frac{a}{(s+a)^2+\omega^2} \tag{4.26}$$

$$Phase = \text{Decaying Sinusoidal Wave} = \frac{s+a}{(s+a)^2+\omega^2} \tag{4.27}$$

For the Equations in 4.26 and 4.27, the variable a will determine the decay time of the waveform, and will be set by the resonant frequency and Q-factor of the system; and ω is the oscillation frequency of the waveform, determined by the frequency difference between the input drive frequency ω_d and the resonant damped frequency ω_o'. These equations can thus be

converted into the following equations using the characteristic variables developed before:

$$Magnitude = \frac{A\left(\frac{1}{(o_m)(\tau)}\right)}{s^2 + 2\left(\frac{1}{(o_m)(\tau)}\right)s + \left((\omega_d - \omega_o')^2 + \left(\frac{1}{(o_m)(\tau)}\right)^2\right)} \tag{4.28}$$

$$Phase = \frac{A\left(s + \left(\frac{1}{(o_p)(\tau)}\right)\right)}{s^2 + 2\left(\frac{1}{(o_p)(\tau)}\right)s + \left((\omega_d - \omega_o')^2 + \left(\frac{1}{(o_p)(\tau)}\right)^2\right)} \tag{4.29}$$

A is a constant which will determine the amplitude of the response, o_m and o_p are the adjustment factors of the decay rates of the transient responses for magnitude and phase. These models were then step tested and compared to the data recorded previously. For the first test, where the frequency is stepped to the resonant damped frequency, the normalised plots for phase and magnitude appear in Figure 4.2.11.

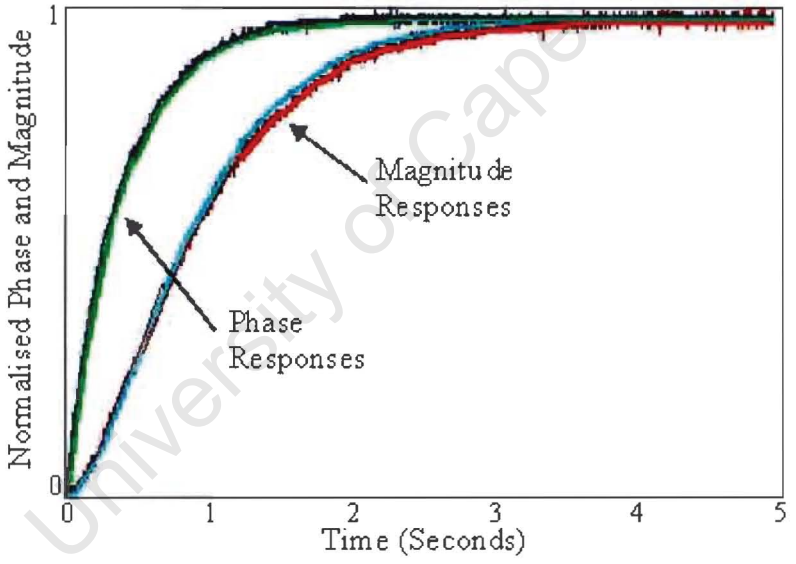

Figure 4.2.11: Step Test Comparison with S-plane Models at Resonant Frequency. *Once again similar measurement techniques were used to determine both the magnitude and phase. The results are also similarly normalised.*

For the step test to the damped resonant frequency, $o_m = 1.2$ and $o_p = 1$. From the test it is clear that not only do the cosine and sine models produce responses that are very similar in shape to the actual response, but, by the manipulation of the transient decay rates, the theoretical models can simulate the speed of response very closely as well. Due to the operating

frequency being the same as the resonant drive frequency, the magnitude response reduces to a double pole system in the s-plane, with both poles existing on the same point on the real axis determined by the decay rate of the system. The phase response reduces to a single pole system with the pole on the real s-plane axis at the same point determined by the decay rate. The results of the second test for the step 0.4Hz off resonance are plotted in Figure 4.2.12.

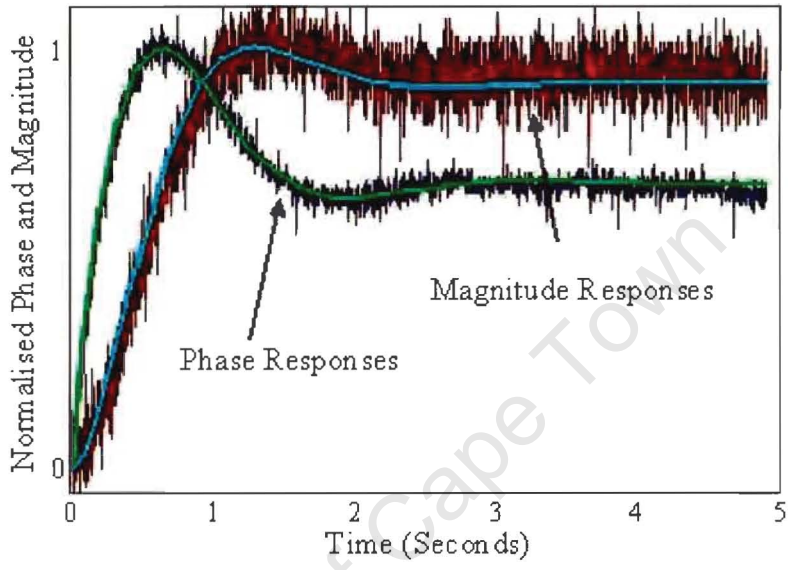

Figure 4.2.12: Step Test Comparison with S-plane Models 0.4Hz off Resonant Frequency. *The increased noise due to the reduced output at frequencies off resonance makes it more difficult to accurately compare the simulated and recorded responses.*

Again the equations seem to give a good model for the system, with $o_m = 1.4$ and $o_p = 1.5$. The shift in operating frequency away from the damped resonant frequency affects the transient decay rate for the phase response more than the magnitude response. The shape of the response is still well modelled by the basic cosine and sine s-plane equations and by a small adjustment of the decay rate of the transient the speed of the response can be simulated accurately as well. Now that good models for the system exist, it remains for the controllers to be designed, to see if these models will work in the controlling of the system.

4.3 Controlling the Crystal

4.3.1 The Model

In the previous section control models or $G(s)$ terms for the magnitude and phase response of the tuning fork crystal were developed. These are given again below.

$$Magnitude = G_m(s) = \frac{A\left(\frac{1}{(o_m)(\tau)}\right)}{s^2 + 2\left(\frac{1}{(o_m)(\tau)}\right)s + \left((\omega_d - \omega_o')^2 + \left(\frac{1}{(o_m)(\tau)}\right)^2\right)}$$

$$Phase = G_p(s) = \frac{A\left(s + \left(\frac{1}{(o_p)(\tau)}\right)\right)}{s^2 + 2\left(\frac{1}{(o_p)(\tau)}\right)s + \left((\omega_d - \omega_o')^2 + \left(\frac{1}{(o_p)(\tau)}\right)^2\right)}$$

Where ω_d is the input drive or operating frequency, ω_o is the resonant frequency, τ is the damping time constant of the system and A is the gain of the system determined by the initial operating conditions. At the resonant frequency the equations 4.28 and 4.29 are reduced to:

$$Magnitude = G_m(s) = \frac{A\left(\frac{1}{(o_m)(\tau)}\right)}{\left(s + \left(\frac{1}{(o_m)(\tau)}\right)\right)^2} \tag{4.30}$$

$$Phase = G_p(s) = \frac{A}{s + \left(\frac{1}{(o_p)(\tau)}\right)} \tag{4.31}$$

Depending on the tuning fork crystal operating point the two control models $G_m(s)$ and $G_p(s)$ for phase and magnitude can be defined. For frequencies at or very near the resonant frequency Equations 4.30 and 4.31 can be used. For frequencies further away from the resonant frequency where the oscillations become more distinct, the original control models in Equation 4.28 and 4.29 should be used.

4.3.2 Closing the Loop

Due to the tuning fork's simple nature, linear feedback control should be adequate in controlling the operating frequency by either using the magnitude or the phase as control variables. The simple feedback block diagram used to form the closed loop response is shown in Figure 4.3.1.

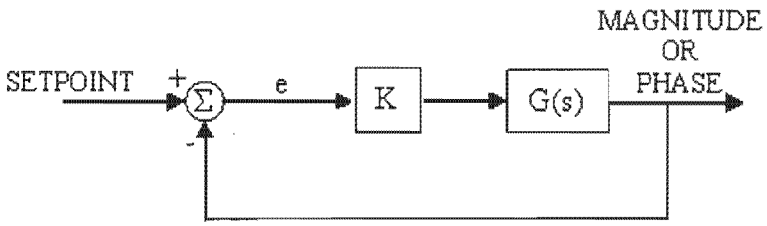

Figure 4.3.1: The Linear Feedback Control Block Diagram. *The output magnitude or phase is compared to a DC setpoint. The result of this comparison generates an error voltage, which will adjust the input drive voltage to the tuning fork crystal via the controller.*

In Figure 4.3.1 K is the gain present in the system and is controlled through the design of the feedback electronics. $G(s)$ is the control model for the system and is derived from the models developed in equations 4.28 and 4.29. For $G(s)$, which can be split into $G_m(s)$ for magnitude and $G_p(s)$ for phase, the original models have been manipulated so that their open loop gain is unity. This combines the gain in equations 4.28 and 4.29 and the gain of the controller into one gain term for the whole feedback system, which is either K_m for magnitude or K_p for phase. The equations are further simplified by substituting variables in for the decay rate and frequency of oscillations, so that $\delta_m = \frac{1}{(o_m)(\tau)}$, $\delta_p = \frac{1}{(o_p)(\tau)}$ and $\omega_n = \omega_d - \omega_o'$. From basic block diagram algebra [6] the closed loop transfer functions $H_m(s)$ and $H_p(s)$ can be determined as follows.

$$H_m(s) = \frac{K_m G_m(s)}{1 + K_m G_m(s)} = \frac{\frac{K_m\left(\omega_n^2+\delta_m^2\right)}{s^2+2\delta_m s+\omega_n^2+\delta_m^2}}{1 + \frac{K_m\left(\omega_n^2+\delta_m^2\right)}{s^2+2\delta_m s+\omega_n^2+\delta_m^2}} = \frac{K_m\left(\omega_n^2+\delta_m^2\right)}{s^2+2\delta_m s+\omega_n^2+\delta_m^2+K_m\left(\omega_n^2+\delta_m^2\right)} \quad (4.32)$$

$$H_p(s) = \frac{K_p G_p(s)}{1 + K_p G_p(s)} = \frac{\frac{K_p(s+\delta_p)\left(\frac{\omega_n^2}{\delta}+\delta_p\right)}{s^2+2\delta_p s+\omega_n^2+\delta_p^2}}{1 + \frac{K_p(s+\delta_p)\left(\frac{\omega_n^2}{\delta}+\delta_p\right)}{s^2+2\delta_p s+\omega_n^2+\delta_p^2}} = \frac{K_p(s+\delta_p)\left(\frac{\omega_n^2}{\delta}+\delta_p\right)}{s^2+2\delta_p s+\omega_n^2+\delta_p^2+K_p(s+\delta_p)\left(\frac{\omega_n^2}{\delta_p}+\delta_p\right)} \quad (4.33)$$

By looking at how the closed loop poles shift for different values of gains K_m and K_p, the characteristic responses of the closed loop systems can roughly be determined.

4.3.2.1 Magnitude

The magnitude frequency response has a peak, which makes it difficult, for a controller using magnitude as an input, to keep the tuning fork crystal operating at the resonant frequency. Any shift in frequency, whether up or down, will result in a drop in magnitude. The tuning fork crystal must be operated away from the resonant frequency along one of the slopes of the peak. The closed loop pole positions for the magnitude response, for the tuning fork crystal operating away from the resonant frequency, can be found by looking at the denominator of equation 4.32.

$$Magnitude\ Poles = \phi_m = s^2 + 2\delta_m s + \left(\omega_n^2 + \delta_m^2\right)(1 + K_m) \tag{4.34}$$

The root locus diagram for the closed loop magnitude response in Figure 4.3.2 is drawn using the quadratic formula to determine the closed loop pole positions for varying values of K_m.

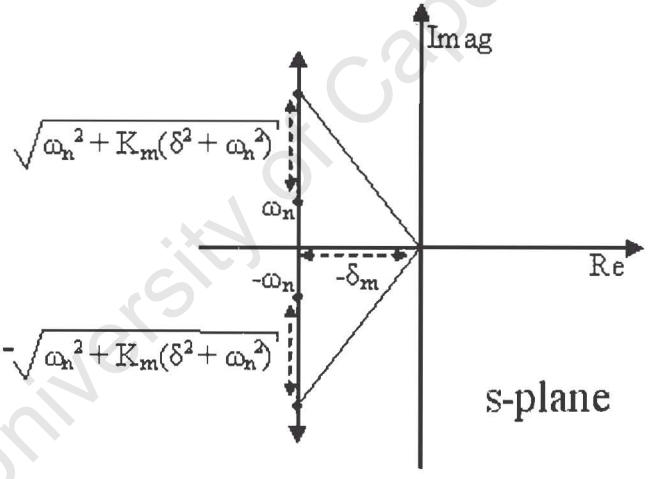

Figure 4.3.2: The Closed Loop Magnitude Pole Positions for Increasing Gain. *The magnitude measurement system forms a double pole system in closed loop. The poles move along the positive and negative imaginary axes for increasing gain. This makes the system more oscillatory but has little effect on system speed or bandwidth.*

From Figure 4.3.2 it can be seen that the general speed of the magnitude response will be set by δ_m, the mechanical damping factor or damping time constant of the mechanical system. For variations in the gain K_m the closed loop response will become more or less oscillatory and the closed loop damping will increase or decrease. So by increasing the gain of the closed loop

system, no speed increases will be obtained. The system will still take the time determined by δ_m to settle to its final value. Closed loop gain can also be calculated using final value theorem for a step input of $\frac{1}{s}$:

$$\begin{aligned} \textit{Closed Loop Gain} &= K_{CLm} = \lim_{s\to 0}\left(s\left(H_m\left(s\right)\right)\frac{1}{s}\right) \\ &= \lim_{s\to 0}\left(\frac{K_m\left(\omega_n^2+\delta_m^2\right)}{s^2+2\delta_m s+\omega_n^2+\delta_m^2+K_m\left(\omega_n^2+\delta_m^2\right)}\right) \\ &= \frac{K_m}{1+K_m} \end{aligned} \tag{4.35}$$

In order to test this control model a basic loop was set up and various step tests were done with varying gain to determine the accuracy of the above closed loop model.

In the following graphs the theoretical responses are compared to actual data taken using magnitude as the feedback parameter. For the simulated data the $G_m\left(s\right)$ for the system is considered to be the voltage controlled oscillator (VCO), tuning fork crystal and the magnitude detector which is just a simple active rectifier. The gain of $G_m\left(s\right)$ is assumed to be unity and then K_m is calculated to give the required gain for the entire system, accounting for all the gains in the VCO, tuning fork crystal and rectifier. This simulated response can then be compared to actual recorded data taken from the system. The first graph in Figure 4.3.3 is the open loop magnitude response for when the system is stepped to a frequency near resonance. The resonant frequency was measured as: $f_0 = 32765.273Hz$ with $Q = 41475$ and $Q_{\sqrt{3}} = 72012$.

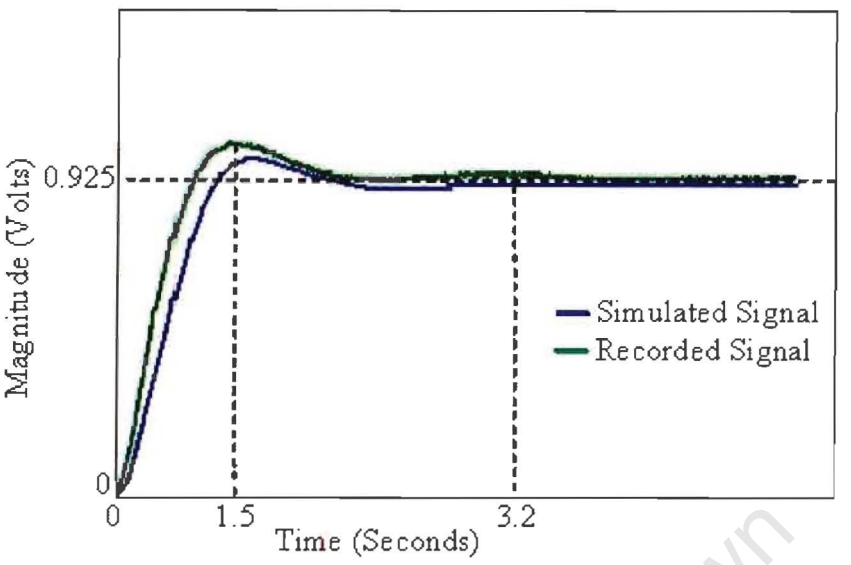

Figure 4.3.3: The Open Loop Magnitude Response ($K_m = 0.925$). *The oscillation in the open loop step response is caused by the settling frequency being off the resonant frequency. Using the measured gain and the measured characteristics of the tuning fork crystal the simulated response can be generated using the system control models developed previously.*

From the above graph the open loop gain of the system can be calculated as $K_m = 0.925$. The oscillations in the graph are caused by the settling frequency being at $f = 32765.982Hz$ which is about $0.29Hz$ from the damped resonant frequency. This results in the oscillation with a period of 3.2 seconds seen in Figure 4.3.3. If the system described by the above graph is theoretically put into feedback, the basic characteristics of the closed loop system can be ascertained from Equation 4.32. For the calculated open loop gain of $K_m = 0.925$, and using $Q_{\sqrt{3}}$ to calculate the value of $\delta_m = 1.429s$ the closed loop poles can be calculated as,

$$\text{Closed Loop Poles} = \phi_m = -1.429 \pm j2.85$$

giving a characteristic equation for the system as:

$$s^2 + 2.858s + 10.18$$

Due to the non-linear Lorentzian response of the magnitude the simulated response could not be generated very accurately. The response was therefore linearised across the operating

range to give a better simulated output. This linearisation pushed the open loop gain up to $K_m = 1.357$, which from Equation 4.35 gives a closed loop gain $K_{CLm} = 0.53$ and adjusted closed loop poles of:

$$Adjusted\ Closed\ Loop\ Poles = \phi_m = -1.429 \pm j3.255$$

This theoretical model can then be compared to data taken from the actual system. The theoretical and actual responses are plotted in Figure 4.3.4.

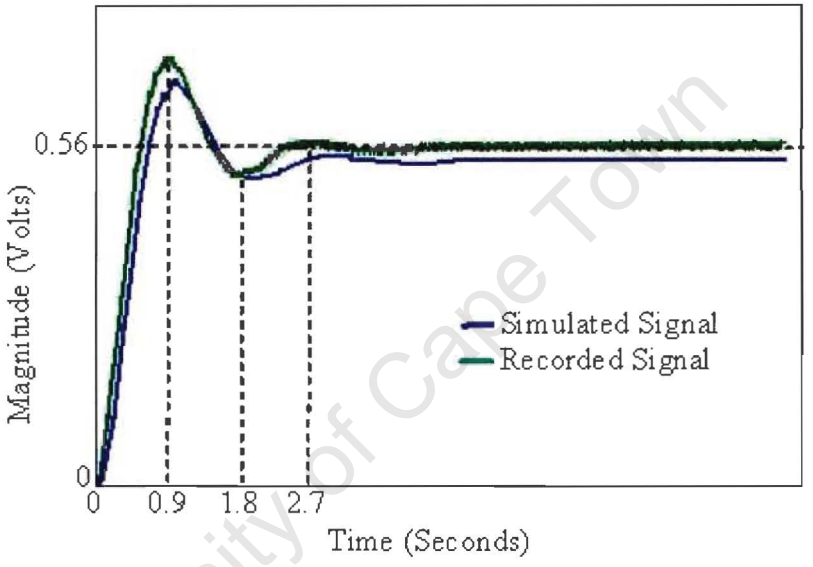

Figure 4.3.4: Closed Loop Magnitude Response for the Simulated and Recorded Signals ($K_m = 0.925$).

From Figure 4.3.4 it can be seen that the theoretical model tracks the actual behaviour fairly closely. The natural frequency of the system is measured at $0.55Hz$, which is close to the theoretical value of $0.52Hz$. The discrepancy could easily be explained by measurement errors and errors brought about by the simulated linearisation of the Lorentzian response. The small error between the actual and theoretical closed loop gains can also be caused by this linearisation process.

Two more theoretical step tests were performed with increasing values of K_m. These results were then compared with data from the actual system with similar increases in open loop gain. The results of the two tests are shown below in Figure 4.3.5 and 4.3.6.

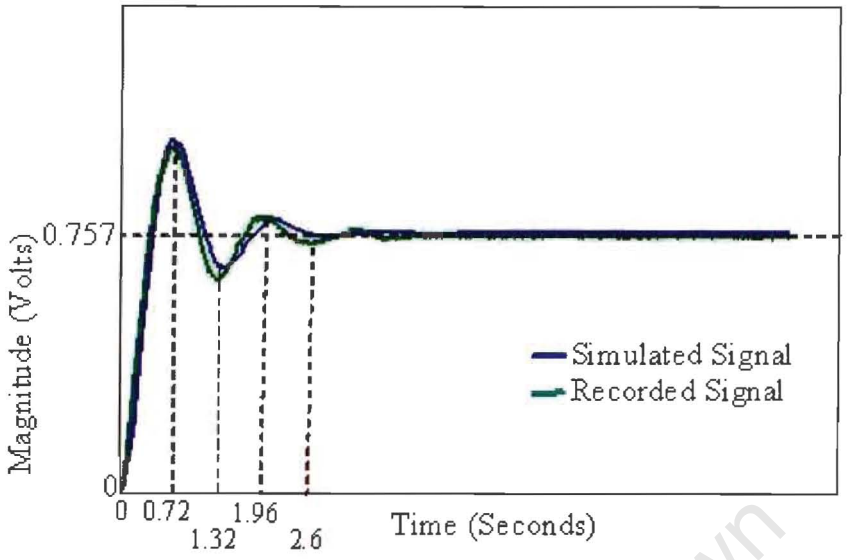

Figure 4.3.5: Closed Loop Magnitude Response for the Simulated and Recorded Signals ($K_m = 3$).

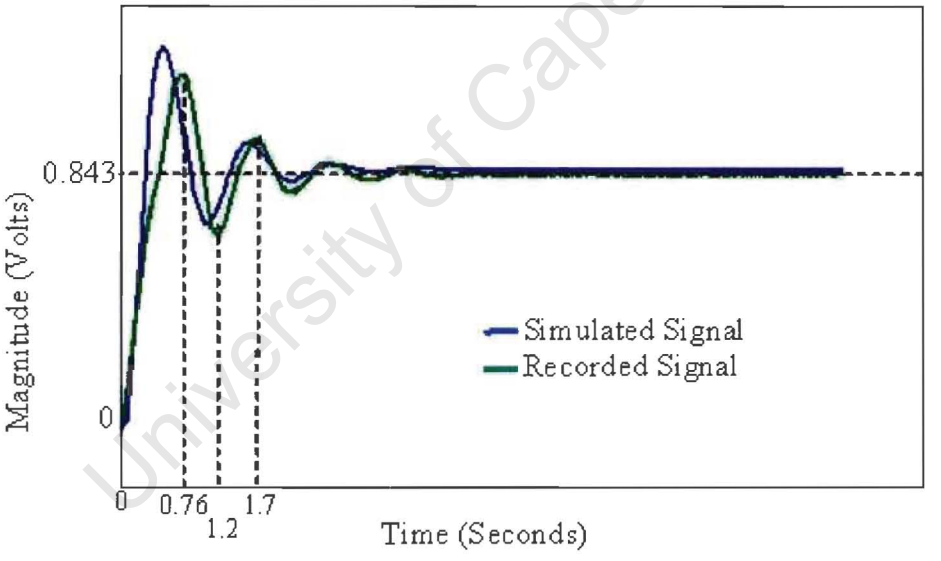

Figure 4.3.6: Closed Loop Magnitude Response for the Simulated and Recorded Signals ($K_m = 6$).

From the graphs in Figures 4.3.4-4.3.6, it is clear that the theoretical and actual results correlate quite closely even for changes in open loop gain. It is also now clear that the initial root locus diagram for increasing gain is an accurate representation of the system. Increasing the gain for the magnitude response in a linear feedback system will have no effect on system

speed, as each one of the above systems reaches 2% of its final value at about the same time. However an increase in gain does affect both the natural frequency and the damping in the system, as well as the closed loop gain. The correlation between the actual and theoretical responses also indicates that the closed loop gain and natural frequency are well described by Equations 4.34 and 4.35.

4.3.2.2 Phase

The frequency response of the phase between the input drive voltage and the output converted current does not have a peak like the magnitude response. This allows the tuning fork crystal to be operated at its resonant frequency, which will greatly simplify the control model governing the response. The closed loop phase response can be determined by simplifying Equation 4.33, and as the operating frequency is equal to the damped resonant frequency, the output oscillation frequency ω_n will equal zero.

$$H_p(s) = \frac{K_p\delta_p}{(s+\delta_p)+K_p\delta_p} \tag{4.36}$$

The poles of the closed loop phase response can be determined by looking at the denominator of Equation 4.36.

$$Phase\ Poles = \phi_p = -\delta_p - K_p\delta_p \tag{4.37}$$

Using the position of the phase poles the root locus diagram for the closed loop phase response can be drawn in Figure 4.3.7.

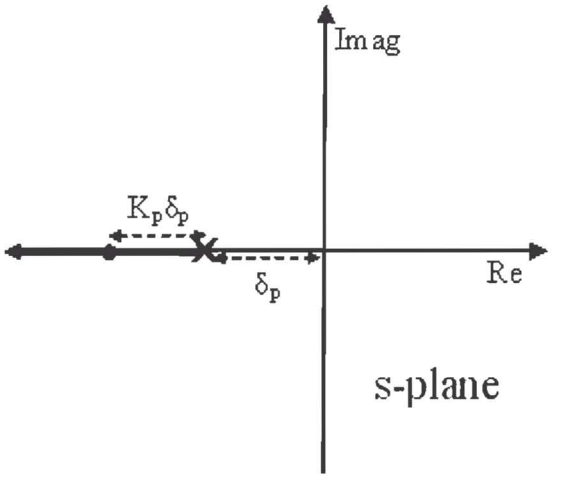

Figure 4.3.7: The Closed Loop Phase Pole Positions for Increasing Gain. *The phase measurement system forms a single pole system in closed loop. The pole moves along the negative real axis towards negative infinity for increasing gain. This makes the system respond faster without increasing the instability on the system.*

From the closed loop phase response root locus diagram it can be seen that, as with the magnitude response, the open loop response is initially determined by δ_p. However, because the simplified phase response consists only of a single pole on the real axis, the closed loop poles will also be on the real axis at a position proportional to K_p. The closed loop response will therefore remain first order with the response time decreasing with an increase in gain. The closed loop gain can be calculated similarly to the magnitude closed loop gain using Equation 4.36 and the final value theorem.

$$\begin{aligned} \textit{Closed Loop Gain} &= K_{CLp} = \lim_{s\to 0}\left(s\left(H_p\left(s\right)\right)\frac{1}{s}\right) \\ &= \lim_{s\to 0}\left(\frac{K_p\delta_p}{s+\delta_p+K_p\delta_p}\right) \\ &= \frac{K_p}{1+K_p} \end{aligned} \tag{4.38}$$

Again the control model was tested using a basic linear feedback loop. Various step tests were done with varying gain to determine the accuracy of the closed loop model.

The theoretical response is once again compared to actual data except this time the phase

is used as the feedback parameter. The $G_p(s)$ of the system includes the VCO and tuning fork crystal as well as the phase detector. As with the magnitude response the gain across $G_p(s)$ is assumed to be unity, with the gains of the VCO, tuning fork crystal and phase detector incorporated in K_p. The phase response through resonance is not a peak like the magnitude response, and thus the problems incorporated with holding the system at resonance do not exist when phase is used as the measurand. The graph in Figure 4.3.8 is the open loop response for when the operating frequency is stepped to the resonant frequency. Again the resonant frequency was measured as $f_0 = 32765.273Hz$ with $Q_{\frac{1}{2}} = 41475$ and $Q_{\sqrt{3}} = 72012$.

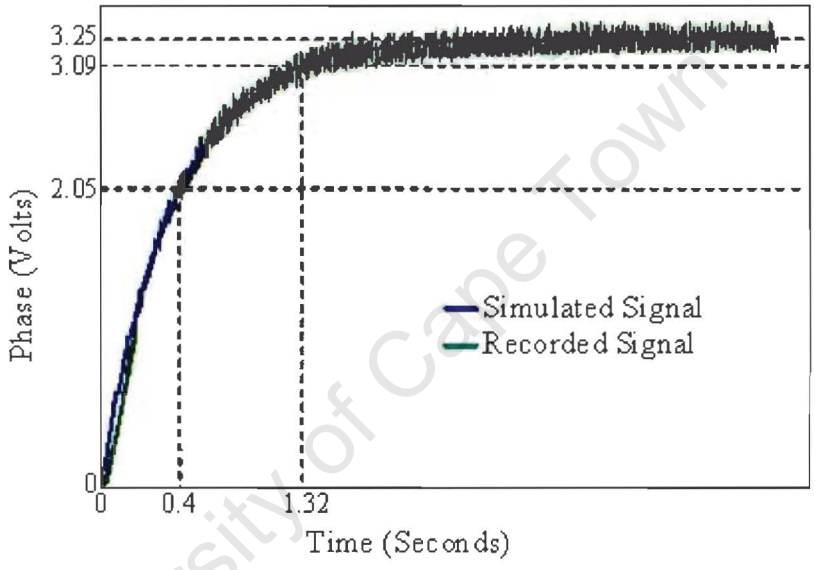

Figure 4.3.8: The Open Loop Phase Response (K_p= 3.25). *As the settling frequency is at the damped resonant frequency there will be no oscillation in the response. Similarly to the magnitude responses the measured gain was combined with the measured characterisitcs of the tuning fork crystal to develop the simulated response.*

In the graph in Figure 4.3.8 as well as Figure 4.3.9-4.3.12 the phase is represented by the voltage output of the phase detector. Using the $Q_{\sqrt{3}}$ value and the decay rate adjustment factor, the open loop time constant can be calculated as $\delta = 2.482s$. This means that the response should reach the 63% of its final value after time $\frac{1}{\delta} = 0.403s$ which compares well to value recorded in the above graph. Following basic first order response theory the response should also then reach within 5% of its final value after time $3\left(\frac{1}{\delta}\right) = 1.209s$ which also compares well with the recorded data. If the system described above is put into a closed loop, its theoretical

response can be calculated using Equation 4.37 with $K_p = 3.25$. The closed loop pole is given below as:

$$Closed\ Loop\ Poles = \phi_p = -2.482 - (2.482)(3.25) = -10.55$$

Therefore the closed loop response should reach 63% of its final value after 0.095 seconds and be within 5% of its final value after 0.285 seconds. The closed loop gain can be calculated from Equation 4.38 as 0.764. Again a linearisation method was used on the phase response in order to simulate the system in linear feedback. The theoretical and actual responses are plotted in Figure 4.3.9 for the closed loop response for $K_p = 3.25$.

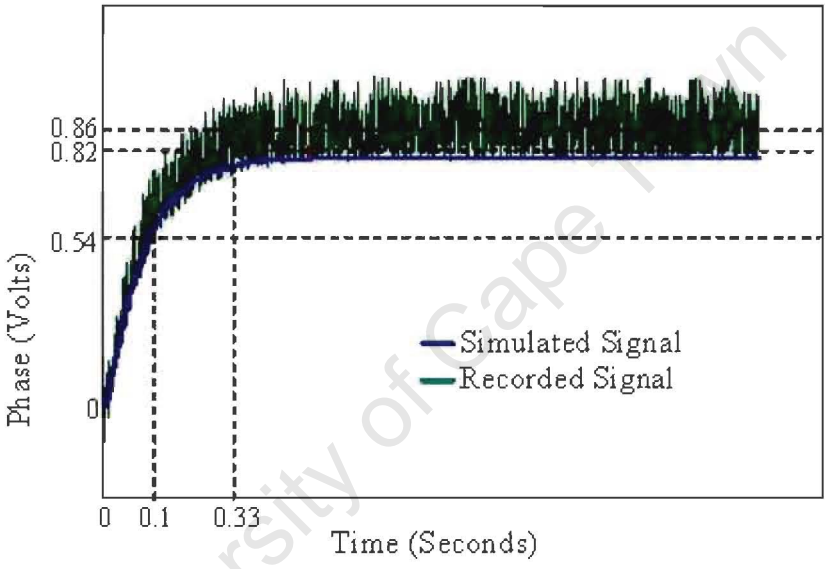

Figure 4.3.9: The Closed Loop Simulated and Recorded Phase Responses (K_p= 3.25). *Once again the simulated signal follows the recorded signal fairly closely with the discrepancies probably due to incorrect measurement and the linearisation used to simulate the signal.*

It is clear from the plot in Figure 4.3.9 that the theoretical response does track the actual response quite closely. The errors between the two responses can again be attributed to both the linearisation process and simple measurement errors due to the rather noisy measured phase signal.

More step tests were done with increasing gain to see if the model continues to track the actual response accurately.

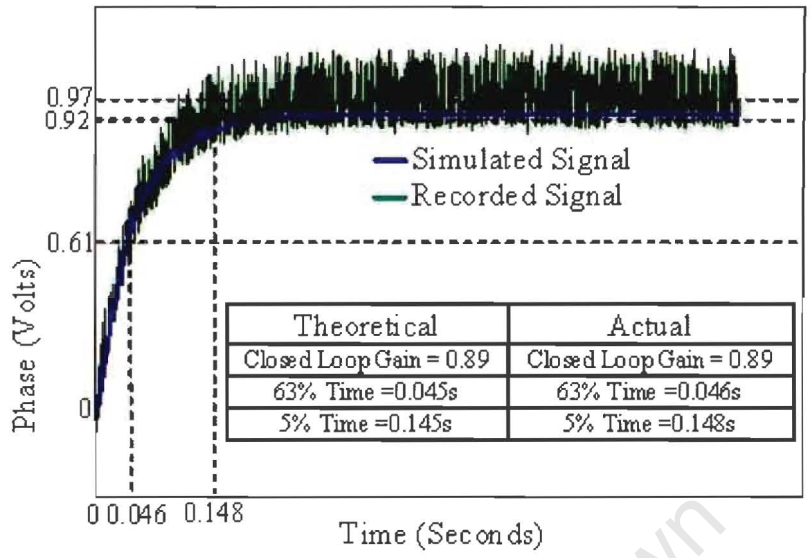

Figure 4.3.10: Closed Loop Theoretical and Recorded Phase Response (K_p= 8).

The system operating characteristics for the theoretical and actual responses are include in the table.

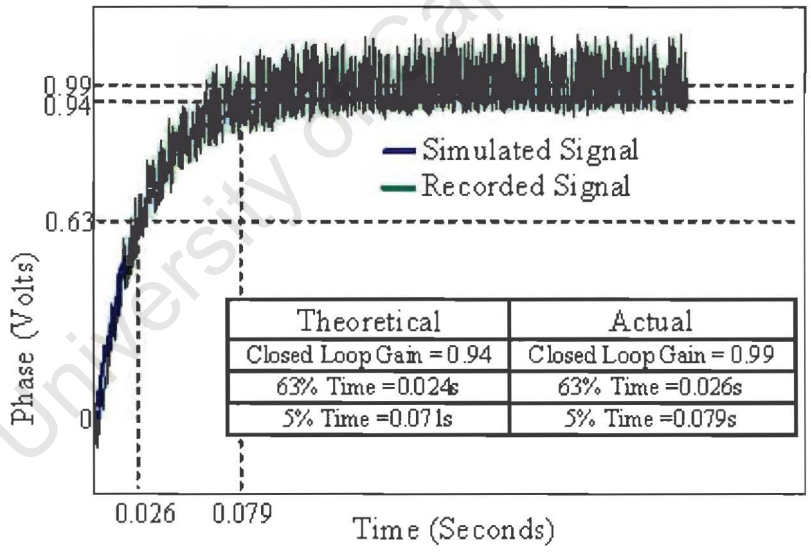

Figure 4.3.11: Closed Loop Theoretical and Recorded Phase Response (K_p= 16).

The system operating characteristics for the theoretical and actual responses are include in the table.

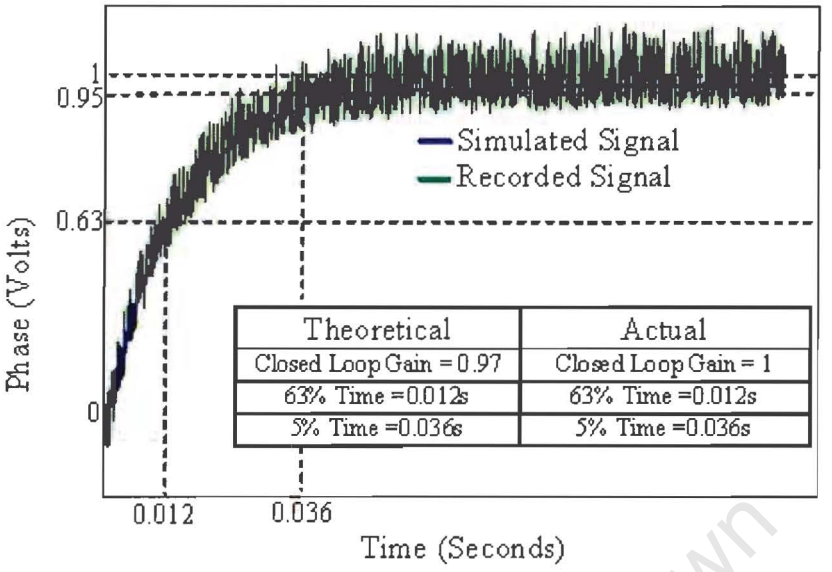

Figure 4.3.12: Closed Loop Theoretical and Recorded Phase Response (K_p= 32).

The system operating characteristics for the theoretical and actual responses are include in the table.

From the tests it is obvious that the model does give a good idea of the phase response even for changing gain values. The errors in the values can be attributed to the factors mentioned previously, such as measurement error and the linearisation of the curve. From the above results the initial model of the system can be considered to be accurate. For increasing gain the system remains first order with only the speed of the response increasing. Now that the control models for the operation of the tuning fork crystal have been developed, their proficiency as displacement sensors in a force feedback system can begin to be explored.

Chapter 5

Applying the Force Feedback Effect

Given that the operation of the tuning fork is fairly well understood, the next step is using the fork as the displacement sensor in a force feedback system. The brief introduction in Chapter 1 outlined the basics behind the force feedback method. The system involves fixing a suspended mass at a certain point and then monitoring how much force is required to keep the mass still. Up till now, all the focus has been on developing the tuning fork as a displacement sensor so that it can be used to monitor the position of the mass. The benefits of using the tuning fork are its extremely good sensitivity and relatively small size. Both the size of the mass spring system and the force transducer must therefore be kept to a minimum, reducing the size of the total system.

There are many ways of setting up the mass spring system and incorporating the force transducer. Most of the systems can provide excellent mechanical sensitivity and good force response, but are all quite big and bulky. The best solution would be to incorporate the mass-spring system and the force transducer into one device. The one way this can be accomplished is using suspended piezoelectric transducers. Different shaped devices can be suspended in different positions so that their mechanical characteristics behave as a suspended mass spring system. The piezoelectric devices are then positioned very closely to the tuning fork as seen in Figure 5.1. Using the displacement reading from the tuning fork the displacement between the suspended piezoelectric device and the tuning fork can be accurately measured. By applying a varying DC voltage to the piezoelectric devices, the displacement between the device and the fork can be regulated, and the force feedback effect can be generated. Bimorph beam and disc

type piezoelectric transducers are used as they provide a high electromagnetic coupling, and do not need to be operated with large voltages to produce the required force. In order to determine the characteristics of the equivalent suspended mass spring system formed by the piezoelectric device, it is important to have a good mechanical model for each piezoelectric device and their various suspension arrangements.

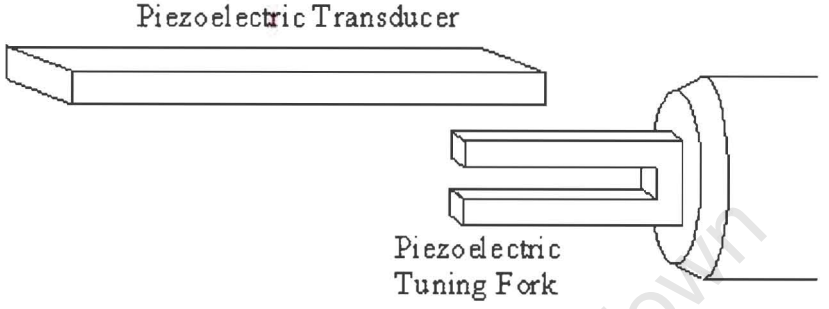

Figure 5.1: The Piezoelectric Transducer Located in Close Proximity to the Tuning Fork. *The small displacement between the tuning fork and transducer is measured. The voltage applied to the transducer is then altered to keep the distance between the transducer and tuning fork constant.*

5.1 Piezoelectric Force Transducers

5.1.1 Piezoelectric Bimorphs

A piezoelectric bimorph, as the name implies, consists of two flat strips of piezoelectric material joined together along their flat sides via a central joining piece[42]. Electrodes are placed along the lengths of the strips so that when a voltage is applied across the electrodes one strip contracts whilst the other expands. This causes a uniform strain, proportional to the piezoelectric constant, in the material. This uniform strain will for a fixed beam produce a stress in the material which will also be uniform throughout each of the strips. For a free beam or a cantilever this stress will produce a uniform moment within the beam. According to the theories of Timshenko in [42] this internal moment will produce an external moment that will bend the beam. The basic structure of the beam is shown in Figure 5.1.1.

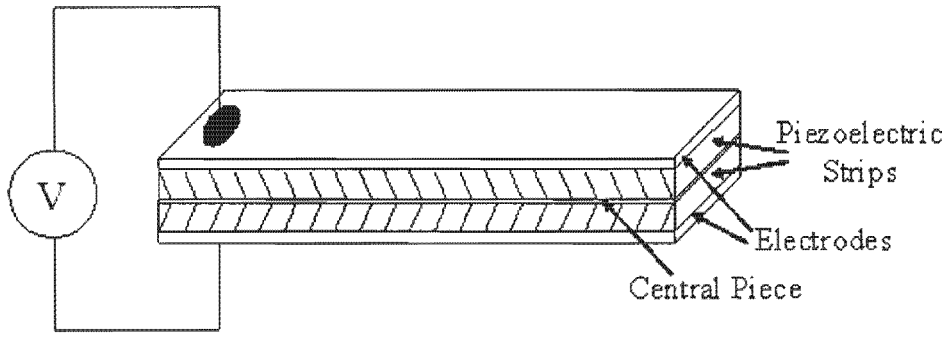

Figure 5.1.1: Piezoelectric Bimorph Driven by an External Voltage Source. *Two strips of piezoelectric material are bonded to a central joining piece. When a voltage is applied across the electrodes one of the piezoelectric strips contracts whilst the other expands, which forces the whole bimorph to bend.*

The piezoelectric bimorphs used were standard items available from many electronics stockists and used in many applications. The beams were measured to be $15mm$ long, $0.6mm$ high and $1.5mm$ wide. Both the Youngs modulus and density of the piezoelectric beam were quoted in [43] as $E = 5 * 10^{10}\ Pa$ and $\rho = 7700\ Kg/m^3$ respectively.

5.1.1.1 Modelling the Piezoelectric Bimorph Beam

Initially the piezoelectric effect of the beam is ignored and only the mechanical characteristics are considered. The beam forms the suspension system for the seismometer, so it is important that the characteristics are well defined. Firstly, the situation where the beam is fixed at one end, forming a cantilever or fixed-free beam, is considered. The mechanics of this system were well defined in Chapter 3 when the model of the piezoelectric tuning fork was developed. The case when both ends are fixed, or fixed-fixed beam, is also considered using the same basic equation as the cantilever. The basic model for the mode shape of the beam was given by Equation 3.27 as:

$$Y(x) = A'(\cos\lambda x + \cosh\lambda x) + B'(\cos\lambda x - \cosh\lambda x) + C'(\sin\lambda x + \sinh\lambda x) + D'(\sin\lambda x - \sinh\lambda x)$$

This equation is then solved for the boundary conditions of the two suspension situations. As mentioned before, the cantilever or fixed free beam is considered first.

5.1.1.1.1 Cantilever Equation 3.27 was solved in Chapter 3 using the boundary conditions of the cantilever. At the fixed end the deflection and the slope will be zero and at the free end the moment and shear will be zero. These boundary conditions are put into the mode equation which is then reduced to form the general solution for the resonant frequencies of the beam. The first resonant mode described in Chapter 3 is given by Equation 3.32

$$\omega_o = \left(\frac{1.875}{l}\right)^2 \sqrt{\frac{EI}{\rho A}}$$

where l is the length, E is the Young's modulus, A is the area of the beam and ρ is the density. The second moment of inertia represented by I is defined for a beam as $I = \frac{BD^3}{12}$[26], where B is the breath or width of the beam and D is the depth or height. Substituting this value back into equation 3.32 leads to the following equation for the first resonant frequency of the beam.

$$f_o = (1.015)\left(\frac{D}{2\pi\,(l)^2}\right)\sqrt{\frac{E}{\rho}} \tag{5.1}$$

Substituting the measured values for the piezoelectric bimorph into Equation 5.1 gives the theoretical resonant frequency of the beam clamped at its very tip as $f_o = 1096Hz$. The spring constant for the beam can now be ascertained, using the equivalent springs method described in Chapter 3. The spring constant, k, can be defined by considering how much the free end of the beam would deflect for a given force. If once again the second moment of inertia for a beam shape is considered it leads to:

$$k = 0.25EB\left(\frac{D}{l}\right)^3 \tag{5.2}$$

In order to increase the sensitivity of the suspension system formed by the cantilever to ground displacement, a mass can be added. If the mass is added at the tip of the cantilever, the new resonant frequency can be calculated by using the effective cantilever mass equation derived in Chapter 3,

$$\omega_o = \sqrt{\frac{k}{0.2427m_c + m_{add}}} \tag{5.3}$$

where m_c is the cantilever mass and m_{add} is the added mass at the tip of the cantilever.

The cantilever mass can be calculated using the dimensions of the beam and its density so that $m_c = \rho(lDB)$. This gives a total mass of $104mg$ and an effective mass of $25mg$ for the cantilever clamped on the very end of the beam. Equation 5.3 shows that any added mass will drop the resonant frequency of the whole system, and considering the small effective mass it would not take much mass to reduce the resonant frequency considerably.

In order to compare this value against real data a real bimorph had to be used. As this beam could not be clamped effectively on its extreme end, a spot $3mm$ from one end was chosen. The same circuit that was used to measure the behaviour of the tuning fork was now used to measure the characteristics of the piezoelectric bimorph cantilever. The package capacitance was eliminated by driving a capacitor with the inverse drive signal in parallel with the cantilever. The output current was once again converted into a voltage using the simple op-amp circuit in Figure 3.3.4.

The measured resonant frequency of the cantilever was $f_{o(m)} = 1670Hz$ which is very close to the theoretical resonant frequency for the new length calculated as $f_{o(Th)} = 1715Hz$. The Q-factor was measured using the full width at half the maximum value, and was calculated to be equal to 50. The mass-spring damping time constant τ for the system can then be calculated as $\tau = \sqrt{3}\left(\frac{Q}{\omega_o}\right) = 0.00825s$. Although the results between the actual and theoretical tests were fairly close, the model was tested further by adding a 0.7 gram mass to the end of the cantilever and then doing the measurements again. Theoretically the added mass should drop the resonant frequency to $f_{o(Th)} = 287Hz$. The measured resonant frequency was $f_{o(m)} = 258Hz$ which is again close to the theoretical value. The new Q-factor for the system with the added mass is 7.58, giving a new damping time constant of $\tau = 0.0081s$. The close comparison between the theoretical and actual measurement values indicates that the model is a fairly good representation of the actual piezoelectric bimorph in a cantilever configuration. The discrepancy in the values can easily be explained by errors in the measurement of the dimensions and fixture of the beam, and inaccurate weighing of the added mass.

5.1.1.1.2 Fixed End or Fixed-Fixed Beam By extending the simple beam theory the situation where both ends of the beam are clamped can also be considered. As both ends of the beam are kept still, the point of maximum deflection will be in the middle of the beam.

The resonant frequency can be determined by solving Equation 3.27 using the new boundary conditions. The boundary conditions at both ends will be the same as the fixed end of the cantilever. The deflection and the slope will both be zero at both ends, which gives rise to the following boundary conditions.

$$\begin{aligned} Y(0) &= 0; \qquad & Y(l) &= 0 \\ \acute{Y}(0) &= 0; \qquad & \acute{Y}(l) &= 0 \end{aligned}$$

where l is once again the length of the beam. Similarly to the cantilever, these boundary conditions can be substituted back into Equation 3.27 to obtain the conditions $A' = C' = 0$ and the following equations:

$$\begin{aligned} Y(l) &= B'(\cos\lambda l - \cosh\lambda l) + D'(\sin\lambda l - \sinh\lambda l) = 0 \\ \acute{Y}(l) &= B'(-\sin\lambda l - \sinh\lambda l) + D'(\cos\lambda l - \cosh\lambda l) = 0 \end{aligned}$$

These equations can be combined simultaneously to form:

$$\cos^2\lambda l - 2\cos\lambda l\cosh\lambda l + \cosh^2\lambda l + \sin^2\lambda l - \sinh^2\lambda l = 0 \tag{5.4}$$

Using the identities from [44], $\cos^2 x + \sin^2 x = 1$ and $\cosh^2 x - \sinh^2 x = 1$, Equation 5.4 can be simplified to give the following equation:

$$\cos\lambda l\cosh\lambda l = 1 \tag{5.5}$$

Equation 5.5 was solved in [28] to give the first two values of λl of the fixed-fixed beam as 4.73 and 7.85. These values can now be used with the Equation 3.32 derived in Chapter 3 to determine the resonant frequency. Once again the second moment of inertia for a beam is used in the solution which is given in the equation below,

$$f_o = (6.46)\left(\frac{D}{2\pi(l)^2}\right)\sqrt{\frac{E}{\rho}} \tag{5.6}$$

where once again D is the depth or height of the beam, E is the beam's Young's modulus and ρ is the density of the beam. The effective mass of the built-in beam, which has both its ends fixed, acting at a point at the centre of the beam can be calculated using the maximum deflection of the beam. For a beam with both ends fixed the maximum deflection is given as [26]:

$$y = \frac{Fl^3}{192EI} \tag{5.7}$$

From basic physics the spring constant or compliance is defined as,

$$k = \left|\frac{F}{y}\right| \tag{5.8}$$

which gives the effective spring constant of the built in beam as:

$$k = 192\frac{EI}{l^3} \tag{5.9}$$

In order to determine the effective mass of a built in beam Equation 5.9 is re-arranged to form,

$$EI = \frac{kl^3}{192} \tag{5.10}$$

and substituted into Equation 3.32 along with the λl value calculated earlier.

$$\omega_o = \left(\frac{4.73}{l}\right)^2 \sqrt{\frac{kl^3}{192\rho A}} = \sqrt{\frac{\left(\frac{4.73}{l}\right)^4 kl^3}{192\rho A}} = \sqrt{\frac{(4.73)^4 k}{192\rho Al}} \tag{5.11}$$

As ρAl will equal the total mass of the cantilever m_c, Equation 5.11 can be rewritten as:

$$\omega_o = \sqrt{\frac{k}{0.3836 m_c}} \tag{5.12}$$

Equation 5.12 can be equated to the substitution equation in Chapter 1 that gives the general expression for the frequency of the fundamental mode of the mass spring system as $\omega_o = \sqrt{\frac{k}{m}}$. This gives the effective mass, in the mass spring model of the fixed-fixed beam as:

$$m_{eff} = 0.3836 m_c \tag{5.13}$$

If the piezoelectric bimorph is set up with both its ends fixed the suspension system of the seismometer will have the mass spring characteristics described above. The mechanical sensitivity of the suspension system can be increased by adding mass to the system. This is most effectively done if the mass is added to the centre point of the beam. This increase in sensitivity will also change the resonant frequency of the beam. Similarly to the cantilever, this change in resonant frequency is governed by the equivalent mass spring system characteristics in the equation shown below:

$$\omega_o = \sqrt{\frac{k}{0.3836m_c + m_{add}}} \tag{5.14}$$

Once again the theoretical model is compared to a real piezoelectric bimorph. The bimorph was glued at both ends onto a metallic washer. The same measurement circuit was used to eliminate the package capacitance and to convert the output current into a measurement voltage. The effective length between the two glued in ends was measured at $13mm$. This would give a theoretical resonant frequency of $f_{o(Th)} = 9303Hz$. The measured resonant frequency was $f_{o(m)} = 9460Hz$ which is very close to the theoretical value. The Q-factor for the full width half maximum was measured as 54.6. This gives a mass spring timing constant of $\tau = \sqrt{3}\frac{Q}{\omega_o} = 0.0016s$. In order to double check the model, a mass of $0.7g$ was added in the centre of the beam. This added mass should theoretically reduce the resonant frequency to $f_{o(Th)} = 2018Hz$. The accurate measurement of the response of the beam became more difficult when the mass was added. The resonant frequency was measured as $f_{o(m)} = 2736Hz$ which is reasonably close to the theoretical frequency. The Q-factor was measured as 83.6, giving a mass spring timing constant of $\tau = 0.0084s$. The errors between the theoretical response and the actual response can also be attributed both to measurement difficulties and inaccurate measurement of the bimorph size, as well as errors in both the mass measurement and its placement at the centre of the beam.

From the results from both the cantilever arrangement and the fixed-fixed beam, it is clear that the models are a fairly accurate representation of the suspension system formed by the piezoelectric bimorphs. These characteristics can now be used to determine the mechanical sensitivity of the suspension system as well as its speed of response. The mass spring time constant of the system remains fairly constant for most of the configurations, as the speed of

response is set by overall shape of the beam and the internal characteristics of the piezoelectric materials. However when the resonant frequency is high enough, this can reduce the mechanical damping time constant as in the case for the unloaded fixed-end beam.

5.1.2 Circular Piezoelectric Diaphragms

Circular piezoelectric diaphragms are made by many people in many different sizes. They are usually used as sound components in a variety of applications. They consist of a circular slab of piezoelectric material with electrodes attached to each side. One of the electrodes is bonded to a circular metal plate. When a voltage is applied across the electrodes the piezoelectric slab either expands or contracts radially due to the piezoelectric effect. This causes the whole system to bend into the centre point. For an alternating voltage the system will vibrate like a speaker cone, and if driven at audible frequencies it will produce audible signals. A basic drawing of the device appears in Figure 5.1.2.

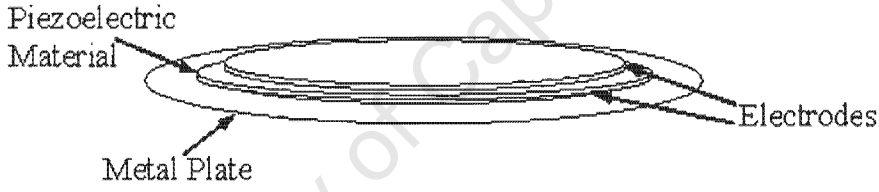

Figure 5.1.2: The Circular Piezoelectric Diaphragm. *A single circular piece of piezoelectric material is bonded between two electrodes. One of the electrodes is subsequently bonded to a metal plate. When a voltage is applied between the upper electrode and the metal plate, the contraction or expansion of the piezoelectric material bends the diaphragm at its centre point.*

Modelling of piezoelectric diaphragms is a difficult task as they consist of different materials besides the actual piezoelectric slab. Unlike the piezoelectric bimorphs, the other materials are present in a much higher relative quantity to the piezoelectric material, which means that they will definitely have a substantial effect on the motion of the diaphragm. Some idea of the properties of the system can be ascertained by considering the diaphragm as a uniform material and averaging the material properties. A similar approach to the bimorph can then be used to model the behaviour. The diaphragm would be used only with its edge clamped so that the displacement sensor can be positioned below the centre of the diaphragm. The centre would be

the point of maximum deflection and thus the most mechanically sensitive point.

The diaphragm can now be modelled as a vibrating disc with its edges fixed. The system model is similar to the one derived earlier for the beam, where the forces on one small component of the beam are considered. In the diaphragm, however, the forces on any segment will be in more than one Cartesian direction. Circular plates are often more simply modelled using polar coordinates as opposed to rectangular coordinates. For the beam the speeds of the longitudinal waves were governed by the ratio between Young's modulus and density so that $C_L = \sqrt{\frac{E}{\rho}}$[45]. In the plate, however, there will be a lateral expansion to accompany the longitudinal vibration, which will be much more pronounced than that of the beam. This adds to the stiffness of the material which means that the correct expression for the velocity is $C_L = \sqrt{\frac{E}{\rho(1-\nu^2)}}$[45] where ν is the Poisson's ratio of the of the material, which is usually about 0.3 for most materials. The general differential equation governing the flexural or bending waves in a flat plate is a subject in many books on elasticity and appears in [46] similarly to the equation below,

$$\frac{\partial^2 \eta}{\partial t^2} + \frac{Eh^2}{12\rho\left(1-\nu^2\right)}\nabla^4 \eta = 0 \tag{5.15}$$

where h is the thickness of the plate and η is the motion of the plate in a specific direction. ∇^4 is an operator linked to the Laplacian or Laplace operator. According to Morse [46], it is used to determine the "bulginess" of the material at different points of the surface. In different coordinate systems the operator takes on different forms, due to the fact that in a flat plate there will be different types of waves. Rectangular coordinates are best for parallel waves, and polar coordinates are best for circular waves. For a flat plate lying in the (x, y) plane undergoing sinusoidal vibration in the z plane, a solution for Equation 5.15 can be given by [45]:

$$Z\left(x, y\right) e^{j\omega t} \tag{5.16}$$

Differentiating the solution in 5.16 and substituting the results back into Equation 5.15 gives the following equation,

$$\nabla^4 Z - \frac{12\rho\left(1-\nu^2\right)\omega^2}{Eh^2} Z = 0 \Longrightarrow \nabla^4 Z - k^4 Z = 0$$

where

$$k^2 = \frac{\sqrt{12}\omega}{h}\sqrt{\frac{\rho(1-\nu^2)}{E}}$$

Bending waves in a plate are dispersive which means that their velocity depends on the frequency [45],

$$v(f) = \frac{\omega}{k} = \sqrt{\frac{\omega h}{\sqrt{12}}\sqrt{\frac{E}{\rho(1-\nu^2)}}}$$

where the frequency of the bending wave is proportional to k^2 giving [45]:

$$\omega = \frac{h}{\sqrt{12}}\sqrt{\frac{E}{\rho(1-\nu^2)}}k^2 \tag{5.17}$$

The values of k that correspond to the normal modes of the vibration depend on the boundary conditions.

For circular plates the Laplacian ∇^2 is expressed in polar coordinates giving $Z(r,\theta)$ as the solution of either $(\nabla^2 + k^2)Z = 0$ or $(\nabla^2 - k^2)Z = 0$ [45][46]. These are solved by a linear combination of ordinary Bessel functions and hyperbolic Bessel functions. k can now be found using the equations and the boundary conditions. For a clamped circular plate where the boundary conditions at the edge are $Z = 0$ and $\frac{\partial Z}{\partial r} = 0$, k is found in [45] as $k = \frac{3.189}{a}$ where a is the outer radius of the circular plate. Substituting this value back into Equation 5.17 gives the resonant frequency of a circular plate clamped at its edge as:

$$f_o = 0.4672\frac{h}{a^2}\sqrt{\frac{E}{\rho(1-\nu^2)}} \tag{5.18}$$

Using the equation for the resonant frequency of a clamped circular disc, the mass spring equivalent can be developed using the same principles as for the tuning fork and bimorph models. Firstly the effective spring constant for the clamped diaphragm must be found using the deflection of the centre point. The effective spring constant can then be substituted into the resonant frequency equation, and the effective mass found using the resonant frequency equation for a mass spring system. The deflection in at the centre point of the suspended

diaphragm will be the maximum deflection and is given as[47][48][49],

$$z = \frac{3\left(1-\nu^2\right)Fa^2}{4\pi Eh^3} \tag{5.19}$$

where F is an external force, or the gravitational force due to the mass of the diaphragm. The spring constant can now be written as a ratio between the force and the deflection giving:

$$k_{eff} = \frac{4\pi Eh^3}{3\left(1-\nu^2\right)a^2} \tag{5.20}$$

Equation 5.20 can now be re-arranged to give:

$$\frac{E}{(1-\nu^2)} = \frac{3a^2k_{eff}}{4\pi h^3}$$

This can now be substituted back into Equation 5.18 to give a new equation for resonant frequency as:

$$\omega_o = \sqrt{\frac{(2\pi)^2\left(0.4672\right)^2h^2 3a^2k_{eff}}{a^4\rho 4\pi h^3}} = \sqrt{\frac{(25.86)\,k_{eff}}{4\pi\rho a^2h}} \tag{5.21}$$

The mass of the diaphragm will be given by $m_d = \rho\pi a^2h$ enabling the mass spring resonant frequency equation to be written as

$$\omega_o = \sqrt{\frac{k_{eff}}{m_{eff}}}$$

where the effective mass $m_{eff} = 0.155m_d$. Any additional mass added to the diaphragm to improve the mechanical sensitivity can now be simply added to the effective mass of the diaphragm to ascertain the new resonant frequency.

The theoretical model was now compared to data taken from an actual piezoelectric diaphragm. The diaphragm used had an outer diameter of $27mm$ with the diameter of the piezoelectric ceramic measuring $20mm$. The thickness of the metal plate was $0.1mm$ and the thickness of the ceramic was $0.23mm$. The diaphragm was clamped around its outer edge so that the effective vibrating diameter was $25mm$. The piezoelectric diaphragm was then driven by a sinusoidal voltage and the output current was monitored whilst the driving frequency was changed. From the output signals it was clear that the system damping was higher than the for the bimorph beams, and the measurement of resonant frequency and Q factor became quite dif-

ficult. Numerous readings were taken to hopefully get a better idea of the actual characteristics of the system.

Theoretically the resonant frequency of the edge clamped diaphragm should be $f_{o(Th)} = 1597Hz$, which is close to the measured value of $f_{o(m)} = 1524Hz$. The Q factor was measured using the full width at half the maximum value and found to be $Q = 28$, which yields a mass spring time constant of $\tau = \sqrt{3}\frac{Q}{\omega_o} = 0.0051s$. To test if the model remained accurate when additional mass was added at the centre of the diaphragm, the tests were repeated for two masses, one of $0.3g$ and the other of $0.7g$. For the $0.3g$ mass the theoretical resonant frequency is $f_{o(Th)} = 845Hz$ and the measured frequency was $f_{o(m)} = 1140Hz$. The Q-factor was measured as $Q = 21$, giving a mass spring time constant of $\tau = 0.0051s$. For the $0.7g$ mass the theoretical value was $f_{o(Th)} = 603Hz$ and the measured resonant frequency was $f_{o(m)} = 760Hz$. The Q-factor was $Q = 21.6$ yielding a mass spring time constant of $\tau = 0.0078s$.

The results of the comparison between the real and theoretical data for the piezoelectric diaphragm are not as good as those for the bimorph beams, but there are many reasons for this. For the diaphragm many more assumptions were made which would affect the results. The diaphragm is considered as one constant circular plate where in reality the effect of the metal plate would also have to be taken into account. The clamping mechanism also does not fix the edges completely. This results in extra moments being created which would change the model of the diaphragm towards the simply supported case. Also, rotational and radial displacement cannot be ruled out and would also cause errors in measurement. Errors would also creep in when adding the mass due both the measuring of the masses and their placement on the diaphragm. This could be a reason why the results of the mass-added tests are further out then the no mass test. As mentioned previously the actual measurement of the resonant frequency and the Q-factor of the system was difficult as the system was highly damped.

Although not perfectly accurate, the model does give a fairly good idea about how the piezoelectric diaphragm will behave as the suspension system in a seismometer. This model can now be used to calculate the mechanical sensitivity and the bandwidth of the suspension system formed by the edge clamped piezoelectric diaphragm.

5.1.3 Sensitivity of the Suspension Systems

In Chapter 1 the sensitivity of inertial seismometers was discussed. The sensitivity of these systems is based on the characteristics of the suspension system. These suspension systems are modelled as mass spring systems and their sensitivity for different types of ground motion was also derived in Chapter 1. Earlier in this chapter, the mass spring characteristics of various piezoelectric devices suspended in different positions were defined. These piezoelectric devices form both the suspension system for the seismometer, and they provide the force feedback effect. The equations governing the behaviour of the piezoelectric devices can now be combined with the equations for the mechanical sensitivity, to determine the mechanical sensitivity for the system.

The behaviour of the mass spring system forming the suspension system can be defined using the same characteristic variables as before. The mass is represented by the variable m, the spring constant represented by the variable k and the damping constant represented by the variable γ. From Chapter 1 the relative output displacement of the mass of a mass-spring system and the ground for an input ground displacement of amplitude A can be given by,

$$Z(\omega) = \frac{A\omega^2}{\sqrt{(\omega^2 - \omega_o^2)^2 + \left(\frac{\omega}{\tau}\right)^2}}$$

where $\omega_o = \sqrt{\frac{k}{m}}$ is the resonant frequency of the system given by and τ is the damping time constant given by $\tau = \frac{m}{\gamma}$. The output displacement magnitude transfer function for an input acceleration was then developed and written as:

$$H_a(\omega) = \frac{Z(\omega)}{A\omega^2} = \frac{1}{\sqrt{(\omega^2 - \omega_o^2)^2 + \left(\frac{\omega}{\tau}\right)^2}} \tag{5.22}$$

The output displacement is a low-pass filter for input acceleration. Its corner frequency is determined by the resonant frequency of the mass-spring system forming the suspension system, as $f_o = \frac{\omega_o}{2\pi}$. The effective operating region of the system is shown in Figure 5.1.3 on the frequency response of output displacement to input acceleration. The area of effective operation is at frequencies below the resonant frequency, where the output displacement will be roughly

the same for an acceleration of constant amplitude but different frequencies. Operation beyond the corner frequency would prove impossible as the output displacement would soon die out as the frequency is increased. The second order system is also an approximation which begins to fail above the resonant frequency [50]. The system becomes uncontrollable even if the gain were to be increased to compensate for the reduced output displacement.

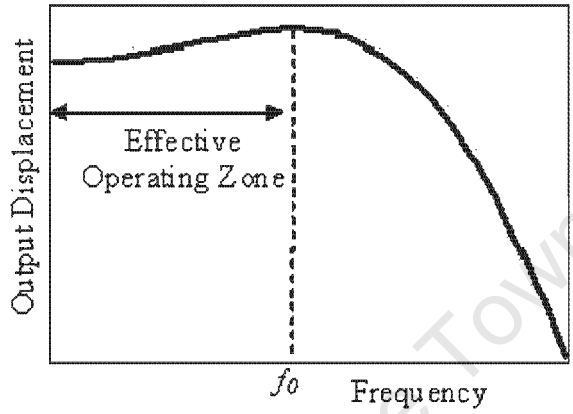

Figure 5.1.3: The Effective Operating Zone of the Seismometer for Input Acceleration. *The low pass frequency response of the output displacment for input acceleration requires that the system be operated below its resonant frequency. The mass-spring model also becomes more inaccurate for frequencies higher than* f_o.

The sensitivity of the output displacement to an input acceleration can be estimated by determining the value of the output displacement at zero frequency. For an input acceleration of A the output displacement at zero frequency can be worked out using Equation 5.22 as:

$$Z = A\frac{m}{k} \tag{5.23}$$

From Equation 5.23 the sensitivity of the output displacement can be maximised either by decreasing the effective spring constant or increasing the mass of the suspension system. For higher damped systems such as the suspended piezoelectric diaphragms, the average sensitivity of the devices for frequencies well below their resonant frequencies can now be estimated using the characteristics of the suspension system. Below is a table showing the mass spring characteristics and the mechanical sensitivities of the three different piezoelectric set ups.

	k	m_e	f_o	*Sensitivity*
Cantilever Bimorph	2.344 kN/m	20.18 $\times$ 10^{-6} kg	1715 Hz	8.6 $\times$ 10^{-9} $m/m.s^{-2}$
Fixed – Fixed Bimorph	117.98 kN/m	34.52 $\times$ 10^{-6} kg	9303 Hz	0.293 $\times$ 10^{-9} $m/m.s^{-2}$
Fixed Edged Diaphragm	11.784 kN/m	117 $\times$ 10^{-6} kg	1597 Hz	9.93 $\times$ 10^{-9} $m/m.s^{-2}$

From the above table the relationship between the mass spring characteristics and the sensitivity of the output displacement to input acceleration is made clear. The cantilever bimorph and the diaphragm are very similar both in terms of sensitivity and their resonant frequency. The fixed-fixed bimorph is much less sensitive but has a much higher resonant frequency. In order to improve the sensitivity of the systems, either the effective spring constant could be decreased or the mass could be increased. The spring constants are determined by the internal structure of the devices and the way they are positioned, and are thus very difficult to change. Mass, however, can simply be altered by adding small weights to the suspension systems. From earlier in the chapter it is already known that the addition of mass will shift the resonant frequency downward. Therefore the link between the resonant frequency and the sensitivity becomes critical in determining the best set up of the suspension system. If the resonant frequency of the three devices is fixed at 200 Hz the new sensitivities are given in the new table below:

	k	m_{Total}	*Sensitivity*
Cantilever Bimorph	2.344 kN/m	1.48 $\times$ 10^{-3} kg	631$\times$ 10^{-9} $m/m.s^{-2}$
Fixed – Fixed Bimorph	117.98 kN/m	74.72 $\times$ 10^{-3} kg	633 $\times$ 10^{-9} $m/m.s^{-2}$
Fixed Edged Diaphragm	11.784 kN/m	7.46 $\times$ 10^{-3} kg	633 $\times$ 10^{-9} $m/m.s^{-2}$

As all the suspension system models are based on the mass spring system, if the resonant frequencies are all set to the same frequency then the sensitivities must also be the same as they rely on the same two characteristics: the mass and spring constant. From the tables it is clear that the sensitivities of the suspended piezoelectric structures can be improved, by an order of magnitude in the case of the fixed-fixed beam, by simply adding mass to the system. The

damping of the system, which determines the height of the peak at the corner frequency, now also becomes important as the above sensitivity measurements are accurate only for frequencies far below the resonant frequency. Another vital component of determining the sensitivity is determining how far the piezoelectric structures move for a given voltage. For the bimorph the piezoelectric force will be the same for a given voltage for both structures, and the distance moved will be determined by the effective spring constant.

5.2 Approach Tests and the Optimal Operating Point

When approaching a surface the tuning fork will experience a combination of forces. There will be the forces resulting from the build up of interatomic forces into intermolecular forces, which in turn combine to form the total intersurface forces between the tuning fork and the surface. There will also be forces caused by the movement of air in between the surface and the tuning fork. The two types of forces combine to form the total interaction potential between the tuning fork and the surface. The size and direction of these forces is dependent on many different factors. The shape and type of the material making up the approached surface as well as the interacting surface area all contribute to the size and direction of the forces. Also due to the various combinations of forces, both the size and direction of the forces vary as the tuning fork gets closer to the surface. By studying how all these forces combine a good idea of the point at which a change in displacement will bring about the biggest change in force can be determined.

To theoretically determine the exact size of all the component forces is a very difficult task. It involves exact characterisation of the material properties of both surfaces, as well as the exact shape and orientation of the interacting surfaces to be known. The orientation and effective interacting surface area will be constantly changing as both surfaces change in relation to each other. Theoretical discussions of the interaction between surfaces very quickly involve quantum mechanics and other complex theories. A far simpler and more practical solution is to use a basic intermolecular approach like the Lennard-Jones potential [18][19], and determine the constants experimentally rather than theoretically. The basic intermolecular potentials can easily be combined to give an idea how the forces will change across surfaces of different sizes

and shapes. The change in total force as the displacement between the tuning fork and the surface changes can then be used to determine the best operating point for the system. A number of experimental tests were done to determine the relative effects of size, shape and surface area of the two interacting surfaces on the total force between the tuning fork and the surface. These are presented below.

5.2.1 Test 1 - Large Surface Area

The first test was performed using a flat piezoelectric bimorph suspended at one end in a cantilever configuration. The bimorph was orientated with its flat surface lying parallel along the length of one of the tines of the tuning fork. The bimorph was positioned at different distances away from the tuning fork first by using a positioning system with a micrometer screw thread. Then, different voltages were applied to the piezoelectric bimorph to bring the surfaces even closer together. The displacement of the bimorph as a function of applied voltages was calibrated using a LVDT displacement detection system. The set up of the first test appears in Figure 5.2.1.

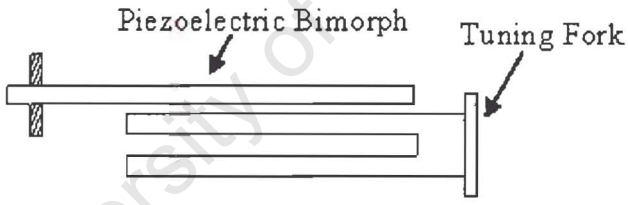

Figure 5.2.1: The Set Up of the First Approach Test. *For this test the contact surface area was maximised by orientating the bimorph along the entire length of the tuning fork crystal.*

The tuning fork crystal was operated continuously at its resonant frequency. The distance between the tuning fork and the piezoelectric bimorph was then altered, and the change in resonant frequency and amplitude of the tuning fork output signal were monitored. The spring force, proportional to the displacement of the fork, between the crystal and the surface can be determined by the change in resonant frequency. The change in magnitude of the arms of the fork at different displacements from the surface can be used to determine the change in the damping factor, which will be proportional to the velocity of the fork arms. Using these

measurements the combined response from both the air effects and the intersurface forces can be determined.

The intermolecular forces between two molecules can be broken up into attractive and repulsive forces. As discussed in Chapter 2 the total interaction potential between two molecules can be theoretically given by the Lennard Jones potential, written in Equation 2.26 in Chapter 2 as:

$$w(r) = 4\epsilon \left[\frac{\sigma^{12}}{r^{12}} - \frac{\sigma^{6}}{r^{6}} \right]$$

where r is the distance between molecules, σ is the distance where the total interaction potential is zero, and ϵ is the maximum attractive interaction potential. All the constants and how they relate to force were explained in Chapter 2. The total interaction potential can now be separated into its attractive and repulsive component:

$$\begin{aligned} w_6(r) &= \frac{-4\epsilon\sigma^6}{r^6} = \frac{-C_6}{r^6} \\ w_{12}(r) &= \frac{4\epsilon\sigma^{12}}{r^{12}} = \frac{C_{12}}{r^{12}} \end{aligned} \tag{5.24}$$

Each of the equations in 5.24 can be substituted into the equation derived for the intermolecular potential combined across two interacting surfaces which was also defined in Chapter 2 as 2.31. This gives the attractive and repulsive interaction potential for surfaces separated by a distance D and a unit interaction surface area as,

$$\begin{aligned} w_6(D) &= \frac{-2\pi C_6 \rho_1 \rho_2}{(n-2)(n-3)(n-4) D^{n-4}} = \frac{-A_6}{12\pi D^2} \\ w_{12}(D) &= \frac{-2\pi C_{12} \rho_1 \rho_2}{(n-2)(n-3)(n-4) D^{n-4}} = \frac{-A_{12}}{360\pi D^8} \end{aligned} \tag{5.25}$$

where A_6 and A_{12} are the Hamaker constants for the attractive and repulsive interactions. The equations in 5.25 can then be combined to form the total interaction potential for two surfaces as,

$$w(D) = -B \left[\frac{\sigma^6}{D^2} - \frac{\sigma^{12}}{30 D^8} \right] \tag{5.26}$$

where B is the combination of the Hamaker constant and other common factors removed from the repulsive and attractive terms. The total interaction force between the two surfaces

can then be given by differentiating Equation 5.26 to give:

$$F(D) = \frac{dw(D)}{dD} = B' \left[\frac{\sigma^6}{2D^3} - \frac{\sigma^{12}}{15D^9} \right] \tag{5.27}$$

B' is a very similar constant to B with only the constants from the differentiation added to it. As mentioned previously both σ and B' will be very difficult to determine theoretically and will be estimated from the experimental measurements.

The forces experienced by the tuning fork due to the passage of air in between the surface and the fork have also been described in detail in Chapter 2. Air effects will produce a change in both the effective stiffness and the resistance of the tuning fork. Once again, developing an accurate theoretical model will be difficult due to the inexact nature of the system. Even the basic idea of the distance dependence changes from model to model. The air effects are better determined empirically rather than by any in depth theoretical study. The model will probably be some kind of combination of the models discussed in Chapter 2, and will have the form:

$$F_a(D) = \frac{C}{D^n} \tag{5.28}$$

where D is the distance between the surfaces and C is a constant determined by the characteristics of the system. Obviously the size of the air effects are inversely distance dependent, with $1 \leq n \leq 3$ from some combination of the air effect models for different conditions. C is dependent on a host of factors, such as size and shape of the interacting surfaces, as well as external factors like the viscosity of the air. By looking at the measurements of the resonant frequency, and the amplitude at different distances, a good idea of the experimental model of the air effects can be determined.

The first test was now completed by recording both the magnitude and the resonant frequency when the piezoelectric bimorph is positioned at various heights above the tuning fork crystal. The height is recorded using the both input voltage to the piezoelectric bimorph, and the position of the micrometer thread. Using the effective mass of one arm of the tuning fork, the change in effective spring constant is calculated from the change in resonant frequency. The results were then compared to the models of the intersurface forces and the forces due to the air effects.

The theoretical intersurface forces are plotted along with the actual measurements in Figure 5.2.2. Looking at change in the effective spring constant as the piezoelectric bimorph approaches the tuning fork, two peaks can be seen. As the bimorph begins to approach the tuning fork, the force due to the air effects begins to reduce the effective spring constant from about $1mm$ away. This continues quite slowly until the tuning fork crystal begins to be affected by the attractive intersurface forces. This effectively increases the spring constant giving the first peak in the distance dependent force response. The air effect forces and the attractive intersurface forces have a similar distance dependence although the attractive intersurface force is much stronger. As they are opposite in direction, the force due to the air has a linearising effect on the attractive force response. This produces an almost linear response to the next peak, after which the repulsive forces are strong enough to reduce the spring constant, and force the resonant frequency response back down. From the graph it is also clear that the air effects also produce a slight shifting of the peaks away from the surface.

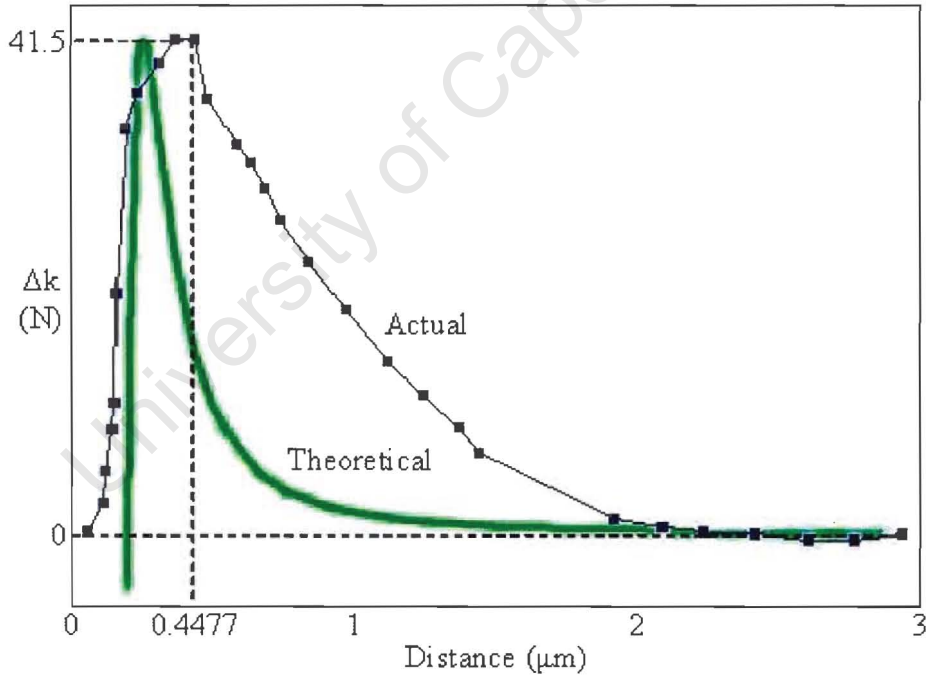

Figure 5.2.2: Theoretical and Actual Force Responses for the Large Surface Area Test. *The attractive force component has been linearised by the air effects. The peak of the response has also moved away from the surface.*

The exact distance dependence of the model was estimated using a breeder genetic algorithm developed by Greene [51]. This method takes a very basic form of the solution with a number of variables, and tries to find exact solutions that best fit the data by manipulating the variables. The solution was formed by subtracting the effects of the repulsive intersurface forces and the air effects, from the attractive intersurface forces, giving the following general equation,

$$F(D) = A\frac{\sigma^x}{D^x} - B\frac{\sigma^y}{D^y} - C\frac{\sigma^z}{D^z} \tag{5.29}$$

where x, y and z are the distance dependences of the various responses and A, B and C are the coefficients determining the forces' relative strengths. Although quite rough, and prone to developing wrong solutions, the breeder genetic algorithm did produce some fairly accurate representations of the response. The breeder genetic algorithm gave the distance dependence of the attractive and repulsive force as about $x = 2.78$ and $y = 8.53$ which is very similar to the theoretical values of 3 and 9. The value for the distance dependence of the air effects was close to that for the attractive force, which also roughly concurs with the theory.

In terms of sensitivity, the distance from the surface at which the tuning fork is most sensitive to a change in distance can be calculated by twice differentiating the equation governing the force response. This equation can then be equated to zero, and the point of maximum rate of force change can be found. From the graphs plotting the response, the greatest change will obviously occur in the repulsive force component before all the motion of the fork is stopped. As the repulsive forces only act very close to the surface, it might be impractical to operate the fork in this region. It might therefore be useful to know where the rate of change is highest before the repulsive region.

By looking at the relationship between the interaction potential and the force developed for the Lennard Jones potential in Chapter 1 it is clear that there will be a peak of rate of force change during the attractive component of the response. Theoretically the rate of force change between two approaching surfaces can be given by the following equation,

$$\frac{d^2F(D)}{d^2D} = \frac{d^2}{d^2D}\left[\frac{\sigma^3}{D^3} - \frac{\sigma^9}{D^9}\right] = 12\frac{\sigma^3}{D^5} - 90\frac{\sigma^9}{D^{11}} \tag{5.30}$$

A more general form of Equation 5.27 has been used to ease the calculation. Equation 5.30 can now be equated to zero to determine the point at which the rate of force change is the highest,

$$\begin{aligned} 12\frac{\sigma^3}{D^5} - 90\frac{\sigma^9}{D^{11}} &= 0 \\ \frac{D^{11}}{D^5} &= \frac{90}{12}\frac{\sigma^9}{\sigma^3} \\ D &= \left(\frac{90}{12}\right)^{\frac{1}{6}}\sigma = 1.4\sigma \end{aligned}$$

The point of maximum force change is therefore at a distance 1.4 times bigger than the zero force distance. It could be more useful to consider the size of the force relative to its maximum positive size at this point of maximum rate of force change. The distance at which the maximum force occurs can be easily calculated using the above method, but using the first derivative instead. This calculation gives the distance at which the maximum force occurs for the theoretical model as 1.2σ. Both these distances can now be substituted back into the initial simplified equation to give the fraction of maximum force at which the maximum rate of force change will occur.

$$\frac{Amplitude\ at\ Maximum\ Rate\ of\ Force\ Change}{Maximum\ Amplitude} = \frac{\frac{\sigma^3}{(1.4\sigma)^3} - \frac{\sigma^9}{(1.4\sigma)^9}}{\frac{\sigma^3}{(1.2\sigma)^3} - \frac{\sigma^9}{(1.2\sigma)^9}} = 0.82$$

This means that the maximum rate of force change for the attractive forces occurs when the force is 0.82, or 82%, of the size that it is at its maximum value. This value does change for different power values in the initial equation, but the value remains around 0.8. Using this property, the value of the maximum rate of force change can be easily worked out by calculating the gradient of the force response at about 80% of its maximum value. The position of maximum rate of force change can be considered the most sensitive point to a change in distance besides the repulsive forces. This value can be used to give the mechanical sensitivity of the tuning fork displacement sensor. As the plotted response is not very smooth and follows the basic shape of the theoretical response, the sensitivity calculations are not very accurate and should

be considered as a general estimate. For the first test the sensitivity works out to be:

$$Sensitivity \simeq 25\ MN/m$$

5.2.2 Test 2 - Reduced Surface Area

The second test was done using a very similar set up to the first test. Once again the piezoelectric bimorph was set up as a cantilever, and orientated with its flat surface lying parallel to one tine of the tuning fork. However in this test the bimorph was placed so that it did not approach the entire length of the fork but rather just the very end. The bimorph was again positioned using the micrometer positioning system as well as voltage applied across the electrodes. The arrangement for the second test appears in Figure 5.2.3.

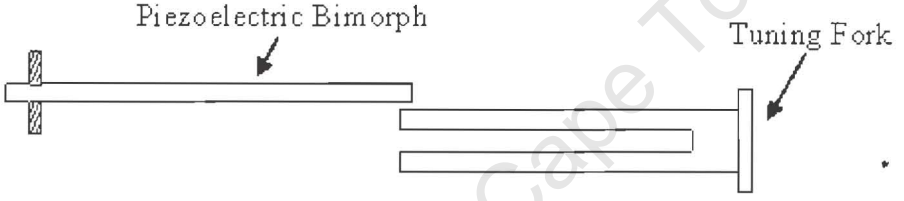

Figure 5.2.3: The Arrangement for the Second Test. *By orientating the bimorph so that just the very tip is close to the tip of the tuning fork the interacting surface area is greatly reduced.*

Once again, the change of resonant frequency and magnitude was monitored by keeping the tuning fork crystal operating at its resonant frequency whilst changing the distance between the bimorph and the fork. The resonant frequency was once again used with the effective mass of one tine, to ascertain the change in effective spring constant as the distance between the bimorph and crystal changes. The magnitude can once again be used to determine the damping factor of the system due to the air effects.

Using the same approach the second test was completed and the results are plotted in Figure 5.2.4. The basic shape of the response is the same but the reduction in surface area of the interacting surfaces has had some noticeable effects. The effect that the movement of air between the surfaces has on the system has been greatly reduced, and the overall strength of the forces between the surfaces has also decreased. As the air motion no longer has such a large effect on the system its linearisation effect on the attractive component of the intersurface

forces is diminished. This will effectively increase the inverse power law of the attractive forces towards the theoretical value. The positive peak of the effective spring force will also be shifted back closer towards the surface.

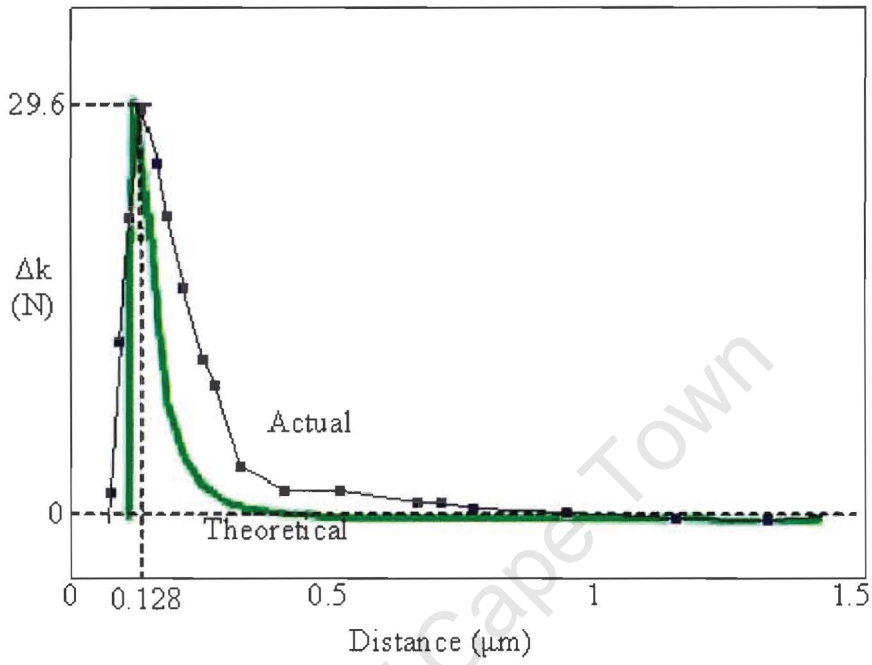

Figure 5.2.4: The Actual and Theoretical Responses for the Reduced Area Test.

The reduction of the air effects limits the linearisation of the intersurface attractive component. The peak of the positive force has also moved closer to the surface.

The sensitivity for the second test was calculated using the gradient of the force response at 80% of its maximum. This should be the most sensitive area on the attractive force component as discussed previously. Due to roughness of the plot the sensitivity calculation was made more difficult, and similarly to the previous test should be considered as an estimate.

$$Sensitivity \simeq 101\ MN/m$$

5.2.3 Test 3 - Approaching with a Tip

To further reduce the air effects a sharp tip was used in the third test to approach the end of one of the tuning fork's tines. A tip was attached to one end of the piezoelectric bimorph whilst the other end was fixed in a cantilever configuration. The tip was then positioned at various

heights above the tine by adjusting the micrometer positioning system and the applied voltage across the bimorph. The same procedure was used in this test to determine the amplitude and the effective change in spring constant. The arrangement of this experiment is shown in Figure 5.2.5.

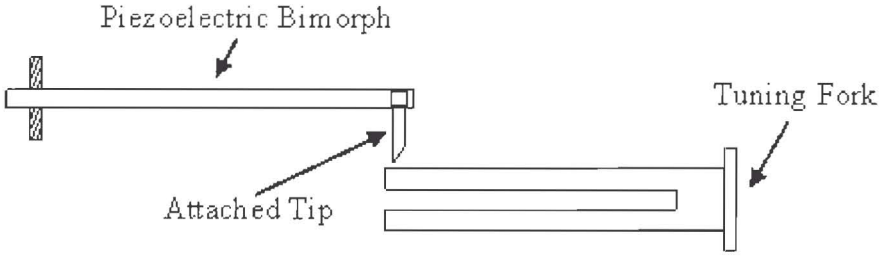

Figure 5.2.5: The Arrangement for the Third Test. *The surface area is further reduced by attaching a point to the end of the bimorph.*

With the surface area so significantly reduced the air effects will almost be zero. However as a tip is now being used, the approach model for two flat surfaces begins to become increasingly inaccurate. The tip was quite roughly cut and sharpened but could probably be better modelled as a small sphere. A model for a spherical tip approaching a surface was developed in [19] and had the following basic shape for the force between the sphere and the surface,

$$F(D) = B'R\left(\frac{\sigma^2}{D^2} - \frac{\sigma^8}{30D^8}\right) \tag{5.31}$$

where once again D is the distance between the spherical tip and a surface, and σ is the distance away from the surface where the total force is zero. B' is the constant containing the Hamaker constant and other common values associated with both the attractive and repulsive terms. R is the radius of the sphere and can for most purposes be lumped with the other constants. This model is quite similar to the two surfaces model but with slightly less strong distance dependence.

The plot for change in effective spring constant as the tip approaches the tuning fork appears in Figure 5.2.6. The further reduction in the surface area of the interaction has all but eliminated the effects that the motion of the air has between the moving surfaces. This reduction in the air effects has moved the positive peak and the zero crossing point closer to the surface.

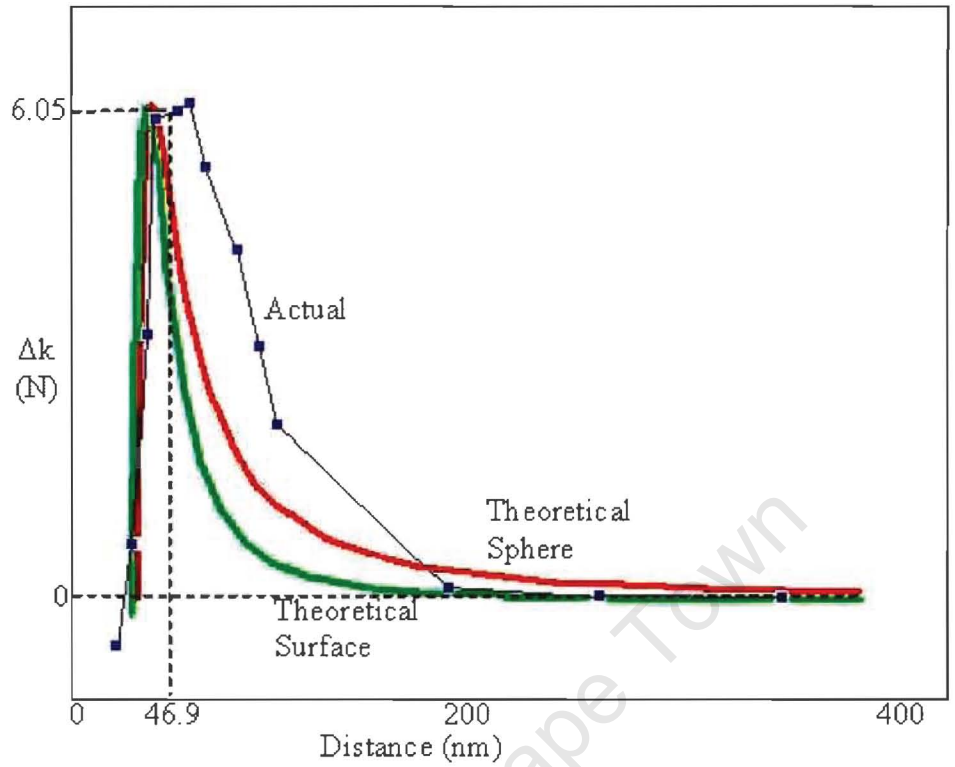

Figure 5.2.6: The Actual and Theoretical Response for the Point Test. *The response falls somewhere in between the theoretical response for a sphere and a surface. With the reduced interacting area the peak of the force has also moved even closer to the surface.*

Both the theoretical response for the intersurface forces between two surfaces and the intersurface forces for a sphere and a surface have been plotted in Figure 5.2.6. From the figure it is clear that the actual response falls somewhere in between both responses as it cuts the theoretical sphere response on the attractive slope but doesn't cut the theoretical surface response. This is probably due to the fact that the tip can neither be modelled as a sphere or as a surface but in reality falls somewhere in between the two. The sensitivity was once again calculated on the attractive component at 80% of the maximum,

$$Sensitivity \simeq 37\ MN/m$$

5.2.4 Test 4 - Approaching from the Top

After looking at the results from the approach tests it was decided to do one more test. So far all the tests had involved approaching only one tine of the fork, from the side. For this test both tines of the fork were approached from the top so that both tines of the fork could be affected at the same time. This should maintain the symmetry of the fork and heighten the Q-factor. The same system was used to position the piezoelectric cantilever tip at different distances from the fork. The same measurement technique was also used. The physical arrangement of the bimorph and the crystal for this test is shown in Figure 5.2.7.

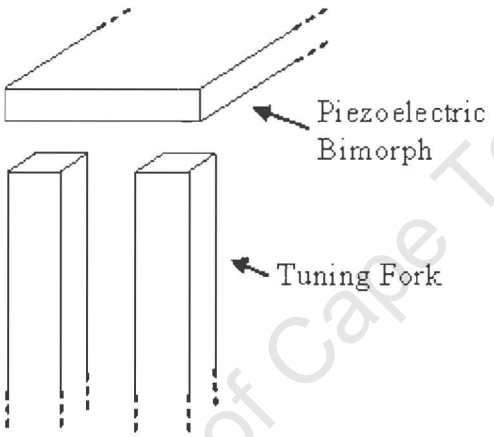

Figure 5.2.7: The Arrangement for the Fourth Test. *The tuning fork was approached from above so that both tines could be affected simultaneously. This should maintain the symmetry within the fork and increase the Q-factor. The tines' motion is now in parallel with the bimorph which will alter both the air effects and the intersurface forces.*

Although not directly impinging in the direction of motion the shear forces between the tuning fork and the piezoelectric bimorph will still affect the operating characteristics of the fork. The forces are now moving in parallel to one another and due to the cantilever action the distance between them will also be changing periodically, albeit on a minuscule level. This parallel movement of the surface will heighten the air effects, as more air now flows between the surfaces. The intersurface forces although now acting perpendicular to the motion should still have a similar effect due to the cantilever motion of the tines of the fork.

Looking at the plot of the response in Figure 5.2.8 it is obvious that the air effects have been increased. The positive peak of the added effective spring force has been pulled much

further away from the surface and the distance dependence of the intersurface forces has also been reduced. The air motion has had a similar linearising effect on the attractive component to that seen in the first large surface area test. This linearisation effect is not as severe as in the first test. This is because although the air effects are not reduced, their shape and distance dependence have been altered, which means they have less effect on the attractive component.

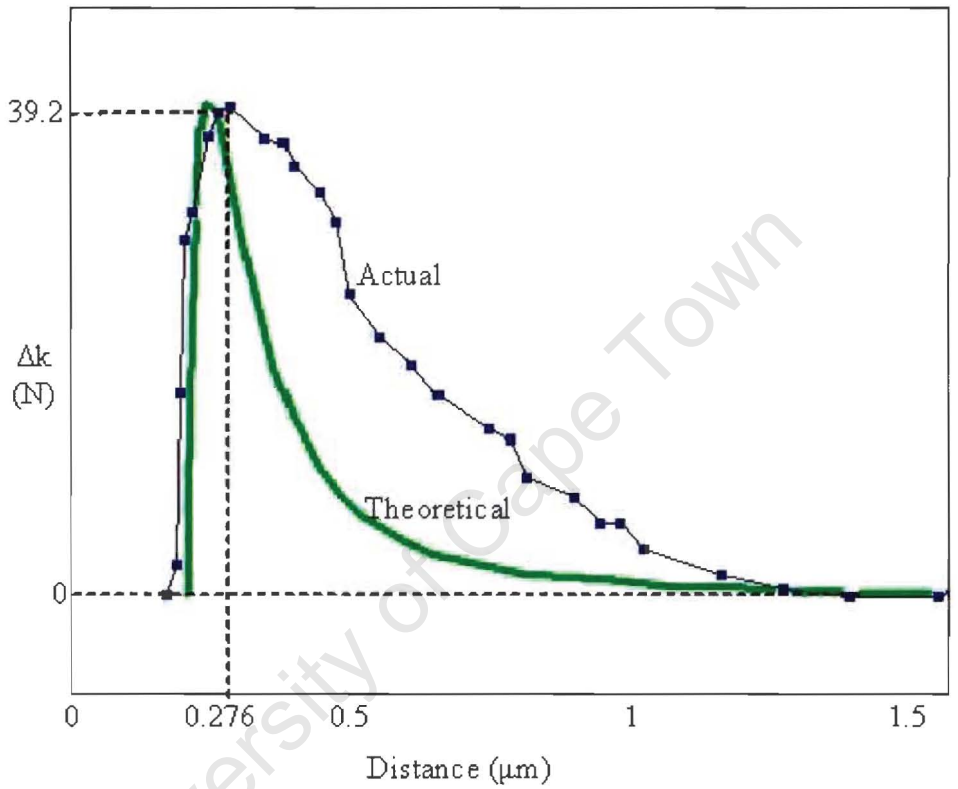

Figure 5.2.8: The Actual and Theoretical Responses for the Top Approach Test.
The increased air effects due to the parallel motion of the tines further linearises the attractive component of the intersurface forces. The peak of the force response has also been pulled further away from the surface making operation on the repulsive slope a possibility.

The sensitivity of the device whilst operating in the attractive force region can be estimated from the gradient at 80% of the maximum force.

$$Sensitivity \simeq 58MN/m$$

As the repulsive forces can now be experienced further away from the surface, and decay less rapidly, the system can be operated in this region more easily. The rate of force change was estimated around the zero force cross over point by calculating the gradient at this region. The sensitivity in this region is estimated as:

$$Alternate\ Sensitivity \simeq 196\ MN/m$$

5.2.5 Using the Approach Tests to Maximise Sensitivity

The information gathered from the approach tests leads directly to the best way to position the components of the system so that maximum sensitivity is achieved. From all the tests it is obvious that if the approaching surface could be positioned close enough to the tuning fork so that it experiences the repulsive forces, the device would be massively sensitive to displacement. Operating in this region will, however, be very difficult. The surface will have to be positioned very carefully and the whole supporting structure will have to be very rigid to prevent the tuning fork hitting the surface and having all its motion stopped. The control system keeping the surface at a fixed distance will also have to be of excellent design to prevent sudden ground motion spikes causing the surface to hit the tuning fork. The only arrangements where this is possible is where the air effects are large enough to pull the entire response away from the surface, making the repulsive region more accessible. Increasing the air effects, however, increases the viscous damping on the system, which decreases the sensitivity as well as making the measurement of the signals more difficult. There is no doubt that ideally to maximise sensitivity the system should be operated in the repulsive force range, but in a practical system the attractive zone should also be considered.

For operation in the attractive region the second test for the reduced surface area proved to be the most sensitive. This is because although the air effects have been reduced, the surface still produces a relatively large force on the tuning fork, as the surface area is still substantial. For the tip, the surface area has been reduced by so much that the attractive forces between the tip and the tuning fork are never very large, so the sensitivity is reduced. For the large surface area a better response could be achieved by approaching the surface in an exactly parallel direction. For an applied voltage the piezoelectric bimorph set up as a cantilever will curve so

different points of the cantilever will be closer to the tuning fork, and the two surfaces will no longer be parallel. As the air effects are different for when tuning fork is approached in different ways, the attractive response is not completely linearised and the sensitivity is increased. The air effects do also have one positive attribute clearly seen in the first test. They pull the positive peak of the attractive force away from the surface, meaning that the highly sensitive repulsive region can be experienced further away where it is easier to operate the system.

5.3 Control System Set Up

Keeping the whole system operating at the desired set points requires two distinct control systems which both take their inputs from the piezoelectric tuning fork. There will be the control system that keeps the fork at a certain specified point in its resonant band and the control system that keeps the piezoelectric transducer at a fixed distance away from the tuning fork. The output measurands of the tuning fork, such as magnitude and phase, are used as the measured inputs for the control systems. The point in the resonant band that the fork operates as well as the fixed distance that the piezoelectric transducer stays from the tuning fork are determined by externally generated set points. All the different outputs from the tuning fork can be used in different combinations in the two control systems with varying ease and accuracy. Two such combinations are considered for this system: the magnitude-phase combination and the phase-resonant frequency combination.

5.3.1 Control Strategies

Two control strategies, each involving two different control systems with their own measured inputs, can be used to operate the system. The first of the strategies involves using the magnitude of the output from the tuning fork crystal to lock the fork at a point in its resonant band by controlling the input frequency to the fork. The displacement between the piezoelectric transducer and the fork is then determined by measuring the phase between the input and output waveforms at the fixed magnitude. The voltage to the piezoelectric transducer is then altered to move the structure, which fixes the displacement at an externally determined set point. The control voltage to the piezoelectric transducer can then be monitored and used as

the output of the force feedback system.

The plot in Figure 5.3.1 shows the basic idea of the control system. From the contact models for the piezoelectric transducer approaching the forks, any change in displacement will change the magnitude of the output and the resonant frequency of the fork. If the fork is locked at a specific magnitude M_1 the change in displacement and the consequent change in the tuning fork characteristics will mean that the operating frequency will shift from f_1 to the frequency where the system with the altered characteristics has the same magnitude f_2. Initially when the system is operating at f_1 the phase between the input voltage and the output signal will be P_1. After the displacement change the phase will move in accordance to the new mass spring characteristics to P_2. This difference in phase can be measured and the control voltage, and thus the distance between the tuning fork and the transducer, can be changed accordingly.

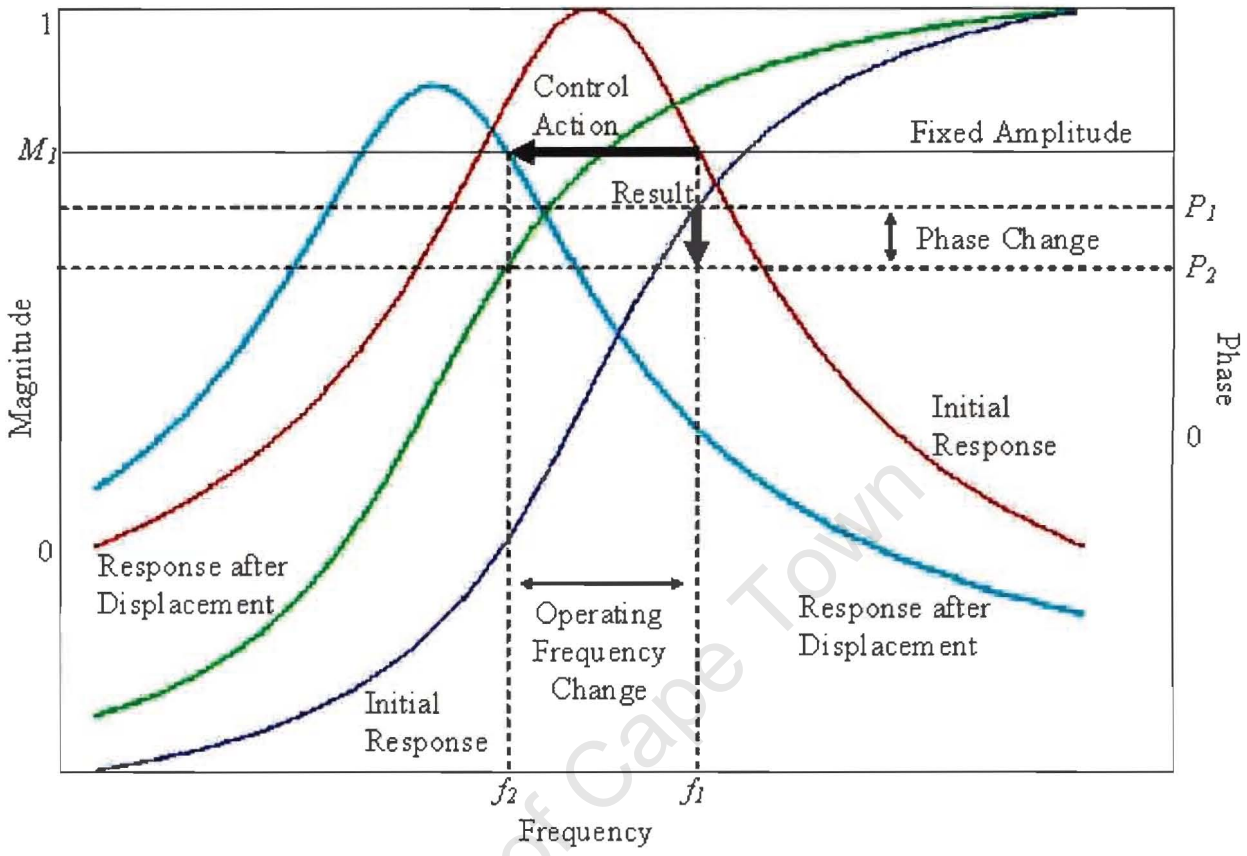

Figure 5.3.1: The Operation of the Magnitude-Phase Control System. *The control system forces the tuning fork crystal to operate at a point where the magnitude is M_1. For a change in displacement the resonant frequency will shift from f_1 to f_2. The magnitude will be maintained at M_1 so the phase will shift from P_1 to P_2. By monitoring the shift in phase the displacement can be fixed at a certain value.*

The second of the two control strategies eliminates the need to use the slower magnitude measurement in favour of using phase and resonant frequency to control the system. This simpler control system appears in Figure 5.3.2. Instead of magnitude, phase is used to determine where in the resonant band the fork is operating. The control system then adjusts the input frequency to the fork, keeping it at a specified point in the resonant band. By locking the operating point of the fork at its resonant frequency, and monitoring the control signal that determines the frequency of the input signal, a value for the resonant frequency can be calculated. This value for resonant frequency can then be used to determine how far the tuning fork

is from the transducer and control the voltage to the transducer accordingly.

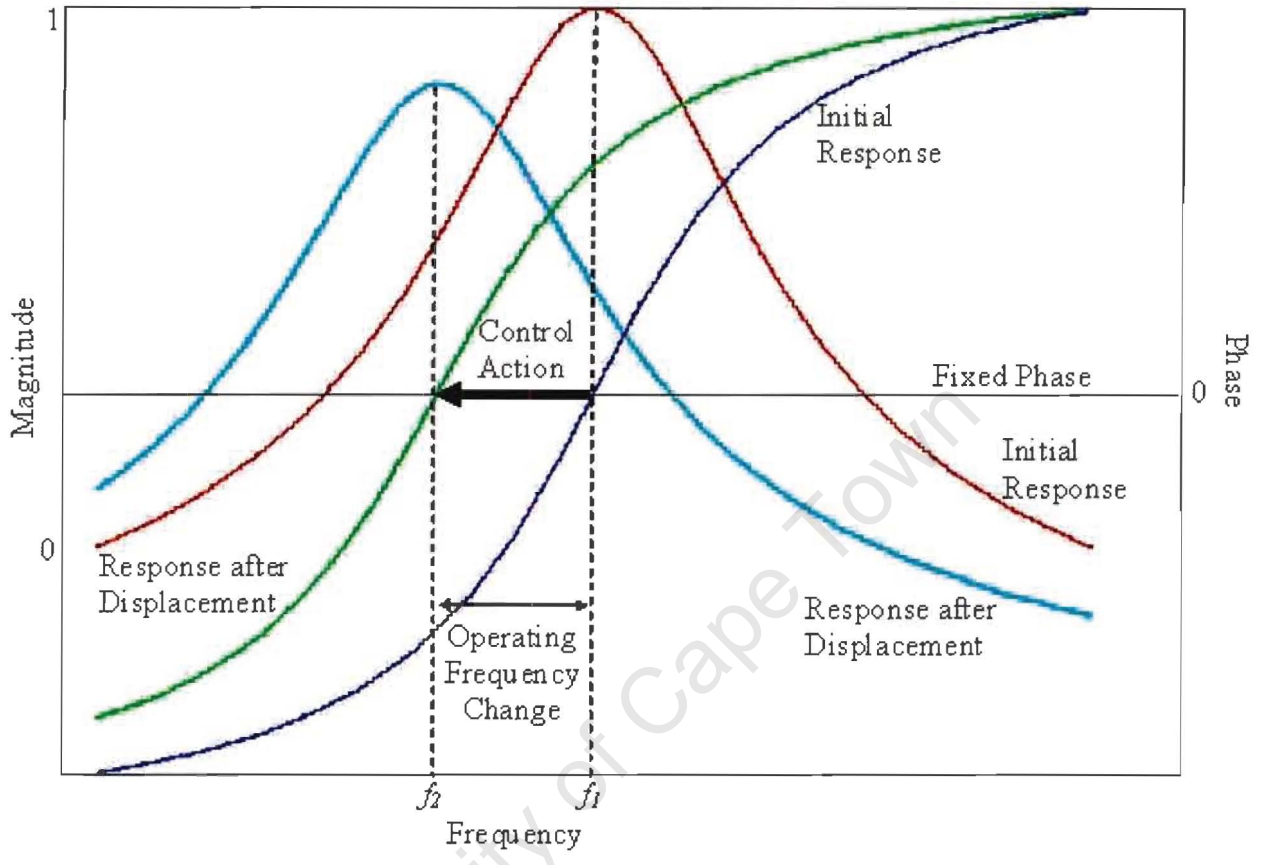

Figure 5.3.2: The Operation of the Phase-Resonant Frequency Control System.

Using the phase the control system keeps the tuning fork operating at point where the waveforms are in phase. For a change in displacement the resonant frequency will shift from f_1 to f_2. By monitoring the input voltage to the voltage controlled oscillator, the shift in resonant frequency can be used to keep the crystal at a fixed displacement.

5.3.2 Magnitude-Phase Control

Models that defined the behaviour of both the phase and the magnitude were developed in Chapter 4 when the operation of the tuning fork as a displacement sensor was discussed. These models can now be used to design the control systems which will allow the whole system to function. The control system maintaining the fork at a point within its resonant band cannot operate near the resonant peak as the magnitude measurement will be the same for both sides

of the peak and the slope will be in different directions leading to difficult design and slow control action [52]. Also, as the transducer moves closer to the fork there will be a drop in magnitude, and if the fixed magnitude is above the new maximum magnitude the controller will not be able to keep the crystal operating correctly. For both these reasons the fork must therefore be operated away from the resonant peak. Consider first the controller that operates the tuning fork crystal using magnitude. The control model for the magnitude of the crystal was given in Equation 4.28 in Chapter 4 as:

$$Magnitude = G_m(s) = \frac{A\left(\frac{1}{(o_m)(\tau)}\right)}{s^2 + 2\left(\frac{1}{(o_m)(\tau)}\right)s + \left(\left(\omega_d - \omega_o'\right)^2 + \left(\frac{1}{(o_m)(\tau)}\right)^2\right)} \tag{5.32}$$

The magnitude will respond to a change in frequency at a speed dictated by $\frac{1}{(o_m)(\tau)}$ and with an oscillation frequency determined by the difference between the operating frequency and the damped resonant frequency given by $(\omega_d - \omega_0')$. Using the simple substitutions $\delta_m = \frac{1}{(o_m)(\tau)}$ and $\omega_n = (\omega_d - \omega_0')$ Equation 4.28 can be reduced using the quadratic formula to:

$$Magnitude = G_m(s) = \frac{A(\delta_m)}{(s + \delta_m + j\omega_n)(s + \delta_m - j\omega_n)} \tag{5.33}$$

In order to control the system it will be put into a closed loop configuration in series with a controller circuit. The controller can then be designed to improve the open loop characteristics of the response. A closed loop block diagram for the control system is shown in Figure 5.3.3.

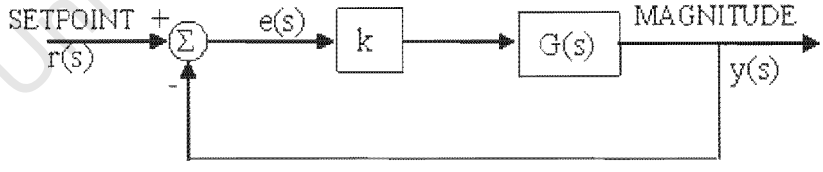

Figure 5.3.3: Closed Loop Block Diagram. *The error voltage $e(s)$ is the difference between the input set point $r(s)$ and the output signal voltage $y(s)$. The controller k will interpret the error voltage and adjust the input to the tuning fork system $G(s)$.*

A variety of different controllers can be designed for the system. Equations for the new open loop response $q(s) = kG(s)$ and the closed loop response $H(s) = \frac{q(s)}{1+q(s)}$ are useful in designing the control systems, as the effect of the controller can easily be determined. Also useful is the

analysis of the error voltage to see if the controller is able to keep the crystal operating at a point exactly without any error. The error voltage as a function of the input set point can be calculated using block diagram algebra as [6]:

$$e(s) = \frac{1}{1+q(s)} r(s) \tag{5.34}$$

The value of this error for a unit step ($r(s) = \frac{1}{s}$) once the system has settled is determined using final value theorem [6][41] as:

$$e_{final} = \lim_{s \to 0} s\,(e(s)) = \lim_{s \to 0} s \left(\frac{1}{1+q(s)} \right) \frac{1}{s} = \lim_{s \to 0} \left(\frac{1}{1+q(s)} \right) \tag{5.35}$$

In Chapter 4 simple proportional control was used to control the tuning fork crystal with some effect. For the proportional controller $k = K$ the closed loop model for the system can be given by:

$$H_m(s) = \frac{KA\delta_m}{\left(s + \delta_m + j\sqrt{\omega_n^2 + KA\delta_m}\right)\left(s + \delta_m - j\sqrt{\omega_n^2 + KA\delta_m}\right)} \tag{5.36}$$

This model shows that for any increase in the gain of the proportional controller, no overall speed increase will be experienced by the closed loop system. The poles of the closed loop will only increase along the imaginary axis of the s-plane so the system will become more oscillatory. Looking at the error signal for a step response of magnitude B, the final value of the error will be given by:

$$e_{m\ final} = \frac{B\left(\delta_m^2 + \omega_n^2\right)}{\delta_m^2 + \omega_n^2 + KA\delta_m} \tag{5.37}$$

The error is proportional to both the size of the step and the gain of the proportional controller. This error will produce inaccuracies in the control system and poor long term stability, and when the transducer begins to interact with the fork further errors will creep into the system. The steady state error can be avoided by introducing an integral component into the equation of the controller. This would not solve the problem of the slow response and the oscillations in the circuit.

A more sophisticated controller is needed to improve the closed loop magnitude response of the tuning fork crystal. The effect of the oscillatory poles should be cancelled out, and the overall speed of response should be improved. The effect of the oscillatory poles can be

cancelled by introducing nearby zeros in the controller. The speed response is determined by the addition of poles to make the controller realisable. The problem with the controller design is that in order for the error signal to be completely eliminated, one of the poles of the controller must be at zero. This slows down the system and makes it difficult for effective controllers to be designed. By reducing the effect of the oscillating poles, the system can respond faster if some steady state error is allowed. However no major speed gains can be achieved without using excessive gains, which are impossible to realise in practical circuits. It seems that utilising magnitude as a measurement can reduce the oscillations of the output to a degree, although it is difficult to completely eliminate the oscillating poles, and any significant speed increases are prohibitively difficult.

Now that control using the magnitude has been discussed, the focus shifts to the phase measurement that will be used to control the distance between the piezoelectric transducer and the tuning fork. The phase is the easier response to control, as its model contains a zero which simplifies the response. The system however is no longer operating at the resonant frequency so the phase response will also oscillate. The phase response model was derived in Chapter 4 and is given using similar substitution as:

$$Phase = G_p(s) = \frac{A(s+\delta_p)}{s^2 + 2\delta_p + \omega_n^2 + \delta_p^2}$$

For a closed loop equation the gain A can be absorbed by the controller k. The equation for the closed loop phase response is,

$$H_p(s) = \frac{k(s+\delta_p)}{\left(s + \left(\delta_p + \frac{k}{2}\right) + j\sqrt{\omega_n^2 - \frac{k^2}{4}}\right)\left(s + \left(\delta_p + \frac{k}{2}\right) - j\sqrt{\omega_n^2 - \frac{k^2}{4}}\right)} = \frac{k(s+\delta_p)}{s^2 + (2\delta_p + k)s + \omega_n^2 + \delta_p^2 + k\delta_p} \quad (5.38)$$

Looking at Equation 5.38 with simple proportional controller $k = K$ there will be a value of K for which the imaginary component of the response will be zero and the oscillations will die out completely. Increasing K will also increase the speed response of the system as the real value of the pole moves further left on the s-plane. Further increasing in K leaves the closed loop poles on the real axis, resulting in no oscillations. There will be some steady state error present in the system but this can be negated by introducing an integral component into the

controller.

Although probably not the best way to operate the system, early on in the research a tuning fork seismometer was constructed using the magnitude-phase control structure. The tuning fork was approached from the top using a piezoelectric diaphragm and was sealed in an aluminium container. It was designed with two second order control loops, one that used magnitude to operate the tuning fork at a point on the upward slope of its resonant peak, and the other to control the distance between the tuning fork and the diaphragm. The device was tested using a similar procedure to the one discussed in Chapter 6. The design of the system and the subsequent test results were compiled, written up and published [53].

5.3.3 Phase - Resonant Frequency Control

From the previous section it is clear that magnitude is a difficult measurement to work with. The systems tends to be oscillatory and slow. In this strategy, the magnitude measurement was eliminated in favour of using phase to control the fork, and the change in resonant frequency to control the height of the piezoelectric bimorph or diaphragm above the surface. Using phase to control the fork means that the system can be operated at the most sensitive resonant frequency, as phase is continuous across the resonant band. The phase control model for operation around the damped resonant frequency can be simplified:

$$Phase = G_p(s) = \frac{A}{s + \left(\frac{1}{(o_p)(\tau)}\right)} = \frac{A}{s + \delta_p} \tag{5.39}$$

In Chapter 4 the phase controlled system was found to work very well under simple proportional control. The closed loop equation for simple proportional controller K was also determined in Chapter 4 as

$$H_p(s) = \frac{K}{s + \delta_p + K} \tag{5.40}$$

where once again the open loop gain has been incorporated in the gain of the controller. For increasing gain the closed loop pole moves more and more to the left of the s-plane, effectively increasing the overall speed of the system. Although relatively stable, this system will have some steady state error proportional to the gain of the controller. This steady state error can be removed by adding an integral component to the controller. The controller can then be

defined as:

$$k = A + \frac{B}{s} = \frac{As + B}{s}$$

This controller will remove the steady state error from the response by placing a pole at the origin of the s-plane. This pole will slow down the response, and its effects need to be reduced. This can be achieved by manipulating the gains of the proportional component and the integral component. These gains manipulate the position of the zero introduced by the controller along the negative real axis. For $A >> B$ the zero is placed near the origin and will have a reducing effect on the pole. The speed of the system can now be increased without the steady state error. The speed limit of the system will be set by the phase detector which due to its rectifier component will behave like a fast pole on the negative real axis of the s-plane.

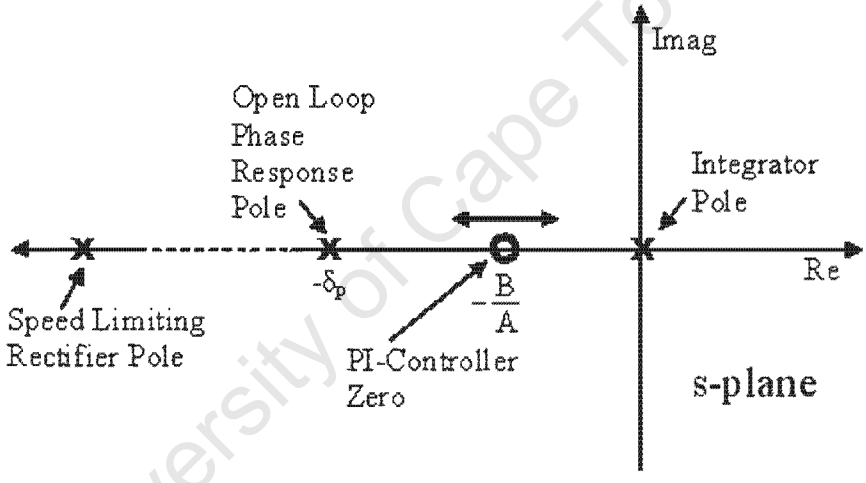

Figure 5.3.4: Open Loop Pole and Zero Positions for PI-Controller. *The position of the open loop phase response pole is determined by the characteristics of the tuning fork. The integrator pole will be on the origin and the controller zero position will be set by the ratio between the integrator gain and the proportional gain in the controller.*

Controlling the piezoelectric device now becomes quite simple, as the measurement for resonant frequency comes straight from the input voltage into the VCO in the tuning fork crystal control loop. The resonant frequency should therefore behave in a very similar fashion to the phase response of the tuning fork crystal. A similar controller comprising a proportional component and an integral component can again be used to good effect. The steady state error will be reduced as long as the gain of the proportional component is much larger than the

integral component. The speed of the closed loop system can be increased by increasing the proportional gain. The speed of this system will be limited by the phase measurement and the speed of response of the piezoelectric devices.

From the development of the tuning fork as a displacement sensor, to the application of the force feedback using a piezoelectric transducer, each component of the tuning fork seismometer has been developed separately in the preceding chapters. What remains now is to construct and test a simple tuning fork seismometer to see how well it functions. The next chapter details the testing procedure and signal extraction.

Chapter 6

Testing, Results and Discussion

6.1 Testing

In order to test the actual operating parameters of the entire tuning fork seismometer system, we needed to simulated ground movements. The system was set up on a large moving coil speaker mechanism capable of operating at very low frequencies. The output from the force feedback control loop was then compared to the outputs from other measurement devices. Various characteristics of the operation of the tuning fork seismometer system can then be extrapolated from these comparisons. These tests were done in order to ascertain whether the system could function as a seismometer, and were not expected to be completely accurate and noise free.

6.1.1 Set-Up

The piezoelectric tuning fork crystal is mounted on a threaded cylinder made of ceramic material. The cylinder is screwed into an aluminium frame, which will allow the tuning fork crystal to be set in various positions. A piezoelectric bimorph is fixed at one end in a second aluminium frame, forming a cantilever. Both the frames are then mounted on a positioning apparatus capable of manipulating the aluminium frames to bring the bimorph and tuning fork crystal into close proximity. The entire apparatus is then placed on the speaker mechanism and the speaker is driven with voltages of varying amplitude and frequency. The large speaker, similar to those used in audio applications, had been used to test accelerometers previously and was

capable of low frequency operation. The arrangement of the testing system is outlined in Figure 6.1.1.

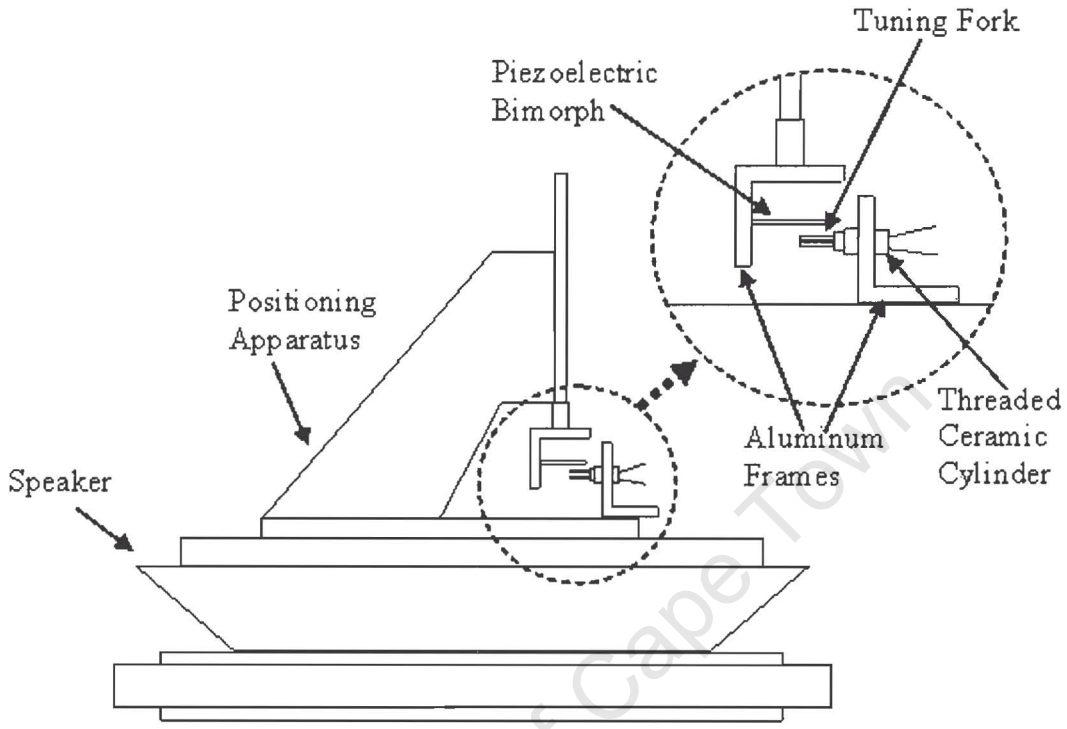

Figure 6.1.1: The Testing Apparatus for the Tuning Fork Seismometer. *Both the piezoelectric tuning fork and the bimorph are mounted in aluminium frames. The aluminium frames are then manipulated, using the positioning apparatus, to bring the bimorph and tuning fork into close proximity. The entire system is then placed on a speaker drive, which provides the generated ground motion for the tests.*

The tuning fork seismometer is operated using the phase-resonant frequency control system described in detail in Chapter 5. The phase detector used in the phase control loop was an exclusive-or logic gate phase detector, utilising two comparators to convert the sinusoidal signals into square waves. The phase between the input drive frequency from the VCO and the output voltage from the current to voltage converter circuit was measured in order to determine the position in the resonant band that the fork was operating. The input voltage to the VCO was adjusted using a simple proportional-integral feedback controller, which kept the crystal operating at its resonant frequency.

The input voltage to the VCO was also the input signal for the control system that fixed the piezoelectric bimorph at a specific height above the crystal. The voltage across the piezoelectric bimorph is controlled with a similar proportional-integral feedback controller to the one used to control the input frequency. In Chapter 5, in the discussion of the approach tests, the most sensitive point to viably operate the system was calculated to be at 80% of the total resonant frequency shift along the attractive force component. Using a generated set point voltage the piezoelectric bimorph is fixed at the distance that corresponds to this 80% sensitivity point. The control voltage signal to the piezoelectric bimorph then becomes the output for the entire tuning fork seismometer system. The circuit diagram appears in Figure 6.1.2.

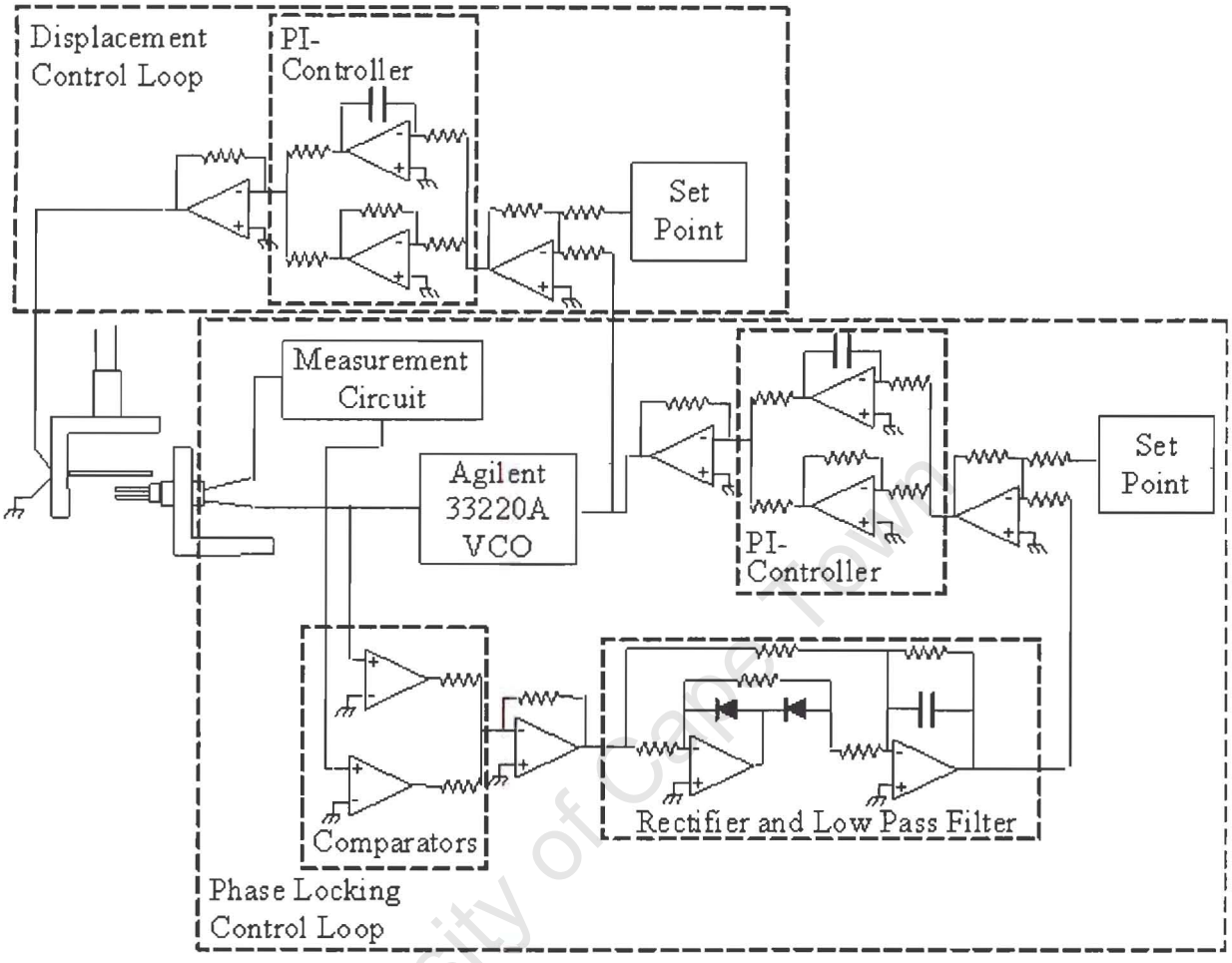

Figure 6.1.2: Circuit Diagram for Testing Circuit. *The phase between the input drive signal from the VCO and the output from the measurement circuit, given in Figure 3.3.4, is measured. This measurement is then compared to a set point and the input voltage to the VCO is adjusted by the PI-controller. The VCO input voltage also functions as the measure of the resonant frequency. This measurement is also compared to a set point and the voltage to the piezoelectric bimorph is adjusted by the other PI-controller.*

For these tests the output from the tuning fork seismometer is then compared to the outputs from two other measurement devices which are also mounted on the speaker. The first device is a ADXL05 MEMS accelerometer. The ADXL05 chip along with a few external components is mounted on a circuit board which is in turn mounted on the speaker. The second device is an SM-4/7 exploratory geophone in a PE-3 case. The prong of the case is pushed into a piece

of polystyrene so that the whole structure can be mounted upright on the speaker.

6.1.2 Calibration

The ADXL05 is a force balanced accelerometer based around a capacitive displacement detection scheme [54]. With three external capacitors and a number of external resistors to set the gain, the accelerometer can quickly be set up to measure either AC or DC acceleration. The accelerometer is calibrated using the DC acceleration of the Earth's gravity. The accelerometer is first positioned upright along its axis of sensitivity and the output voltage is recorded as shown in Figure 6.1.2. The accelerometer should experience an acceleration equal to $1g$ which is approximately equal to $9.81m.s^{-2}$. The device is then rotated 180° around its axis of sensitivity which should now point downwards. The voltage reading should correspond to an acceleration of $-1g$. The difference in voltage readings can then be used to determine the sensitivity of the accelerometer.

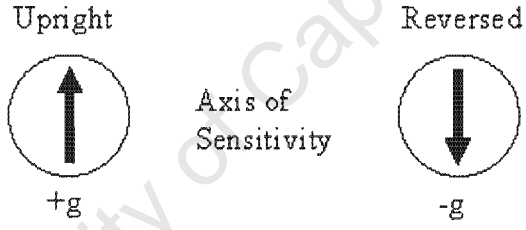

Figure 6.1.3: Calibration of the ADXL05 Accelerometer. *The output sensitivity will be given by* $Sensitivity = \left[\frac{V_1 - V_2}{2g}\right] V/m.s^{-2}$ *where* V_1 *and* V_2 *are the output voltage readings.*

According to the datasheet the ADXL05 accelerometer's sensitivity will remain the same from DC to about $1kHz$. This should give plenty of bandwidth for all the measurements. Although the ADXL05 accelerometer is not very sensitive, its ease of use and simple calibration make it very useful in calibrating and testing the geophone and the tuning fork seismometer.

The SM-4/7 geophones are digital grade geophones designed for long and reliable performance[55]. The device is of a moving coil design with precious metal contacts. They are used in 2-D and 3-D seismic exploration in a bandwidth of about $10Hz - 190Hz$. They produce an output proportional to the velocity of the ground motion. The device used in these experiments was one of a set of well-used $14Hz$ devices with a 375Ω measuring coil and a rated sensitivity of $28.8V/m.s^{-1}$. However, when checking the outputs of a few of the geophones it was clear that

the sensitivity varied between devices and that due to wear and age their sensitivity was no longer at its rated level.

The geophone was then calibrated using the accelerometer at a variety of frequencies to ascertain the actual sensitivity. It was also important to define the sensitivity of the geophone within its resonant band and below, as this is where much of the seismic activity exists. The output of the accelerometer was first converted into a measure of acceleration using the above mentioned calibration. The acceleration was converted into the velocity using the simple formula, $Velocity = \frac{Acceleration}{(2\pi f)}$. The geophone sensitivity was calculated by comparing the geophone output to the actual velocity across the measured frequency range. The plot of the geophone sensitivity to ground velocity is plotted in Figure 6.1.4.

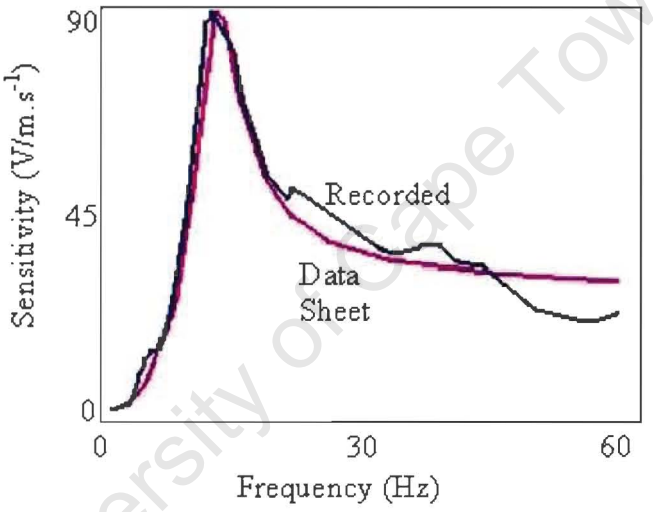

Figure 6.1.4: The Recorded Sensitivity of the Geophone. *The geophone was calibrated using the ADXL05 accelerometer. There is a close comparison between the recorded sensitivity and that which appears in the data sheet[55].*

The above plot of geophone sensitivity is very similar in shape to the rated version seen in the data sheet. The geophone is more sensitive to small ground motion than the ADXL05 accelerometer, and once calibrated should give a clearer picture of the sensitivity of the tuning fork seismometer system. Although errors in measurement and system noise will produce inaccuracies in the calibrations of both the accelerometer and the geophone, the rough correspondence should be enough to give a fairly good idea of the characteristic of the tuning fork seismometer system.

6.1.3 Testing Procedure

For a given input voltage to the speaker drive there will be a corresponding input "seismic" signal to the various measurement devices. The output from all the measurement devices can then be split into two components. There will be a component associated with the seismic signal generated by the speaker drive, and another component associated with the various noise sources present in the output signals. In order to accurately determine the sensitivity and bandwidth of the tuning fork seismometer, it is important to identify all these noise signals present in the output signal. Therefore at first, measurements were taken when the input voltage to the speaker drive was zero, so that just the background noise could be measured. The outputs of the various measurement devices can then be compared to determine all the external noise sources of the tuning fork seismometer.

Once the noise sources have been accurately catalogued, the sensitivity and bandwidth of the tuning fork seismometer can be determined by monitoring the outputs of the measurement devices for various input seismic signals generated by the speaker drive. The different frequencies tested were $10Hz$, $15Hz$, $20Hz$, $25Hz$ and $30Hz$. Once all the tests were completed, the outputs of the various measurement devices were analysed and compared to characterise the sensitivity and bandwidth of the tuning fork seismometer. A more detailed description on how the signal analysis appears in the next section.

6.2 Results

6.2.1 Signal Extraction

For each of the measured outputs from the tests it is important to know what components of the signal come from what source. Besides the signal for the ground motion of the speaker for each test there will be a number of noise components. There will be electrical measurement noise for each device. This measurement noise includes ripple noise from the control loops and the filters, as well as contamination noise from the mains power supply. There will be environmental noise due to pressure and temperature change, as well as other environmental conditions that affect the measurement devices. There will also be some background seismic noise due to ground motion other than that controlled by the input voltage to the speaker.

It is important to understand and isolate all these noise signals so that the measured outputs from each device can be accurately characterised and so that the parameters of the tuning fork seismometer system can be determined.

The most common technique for isolating the individual components of a signal uses coherence, or the fraction of the power of one signal that appears in another. For two signals it is used to determine which components are unique to each signal and which are common to both. It has been successfully used to determine the instrument noise of geophones by Barzilai, van Zandt and Kenny [56]. The outputs for a specific seismic signal from two different devices are compared so that the noise of each device can be separated from the input seismic signal. For a seismic signal $S(t)$ the system can be illustrated in Figure 6.2.1 [53].

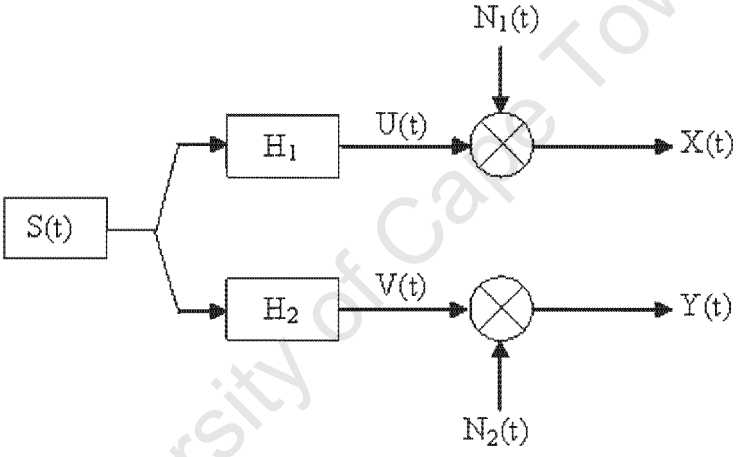

Figure 6.2.1: Block diagram for the signal extraction process. *$S(t)$ is the seismic signal. $H_{1,2}$ are the transfer functions for each of the sensors which produce the signals $V(t)$ and $U(t)$ which are dependent on the seismic signal. $N_{1,2}(t)$ are the two independent noise signals for each of the measurement devices. $X(t)$ and $Y(t)$ are the two measured outputs of the devices.*

The mathematical techniques behind coherence are explained in detail in the book by Bendat and Piersol[57] and are outlined as follows. Coherence is defined for two measured signals X and Y as

$$Coherence = \gamma^2_{XY}(f) = \frac{|G_{XY}(f)|^2}{G_{XX}(f)\,G_{YY}(f)} \tag{6.1}$$

where $G_{XY}(f)$ is the cross spectral density of the two signals X and Y, and $G_{XX}(f)$ and

$G_{YY}(f)$ are the power spectral densities of the individual signals. The full cross spectral density function is defined as the Fourier transform of the correlation function, represented by $R_{XY}(\tau)$, between two time based input functions $X(t)$ and $Y(t)$,

$$S_{XY}(f) = \int_{-\infty}^{\infty} R_{XY}(\tau)\, e^{-j2\pi\tau} d\tau \tag{6.2}$$

(where τ is a variable of the correlation function and should not be confused with the mechanical damping constant). The power spectral density is a special case of the cross spectral density where $X(t) = Y(t)$. For practical purposes only the positive frequencies are considered, which gives the one sided cross spectral density function that is used in the coherence calculations as

$$G_{XY}(f) = 2S_{XY}(f) = 2\int_{-\infty}^{\infty} R_{XY}(\tau)\, e^{-j2\pi\tau} d\tau \tag{6.3}$$

where the equation will equal zero for all negative frequencies. To increase the accuracy of the coherence calculation, many samples of both signals should be taken, and the calculation averaged to determine exactly what signals are consistently common to both signals. The power spectral densities for the signals X and Y can be broken up into their signal components as follows:

$$\begin{aligned} G_{XX}(f) &= G_{UU}(f) + G_{N_1N_1}(f) = H_1 G_{SS}(f) + G_{N_1N_1}(f) \\ G_{YY}(f) &= G_{VV}(f) + G_{N_2N_2}(f) = H_2 G_{SS}(f) + G_{N_2N_2}(f) \end{aligned}$$

In order to determine the noise signal of a single device, either the outputs from two identical devices can be compared, or a number of samples from one output for the same seismic signal can be compared. Using the coherence the constant noise sources can be found and removed from the system, leaving only the measured value of the seismic motion. This measured value can then be converted using the known transfer function for the device into the actual seismic signal. This seismic signal can be used to determine the noise of the unknown device by using the coherence between the seismic signal and the measured output from the unknown device.

6.2.2 Test Results and Discussion

Firstly test results were compiled for no input signal to the speaker drive, so that only the background noise was affecting the measurement devices. A number of readings from the output of the geophone were averaged together, and then converted to velocity using the sensitivity calibration developed in the calibration section. Once the actual background velocity of the system was known it could be compared to the output of the tuning fork seismometer. Both signals were also passed through a high pass filter with a cut off of $9Hz$. Although there was no low frequency noise on the geophone signal, the converted velocity signal was filtered because as the sensitivity falls towards zero, the calculated velocity readings will grow very large. These calculated velocities are for frequencies well below the resonant peak of the geophone and are probably inaccurate. There is, however, large low frequency noise on the output for the tuning fork seismometer. Much of this noise can be attributed to changes in air pressure and temperature. Air flow from nearby breathing and air currents also produced low frequency noise signals. The tuning fork seismometer output also comes from the control voltage to the bimorph which will have a DC component which has to be filtered out. Although the tuning fork seismometer is also sensitive to ground vibration at frequencies below $9Hz$, in order to compare its output with the velocity measurements from the geophone its signal had to be filtered. Both the filtered geophone and tuning fork seismometer outputs are plotted in Figure 6.2.2, with the geophone output converted from a voltage into velocity. From the plot it clear that there are many noise sources in both signals, but overall there is substantial correlation between the signal measured by the geophone and that measured by the tuning fork seismometer. There is a background seismic signal in both outputs at about $11Hz$, which is attributed to background vibration caused by equipment in the building. Most obvious from the output from the tuning fork seismometer is that the noise from mains power contamination at $50Hz$ is the chief source of instrumentation noise. The mains power contamination noise leaks into all parts of the circuit and has a large detrimental effect on the control loops, as the noise signal forms part of the signal loop, and increases for increasing gain.

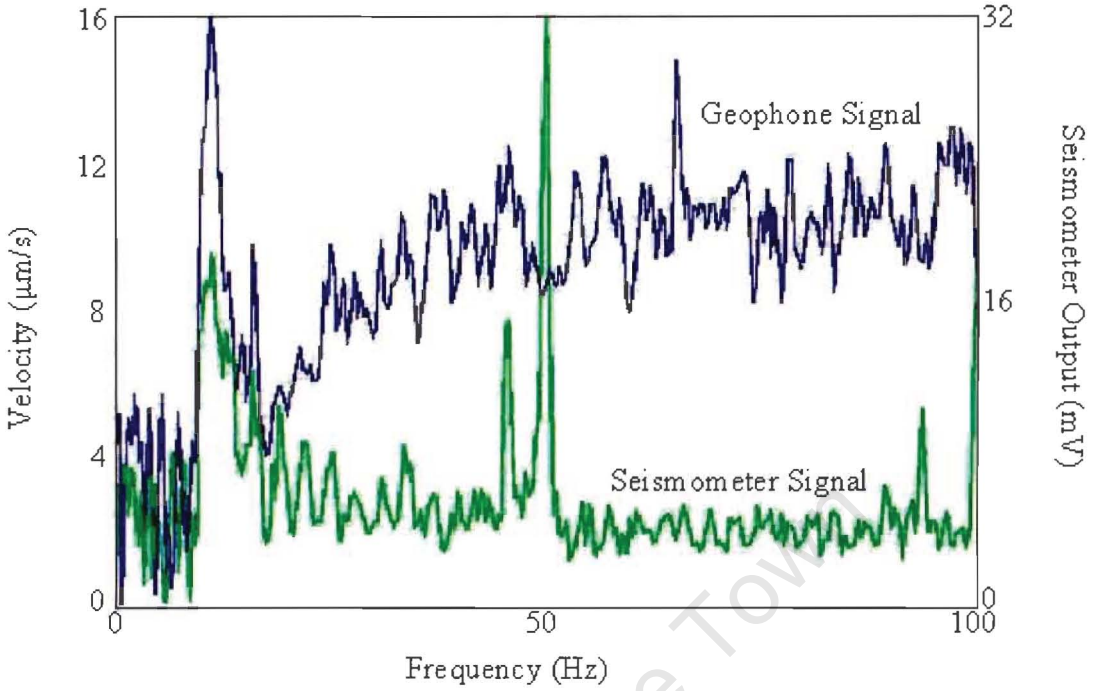

Figure 6.2.2: The Background Noise Velocity Measured by the Geophone and the Corresponding Output from the Tuning Fork Seismometer. *The geophone signal is converted into a voltage using the sensitivity calibration done earlier to give the velocity magnitude at each frequency. The seismometer signal is the magnitude of the output at each frequency calculated using the power spectral density of a sample. The readings below* $10Hz$ *have been reduced with filtering because of the large amount of low frequency noise.*

Now that the noise sources for the tuning fork seismometer output have been defined, they can be used to determine the sensitivity and bandwidth of the tuning fork seismometer. A drive signal was now applied to the speaker drive and the outputs from the geophone and tuning fork seismometer were recorded for a number of different frequencies. The different frequencies tested were $10Hz$, $15Hz$, $20Hz$, $25Hz$ and $30Hz$. Using the geophone noise signal waveform, the geophone output signal and the geophone sensitivity calibration the actual acceleration of the speaker drive at each of the frequencies is calculated. To calculate the sensitivity and bandwidth of the tuning fork seismometer, the actual acceleration is compared to the output from the tuning fork seismometer for each of the measured frequencies. The output of the tuning fork seismometer for the $15Hz$ test and the corresponding actual acceleration is shown

below in Figure 6.2.3. A similar high pass filter with a cut off of $9Hz$ was used to produce these results.

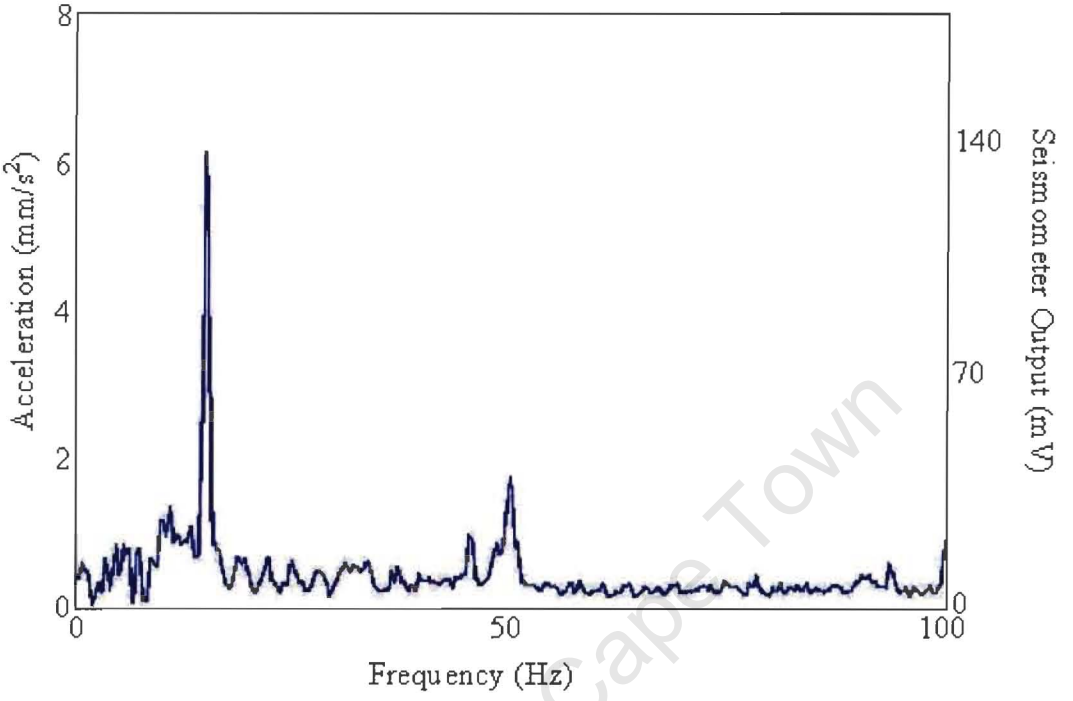

Figure 6.2.3: The Output Voltage from the Tuning Fork Seismometer and the Corresponding Measured Acceleration at $15Hz$**.** *The acceleration is measured by converting the geophone output voltage. Once again the signals below* $10Hz$ *have been reduced by filtering.*

The calculated sensitivity for each measured frequency is then shown in the following table.

Frequency (Hz)	*Acceleration* (mm/s^2)	*Output* (mV)	*Sensitivity* $(V/m.s^{-2})$
10	8.46	194.5	22.99
15	6.01	134.8	22.429
20	3.01	70.5	23.42
25	3.89	41.3	10.617
30	13.14	78.6	5.98

From the measurements in the table the average sensitivity for frequencies below about $22Hz$ is about $23V/m.s^{-2}$. Above $22Hz$ the control systems begin to fall behind and the sensitivity of the tuning fork seismometer begins to taper off. This bandwidth could be increased by increasing the gain in the control loops but this increases the noise in the system, making the tuning fork seismometer less sensitive. The tuning fork seismometer works right down to very low frequencies. Although for these results the low frequencies have been filtered out to get rid of external noise sources the tuning fork seismometer picked up external vibrations at frequencies under $1Hz$. Using the average sensitivity, the smallest measurable acceleration that can be measured can now be calculated using the noise plot of the seismometer. Taking the mains contamination noise at $50Hz$ as the largest source of noise, the smallest measurable acceleration is calculated as:

$$Smallest\ Measurable\ Acceleration = \frac{Noise\ Signal}{Sensitivity} = 1.4\ mm/s^2 = 0.14mg$$

The $50Hz$ noise signal, as it is has a relatively constant frequency and magnitude, cannot be considered as actual RMS noise signal and can therefore not be represented in terms of $\sqrt{Hz}$. The $50Hz$ noise is better described as an artefact signal in the measured signal. If, however, the $50Hz$ noise is eliminated and the background seismic noise compensated for, the next lowest electrical noise signal is at about $5mV/\sqrt{Hz}$. Calculating the smallest measurable acceleration for this noise source yields:

$$Smallest\ Measurable\ Acceleration = \frac{Noise\ Signal}{Sensitivity} = 217\ \mu m/s^2/\sqrt{Hz} = 23\mu g/\sqrt{Hz}$$

6.2.3 Comparison with a "Perfect" Tuning Fork Seismometer

All the results so far in Chapter 6 have shown that the simple tuning fork seismometer constructed for these tests does function well. As mentioned previously the simple device used in the tests was never supposed to be completely noise free but was rather just supposed to be used to test the ideas behind a tuning fork seismometer. In this section the sensitivity results for the actual seismometer will be compared to theoretical results calculated for a perfect ultra-low noise seismometer.

In Chapter 3, in the noise analysis of the piezoelectric tuning fork, Equation 3.90 was derived to calculate the effective noise force floor. If we assume that the thermal noise of the tuning fork is indeed the largest source of noise, the force noise floor of the tuning fork can be calculated as:

$$S_f^{\frac{1}{2}} = \sqrt{\frac{4}{\omega_o Q}} \left(\frac{k_B T}{x_{RMS}} \right) = 0.25 pN/\sqrt{Hz}$$

where k_B is the Boltzmann constant and T is the temperature. In a perfect seismometer the system would be operated in a vacuum to reduce the air effects. Q-factor values as high as 70 000 were measured in Chapter 4, but because of imperfect vacuum there will still probably be some viscous damping so a Q-factor of 50 000 was chosen. The random motion of one arm of the fork x_{RMS} was calculated in [17] as $0.321pm$.

The theoretical noise floor can now be combined with the sensitivity equations derived in the approach tests in Chapter 5. The most sensitive approach test for the attractive region was when the bimorph was orientated so just the very tip approaches the tip of one tine of the tuning fork. The sensitivity was calculated as:

$$Sensitivity = 101\ MN/m$$

This force sensitivity should be seen as fairly conservative as it is taken at the most sensitive point on the attractive response, and in a perfect seismometer we would operate on the far more sensitive repulsive response slope. Also, as we are operating in vacuum the masking of the intersurface forces by the air effects would be reduced, and the sensitivity of the seismometer would be further enhanced. The measurable displacement noise floor can now be calculated as:

$$Displacement\ Noise\ Floor = D_f = 2.47 zm/\sqrt{Hz}$$

The mechanical sensitivity of the suspension system formed by the piezoelectric transducer was derived in the beginning of Chapter 5. The sensitivity of the piezoelectric bimoprh in a cantilever arrangement was calculated as:

$$Cantilever\ Bimorph\ Sensitivity = 8.6\ \times\ 10^{-9}\ m/m.s^{-2}$$

Assuming that the thermal noise of the piezoelectric bimorph, as it is operated below its resonant frequency, is less than the thermal noise of the tuning fork, the output displacement sensitivity to an input acceleration can be used to calculated the measurable acceleration noise floor as:

$$Acceleration\ Noise\ Floor = A_f = 287fm.s^{-2}/\sqrt{Hz} = 28.7fg/\sqrt{Hz}$$

The results in this section are based on a number of assumptions: particularly the fact that the thermal noise floor of the tuning fork is the biggest noise source and the fundamental limit to the sensitivity of the seismometer. We also assume that the measurement and control electronics are both noise free and highly sensitive, and do not affect the sensitivity calculations at all. Although the simple tuning fork seismometer constructed and tested in Chapter 6 shows that the system can work well practically, the results in this section, which should be considered theoretical with all the assumptions, show the operational potential of a truly low noise device.

Chapter 7

Conclusions, General Discussion and Future Work

7.1 Conclusions

The novel idea of using a miniature piezoelectric tuning fork as a displacement sensor in conjunction with a piezoelectric bimorph in a force feedback accelerometer system has been demonstrated. The piezoelectric bimorph operates as both the suspension system and the force transducer in the force feedback accelerometer system. Models for the behaviour of each component of the system have been developed and tested. Control systems have been developed to operate both the tuning fork crystal and the piezoelectric bimorph. The entire system was then calibrated using other vibration measurement devices to determine both the sensitivity and bandwidth of the tuning fork seismometer. Although successful, the system is not without its problems and a number of options could be explored to improve both the sensitivity and the bandwidth of the device.

Each tine of the piezoelectric tuning fork was modelled separately as a vibrating cantilever. The forces acting on a single element within the cantilever were defined and then built up to obtain the vibration modes of each tine of the tuning fork. The vibration mode equations were then combined with the equations describing the behaviour of a damped mass spring system, to form the complete response of the piezoelectric tuning fork to an external drive force. The piezoelectric effect of the tuning fork and its equivalent circuit were used to determine how an

external driving voltage is converted into a mechanical force and how the tuning fork's response to the mechanical force is converted back into an electrical signal. The mechanical and electrical noise characteristics of the system were discussed in order to determine the piezoelectric tuning fork's fundamental limits of displacement sensing.

The two main measurand outputs from the tuning fork are: the magnitude of the output current, and the phase between the input drive voltage and the output current. Both the magnitude and phase of the output current are dependent on the mechanical characteristics of the tuning fork. The different methods of measuring both the magnitude and phase of the output current and how to improve the speed and accuracy of these measurements was discussed in detail so the best measurement method could be found. Using the equations that describe the motion of the tuning fork, a displacement change can be modelled as a change in operating frequency. The various components of the motion, such as the steady state and transient components, can be re-combined to determine the theoretical response of both the output magnitude and phase for a change in displacement. The theoretical response compared quite accurately with actual measurements taken from the piezoelectric tuning fork. Although some small adjustments were made to the decay rate of the transients, the overall shape of the response was well defined by the theoretical models. The theoretical models were then converted into s-plane control models, which were also thoroughly tested and found to be quite accurate. Simple feedback controllers were then developed to keep the tuning fork operating at set points within its resonant band.

The interaction between the piezoelectric tuning fork and the bimorph can be divided into two components. Interatomic forces combine to form intermolecular forces, which in turn combine to form the intersurface forces between the tuning fork and the bimorph. There will also be forces due to the passage of air between the vibrating fork and the bimorph. The theoretical shape and strength of these forces was used along with measurements from the tuning fork to determine the best physical set up to maximise the sensitivity. The various tests for different physical arrangements were completed by monitoring the resonant frequency and changing the displacement between the tuning fork crystal and the bimorph.

Using the control models, the displacement between the bimorph and the piezoelectric tuning fork can now be fixed at the point where the tuning fork is the most sensitive to dis-

placement. Two different control strategies were discussed with reference to speed and accuracy of the measurands. As the system can be operated at the resonant frequency when phase is used to control the drive frequency, this strategy, along with using the resonant frequency to determine the displacement, is regarded as the best way to operate the system. The output from the complete tuning fork seismometer was then compared to other measurement devices for simulated ground motion to determine the sensitivity and bandwidth of the device. For its small size and the relatively low mechanical sensitivity of the piezoelectric bimorph, the tuning fork seismometer performed with reasonable sensitivity right down to frequencies below $1Hz$.

7.2 General Discussion

Although the tuning fork seismometer does work well there are a number of problems that need to be discussed. There are numerous noise sources that affect both the sensitivity and the bandwidth of the device. There are also different ways to operate the system that could improve the sensitivity, reduce the noise and extend the bandwidth. The isolation and testing of the device also needs to be improved to further separate out the system noise.

7.2.1 Noise Analysis

The fundamental noise signals for the piezoelectric tuning fork were discussed in Chapter 3. Due to the Brownian motion of the tines of the tuning fork, there will be a current noise signal produced by the piezoelectric effect in the crystal. This noise signal is converted to a voltage by the simple electronic circuit also discussed in Chapter 3. The noise due to the Brownian motion of the tuning fork combines with the Johnson resistor noise of the components in the electronic measurement circuit to produce the total noise for the simple tuning fork and measurement electronics system. This noise is largely unavoidable, and although better components can be used in the electronic measurement circuit, from the analysis of the noise equations in Chapter 3, for frequencies near the resonant frequency, the noise signal will be dominated by the signal due to the Brownian motion of the tuning fork tines. This noise signal due to the Brownian motion of the tuning fork tines is unavoidable, and can therefore be identified as the fundamental limit in the operation of the tuning fork as a displacement sensor.

Looking at the results from the tests, for both the zero ground motion and for simulated ground motion, what is immediately obvious is that the recorded noise signals are much larger than the theoretical noise signals discussed in Chapter 3. Although there will be some mechanical noise due to the random Brownian motion of the piezoelectric bimorph, it is obvious that most of the extra noise is electrical in nature. This extra electrical noise comes from a number of sources. The mains power supply noise at $50Hz$ is one of the larger components of the extra electrical noise and comes from the power supply rails for the electrical circuit and is radiated through the air and picked up by the wires in the circuit. This noise is at a low enough frequency to be right in the middle of the desired measurement band of frequencies. The noise at $50Hz$ leaks into the control loops operating the system, and grows accordingly with an increase in gain in the control loops. Another large source of electrical noise is the ripple produced in the measurement of both magnitude and phase. As low pass filters are used in the measurement there will be a ripple at the operating drive frequency with an magnitude which is dependent on the speed of the low pass filter. This noise source is at a frequency far above the measurement band and thus has less of an effect on the response as the $50Hz$ mains power leakage noise. The other electrical noise sources are the Johnson noise for all the other external components needed to operate the system, and the minute noise signals from the operational amplifiers and the other integrated circuits used in the circuitry. Most of these signals are much smaller than the mains power noise or the filter ripple, and could be smaller than the mechanical noise from the Brownian motion of the tuning fork tines.

These extra noise signals increase the total noise in the system, which reduces the effectiveness of the piezoelectric tuning fork as a displacement sensor. Although some of the noise sources are unavoidable, as some extra circuitry is required to operate the system, the large noise sources such as the mains power and the filter ripple should be reduced so that the tuning fork can achieve its optimal sensitivity.

7.2.2 Q-Factor

Another important consideration to come out of the analysis in Chapter 3 is that the sensitivity of the piezoelectric tuning fork is dependent its Q-factor and operational frequency. To achieve optimal sensitivity the Q-factor should be maximised and the system should be operated at the

resonant frequency. From previous discussions using phase to control the operating frequency and a measure of the resonant frequency to control the displacement is the simplest and best way to keep the system operating at resonant frequency. Maximising the Q-factor, however, is more of a challenge. The Q-factor, in the mass spring model, is determined by the resonant frequency and the viscous damping, which is proportional to velocity. The resonant frequency will remain fairly constant and the change in the damping factor will have by far the greatest effect on the Q-factor. From the discussion of the contact model in Chapter 2, the viscous damping is largely caused by the passage of the piezoelectric tuning fork tines through the air. The effect of the passage of the air on the tuning fork grows as the tuning fork approaches a surface and the sir has to be forced out of the gap between the tines and the surface. Therefore in order to maximise the Q-factor, and thus the sensitivity, the air effects must be minimised. This can be done by reducing the interacting surface area between the tuning fork and the surface. This, however, will also reduce the size of all the other interaction forces and will decrease the sensitivity of the piezoelectric tuning fork to displacement. A better solution would be to remove the air effects entirely by removing the air. This could be done by placing the whole system in a vacuum. This would also decrease the masking of the intersurface forces and could greatly improve the sensitivity of the whole system. By placing the system in a vacuum the noise signals from air movement and pressure change could also be avoided.

Earlier in the research the piezoelectric tuning fork was tested inside a vacuum chamber. As expected there was an increase in the Q-factor as the viscous damping was reduced. The masking of the intersurface forces was also reduced making the attractive and repulsive forces stronger and more pronounced. Unfortunately operation inside the vacuum chamber was somewhat limited as the motor used to produce the vacuum caused large vibrations which interfered with any measurements. Also slight changes in vacuum pressure would alter the vibration characteristics of the tuning fork which also caused problems. Operating inside the vacuum chamber also meant that control and measurement wires had to be run inside the chamber. The extension of the wires compounded the electrical noise problems experienced in the system.

7.2.3 Physical System

The physical arrangement and the manipulation the various components of the system could also cause the tuning fork seismometer to not operate to its full potential. The positioning apparatus may not fix the position of the piezoelectric bimorph and the tuning fork exactly, so it is difficult to know the exact relative positions of both components. This doesn't allow for exact positioning and the bimorph and tuning fork might not be in the position that maximises the sensitivity of the entire seismometer system. The positioning structure was also not completely rigid which resulted in mechanical instability in the system. When under vibration mechanical resonances within the structure could also affect the operation of the tuning fork seismometer. Ideally a positioning structure that could initially set the position of the tuning fork and the piezoelectric transducer precisely, and then remain fixed in that position, is required.

7.3 Future Work

Although the tuning fork seismometer system as constructed functions fairly well, there is much that can be done to improve its performance. Many of these improvements will have to do with reducing the noise levels in the electronic circuitry, to drop the overall noise levels to the fundamental noise limits discussed in Chapter 3. More work should also be done on the measurement of phase and magnitude to improve both the sensitivity and bandwidth. Investigating the system in vacuum conditions should also lead to improvements.

7.3.1 Noise Reduction

From the analysis of the system tests the main noise components were identified as: the mains power noise from the surrounding power supplies, the ripple noise from the filters in the measurement circuits, external noise sources such as background seismic motion and changes in atmospheric conditions. Both the noise from the mains power supply and the external noise sources could be largely eliminated by adequately shielding the tuning fork seismometer. The device should be sealed in an atmospherically stable chamber that is also isolated from external ground motion. The tuning fork seismometer system must also be shielded from any electronic equipment that relies on the mains power supply. New monitoring equipment and power sup-

plies that run on DC batteries should be sourced to power the device and monitor the various outputs. A reduction in the ripple noise from the filters in the measurement circuitry requires a change in the actual filter and measurement circuit design. With all the other noise sources reduced the filters would set both the maximum speed of the system as well as the upper noise limit of the device.

7.3.2 Improved Measurement

Both the measurement of phase and magnitude requires at least one complete output waveform from the input drive voltage and the converted output current. This sets the absolute limit of the measurement speed as the period of the resonant frequency, which is around $32.768kHz$. As magnitude is the slower more oscillatory measurement using it should be avoided in future work. This leaves phase which is detected using an exclusive-or gate logic detector so that the magnitude will not affect the measurement. This type of phase detector when used in an analogue system requires filters to convert the output square wave in to a control voltage signal. These filters reduce the upper limit of the measurement speed and produce the ripple noise discussed previously. In Chapter 4 a method for increasing the operating frequency was discussed. The method involves multiplying the measurement signals by themselves to produce signals with components at twice the initial frequency. The multiplication not only increases the frequency of the measured signals but can also increase the phase sensitivity. Although theoretically simple, the actual design and construction of the multiplying circuit boards is more of a struggle. The unwanted component of the multiplied signals needs to be filtered out and the lower frequencies tend to leak into the signals at higher frequencies. Increasing the phase sensitivity by increasing the measured frequency also makes the frequency response of the phase oscillate so the control of the system needs to be a lot more carefully done. A good solution may be to use a number of phase detectors at different frequencies each with their own control loops of varying strength. The less sensitive control loops can then be used to get the bimorph into roughly the right position, and the more sensitive control loops could be used for fine adjustment and measurement. The increase in frequency will also allow the filters to be designed with higher cut-off frequencies, which should reduce the ripple noise without slowing down the system.

7.3.3 Operating in a Vacuum

Another avenue of future research that should be investigated is when the entire system is placed in a vacuum. This should reduce the forces on the tuning fork due to the passage of air. This should increase the Q-factor of the tuning fork crystal, which will make it more sensitive to changes in displacement. Reducing the air pressure will also mean that the intersurface forces will be larger and act over a greater range. However, placing the system in a vacuum chamber will require that a far better physical system for manipulating the tuning fork crystal and the piezoelectric bimorph will have to be built. At the moment the relative position of the piezoelectric bimorph and the tuning fork is roughly adjusted by hand using a positioning apparatus equipped with a micrometer thread. Varying voltages are then applied to the piezoelectric bimorph to finely adjust its displacement from the tuning fork crystal. Once placed in a vacuum chamber no manipulation of the micrometer thread in the current system would be possible, and as the interaction forces will change in the vacuum, setting the position before sealing the chamber will also be difficult. A physical manipulation system that is capable of making adjustments once the chamber is sealed needs to be developed. Or another option, would be to investigate other piezoelectric devices that might provide greater range than the current piezoelectric bimorphs without sacrificing precision. Other problems such as how to get signals in and out of the vacuum chamber also exist. Most vacuum systems also require pumps that produce vibrations which will obviously affect seismic measurements. Keeping a constant low air pressure within the vacuum chamber is very important as changes in the air pressure will have massive effects on both the intersurface forces and the resonant frequency of the crystal. All in all operation in a vacuum will probably require a custom built sensor in which both the tuning fork crystal and the piezoelectric bimorph are permanently sealed.

References

[1] E. Wielandt. *Seismometry.* Available at: http://www.geophys.uni-stuttgart.de/seismometry/hbk_html/hbk_html.html. Last Visited On: 10 August 2005.

[2] J. Havskov, G. Alguacil. Instrumentation in Earthquake Seismology. Preliminary Version, June 2002. Chapter 2: Seismic Sensors, pg. 14-70.

[3] R. Baierlein. *Newtonian Dynamics.* McGraw-Hill, New York, 1983. Chapter 2: The Harmonic Oscillator, pg 45-63.

[4] D.G. Fertis. *Mechanical and Structural Vibrations.* John Wiley & Sons, Inc., New York, 1995. Chapter 2: Vibration Analysis of Simple Systems, pg 41-56, Chapter 3: Forced Vibrations of Simple Systems, pg 118-127.

[5] A. Barzilai. PhD Defence Presentation, Stanford University, 25 January 2000. Available at: http://micromachine.stanford.edu/smssl/projects/Geophones. Last Visited On: 15 August 2005.

[6] M. Braae. *Control Theory for Electrical Engineering.* UCT Press, Cape Town, 1994. Chapter 4: Dynamic Variables and Laplace Transforms, pg 52-60.

[7] E.O. Doebelin. *Measurement Systems: Application and Design.* McGraw-Hill, New York, 1966. Chapter 4: Motion Measurement, pg. 212-331.

[8] P.H. Sydenham. *Handbook of Measurement Science Volume 2: Practical Fundamentals.* John Wiley & Sons, New York, 1983. Chapter 24: Transducer Practice: Displacement, pg. 1037-1069.

[9] MicroStrain Microminiature Sensors. Available at: http://www.microstrain.com/displacement-transducers.aspx. Last Visited On: 9 August 2005.

[10] Data Week News. Available at: http://dataweek.co.za/news.asp?pklNewsID=17569&pklIssueID=496&pklCategoryID=79. Last Visited On: 9 August 2005.

[11] Table of Dielectric Constants. Available at: http://hyperphysics.phy-astr.gsu.edu/hbase/tables/diel.html. Last Visited On: 10 August 2005.

[12] D. Morioli, E. Sardini, A. Taroni. High Accuracy Measurement Techniques for Capacitance Transducers. *Measurement Science and Technology*, 4, 1993, pg. 337-343.

[13] L.W. Kessler. Acoustic Microscopy Commentary: SLAM and SAM. *IEEE Transactions on Sonics and Ultrasonics*, SU-32, 1985, pg. 136-139.

[14] C. F. Quate. Acoustic Microscopy: Recollections. *IEEE Transactions on Sonics and Ultrasonics*, SU-32, 1985, pg. 132-136.

[15] C.H. Liu, A. Barzilai, J.K. Reynolds, A. Partridge, T. Kenny. Characterisation of a High-Sensitivity Micromachined Tunneling Accelerometer with Micro-g Resolution. *Journal of Microelectromechanical Systems*, 7, 1998, pg. 235-244.

[16] D. Sarid. *Scanning Force Microscopy.* Oxford University Press, Oxford, 1991. Chapter 4-10, pg. 55-128.

[17] R.D. Grober, J. Acimovic, J. Schuck, D. Hessman, P.J. Kindlemann, J. Hespanha, A.S. Morse, K. Karrai, I. Tiemann, S. Manus. Fundamental Limits to Force Detection Using Quartz Tuning Forks. *Review of Scientific Instruments*, 71, July 2000, pg 2776-2780.

[18] J.N. Israelachvili. *Intermolecular and Surface Forces.* Second Edition, Academic Press, 1993. Part One: The Forces Between Atoms and Molecules, pg. 3-122, Part Two: The Forces Between Particles and Surfaces, pg. 199-213.

[19] D. Sarid. *Scanning Force Microscopy.* Oxford University Press, Oxford, 1991. Chapter 13: Atomic Force Microscopy, pg. 181-231.

[20] E. Rule, F.J. Suellentrop, T.A. Perls. Second-Order Instrumentation Systems with Frequency Dependent Stiffness and Damping. *The Journal of the Acoustical Society of America*, 31, 11, November 1959, pg.1457-1462.

[21] I.B. Crandall. *Theory of Vibrating Systems and Sound.* D. Van Nostrand Company, Inc., New Jersey, 1926. Chapter 1: Simple Vibrating Systems, pg. 1-41.

[22] G. Lévêque, P. Girard, S. Belaidi, G. Cohen Solal. Effects of Air Damping in Noncontact Resonant Force Microscopy. *Review of Scientific Instruments*, 68, 11, 1997, pg. 4137-4144.

[23] M. Christen. Air and Gas Damping of Tuning Forks. *Sensors and Actuators*, 4, 1983, pg. 555-564.

[24] K. Karrai, R.D. Grober. Piezoelectric Tip-Sample Distance Control for Near Field Optical Microscopes. *Applied Physics Letters*, 66, 1995, pg.1842-1844.

[25] D. Sarid. *Scanning Force Microscopy.* Oxford University Press, Oxford, 1991. Chapter 1: Mechanical Properties of Levers, pg. 1-19.

[26] E.J. Hearn. *Mechanics of Materials 1.* Third Edition, Butterworth-Heinemann, Oxford, 1997.

[27] D.G. Fertis. *Mechanical and Structural Vibrations.* John Wiley & Sons, Inc, New York, 1995. Chapter 1: Fundamentals of Vibratory Motion, pg 23-25, Chapter 2: Vibration Analysis of Simple Systems, pg 95-101.

[28] E. Volterra, E.C. Zachmanoglou. *Dynamics of Vibrations.* Charles E. Merril Books, Inc., Columbus, 1965. Chapter 4: Vibrations of Continuous Systems, pg. 257-439.

[29] S. Whitney. *Vibrations of Cantilever Beams: Deflection, Frequency, and Research Uses.* Available at: http://em-ntserver.unl.edu/Mechanics-Pages/Scott-Whitney/325hweb/Beams.htm, Last Visited On: January 2005.

[30] W.G. Cady. *Piezoelectricity.* McGraw-Hill, Inc., New York, 1946. Chapter 1: Introduction, pg. 1-9.

[31] V.E. Bottom. *Introduction to Quartz Crystal Unit Design.* Van Nostrand Reinhold Company, New Jersey, 1982. Chapter 6: Equivalent Circuit of the Quartz Resonator, pg. 82-101.

[32] W.P. Mason. *Electromechanical Transducers and Wave Filters.* D. Van Nostrand Company, Inc., New Jersey, 1942. Chapter 8: Application of Electromechanical Impedance Elements in Electrical Wave Filters, pg.248-291.

[33] W.H.J. Rensen, N.F. van Hulst, A.G.T. Ruiter, P.E. West. Atomic Steps with Tuning Fork Based Noncontact Atomic Force Microscopy. *Applied Physics Letters*, 75, 1999, pg 1640-1642.

[34] T.R. Albrecht, P. Grütter, D. Horne, D. Rugar. Frequency Modulation Detection Using High-Q Cantilevers for Enhanced Force Microscope Sensitivity. *Journal of Applied Physics*, 69, 1991, pg. 668-673.

[35] H. Edwards, L. Taylor, W. Duncan, A.J. Melmed. Fast, High-Resolution Atomic Force Microscopy Using a Quartz Tuning Fork as Actuator and Sensor. *Journal of Applied Physics*, 82, 1997, pg. 980-984.

[36] P. Horowitz, W. Hill. *The Art of Electronics.* Cambridge University Press, Cambridge, 1989. Chapter 7: Precision Circuits and Low Noise Techniques, pg. 361-466.

[37] H.D. Young. University Physics. Eighth Edition, Addison-Wesley, New York, 1992. Chapter 16: Thermal Properties of Matter, pg. 450-481.

[38] W.F. Egan. *Phase-Lock Basics.* John Wiley & Sons, Inc., New York, 1998. Chapter 3: Loop Components, pg.31-43.

[39] A.G.T. Ruiter, J.A. Veerman, K.O. van der Werf, N.F. van Hulst. Dynamic Behavior of Tuning Fork Shear Force Feedback. *Applied Physics Letters*, 71, 1997, pg. 28-30.

[40] F.J. Giessibl. High-Speed Force Sensor for Force Microscopy and Profilometry Utilizing a Quartz Tuning Fork. *Applied Physics Letters*, 73, 1998, pg. 3956-3958.

[41] J.J. DiStefano(III), A.R. Stubberud, I.J. Williams. *Feedback and Control Systems.* Second Edition, McGraw-Hill, Inc., New York, 1995. Chapter 4: The Laplace Transform and the Z-transform, pg. 74-114.

[42] J.G. Smits. Dynamic Admittance Matrix of Piezoelectric Cantilever Bimorphs. *Journal of Microelectromechanical Systems*, 3,1994, pg. 105-111.

[43] Piezoelectric Bimorph Properties. Available at: http://www.mide.com/quickpack_power-act/qp_piezo_material_properties.html. Last Visited 16 March 2005.

[44] J. Stewart. *Calculus Concepts and Contexts.* Brooks/Cole, New York, 1998.

[45] T.D. Rossing, N.H. Fletcher. *Principles of Vibration and Sound.* Springer-Verlag, 1995. Chapter 3: Two Dimensional Systems Membranes and Plates, pg. 65-92.

[46] P.M. Morse. *Vibration and Sound.* Second Edition, McGraw-Hill, Inc., New York, 1948. Chapter 5: Membranes and Plates, pg. 172-213.

[47] E.J. Hearn. *Mechanics of Materials 2.* Second Edition, Butterworth-Heinemann, Oxford, 1985. Chapter 22: Circular Plates and Diaphragms, pg. 623-650.

[48] F.B. Seely, J.O. Smith. *Advanced Mechanics of Materials.* Second Edition, John Wiley & Sons, New York, 1952. Chapter 8: Flat Plates, pg. 220-264.

[49] A.P. Boresi, R.J. Schmidt, O.M. Sidebottom. *Advanced Mechanics of Materials.* Fifth Edition, John Wiley & Sons, Inc., New York, 1993. Chapter 13: Flat Plates, pg. 509-542.

[50] J. Tapson, J.R. Greene. The Resonant Behaviour of Segmented Piezoceramic Tubes. *Review of Scientific Instruments*, 68, 1997, pg. 2797-2799.

[51] J. Greene. *An Adaptively Mutating Breeder Algorithm for Global Stochastic Optimisation.* Course Notes, EEE496S, University of Cape Town, 2003.

[52] T. de Bruyn, I. de Vries, B.J.P. Mortimer, J. Tapson. High Power Resonant Tracking Amplifier Using Admittance Locking. *Ultrasonics*, 39, 2001, pg.257-261.

[53] D. Stuart-Watson, J. Tapson. Simple Force Balance Accelerometer/Seismometer Based on a Tuning Fork Displacement Sensor. *Review of Scientific Instruments*, 75, 2004, pg. 3045-3049.

[54] ADXL05 1g-5g Single Chip Accelerometer Data Sheet. Available at: http://user.cs.tu-berlin.de/~remuss/files/datasheet_adxl05.pdf. Last Visited 14 August 2005.

[55] SM-4/7 Geophone Data Sheet. Available at: http://www.i-o.com/Products/Product_Datasheets/. Last Visted 14 August 2005.

[56] A. Barzilai, T. VanZandt, T. Kenny. Technique for Measurement of the Noise of a Sensor in the Presence of Large Background Signals. *Review of Scientific Intruments*, 69, 1998, pg. 2767-2772.

[57] J.S. Bendat, A.G. Piesol. *Engineering Applications of Correlation and Spectral Analysis.* John Wiley & Sons, New York, 1980. Chapter 3: Correlation and Spectral Density Functions, pg. 43-76.

Appendix A

Appendix

A.1 Simple Bending Theory

A.1.1 Stress and Strain

Consider a cubic body located in a rectangular coordinate system. A force F_x acts perpendicular to one of the faces of the cube along the x-axis. If each face of the cube has an area A the normal stress on the face perpendicular to the force can be defined as:

$$\sigma_{xx} = \frac{F_x}{A_x} \tag{A.1}$$

The faces in the other two planes would experience a shear stress τ parallel to the face that is defined using the formula:

$$\tau_{yx} = \frac{F_x}{A_y} \text{ or } \tau_{zx} = \frac{F_x}{A_z} \tag{A.2}$$

The body along with the stresses are shown in Figure A1.1.

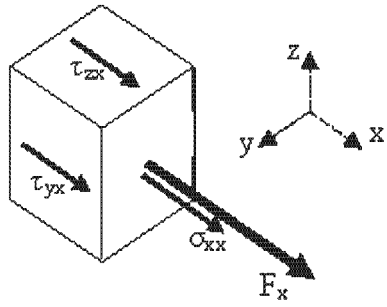

Figure A1.1: The Normal and Shear Stresses in the Cubic Body due to the Application of Force F_x.

This body when acted on by the force will experience a deformation. This deformation will occur in two ways, there will be an elongation of the cube parallel to the force and as volume remains constant there will be a reduction in of the plane perpendicular to the force. The first deformation or strain ϵ describes the elongation δ with respect to the cube length l and is defined as:

$$\epsilon = \frac{\delta}{l} \tag{A.3}$$

The strain ϵ is in the same direction and proportional to the stress. The proportionality can be expressed by

$$\sigma = E\epsilon \tag{A.4}$$

where E is the Youngs modulus of the material. The second type of strain γ defines the deformation perpendicular to the force. It is proportional to the shear stress and their relationship is given by:

$$\tau = G\gamma \tag{A.5}$$

The constant G is the shear modulus of elasticity. The constants E and G described the body's resistance to the force.

A.1.2 Moments

Considered the unstressed beam in Figure A1.2(a) undergoing pure bending to a radius R as shown in Figure A1.2(b). As a result of this bending the upper part of the beam will be subject

to compression and the lower part would be subject to tension. Therefore somewhere between the upper and lower surfaces there will be points at which the stress is zero. The line formed by all the points is termed the neutral axis and for uniform symmetrical beams it also forms the axis of symmetry in the unbent beam.

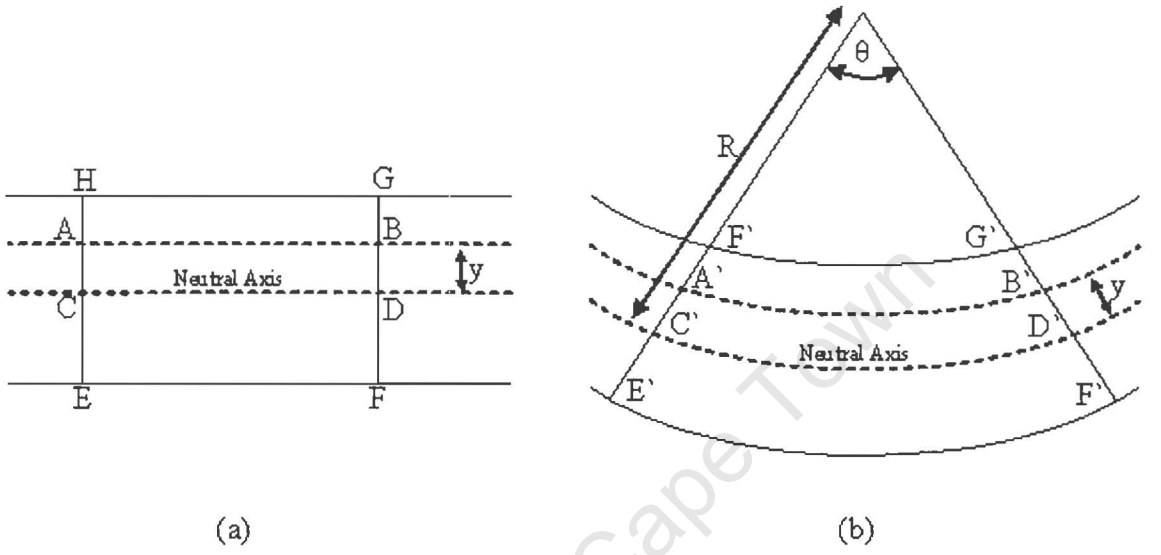

Figure A1.2: Beam Subject to Pure Bending.

Looking now at the cross sections HE and GF which are parallel in Figure A1.2(a). In the bent beam these sections remain straight but are no longer parallel but will rather subtend to some angle θ. Consider a fibre AB in the material a distance y away from the neutral axis. This fibre will be compressed to form $A`B`$ with the strain along the fibre given by:

$$\text{Strain in Fibre AB} = \frac{Extension}{Original\ Length} = \frac{AB - A`B`}{AB} \tag{A.6}$$

As AB is equal to CD and since the neutral axis has no stress $CD = C`D`$ the strain can be re-written as:

$$Strain = \frac{A`B` - C`D`}{C`D`} = \frac{(R+y)\,\theta - R\theta}{R\theta} = \frac{y}{R} \tag{A.7}$$

Equating the Equation A.7 for strain with Equation A.4 gives:

$$\frac{\sigma}{E} = \frac{y}{R} \text{ or } \frac{\sigma}{y} = \frac{E}{R} \tag{A.8}$$

Now looking at the cross-section of the beam in Figure A1.3:

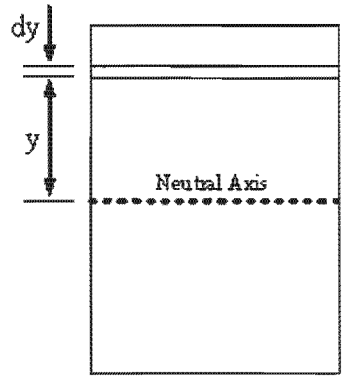

Figure A1.3: Cross Section of the Beam.

The stress on the fibre at a distance y from the neutral axis is:

$$\sigma = \frac{E}{R}y \tag{A.9}$$

If the strip is of area dA the force on the strip is:

$$F = \sigma dA = \frac{E}{R}ydA \tag{A.10}$$

This has a moment about the neutral axis of:

$$Fy = \frac{E}{R}y^2dA \tag{A.11}$$

The total moment for the whole cross section is therefore:

$$M = \sum \frac{E}{R}y^2dA = \frac{E}{R}\sum y^2dA \tag{A.12}$$

The term $\sum y^2dA$ is called the second moment of area of the cross section and given the symbol I, therefore:

$$M = \frac{E}{R}I \tag{A.13}$$

Combining Equation A.13 with Equation A.8 gives the important bending theory equation as:

$$\frac{M}{I} = \frac{E}{R} = \frac{\sigma}{y} \tag{A.14}$$

A.2 Mass Spring Systems

A.2.1 Damped Harmonic Oscillator

Consider an object attached to a spring moving through a viscous fluid. Three balanced forces act on the object. The spring exerts a restoring force proportional to the displacement of the object from the neutral position. Moving through the viscous fluid saps energy from the mass and this results in a damping force exerted by the fluid on the object proportional to the velocity of the object. The third force acting on the object will be from Newton's second law and thus proportional to the acceleration of the object. The three forces are given by the following equations,

$$\begin{aligned} Spring\ Force &= -k\ x \\ Damping\ Force &= -\gamma \dot{x} \\ AccelerationForce &= -m\ddot{x} \end{aligned} \tag{A.15}$$

where k is the spring constant of the spring, γ is the viscous damping factor of the fluid and m is the mass of the object. The forces are equated to form the equation:

$$m\ddot{x} = -k\ x - \gamma \dot{x} \tag{A.16}$$

Equation A.16 is a linear, homogenous equation, the dependant variable x or a derivative of it is present in each term linearly. The coefficients are merely constants . This suggests a solution of the form $x = Ae^{pt}$, as differentiating an exponential produces the exponential times

a constant, which in this case is p.

$$\begin{aligned} x &= Ae^{pt} \\ \dot{x} &= Ape^{pt} \\ \ddot{x} &= Ap^2e^{pt} \end{aligned} \tag{A.17}$$

Substituting Equation A.17 into Equation A.16 gives:

$$m\left(Ap^2e^{pt}\right) = -k\left(Ae^{pt}\right) - \gamma\left(Ape^{pt}\right) \Longrightarrow mp^2 = -k - \gamma p \tag{A.18}$$

Application of the quadratic formula yields the following solution for Equation A.18:

$$p = \frac{-\gamma}{2m} \pm \sqrt{\left[\left(\frac{\gamma}{2m}\right)^2 - \frac{k}{m}\right]} \tag{A.19}$$

Using this equation for p a new solution to the one given in Equation A.17 can be given,

$$x(t) = A_1e^{p_+t} + A_2e^{p_-t} \tag{A.20}$$

where A_1 and A_2 are constants and p_+ and p_- are the roots given by Equation A.19. Substituting Equation A.19 into Equation A.20 gives the following equation:

$$x\left(t\right) = e^{-\left(\frac{\gamma}{2m}\right)t}\left(A_1e^{\left[\sqrt{\left(\frac{\gamma}{2m}\right)^2 - \frac{k}{m}}\right]} + A_2e^{-\left[\sqrt{\left(\frac{\gamma}{2m}\right)^2 - \frac{k}{m}}\right]}\right) \tag{A.21}$$

The factor $e^{-\left(\frac{\gamma}{2m}\right)t}$ is an exponentially decaying function of time, which indicates that the damped vibratory motion has an exponentially decaying amplitude with time. By examining the terms under the square root three different types of operation can be discerned: over, critical and underdamping.

1. Over Damping - If the sum of the terms under the radical is positive the inequality $\left(\frac{\gamma}{2m}\right)^2 > \frac{k}{m}$ is formed. This is known as the condition of overdamping In this case the motion is aperiodic and p_+ and p_- are always real and negative.

2. Critical Damping - If the sum of the terms is equal to zero then $\left(\frac{\gamma}{2m}\right)^2 = \frac{k}{m}$, yielding $p_{\pm} = \frac{-\gamma}{2m}$ this type of damping represents the transition from oscillatory to non-oscillatory motion. and is known as the condition of critical damping. In this case if motion starts at an initial position and velocity the mass will return to rest without oscillation.

3. Under Damping - The condition of under damping occurs when the sum of the terms under the square root is negative. Under this condition, the spring mass system will vibrate with decreasing amplitude. Most structural and mechanical systems are under the influence of light damping making this condition the subject of further study in this section.

A.2.1.1 Under Damping

The condition of under damping occurs when the condition $\left(\frac{\gamma}{2m}\right)^2 < \frac{k}{m}$ is met and the argument of the square root operation is negative. Factoring out $-\frac{k}{m}$ Equation A.19 can be re-written as:

$$p = \frac{-\gamma}{2m} \pm i\sqrt{\frac{k}{m}}\left[\sqrt{1 - \frac{m}{k}\left(\frac{\gamma}{2m}\right)^2}\right] \tag{A.22}$$

Using the abbreviations $\omega_o = \sqrt{\frac{k}{m}}$ and $\tau = \frac{m}{\gamma}$ Equation A.22 can be re-written as:

$$p = -\frac{1}{2\tau} \pm i\omega_o\sqrt{1 - \left(\frac{1}{2\tau}\right)^2\left(\frac{1}{\omega_o^2}\right)} \tag{A.23}$$

Now using the Euler identity $e^{a+ib} = e^a\left(\cos(b) + i\sin(b)\right)$ the exponential factor in Equation A.17 can be re-written as:

$$e^{pt} = e^{\frac{-t}{2\tau}}\left(\cos\left(\left[\omega_o\sqrt{1 - \left(\frac{1}{2\omega_o\tau}\right)^2}\right]t\right) \pm i\sin\left(\left[\omega_o\sqrt{1 - \left(\frac{1}{2\omega_o\tau}\right)^2}\right]t\right)\right) \tag{A.24}$$

Similarly to Equation A.21 the first part of the equation gives the exponential time delay of the equation. This identifies τ as the characteristic damping time. The characteristic damping time is obviously inversely proportional to the damping constant γ. The trigonometric expressions of Equation A.24 produce the oscillations which are generally sinusoidal. If γ were zero so that τ is infinite, the oscillations would be at an angular natural frequency ω_o.

Reconstructing Equation A.19 as:

$$p_{\pm} = -\frac{1}{2\tau} \pm i\omega_o'$$

where $\omega_o' = \omega_o\sqrt{1-\left(\frac{1}{2\omega_o\tau}\right)^2}$ is the damped natural or resonant frequency. The general solution described by A.20 can now also be re-written as:

$$\begin{aligned} x(t) &= e^{\frac{-t}{2\tau}}\left[A_1\left(\cos\left(\omega_o't\right)+i\left(\sin\left(\omega_o't\right)\right)\right)+A_2\left(\cos\left(\omega_o't\right)-i\left(\sin\left(\omega_o't\right)\right)\right)\right] \\ &= e^{\frac{-t}{2\tau}}\left[\left(A_1+A_2\right)\cos\left(\omega_o't\right)+i\left(A_1-A_2\right)\sin\left(\omega_o't\right)\right] \end{aligned} \tag{A.25}$$

Constants A_1 and A_2 are chosen so that the initial conditions of motion are met. Equation A.25 and its derivative are evaluated at $t = 0$ which yields,

$$\begin{aligned} x\left(0\right) &= A_1 + A_2 \\ \dot{x}\left(0\right) &= -\frac{1}{2\tau}\left(A_1+A_2\right)+i\left(A_1-A_2\right)\omega_o' \end{aligned} \tag{A.26}$$

Solving and putting these values into Equation A.25 yields:

$$x(t) = e^{\frac{-t}{2\tau}}\left[\left(x\left(0\right)\right)\cos\left(\omega_o't\right)+\frac{1}{\omega_o'}\left[\dot{x}\left(0\right)+\frac{x\left(0\right)}{2\tau}\right]\sin\left(\omega_o't\right)\right] \tag{A.27}$$

The solution is now entirely real, meets the initial conditions and, as can be confirmed by substitution, satisfies Equation A.16. It describes damped oscillatory motion at an angular frequency ω_o'. The smaller the damping the closer ω_o' is to natural undamped frequency ω_o.

A.2.2 Energy

In the damped mass spring system the potential energy will be provided by the restoring force from the spring. This potential energy can be written as:

$$U\left(x\right) = -\int_{x_A}^{x}\left(-kx\right)dx + U\left(x_A\right) \tag{A.28}$$

If $x_A = 0$ and $U\left(0\right) = 0$, then the potential energy will be equal to $-kx^2$.

The viscous damping is a process that transfers energy from the mass to the fluid. There is no associated potential energy with this process and the energy associated with mass is written as:

$$E = \frac{1}{2}m\dot{x}^2 + \frac{1}{2}kx^2 \tag{A.29}$$

The damping is considered by how it reduces the numerical value of the energy with time. Differentiating the energy expression with respect to time yields:

$$\frac{dE}{dt} = m\dot{x} + kx \tag{A.30}$$

From Equation A.16

$$m\ddot{x} + kx = -\gamma\dot{x} \implies (m\ddot{x} + kx)\,\dot{x} = (-\gamma\dot{x})\dot{x}$$

therefore

$$\frac{dE}{dt} = m\dot{x}\ddot{x} + kx\dot{x} = -\gamma\dot{x}^2 \tag{A.31}$$

The right hand side of Equation A.31 is never positive, the damping always take energy from the system and never replaces any.

Equation A.31 gives the instantaneous rate of energy loss. For light damping the energy loss per cycle is quite small and the mass will make many oscillations before the cumulative effects of damping become apparent. For these cases averages over one period can become sufficient for system analysis. Equation 3.33 can be reduced to,

$$x = Ae^{\frac{-t}{2\tau}}\cos\left(\omega_o' t + \alpha\right) \tag{A.32}$$

where A and α are constants determined by the initial conditions. Now for light damping where $\omega_o\tau \gg 2\pi$ then $\omega_o' \approx \omega_o$, and for the differential of Equation A.32, the derivative of the exponential which would describe the slow change in amplitude can be ignored, this gives:

$$\dot{x} \approx -\omega_o A e^{\frac{-t}{2\tau}}\sin\left(\omega_o t + \alpha\right) \tag{A.33}$$

Equation A.31 for energy now becomes:

$$\frac{dE}{dt} \approx -\gamma\omega_o^2 A^2 e^{\frac{-t}{\tau}} \sin^2(\omega_o t + \alpha) \tag{A.34}$$

Using the identity $\sin^2(\alpha) + \cos^2(\alpha) = 1$ and the fact that $\sin^2(\alpha)$ and $\cos^2(\alpha)$ will have the same average amount, the sinusoidal component of Equation A.34 can be reduced to $\frac{1}{2}$ leaving:

$$\frac{dE}{dt} \approx -\frac{1}{2}\gamma\omega_o^2 A^2 e^{\frac{-t}{\tau}} \tag{A.35}$$

The energy equation A.29 can be similarly simplified as follows:

$$\begin{aligned} E &= \frac{1}{2}m\dot{x}^2 + \frac{1}{2}kx \\ &\approx \frac{1}{4}m\omega_o^2 A^2 e^{\frac{-t}{\tau}} + \frac{1}{4}kA^2 e^{\frac{-t}{\tau}} \\ &\approx \frac{1}{2}m\omega_o^2 A^2 e^{\frac{-t}{\tau}} \end{aligned} \tag{A.36}$$

where k is eliminated in terms of ω_o^2. Substituting Equation A.36 into Equation A.35 yields:

$$\frac{dE}{dt} = -\frac{1}{\tau}E \tag{A.37}$$

From Equation A.37 it can be seen that energy decays at a rate set by τ. Now the energy dissipated per period can be calculated and compared to the energy itself. Therefore if the energy dissipated per period is given by E_p

$$\begin{aligned} E_p &= \left|\frac{dE}{dt}\right| (period) \\ &= \frac{1}{\tau}|E|\frac{2\pi}{\omega_o} \end{aligned} \tag{A.38}$$

A comparison with the energy still stored takes the form,

$$\frac{E_p}{E} = \frac{2\pi}{\omega_o \tau} \tag{A.39}$$

When looking at the previous function it can be seen that the energy dissipated per period

compared to the energy left is

$$\frac{\frac{2\pi}{\omega_o}}{\tau} = \frac{Natural\ Period}{Damping\ Time} \tag{A.40}$$

which for light damping will be very small indeed.

A.2.3 Sinusoidally Driven Oscillator

Of all the forces that could be applied to the mass spring system, the most common is a force that varies sinusoidally with time. Considering a one degree mass spring system operating under viscous damping and subjected to a sinusoidal force $F\cos(\omega_d t)$. The differential equation of motion for the system is now of the form:

$$m\ddot{x} = -kx - \gamma\dot{x} + F\cos(\omega_d t) \Longrightarrow \ddot{x} = -\omega_o^2 x - \frac{1}{\tau}\dot{x} + \frac{F}{m}\cos(\omega_d t) \tag{A.41}$$

The solution of this equation consists of two parts the complimentary (transient) solution $x_c(t)$ and the particular (steady state) solution $x_p(t)$ so that,

$$x(t) = x_c(t) + x_p(t) \tag{A.42}$$

The complimentary or transient solution can be considered as the free vibration of the system and can be determined using the Equation 3.33 which can be re-written in reduced form as in Equation A.32 as,

$$x_c(t) = Ce^{\frac{-t}{2\tau}}\cos(\omega_0' t + \alpha) \tag{A.43}$$

The particular solution is based on the forcing function and can have either of the following forms,

$$\begin{aligned} x_p(t) &= A\cos(\omega_d t) + B\sin(\omega_d t) \\ x_p(t) &= Y\cos(\omega_d t + \varphi) \end{aligned} \tag{A.44}$$

Where the constants in each of the solutions are related as follows,

$$\begin{aligned} Y &= \sqrt{A^2 + B^2} \\ \tan(\varphi) &= \frac{B}{A} \end{aligned} \tag{A.45}$$

The solutions for the other components of the initial equation of motion can be developed from the first solution and are given below,

$$\begin{aligned} x_p(t) &= A\cos(\omega_d t) + B\sin(\omega_d t) \\ x_p(t) &= -\omega_d A\sin(\omega_d t) + \omega_d B\cos(\omega_d t) \\ x_p(t) &= -\omega_d^2 A\cos(\omega_d t) - \omega_d^2 B\sin(\omega_d t) \end{aligned} \tag{A.46}$$

Substituting these solutions into Equation A.41 yields:

$$-\omega_d^2 A\cos(\omega_d t) - \omega_d^2 B\sin(\omega_d t) = -\omega_o^2 A\cos(\omega_d t) - \omega_o^2 B\sin(\omega_d t) + \frac{1}{\tau}\omega_d A\sin(\omega_d t) - \frac{1}{\tau}\omega_d B\cos(\omega_d t) + \frac{F}{m}\cos(\omega_$$

$$\therefore \left(-\omega_d^2 A + \omega_o^2 A + \frac{1}{\tau}\omega_d B\right)\cos(\omega_d t) + \left(-\omega_d^2 B + \omega_o^2 B - \frac{1}{\tau}\omega_d A\right)\sin(\omega_d t) = \frac{F}{m}\cos(\omega_d t) \tag{A.47}$$

When $\sin(\omega_d t) = 0$, $\cos(\omega_d t) = 1$ and vice versa. Equation A.47 will be satisfied for all values of t if the expressions of the coefficients of both sine and cosine terms on both sides of the equation are matched. This gives,

$$\begin{aligned} -\omega_d^2 A + \omega_o^2 A + \frac{1}{\tau}\omega_d B &= \frac{F}{m} \\ -\omega_d^2 B + \omega_o^2 B - \frac{1}{\tau}\omega_d A &= 0 \end{aligned} \tag{A.48}$$

Solving the equations in A.48 simultaneously yields the following expressions for the con-

stants A and B:

$$\begin{aligned} A &= \frac{\frac{F}{m}\left(\omega_o^2-\omega_d^2\right)}{\left(\omega_o^2-\omega_d^2\right)^2+\left(\frac{1}{\tau}\omega_d\right)^2} \\ B &= \frac{\frac{F}{m}\frac{1}{\tau}\omega_d}{\left(\omega_o^2-\omega_d^2\right)^2+\left(\frac{1}{\tau}\omega_d\right)^2} \end{aligned} \tag{A.49}$$

Now substituting these solutions into Equation A.45 the constants Y and φ can be found,

$$\begin{aligned} Y &= \frac{\frac{F}{m}}{\sqrt{\left(\omega_o^2-\omega_d^2\right)^2+\left(\frac{1}{\tau}\omega_d\right)^2}} \\ \tan\left(\varphi\right) &= \frac{\frac{1}{\tau}\omega_d}{\omega_o^2-\omega_d^2} \end{aligned} \tag{A.50}$$

Using A.50 the particular solution $x_p\left(t\right)$ can now be written:

$$x_p\left(t\right) = \frac{\frac{F}{m}}{\sqrt{\left(\omega_o^2-\omega_d^2\right)^2+\left(\frac{1}{\tau}\omega_d\right)^2}}\cos\left(\omega_d t-\left(\tan^{-1}\left(\frac{\frac{1}{\tau}\omega_d}{\omega_o^2-\omega_d^2}\right)\right)\right) \tag{A.51}$$

and the complete solution can be written more simply as,

$$x\left(t\right) = Ce^{\frac{-t}{2\tau}}\cos\left(\omega_o' t+\alpha\right)+Y\cos\left(\omega_d t+\varphi\right) \tag{A.52}$$